THE UNIVERSITY *of* EDINBURGH

This thesis has been submitted in fulfilment of the requirements for a postgraduate degree (e.g. PhD, MPhil, DClinPsychol) at the University of Edinburgh. Please note the following terms and conditions of use:

This work is protected by copyright and other intellectual property rights, which are retained by the thesis author, unless otherwise stated.
A copy can be downloaded for personal non-commercial research or study, without prior permission or charge.
This thesis cannot be reproduced or quoted extensively from without first obtaining permission in writing from the author.
The content must not be changed in any way or sold commercially in any format or medium without the formal permission of the author.
When referring to this work, full bibliographic details including the author, title, awarding institution and date of the thesis must be given.

New Tools for Visualising Nanoparticle Drug Delivery

Sally Vanden-Hehir

THE UNIVERSITY *of* EDINBURGH

A thesis submitted for the degree of

Doctor of Philosophy

The University of Edinburgh

2019

Declaration

This thesis is submitted in part fulfilment of the requirement for the degree of Doctor of Philosophy at the University of Edinburgh. Unless otherwise stated, the work described in this thesis is original and has not been submitted previously in whole, or in part for any degree or qualification at this, or any other university. In accordance with the dissertation regulations as specified by The University of Edinburgh, this thesis does not exceed 100,000 words in length.

Sally Vanden-Hehir

August 2019

Acknowledgements

I would like to express my thanks to my supervisors. Firstly, to Alison Hulme; your enthusiasm for research and all things Raman is inspiring, and you have always given me the encouragement and freedom to pursue my own ideas. Thank you to Anna Williams for your invaluable advice on all my biology work, and for putting me in touch with others to help with my nanoparticle synthesis. Thanks also to Valerie Brunton for all your input and for your comments on my manuscripts. It has been a great inspiration to work alongside three talented women in science.

I thank the BBSRC and the Eastbio DTP for the funding which has allowed me to undertake this work. I am also grateful for the opportunity this programme gave me to carry out a three month internship. Thank you to everyone at Elsevier for welcoming me, and to all who made my time in Amsterdam so enjoyable.

With such an interdisciplinary project, many people have helped with my lab work, but without two people in particular my project would not have been what it was. Special thanks go to Stefan Cairns for synthesising PLGA-alkyne, and to Martin Lee for all of your help with the SRS imaging. I am extremely grateful for the expertise and effort you gave to my project.

Thank you Monica Kim, Matthew Swire, Marie Bechler, and anyone else who provided me with microglia. Thanks to Amanda Boyd and Matthew Swire for carrying out the live animal work for me, and for all your help and advice. Thank you to Lida Zoupi for all the time you took to help me with the brain slices and immunostaining. Thanks also to members of the Campopiano, Bradley and Clarke groups for generously letting me use your equipment, without this I would not have been able to carry out my experiments.

I would like to thank all members, past and present, of the Hulme group for being great lab mates for making the everyday life of my PhD so enjoyable. Thank you to my ‘line manager’ Richard Brewster and also to Fergus McWhinnie for all your input and advice, especially in my first year. Special thanks go to Alisia Sim and Alan Zhao for your friendship and support. Thank you also to all the members of the Williams and ffrench-Constant groups for making me feel so welcome at SCRM, and for answering all my biology questions.

My thanks go to all support staff in the school of chemistry and beyond whose hard work has made everyday life run smoothly. Thank you to Steve Mitchell for help with electron microscopy, Elizabeth Blackburn for DLS, and Margaret Paterson for NTA.

A massive thanks goes to my family for all their support and encouragement during this time, and especially to my mum for all of her proofreading. I am very lucky to have a professional author as a proof reader! Thanks to all my friends in Edinburgh and beyond who have made these four years so enjoyable.

Finally, to Eric. I can't even begin to count all of the ways you have helped me over these years, from taking out the bins to explaining principal component analysis to me! Thank you for always being there to listen to my problems, and for all your advice and support. Du bist ein kleiner Kuchen, ich liebe dich.

Abstract

Encapsulating drugs in polymeric nanoparticles (NPs) is becoming increasingly popular for targeted and sustained drug delivery. NP drug delivery systems can increase the lifetime of therapeutics *in vivo*, they can improve safety by allowing a lower dose to be administered, and they are able to pass the blood brain barrier. Chapter 1 will discuss the anatomy of the brain, how it can be affected by multiple sclerosis (MS) and why NP drug delivery has an important part to play in treating this disease.

Due to the nanoscale size of these drug delivery systems, it is challenging to image their uptake, distribution and fate in a biological environment. Raman scattering is a vibrational technique which can probe the chemical bonds in a sample, however, it is a very weak effect. Stimulated Raman scattering (SRS) is a dual laser technique which increases the observed Raman signal and has been used to image biological samples at video-rate. Intracellular contrast can be increased further by introducing spectroscopically bioorthogonal chemical labels to the NPs, which appear in the so called cell-silent region of the Raman spectrum. Previous work to image NPs with fluorescence and Raman microscopies will be discussed in Chapter 1.

In this thesis, Raman spectroscopy was used to image bioorthogonally labelled polymeric NPs in *in vitro* cellular and *ex vivo* tissue models of the brain. The polymer poly(lactic acid-*co*-glycolic acid) (PLGA) was chosen as a biocompatible and biodegradable polymer widely used in drug delivery. Chapter 2 describes the synthesis of PLGA with both carbon-deuterium and alkyne modifications which both produce Raman peaks in the cell-silent region. The optimisation of NP synthesis from these labelled polymers by the emulsification-evaporation method is discussed in Chapter 3.

In Chapter 4, the NPs synthesised from both the deuterium and alkyne analogues of PLGA were imaged with SRS in biological models of the brain. Tuning to the bioorthogonal peaks allowed imaging of the NPs without cellular background. Both NP analogues were imaged in primary rat microglia, the macrophages of the brain, and additionally the alkyne labelled NPs were imaged in *ex vivo* cortical mouse brain slices. Immunohistochemical analysis of these brain slices confirmed that the NPs were selectively taken up into microglia.

Lay Abstract

Delivering drugs to their target is of upmost importance for their success in treating diseases, and in reducing harmful side effects. One drug delivery strategy is to load drugs into biocompatible and biodegradable particles. This strategy is especially important for delivering drugs to the brain to treat diseases like MS. The brain is encased in a protective layer, which prevents many drug molecules from entering, but allows the passage of small particles.

In order to study the effects and distribution of these particles in the body, it is important to be able to visualise them. However, due to their small size (~1000 times smaller than a cell), imaging these particles can prove challenging. In this project, new particles have been developed that can be imaged by Raman spectroscopy, a technique which can fingerprint specific bonds inside molecules. It has been shown that these particles can be selectively imaged in isolated rat brain cells, and also in cultured slices of mouse brain. These promising results pave the way for future studies in live animals to better address drug targeting and improve the treatment of brain diseases.

Contents

Chapter 1 Introduction

1.1 Drug Delivery to the Brain

As the average age of our society increases, the prevalence of neurodegenerative diseases of the brain are also increasing.[1] There is extensive ongoing research into the development of drugs to treat these diseases, but the biology and anatomy of the brain can pose challenges for delivering these drugs to their target site.

1.1.1 Anatomy of the brain

The cells in the brain can be divided into neural cells which send and receive electrical messages, and non-neuronal glial cells which act to support and nourish the neurones. Glial cells include microglia which are the immune cells of the brain and act as macrophages to engulf foreign substances,[2] astrocytes which give support to the neurones,[3] and oligodendroglia which are involved in myelin production.[4] Myelin production is essential for fast electrical conductance in axons and will be discussed further in Section 1.1.2.

The blood vessels of the brain form part of the blood brain barrier (BBB) (Figure 1.1). While the skull acts to protect the brain against physical damage, the role of the BBB is to protect the brain from harmful chemicals and pathogens, and is a selectively permeable layer.

Blood vessels are lined with endothelial cells, and in areas other than the brain, there are pores between these cells that allow the diffusion of substances in and out of the blood. In the brain, these endothelial cells form tight junctions between each other which will only allow the selective diffusion of some molecules and gases. The BBB is supported further by astrocyte end feet and pericytes, which wrap around the blood vessel. Molecules that can freely permeate the BBB must be highly lipophilic and less than 500 Da.[5] Other essential molecules such as glucose are transported across the BBB by carrier-mediated transport. Unfortunately, many drug molecules do not fit the criteria for passage across the BBB, making the treatment of neurological diseases challenging.

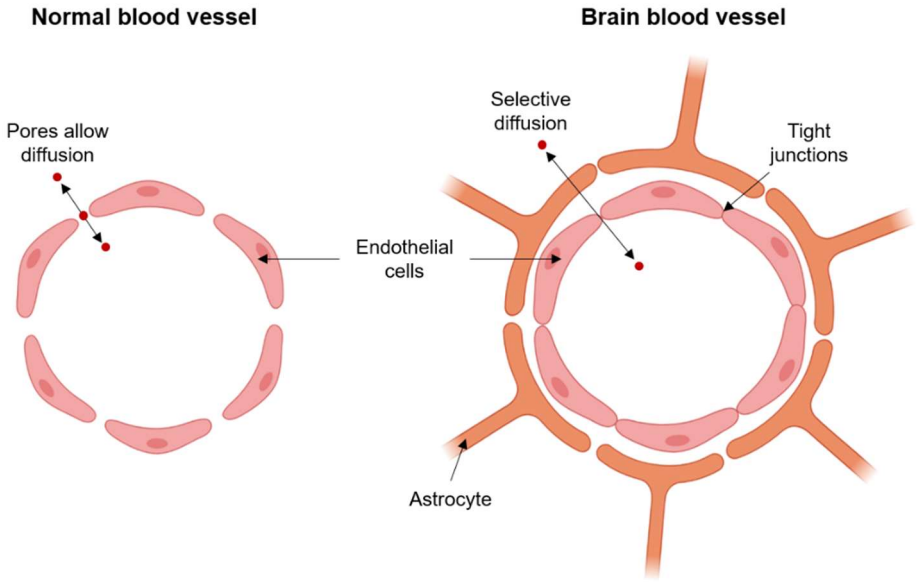

Figure 1.1 Anatomy of the BBB. Normal blood vessels have pores that allow diffusion of substances, but blood vessels in the brain have tight junctions that only allow selective transport. The BBB is supported by astrocyte end feet. Image created with Biorender.com.

1.1.2 Multiple sclerosis and remyelination

MS is a degenerative disease of the central nervous system (CNS) that is pathologically characterised with areas of focal demyelination in the brain.[6] Myelin is a fatty tissue composed of proteins and lipids, and forms a protective sheath around axons in the CNS.[7] Both healthy and demyelinated neurones are shown in Figure 1.2. Normally, oligodendrocytes will produce myelin sheaths that wrap around axons. This allows fast electrical conductance of signals down the axons via saltatory conduction between the gaps in the myelin sheath, known as nodes of Ranvier. In MS, the myelin sheath is damaged, degrades and, as efficient salutatory conduction can no longer occur, causes the symptoms and disabilities associated with MS.[8] As oligodendrocytes also provide metabolic support via the myelin sheath to the underlying axon,[9,10] loss of the myelin sheath can lead to axonal degradation and permanent disability.

Remyelination, a process where the myelin sheath is regenerated, can take place but is not efficient enough over time to regenerate all damaged myelin sheaths and halt the effects of MS. After demyelination, oligodendrocyte precursor cells (OPCs) are activated and will migrate to the site of injury. Once there, the OPCs will mature into oligodendrocytes which can then carry out remyelination.[8] The myelin sheaths on the

remyelinated axons have a smaller width and length than the original sheath, but can still lead to sufficient functional recovery of the axon.

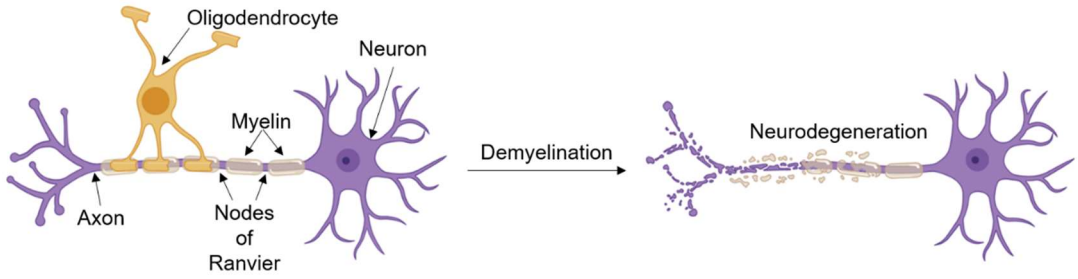

Figure 1.2 Demyelination causes neurodegeneration. In a healthy axon, oligodendrocytes produce a myelin sheath and electrical signals can jump between the nodes of Ranvier. After demyelination, neurodegeneration can occur (unless remyelination happens) leading to the symptoms of MS. Image created with Biorender.com.

MS is widely accepted to be an autoimmune disease whereby an incorrect immune response is triggered, causing the body's own immune system to degrade the myelin sheath. T cells are able to cross the BBB, stimulate local inflammation and lead to degradation of the myelin.[11] Immunosuppressant therapies can be given to reduce this inflammatory response and avoid new MS lesions in patients.[12] However, once the lesion has formed, can we promote remyelination and avoid subsequent neurodegeneration?

Currently, clinical trials are being carried out on therapies that promote remyelination. For example, clemastine fumarate (M_w = 460 Da, Appendix 2), which is currently licenced as an antihistamine, has recently been shown to enhance myelin repair in a preclinical model and improve nerve conduction a small amount (suggestive of remyelination) in humans.[13] Another potential therapy is Anti-LINGO-1 antibodies which act to block a protein called LINGO-1 which is known to inhibit myelin production.[14] However, because anti-LINGO-1 is an antibody (M_w = 83 kDa) which is large and hydrophilic, it has low penetration across the BBB and high doses have to be given. Alternative strategies are therefore needed to facilitate the delivery of drugs to the brain.

1.1.3 Strategies for delivering drugs to the brain

Some lipophilic small molecule drugs can naturally penetrate the BBB, but for other brain therapies, especially proteins, strategies have to be employed to help their passage.

In certain diseases, such as glioblastoma, the BBB can become leaky, and this has been taken advantage of to deliver drugs to the brain. In 2017, a clinical trial in humans with glioblastoma found that olaparib (M_w = 434.5 Da, Appendix 2), a drug licenced for treatment of ovarian cancers, was able to cross the BBB and was detected in the brain tumors.[15] The BBB can also be selectively opened for a short amount of time by the injection of microbubbles into the blood stream, followed by application of ultrasound. This technique has been used to deliver drugs to the brains of mice,[16] and in 2018, a phase I clinical trial successfully used this technique to open the BBB of Alzheimer's patients.[17]

The use of nanoscale drug delivery systems has also been demonstrated as an attractive way of delivering drugs to the brain.[18] This was first achieved in 1995 by Kreuter *et al.* who successfully delivered the peptidic therapeutic dalargin (M_w = 726 Da, Appendix 2) to the CNS of mice when encapsulated in poly(butylcyanoacrylate) (Appendix 3) NPs.[19] The NPs were phagocytosed by endothelial cells in the blood brain vessels and could then release the drug inside the brain.

In 2015, Rittchen *et al.* delivered leukaemia inhibitory factor (LIF) encapsulated inside PLGA NPs to the CNS of mice to promote remyelination in a MS disease model.[20] LIF was shown to promote the maturation of OPCs to myelinating oligodendrocytes *in vitro*, and remyelination *in vivo* was increased when mice were administered with LIF loaded NPs. However, although directly injected into the brain, the location of the NPs over time was not detectable in *ex vivo* brain tissue, highlighting the need for a robust imaging platform capable of visualising NPs in a biological environment.

1.2 Raman Spectroscopy for Biomedical Imaging

Raman spectroscopy is a vibrational analytical technique, which measures the inelastic scattering of light upon interaction with a molecule. This scattering produces a molecular fingerprint of a sample of interest. Raman spectroscopy was first observed by C.V. Raman in 1928 who noticed modified scattering of light when a beam of sunlight was used to irradiate a variety of samples.[21] Raman scattering is a very weak effect, as most of the light absorbed by a molecule is scattered at the same energy, in a process known as Rayleigh scattering. However, around one in every

million molecules will scatter light at either a lower or higher energy than the incident light, known as Stokes or anti-Stokes scattering respectively (Figure 1.3).[22]

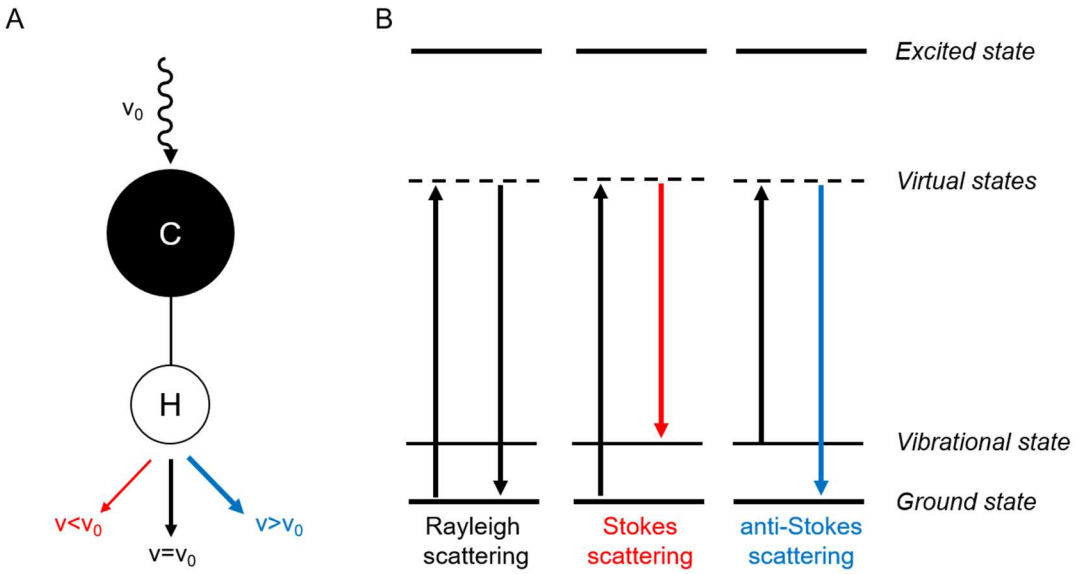

Figure 1.3 The energy of Raman scattering. A) The bonds in a molecule (for example C-H bonds) will be excited up on irradiation with incident light (v_0). Most of the light is scattered at the same frequency, but a small amount is Raman scattered at a higher or lower frequency. B) Jablonski energy level diagrams of Rayleigh ($v=v_0$), Stokes ($v<v_0$) and anti-Stokes ($v>v_0$) scattering.

1.2.1 Spontaneous Raman scattering

Spontaneous Raman spectroscopy is the simplest form of Raman spectroscopy where a single laser is used to excite all of the bonds in a molecule to produce a fingerprint. The Stokes scattering is usually detected since more molecules populate the ground state at ambient temperature, which leads to a stronger signal.

In contrast to infrared spectroscopy, water gives low Raman scattering meaning that it is an ideal technique for analysing biological samples.[23] Figure 1.4 shows the spontaneous Raman spectrum of microglia. Plotting Raman intensity resulting from excitation with a 532 nm laser against Raman shift gives rise to the characteristic cellular spectrum. There are large peaks for CH_3 (2939 cm^{-1}) and CH_2 (2856 cm^{-1}) which are indicative of cellular proteins and lipids respectively, and smaller peaks in the fingerprint region due to carbonyl bonds in the protein backbone (1663 cm^{-1}) and the aromatic ring in the amino acid phenylalanine (1004 cm^{-1}). There is an absence of any cellular peaks between 1800 and 2800 cm^{-1}, known as the cell-silent region.

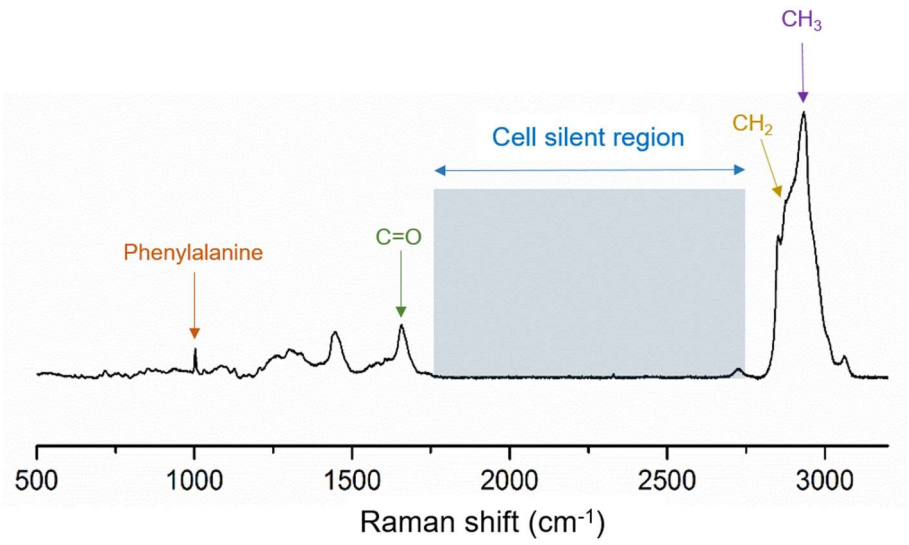

Figure 1.4 The spontaneous Raman spectrum of primary rat microglia. Microglia were analysed by spontaneous Raman spectroscopy, λ_{ex} = 532 nm, showing characteristic cellular peaks and the cell silent region.

The laser detection system for spontaneous Raman spectroscopy can be appended to a confocal microscope, and this system can be used to image cells and tissues by taking a Raman spectrum at each pixel.[24] This allows a distribution image of chemical species corresponding to cellular organelles to be built up, allowing label-free imaging.

1.2.2 Analysis of Raman imaging data

Large amounts of data can be generated when spontaneous Raman spectroscopy is interfaced with the spatial power of a scanning imaging technique. Hyperspectral Raman imaging, or Raman mapping, involves acquisition of a Raman spectrum at each pixel; it has been used to image plaques in the brains of Alzheimer's patients,[25] and for the diagnosis of cancer.[26–28] The raw data acquired from the Raman spectrometer may be processed with chemometric methods to distinguish small changes in spectroscopic peaks in order to de-convolute chemical substances in each pixel. Two common chemometric methods are principal component analysis (PCA) and vertex component analysis (VCA).[29,30] Both methods allow the deconvolution of each pixel's spectrum into main spectral components which can then be used to build up a quantitative representation of each cell.

1.2.3 Surface enhanced Raman scattering

Since Raman scattering is a very rare event, acquisition of spectra from biological specimens can be slow and have low intensity. As such, various chemical and

instrumental methods have been designed to amplify the Raman signal. Surface enhanced Raman spectroscopy (SERS) is a technique where a Raman reporter is appended to a roughened metal surface,[31] usually a gold or silver NP, to achieve an enhancement of signal in the order of 10^4 to 10^8 compared to spontaneous Raman.[32] SERS has been used for many biological applications such as lipid bilayer characterisation,[32] sensing intracellular redox potentials,[33] and pathogen diagnosis.[34]

1.2.4 Coherent Raman scattering

Coherent Raman scattering describes non-linear techniques where two incident lasers are used to excite and image a particular vibration of interest and increase Raman signal. Coherent anti-Stokes Raman scattering (CARS) and SRS are two coherent Raman techniques which have been used in many biological applications.[35,36] CARS uses two lasers, the pump laser (ω_p) and Stokes laser (ω_s), which interact with the sample in a four-wave mixing process to generate signal at the anti-Stokes frequency, Ω ($\omega_{as} = 2\ \omega_p - \omega_s$) (Figure 1.5 A). CARS can achieve video-rate imaging of biological samples, and is also suited to depth analysis of cells and tissues.[37] When Ω matches a molecular vibration of interest, contrast is derived from the chemical bonds in the sample,[38] but the process can also occur in non-resonant conditions leading to issues with high background noise.

The development of SRS for biological imaging overcame this issue as it does not suffer from non-resonant background.[39,40] Like CARS, SRS also employs the excitation of a sample with a pump and Stokes laser, and SRS occurs when Ω matches a molecular vibration (Figure 1.5 A). The stimulated emission is detected as a loss of intensity in the pump beam (stimulated Raman loss, SRL) or a gain in intensity of the Stokes beam (stimulated Raman gain, SRG).[41] SRL and SRG do not occur when Ω does not match a molecular vibration, and so there can be no non-resonant background. There is also a quantitative linear relationship between concentration of a molecule of interest and SRS intensity.[42] Compared to spontaneous Raman spectroscopy, SRS gives a signal enhancement in the order of 10^8,[43] and also a 1000 fold improvement in the speed of image acquisition, making it highly suited to live biological imaging.[44]

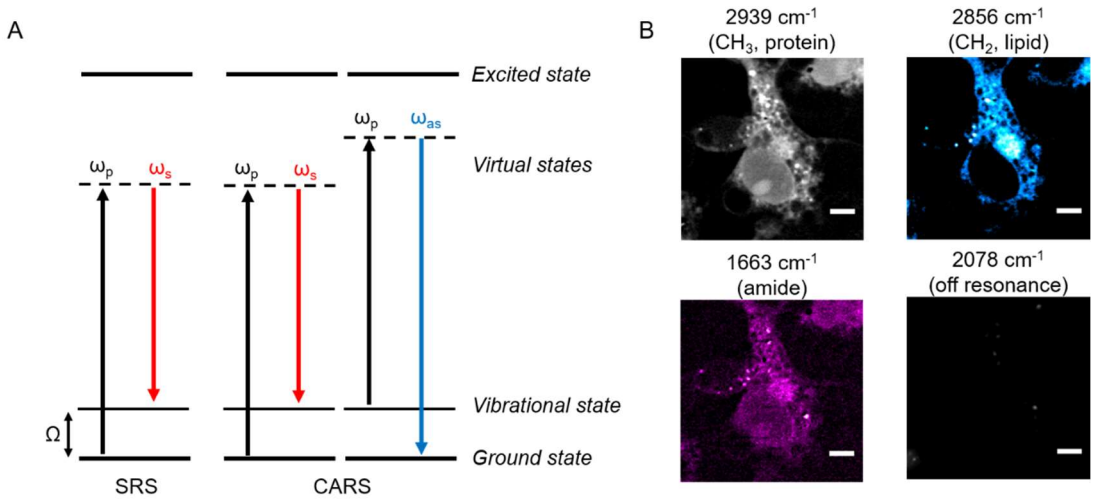

Figure 1.5 Coherent Raman scattering. A) Energy level diagrams showing the process of SRS and CARS. In SRS, a sample is excited with a pump and Stokes laser to create an image when Ω matches a molecular vibration. CARS is a four wave mixing process where Ω is tuned to the anti-Stokes frequency. B) SRS images of primary rat microglia when Ω = 2939 cm^{-1} (CH_3, proteins, grey), 2856 cm^{-1} (CH_2, lipids, cyan), 1663 cm^{-1} (amide I, magenta) and 2078 cm^{-1} (off-resonance, grey). Scale bars = 5 μm.

Figure 1.5 B shows representative SRS images acquired of a microglia. Tuning Ω to the large CH_3 peak at 2939 cm^{-1} produces a label-free image indicative of the cellular protein content. Similarly, tuning Ω to 2856 cm^{-1} builds up a strong signal from the CH_2 content which is present in membranous structures in the cell and absent from the nucleus. The amide I peak at 1663 cm^{-1} also shows the cellular proteins, but with a weaker signal than the CH_3 peak. Importantly, tuning to 2078 cm^{-1}, which is in the cell-silent region, produces very little signal.

1.2.5 Bioorthogonal Raman labels

Bioorthogonal chemical reactions are defined as ones that can react with, or label, biomolecules in their natural environment without causing any toxicity or perturbation to the living system.[45] As such, the term bioorthogonal has been adopted for Raman labels that consist of bonds not found in the native biological environment and lie in the cell-silent region, but that will also not cause toxicity.

As shown in Figure 1.4, there is a region absent of any cellular Raman peaks from ~1800–2800 cm^{-1}. This region can be exploited with small, bioorthogonal chemical labels so that molecules of interest can be imaged free of cellular background. Examples of these labels are alkynes (C≡C), nitriles (C≡N), azides (N_3) and carbon-

deuterium bonds (C-D). An advantage of Raman imaging over fluorescence is that these chemical labels are small compared to fluorophores which should limit perturbation of biological function.[46] Molecules that already contain one of these bonds in their natural structure can be imaged label-free, for example the tyrosine kinase inhibitor neratinib **1** which contains an intrinsic nitrile (Figure 1.6 A).[47] Molecules can also be chemically modified to contain one of these bonds.

The majority of previous work has focused on alkyne bioorthogonal labelling because of its superior Raman signal.[46] 5'-Ethynyl-2'-deoxyuridine (EdU) **2** is an analogue of the nucleobase thymine and is often used to image DNA in live cells, either by conjugation of a fluorophore to the alkyne through a copper-catalysed azide-alkyne click (CuAAC) reaction, or more recently by imaging the alkyne with SRS microscopy (Figure 1.6 B).[42] Hu *et al.* have produced an alkyne tagged analogue of glucose **3** and showed that it is taken up into various cell and tissue types, with Figure 1.6 C showing uptake into mouse neurones.

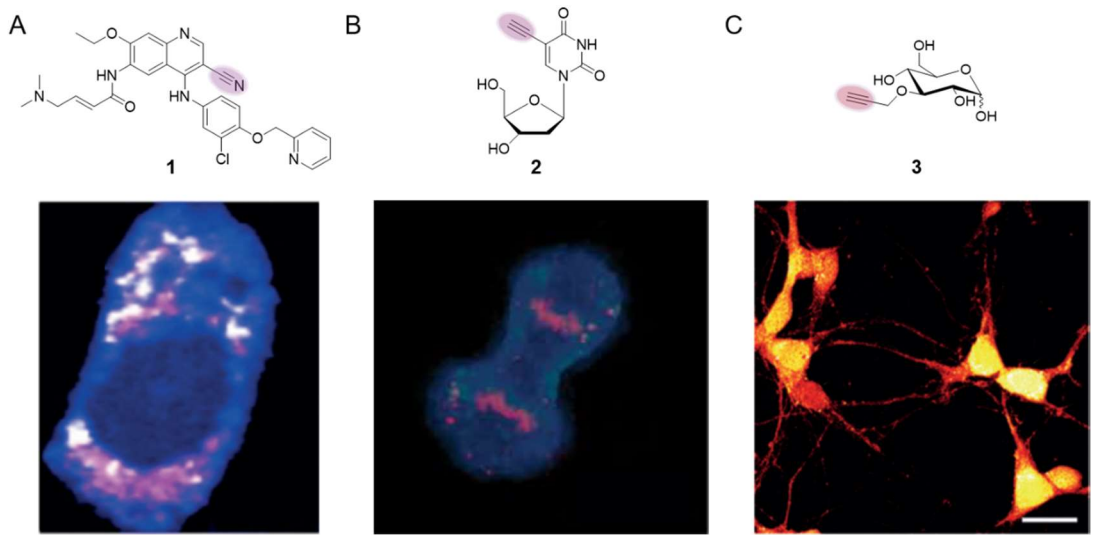

Figure 1.6 Imaging with bioorthogonal Raman labels. A) The tyrosine kinase inhibitor neratinib **1** contains an intrinsic nitrile and was imaged by Raman spectroscopy in SKBR-3 cells, C-H in blue (cellular proteins) and C≡N in red (neratinib). Reproduced with permission,[47] copyright John Wiley and Sons. B) EdU **2** allows visualisation of cell division in HeLa cells, C=O in blue (cellular proteins) and C≡C in red (DNA). Reproduced with permission,[42] copyright Springer Nature. C) Primary mouse neurones can be imaged when incubated with alkyne labelled glucose **3**. Scale bar = 40 μm. Reproduced with permission,[48] copyright John Wiley and Sons.

1.2.6 Medical applications of Raman spectroscopy

Raman spectroscopy is highly compatible with biological samples, and is also non-destructive, so has become an attractive analytical technique for many biomedical applications.[49] Spontaneous Raman has been used for label free diagnostics on tissue samples, as healthy and diseased cells will often display different spectroscopic fingerprints,[50] and coherent Raman imaging methods can be used in parallel with traditional histological staining.[51] The majority of diagnostic studies have been carried out on cancers. Metastatic tumours are often associated with expression of surface sialic acid. Shashni *et al.* used a SERS probe to target this sialic acid to better diagnose metastatic cancers.[52] Raman spectroscopy can also be combined with other analytical techniques such as fluorescence or mass spectrometry to give a more detailed picture of the properties of the sample.[53]

Raman is also compatible with fibre-optics, and Raman probes have been attached to the end of probes used in endoscopies to provide *in vivo*, live spectroscopic information. Near infrared excitation lasers (e.g. 785 nm) are usually used for *in vivo* applications for enhanced tissue penetration, and to limit tissue auto-fluorescence which can easily mask the Raman signal.[54] Again, cancer diagnosis has been prominent in the field of Raman fibre-optics. In 2017, Lin *et al*. reported Raman diagnosis of nasopharyngeal carcinoma, a type of throat cancer, during endoscopy.[55] This involved study of 57 healthy and 38 cancer subjects, and the diagnostic accuracy was 93%. As well as during endoscopy, Raman probes have also been used to diagnose skin cancer.[56,57] These studies show the potential of Raman spectroscopic analysis to give real-time clinical diagnostics without the invasiveness of a biopsy.

1.3 Nanoparticle Imaging

As discussed in Section 1.1.3, NP drug delivery has the potential to increase *in vivo* efficacy and deliver drugs to the brain. In order to study the mode of action of the NPs and to address safety concerns, it is critical to be able to image the NPs in a biological environment. Previously, polymeric and lipid-based NPs have been imaged using fluorescence, confocal Raman and coherent Raman microscopies.[58] When imaging a fluorescent payload, this can leak out of the NP over time and can also suffer from photobleaching. In contrast, NPs can be imaged directly with Raman spectroscopy (Figure 1.7).

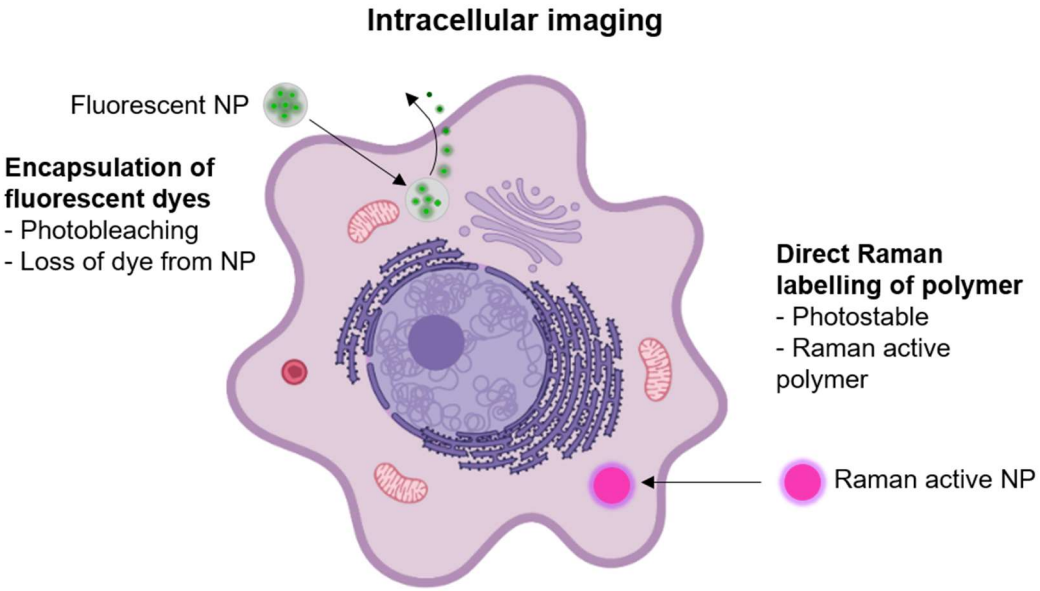

Figure 1.7 Strategies for intracellular imaging of NPs. NPs can be loaded with a fluorescent dye to allow imaging with fluorescence microscopy, but this can suffer from issues such as leakage of the dye or photobleaching. NPs can be imaged directly, with or without bioorthogonal labels, by Raman spectroscopy.

1.3.1 Fluorescence

Fluorescent NPs are common in biomedical imaging applications as they often have increased brightness, higher photostability and lower toxicity than traditional fluorophores.[59] A variety of materials can be formulated into fluorescent NPs including silica,[60] organic polymers and quantum dots.[61] Many of these NPs are commercially available with surface groups to allow further chemical functionalisation.

Andreiuk *et al*. synthesised a palette of fluorescent PLGA NPs and used them to label cells and track them over time in both co-cultures and zebrafish embryos.[62] They encapsulated red, blue and green cyanine dyes inside PLGA NPs and incubated these NPs with different cell lines to yield red, green and blue cells. Culturing cells with combinations of these NPs also produced yellow, magenta and cyan cells (Figure 1.8 A). These cells were then co-cultured and each cell line could be identified by its unique colour (Figure 1.8 B). This labelling strategy was also applied to cancer cells which were injected into a zebrafish embryo, allowing their fate to be tracked *in vivo*.

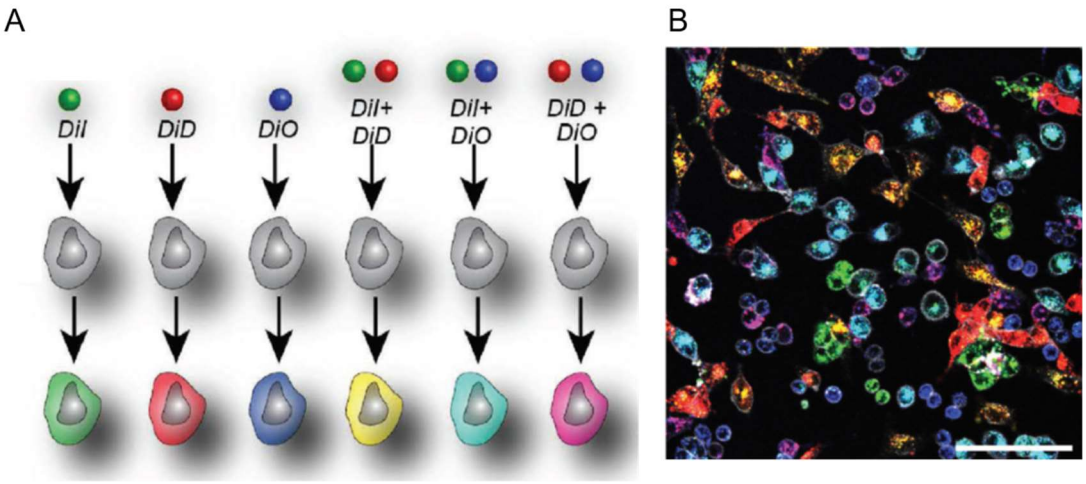

Figure 1.8 Labelling cells with fluorescent NPs. A) PLGA NPs were loaded with green (DiI), red (DiD) and blue (DiO) cyanine dyes and incubated with different cell lines. Incubating with two different NPs produced yellow, cyan and magenta coloured cells. B) Six different cell lines were cultured with NPs to produce six different coloured cells which were then co-cultured. Scale bar = 100 μm. Reproduced with permission,[62] copyright John Wiley and Sons.

Kalluru *et al.* used PLGA NPs to deliver antibiotics to a cellular model of *Myobacterium tuberculosis*, and also loaded the NPs with the fluorescent dye coumarin-6 in order to study their cellular location and fate.[63] They observed that the NP signal co-localised with lysosomes, and that the fluorescent signal dropped off steadily over 13 days. PLGA degrades by hydrolysis in an aqueous environment,[64] so the authors hypothesised that the loss of fluorescent signal was due to diffusion of the dye out of the NP over time, making it a good model of intracellular drug release.

In addition to loading polymer NPs with a fluorescent dye, NPs can also be fabricated from fluorescent polymers. Conjugated polymer NPs are an attractive class of fluorescent NPs, and have been used for biomedical imaging and theranostic applications.[65,66] Poly(phenylene ethynylene) (PPE) (Appendix 3) is a conjugated polymer used for both imaging and drug delivery. Chen *et al*. loaded PPE NPs with the anticancer drug doxorubicin and showed that they could image the NPs with fluorescence microscopy, and that cell death was caused upon release of the drug.[67] Additionally, conjugated polymers capable of producing reactive oxygen species have been loaded into a NP matrix and targeted to cancer cells.[68] These NPs can be used for imaging, and photodynamic therapy when irradiated.

1.3.2 Confocal Raman

As discussed in Section 1.2.1, a Raman laser can be appended to a confocal microscope to give a set-up capable of using Raman scattering to image cells and tissues by scanning across the sample and taking a Raman spectrum at each pixel. Confocal Raman has been used to image polymeric NPs both label-free, and utilising small bioorthogonal tags.

In 2017, Li *et al*. used water soluble analogues of the conjugated polymer PPE, which contains an intrinsic alkyne, to fabricate NPs which could then be imaged in HeLa cells with Raman microscopy by tuning to the alkyne peak.[69] The chemical structure of PPE makes it a good candidate for bioorthogonal Raman imaging because the alkyne produces a bioorthogonal peak in the cell silent region, and the conjugation of this alkyne bond between aromatic rings greatly enhances its Raman signal.

In a similar way to loading with fluorescent dyes, NPs can be loaded with a bioorthogonally Raman active payload and imaged. Two studies have used this approach to investigate the uptake of NPs to cells over time. The kinetics of NP uptake can be affected by particle size, composition and zeta potential.[70] Chernenko *et al*. loaded polymer NPs with a deuterated analogue of the drug ceramide (M_w = 408.7 Da, Appendix 2) which allowed the NPs to be visualised in SKOV-3 cells after VCA (Figure 1.9 A).[71] SKOV-3 cells are a model of ovarian cancer and are known to express epidermal growth factor receptor (EGFR). The NPs could be targeted to EGFR and these NPs were shown to be preferentially taken up into the cells over non-targeted NPs.

Matthäus *et al*. loaded PLGA-NPs with β-carotene which allowed the NPs to be imaged with Raman spectroscopy in murine NIH-3T3 cells.[72] β-Carotene (M_w = 537 Da, Appendix 2) has an extended conjugated structure, and this means that resonance Raman spectroscopy can be employed where the energy of the incident laser matches the electronic transition of the sample. This can lead to an enhancement of Raman signal of 10^3 to 10^4 over spontaneous Raman spectroscopy,[73,74] which in turn allowed the uptake of the NPs to be imaged over time (Figure 1.9 B).

The uptake of deuterated liposomes has also been studied by Raman spectroscopy.[75] One treatment group of liposomes were conjugated to TAT peptide, an amino acid sequence known to increase cellular penetration.[76] It was found that the TAT-

conjugated liposomes were visible in MCF-7 cells after 6 hours, while the un-conjugated liposomes were not detected until 12 hours.

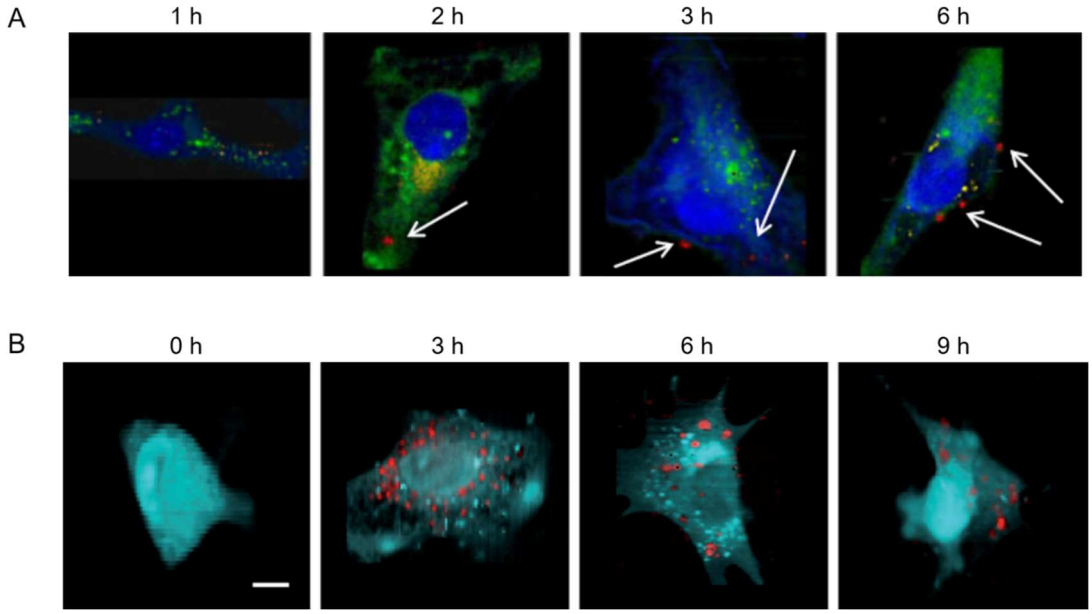

Figure 1.9 Imaging NPs with confocal Raman. A) The uptake of EGFR targeted NPs to SKOV-3 cells over time shows intracellular NPs after two hours. Images are created from VCA analysis by overlaying the cell body and nucleus (blue), membranous organelles (green), early endocytic vesicles (yellow), and nanoparticles (red). White arrows show regions of nanoparticle aggregation. Reproduced with permission,[71] copyright Springer Nature. B) The uptake of β-carotene loaded PLGA nanoparticles into murine NIH-3T3 cells by VCA analysis showing the cell body (cyan) and nanoparticles (red). Scale bar = 10 μm. Reproduced with permission,[72] copyright John Wiley and Sons.

In addition to studying NP uptake, the degradation of NPs can be inferred by observing their signal reduction with Raman imaging. This is important for addressing safety concerns about the long-term fate of NPs. In 2004, van Apeldoorn *et al.* used spontaneous Raman spectroscopy to study the degradation of PLGA microspheres in macrophages.[77] PLGA degrades via hydrolysis of its ester bonds, and this corresponded to a decrease in the ester peak (1768 cm^{-1}) of the microspheres after being exposed to macrophages for two weeks. Figure 1.10 A shows the decrease in this ester peak, and that there is also an increase in cellular peaks (1658, 1440 and 1004 cm^{-1}) which fill the void left by the microsphere. Control experiments showed that microspheres not exposed to macrophages did not show any degradation over the same timescale.

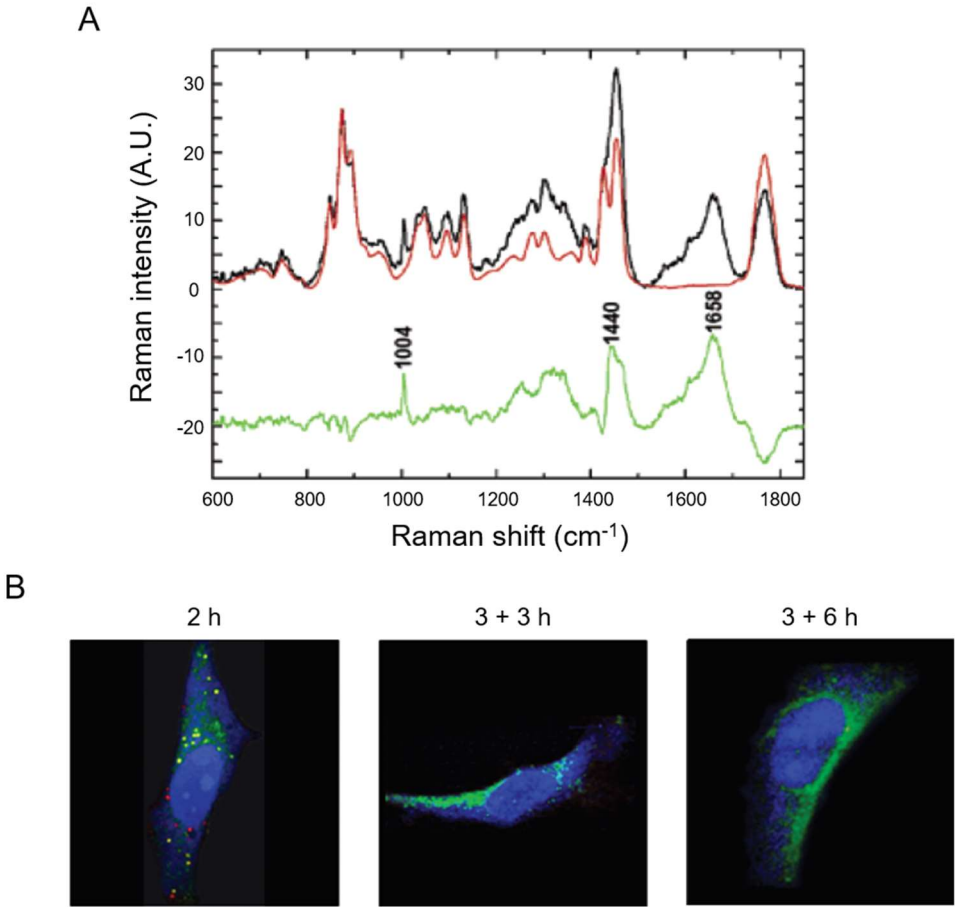

Figure 1.10 Raman analysis of NP degradation. A) The degradation of PLGA nanoparticles in macrophages over two weeks. Comparison of control PLGA (black spectrum) and PLGA that has been incubated with macrophages for two weeks (red spectrum). The green spectrum is the difference between the two. Reproduced with permission,[77] copyright American Chemical Society. B) Images of HeLa cells and PLGA NPs from VCA analysis showing proteins in blue, lipids in green, and nanoparticles in red. After two hours of incubation with NPs they were visible by Raman. After three hours incubation with NPs then three or six hours of incubation with fresh media, NPs were no longer visible. Reproduced with permission,[78] copyright American Chemical Society.

Chernenko *et al.* carried out label-free imaging of PLGA NPs in HeLa cells and used VCA to un-mix the individual spectra of the NPs from the proteins, lipids and membranous structures of the cell.[78] After two hours of exposure to the NPs, they were visible in the cells (Figure 1.10 B, left image). After three hours of exposure to the NPs, followed by exposure to fresh media for either three or six hours, it was found that the NPs were no longer visible (Figure 1.10 B, centre and right images).

1.3.3 Coherent Raman

As mentioned in Section 1.2.4, SRS and CARS have been popular techniques for biological imaging, including the imaging of NPs in cells and tissues. In 2017, Hu *et al.* synthesised styrene-based polymer dots with bioorthogonal alkyne, nitrile and carbon-deuterium Raman labels, and imaged them in HeLa cells with SRS.[79] These peaks all appear in the cell-silent region and do not overlap with each other making them mutually orthogonal. This is a significant advantage of Raman over fluorescence, as the narrow Raman peaks allow enhanced multiplex imaging. Figure 1.11 shows the three polymer dots imaged in live HeLa cells. A further experiment saw the three colours of dots being incubated with three different cell lines which were then co-cultured and could be sorted by their Raman label.

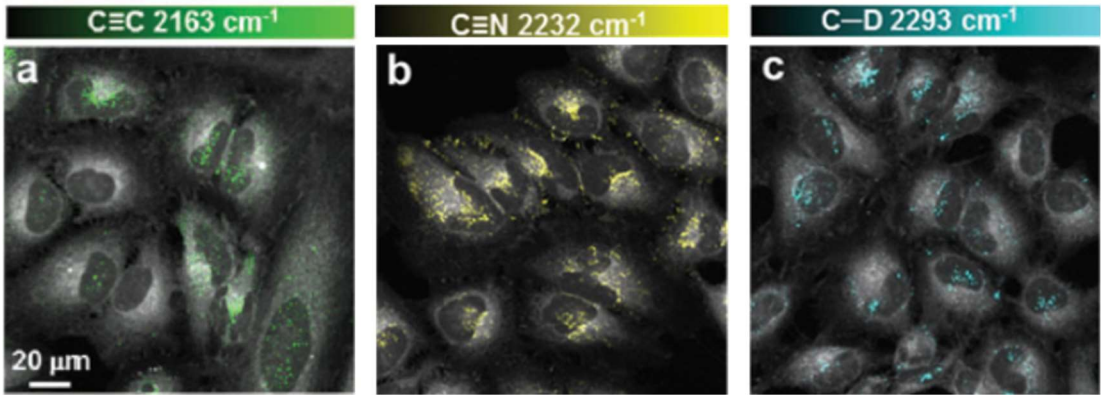

Figure 1.11 Imaging bioorthogonal polymer dots in HeLa cells with SRS. Alkyne (A), nitrile (B) and carbon-deuterium (C) bonds were introduced into styrene based polymer dots which were mutually orthogonal and could be imaged in live HeLa cells with SRS. Reproduced with permission,[79] copyright Royal Society of Chemistry.

Both CARS and SRS have also been used to image NPs in tissue samples. A tissue model of topical drug delivery to the skin was treated with deuterated methyl methacrylate NPs, and the penetration of these NPs into the skin was visualised with SRS.[80] Additionally, CARS has been used to assess the distribution of deuterated quaternary ammonium palmitoyl glycol chitosan NPs *ex vivo* in various organs.[81–83]

These studies show the potential of coherent Raman spectroscopy to image bioorthogonally labelled NPs in cells, and also to track their fate in *ex vivo* tissues.

1.4 Conclusions

The treatment of diseases of the brain, including MS, is hindered by the inability of many drugs to cross the BBB.[84] The encapsulation of drugs into biodegradable and biocompatible nanoscale carriers has been shown to successfully deliver drugs across the BBB in a variety of disease models. However, visualisation of this delivery proves challenging because of the small size and poor signal-to-background contrast of these NPs.

NPs have been imaged in cells and tissues with a variety of techniques including fluorescence and Raman microscopies. Raman scattering can provide a platform for label-free NP imaging, but small bioorthogonal labels have also been shown to improve contrast of these NPs against the cellular background. Raman spectroscopy therefore has the potential to allow the imaging of NPs for applications in drug delivery to the brain. Imaging NPs is particularly important for an enhanced understanding of drug delivery systems as more clinical NP applications are realised.

1.5 Project Aims

The aims of this project are to use SRS microscopy to image spectroscopically bioorthogonal analogues of PLGA NPs for applications in drug delivery to the brain. The previous work discussed in this chapter has highlighted how Raman scattering can be used to successfully image a variety of NPs in biological environments, with or without bioorthogonal labels. The aim of the current work is to conjugate bioorthogonal labels to PLGA, which is a highly relevant polymer for drug delivery and has not been imaged by SRS before. Once these polymers have been synthesised, they will be fabricated into NPs and surface functionalisation and targeting strategies will be explored. Finally, SRS microscopy will be used to image these NPs in cellular and tissue models of the brain.

Chapter 2 Synthesis of Bioorthogonal Raman Labelled Polymers

2.1 Introduction

2.1.1 Polymer synthesis

Polymers are versatile materials that are composed of a repeating unit of monomers. This broad definition of polymers includes natural biopolymers, such as proteins, which are made of repeating units of amino acids, and synthetic materials used for plastics such as polyesters, which will be the focus of this thesis.

As a global concern for the overuse and waste management of plastics grows, research into biodegradable polymers is becoming prominent.[85] Poly(lactic acid-*co*-glycolic acid) (PLGA) **8** is a biodegradable and biocompatible polyester that has been used extensively in medical research,[64,86–88] and has a circular 'lifecycle' as shown in Figure 2.1.

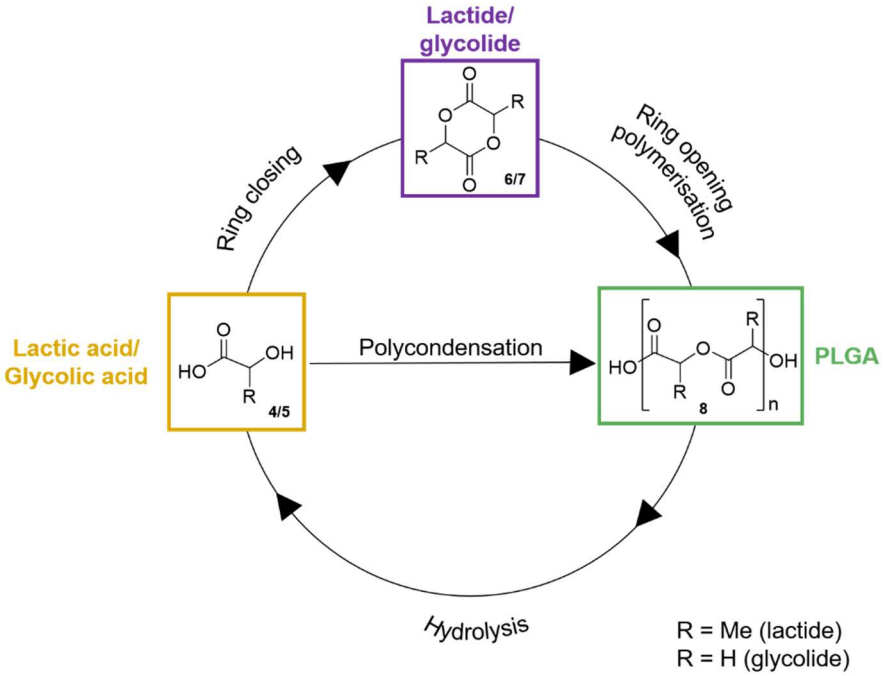

Figure 2.1 The lifecycle of PLGA. Lactic acid **4** and glycolic acid **5** can be polymerised via a polycondensation reaction to form PLGA **8**, which subsequently breaks down over many hydrolysis steps back to lactic and glycolic acid. Alternatively, lactic and glycolic acid can be ring closed to form the cyclic di-esters lactide 6 and glycolide 7 respectively, which can then undergo ring opening polymerisation (ROP) to produce higher molecular weight PLGA.

Synthesis of Bioorthogonal Raman Labelled Polymers

Lactic acid can be produced from biomass, which is a renewable source; however, there are significant costs associated with its isolation and purification. The advantage of using this method over traditional chemical synthesis is that D,L-lactic acid **4** can be prepared.[89] Glycolic acid **5** is an achiral α-hydroxy acid that has traditionally been produced chemically from fossil fuels, however, research is ongoing into renewable production, with glycolic acid biosynthesis in yeast reported in 2013.[90]

These two monomers can be co-polymerised to produce PLGA. The physical and chemical properties of the resulting polymer may be tuned by variation of the ratio of lactic acid to glycolic acid used in the monomer feedstock. A higher proportion of lactic acid produces a more hydrophobic polymer that will take longer to degrade in a biological environment; this is an important consideration when designing a drug delivery vehicle.[91,92]

Figure 2.1 shows two ways of producing PLGA: a direct polycondensation from lactic and glycolic acid, and ring opening polymerisation (ROP) from the cyclic di-esters lactide **6** and glycolide **7**. New developments of these methods of polymerisation for poly lactic acid (PLA) have recently been reviewed by Hu *et al*.[93]

Polycondensation is driven by the elimination of water as two molecules of lactic/glycolic acid join together in a condensation reaction. This process repeats itself to produce chains of increasing molecular weights. A limiting factor of this method is that the presence of water can cause the reverse hydrolysis reaction to take place, and thus limit the molecular weight of the polymer. However, steps can be taken to remove this water such as adding molecular sieves to the reaction, or fitting the set-up with a Dean-Stark trap.

ROP is an attractive process for polymer formation due to its ability to produce high molecular weights and low polymer dispersity (Đ),[94] and is often used in the production of PLGA **8**. Lactic/glycolic acid first have to be ring closed to their corresponding cyclic di-esters lactide and glycolide. Traditionally, this has been achieved by first dehydrating the α-hydroxy acid to form oligomers, and then adding a metal catalyst to cause a back-biting reaction which in turn produces the cyclic structure.[95] This is often a low yielding reaction requiring high temperatures and pressures, and produces a mixture of enantiomers. Current research is focused on finding more sustainable one-step syntheses of lactide including shape selective zeolite catalysis,[96] and a gas phase synthesis which has recently been reported by Heo *et al*.[97]

The ROP reaction proceeds via a coordination-insertion mechanism, generally catalysed by a metal alkoxide catalyst, with the mechanism shown in Scheme 2.1.

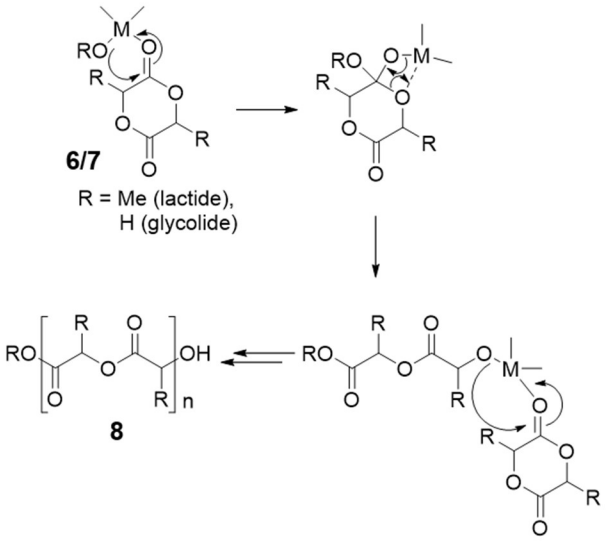

Scheme 2.1 The coordination-insertion mechanism of ROP. PLGA **8** is synthesised through ROP of the cyclic di-esters lactide **6** and glycolide **7**.[98] Firstly, a metal pre-catalyst is mixed with an alcohol to form the active metal alkoxide catalyst. Through a coordination-insertion mechanism this catalyses ring opening of the cyclic di-esters.

The most popular catalyst for ROP is tin(II) 2-ethylhexanoate ($Sn(oct)_2$) due to its high solubility in organic solvents or melts, and ability to produce high molecular weight polymers. However, although the catalyst is FDA approved,[99] the residual tin contamination is a concern, especially for biomedical applications. Research is ongoing into the use of alternative, less toxic metals such as aluminium,[100,101] and also into organocatalysts.[102–104]

2.2.2 Polymer characterisation

PLGA **8** is characterised by ^{1}H NMR spectroscopy in order to determine the ratio of poly(lactic acid) (PLA) to poly(glycolic acid) (PGA) in the final polymer (Section 2.3.1). Polymer molecular weight is determined by gel permeation chromatography (GPC). GPC determines the weight average molecular weight, M_w, and the number average molecular weight, M_n. The dispersity of the polymer (Đ) is defined as M_w/M_n and would be 1.0 for a polymer where all the chains are the same length. The dispersity gives a good indication of the control the catalyst has on the polymerisation, as side reactions can increase the dispersity.

2.2 Routes to Deuterated Monomers

In order to be able to image PLGA **8** with bioorthogonal SRS imaging in the cell-silent region, the aim was to introduce carbon-deuterium bonds into the polymer. The Raman shift of a chemical bond is proportional to its reduced mass,[105] so a 100% increase of mass, as is the case with a hydrogen to deuterium substitution, will decrease the frequency of the bond and move the Raman shift into the cell-silent region (1800–2800 cm^{-1}).

To give the highest chance of obtaining a sufficient Raman signal, as the carbon-deuterium stretch is known to have a relatively small Raman cross-section,[46] it was decided to introduce carbon-deuterium bonds into a PLGA monomer, so that each repeating unit of the polymer would contribute to the Raman signal.

2.2.1 Alkylation route

2.2.1.1 Synthesis of lactic acid-d_3

Lactic acid **4** contains a CH_3 group, and the aim was to substitute this CH_3 group to a CD_3 to produce Raman peaks in the cell-silent region. To produce lactic acid-d_3, a synthetic route was derived using deuterated iodomethane (CD_3I) as an alkylating agent. Firstly, two protection steps were carried out to protect the free acid and free alcohol of glycolic acid (Scheme 2.2). The first step involved the reaction of bromoacetic acid **9** with potassium *tert*-butoxide **10** to obtain 2-(*tert*-butoxy)acetic acid **11**, which was high yielding and easily scalable.

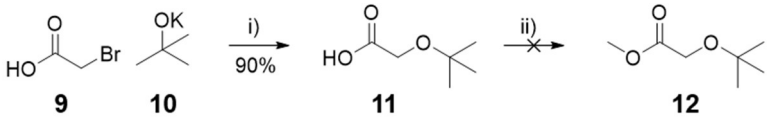

Scheme 2.2 Formation of methyl 2-(*tert*-butoxy)acetate **12**. Reagents and conditions: i) THF, 75°C, 1 h; ii) TMSCl, MeOH, rt, 0.5 h.

The second step attempted to protect the free acid as a methyl ester utilising TMSCl and methanol, with crude NMR analysis showing that the desired product **12** had been formed. However, after working up the reaction, NMR analysis showed that the product had decomposed, specifically that the *tert*-butyl group had been cleaved. It was hypothesised that the hydrochloric acid produced as a side product in the reaction, combined with the heat from the rotary evaporator, gave sufficient conditions to cleave the *tert*-butyl group. It was also observed that much of the product was being lost on the rotary evaporator. To overcome these problems, a Steglich esterification strategy

(Scheme 2.3) was successfully employed using 1-ethyl-3-(3-dimethylaminopropyl)carbodiimide (EDC), 4-dimethylaminopyridine (DMAP) and benzyl alcohol.[106] Benzyl alcohol was chosen instead of methanol to try to increase the boiling point of the product, so that it would not be lost during solvent removal.

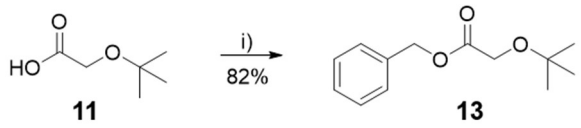

Scheme 2.3 A Steglich esterification for the formation of benzyl 2-(*tert*-butoxy)acetate **13**. Reagents and conditions: i) benzyl alcohol, EDC, DMAP, DCM, rt, 18 h.

In the third step, a strong, non-nucleophilic base was used to form the enolate of benzyl 2-(*tert*-butoxy)acetate **13**, which was subsequently quenched by the addition of deuterated iodomethane (Scheme 2.4).

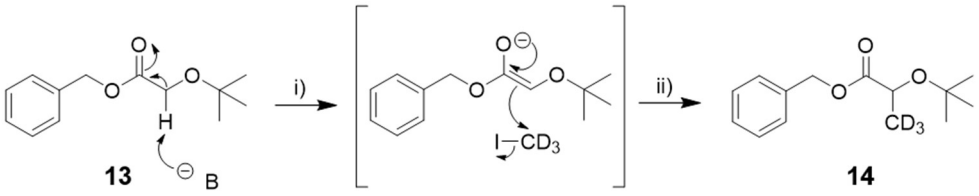

Scheme 2.4 Alkylation proceeded via an enolate intermediate to produce benzyl 2-(*tert*-butoxy)(3,3,3-$^2H_3$)propanoate **14**. Reagents and conditions: i) Li/KHMDS, THF, -78°C, 0.5 h; ii) CD_3I, THF, -78°C – rt, 0.5 h.

Initially this reaction was low yielding (~20%), so a number of bases and solvents were screened, along with further purification of the benzyl 2-(*tert*-butoxy)acetate **13** starting material. The conditions used in these reactions and their resulting yields are tabulated in Table 2.1. All reactions were carried out on a 0.5 g scale on the same timescale and temperature as stated in Scheme 2.4.

Table 2.1 Conditions screened to improve the alkylation yield.

Base	Equivalents of base	Equivalents of CD_3I[a]	Solvent	Purification of starting material **13**	% isolated yield
KHMDS	1.5	1.1	THF	No column	22
LiHMDS	1.5	1.1	THF	No column	25
KHMDS	1.5	1.1	THF	Column	29
KHMDS	1.5	1.1	Toluene	Column	11
LiHMDS	1.5	1.1	THF	Column	28
LiHMDS	2.5	1.1	THF	Column	34
KHMDS	2.5	2.0	THF	Column	45
LiHMDS	2.5	2.0	THF	Column	38

[a] CD_3I was filtered through a plug of anhydrous potassium carbonate prior to use.

Table 2.1 shows that the optimum conditions for alkylation used THF as the solvent, 2.5 equivalents of KHMDS and 2 equivalents of iodomethane. The yields listed in Table 2.1 are not higher than 45% which is due, in part, to the formation of an impurity. Thin layer chromatography (TLC) analysis during the reaction showed that all the starting material was consumed, but that there was another spot in addition to the product. The product **14** and impurity **16** were separated by flash column chromatography, and NMR analysis provides evidence that the impurity is the Claisen condensation product from two molecules of the starting material (Scheme 2.5).

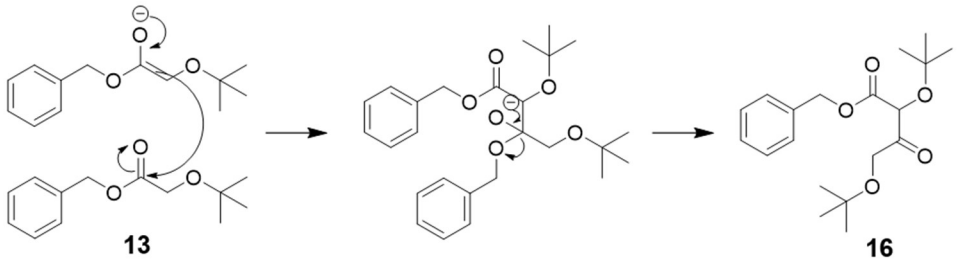

Scheme 2.5 An impurity **16** is formed due to a competing Claisen condensation.

To try and minimise the formation of this impurity **16**, additional equivalents of iodomethane could have been added to push the equilibrium towards the desired product, or shorter reaction times could have been investigated.

The protonated analogue, benzyl 2-(*tert*-butoxy)propanoate **15**, was also synthesised and both ^{1}H and ^{13}C NMR provide evidence for the CD_3 group, with a comparison of the two ^{1}H NMR spectra shown in Figure 2.2.

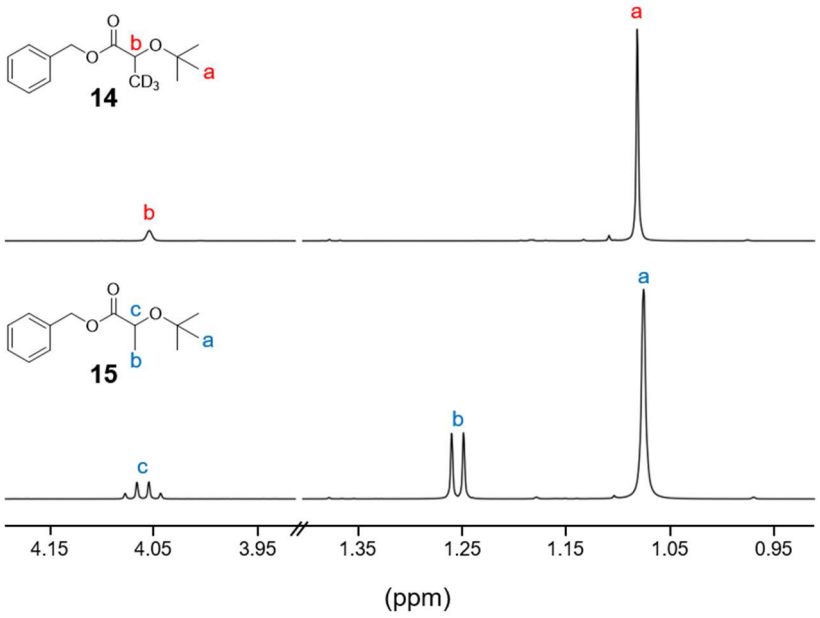

Figure 2.2 Comparison of the ^{1}H NMR spectra of benzyl 2-(*tert*-butoxy)(3,3,3-$^{2}H_3$)propanoate **14** (top) and benzyl 2-(*tert*-butoxy)propanoate **15** (bottom).

Benzyl 2-(*tert*-butoxy)propanoate **15** shows a doublet corresponding to the methyl group at ~1.25 ppm, which is absent in the deuterated analogue benzyl 2-(*tert*-butoxy)(3,3,3-$^{2}H_3$)propanoate **14**.

Evidence for the CD_3 can also be seen in the ^{13}C NMR; the carbon of the CD_3 group appears as a septet, whereas the protonated analogue shows a singlet (Figure 2.3).

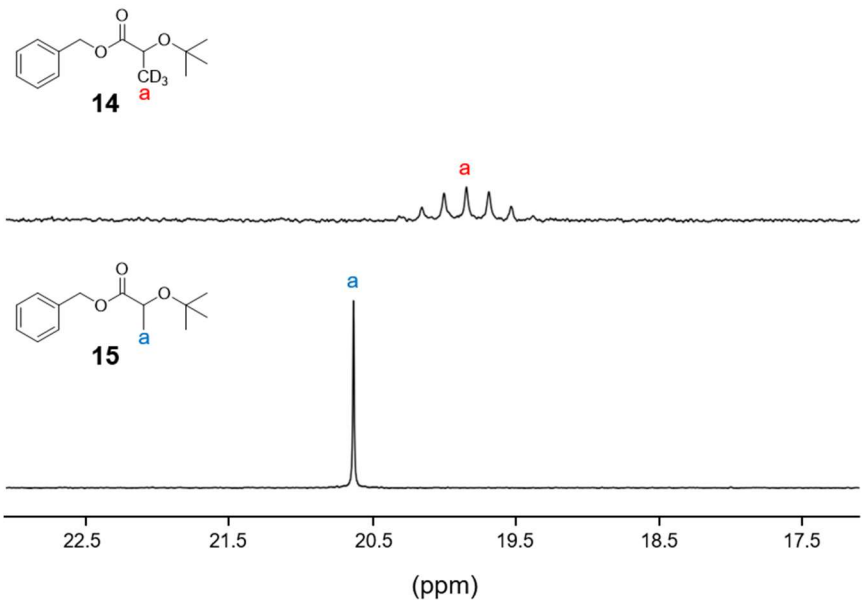

Figure 2.3 Comparison of the ^{13}C NMR spectra of benzyl 2-(*tert*-butoxy)(3,3,3-$^{2}H_3$)propanoate **14** (top) and benzyl 2-(*tert*-butoxy)propanoate **15** (bottom).

Subsequently, two deprotection steps were carried out to afford lactic acid-d_3. It was decided to utilise orthogonal protecting groups, and remove them sequentially, as after cleavage of the *tert*-butyl group the product could be purified by flash column chromatography which would not be possible if both were cleaved at the same time. Initially, trifluoroacetic acid in DCM was used to remove the *tert*-butyl group (Scheme 2.6), but this gave long reaction times and moderate yields.

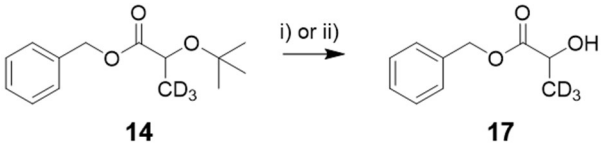

Scheme 2.6 Deprotection of benzyl 2-(*tert*-butoxy)(3,3,3-$^{2}H_3$)propanoate **14** to afford benzyl 2-hydroxy(3,3,3-$^{2}H_3$)propanoate **17**. Reagents and conditions: i) TIS, TFA (5% v/v), DCM, rt, 24 h, 67%; ii) $TiCl_4$ (1 M in DCM, 10% v/v), DCM, -78 °C, 15 min, 94%.

Titanium tetrachloride in DCM (Scheme 2.6) gave a higher yield and significantly shorter reaction times.

Finally, the benzyl protecting group was removed via a hydrogenation reaction to afford the final product, lactic acid-d_3 **18** (Scheme 2.7). The optimised five-step sequence gave an overall yield of 28%.

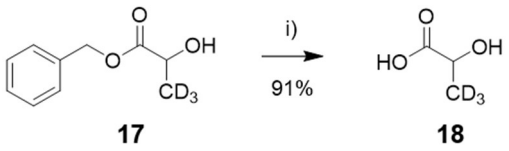

17 18

Scheme 2.7 Benzyl deprotection of benzyl 2-hydroxy(3,3,3-$^2H_3$)propanoate **17** to give lactic acid-d_3 **18**. Reagents and conditions: i) Pd/C, H_2, THF, rt, 3 h.

2.2.1.2 Comparison with commercial lactic acid-d_3

Lactic acid-d_3 is also commercially available, so a sample of the commercial material was used to compare the characterisation with the material made in-house. Figure 2.4 shows that the ^1H and ^{13}C NMR spectra of the commercial material is identical to the material synthesised in-house, confirming that the synthetic route has been successful.

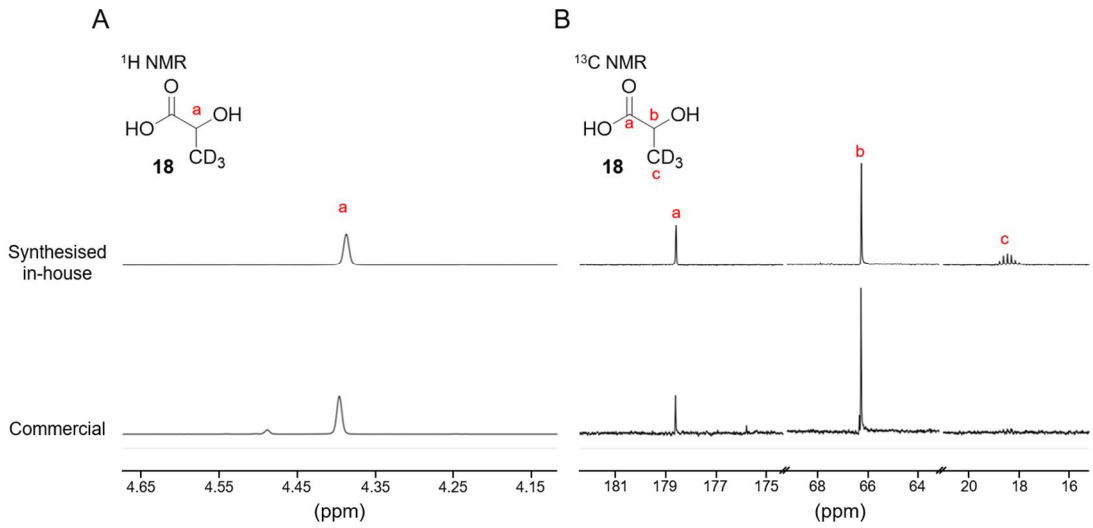

Figure 2.4 Comparison of the ^1H (A) and ^{13}C (B) NMR spectra of commercial lactic acid-d_3 (bottom) with material synthesised in-house (top). The small impurity peak present in the ^1H NMR of the commercial product could be due to oligomers that can form in an aqueous solution.

Evidence for the presence of deuterium is clear from the septet in the carbon NMR, and the material synthesised in-house was also analysed by spontaneous Raman spectroscopy and ^2H NMR, which both show deuterium peaks (Figure 2.5).

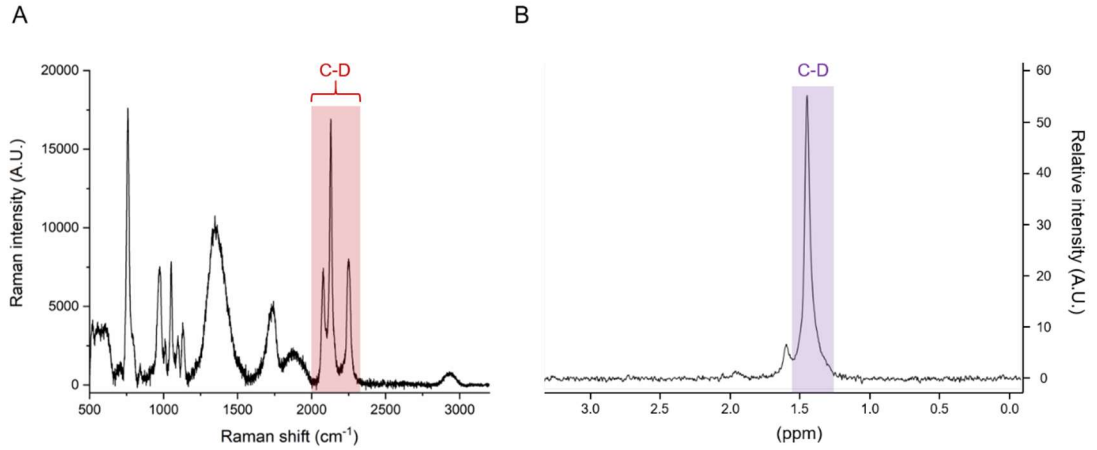

Figure 2.5 Analysis of lactic acid d_3 **18** by spontaneous Raman spectroscopy, λ_{ex} 785 nm (A) and ^{2}H NMR (B).

2.2.1.3 Ring closing reactions

As the most common route to PLGA **8** is via ring opening polymerisation, which gives superior molecular weights and dispersity when compared to the direct condensation method,[94] ring closing reactions were investigated in order to produce lactide-d_6 **20**. Considering the number of steps taken to produce lactic acid-d_3 **18** and the high cost of buying it commercially, the investigative reactions were carried out on lactic acid **4**, which is inexpensive and commercially available.

Throughout the literature, modest yields are reported for the ring closing of lactic acid **4** to lactide **6**, as longer oligomers are formed as by-products.[95] The first method attempted was the two-step reaction, where the lactic acid was dehydrated to form oligomers, followed by a back-biting reaction catalysed by tin to afford ring closed lactide, which could be removed by distillation from the oligomers (Scheme 2.8).

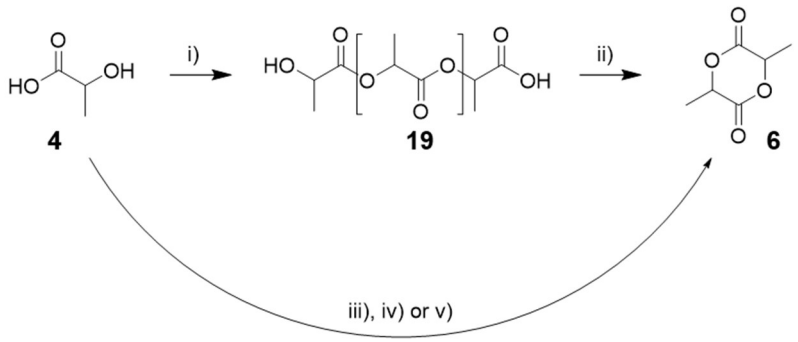

Scheme 2.8 Formation of lactide **6** from lactic acid **4** in one or two-step processes. Reagents and conditions: i) 230°C, 6 h; ii) $Sn(oct)_2$, 230°C, 20 mbar, 2 h; iii) *para*-TSA, toluene, 130°C, 4 days; iv) Yt(III) triflate, toluene, 130°C, 18 h; v) H-beta zeolite, toluene, 130°C, 3 h.

The two-step reaction in Scheme 2.8 (i, ii) was very low yielding, with only a 2% yield of racemic lactide. The yield of the crude lactide was higher due to racemisation producing meso lactide, but after purification by recrystallization or column chromatography much of the material was lost. It was also clear during the reaction that there were a lot of discoloured oligomers left in the flask that had not converted to lactide, with the heat and reduced pressure also facilitating reaction of the oligomers to form longer chains.

To try and improve the yield, and remove the need for the initial oligomerisation step, several one-pot reactions were investigated utilising various catalysts to favour the formation of lactide over PLA oligomers **19** (Scheme 2.8, iii, iv or v). All of these reactions were setup with a Dean-Stark trap to remove water from the system. The yields of these reactions are listed in Table 2.2.

Table 2.2 One-pot ring closing reactions with various catalysts

Reagents[a]	Conditions	% yield lactide
p-TSA in 400 mL toluene	Reflux, 4 days	Only oligomers
Yt(III) triflate in 400 mL toluene[b]	Reflux, 18 h	3
H-beta zeolite[c] in 10 mL toluene	Reflux, 3 h	34

[a]Reactions were carried out on 1.2 g lactic acid (85%, aq)
[b]The starting material for this reaction was ammonium lactate produced by reacting lactic acid with ammonium hydroxide
[c]Zeolite was calcined at 550°C overnight prior to use, 0.5 wt% used

The *p*-TSA and Yt(III) triflate reactions were carried out at very dilute concentrations (0.028 M) in the hope that only two molecules of lactic acid would meet each other and ring close as opposed to oligomerise. However, this was not the case with oligomers being almost exclusively produced in both cases. Dusselier *et al.* reported that H-beta zeolite could be used to give 'shape selective catalysis' of lactic acid **4** to lactide **6**, as the reaction is thought to take place inside the zeolite cavity, which favours the ring formation.[96] The zeolite reaction is also advantageous over the two-step reaction in Scheme 2.8 as the catalyst is heterogeneous so does not introduce any harmful metal ions, such as tin, into the polymer which could have negative effects in biological applications. Also, unlike the two other methods, the zeolite reaction produced lactide that did not need any further purification.

Several other reactions were carried out using H-beta zeolite (Table 2.3) which showed that it was important that the zeolite was calcined at 550°C before use, and that the reaction was carried out in toluene at 1.10 M.

Table 2.3 Ring closing reactions with H-beta zeolite.

Catalyst pre-treatment	Solvent	Concentration (M)	% isolated yield
250°C[a]	Toluene	1.10	19
550°C[b]	Toluene	1.10	34
550°C[b]	Toluene	0.22	24
550°C[b]	*o*-Xylene	1.10	impure

[a]Zeolite was held at 250°C under vacuum for 18 h
[b]Zeolite was heated in a furnace in air to 550°C over 6 h, held at 550°C for 6 h and then cooled back to room temperature over 6 h
Reactions were carried out on 1.2 g lactic acid (85%, aq) and 0.5 g H-beta zeolite

To try and further increase the yield from the zeolite reaction, the oligomers produced as a side product **19** were isolated and then hydrolysed back to lactic acid **4** for recycling. The isolation of the oligomers was achieved by extraction into water; the oligomers **19** all have free acid end groups making them water soluble, unlike the lactide **6** which extracts into the organic phase. After isolation, the aqueous phase was lyophilised and NMR analysis showed that a variety of oligomeric species and lactic acid **4** were present. The mixture was then heated to 180°C in water for three to four hours, with NMR analysis showing an increase in the lactic acid peak indicating hydrolysis of the monomers. The aim was to use this hydrolysis method to recycle the more precious deuterated lactic acid.

The optimised zeolite ring closing reaction was then carried out on lactic acid-d_3 **18**, which did not show the same reactivity as the lactic acid. In toluene, the reaction was unsuccessful with no product formed. The reaction was then attempted in *o*-xylene, which did produce a new product peak by TLC. The product of this reaction was very impure, but there was a peak present in the ^{1}H NMR spectrum at 5.00 ppm, which is at a similar position as the methine proton of lactide (Figure 2.6), however, the crude mixture proved difficult to purify by column chromatography.

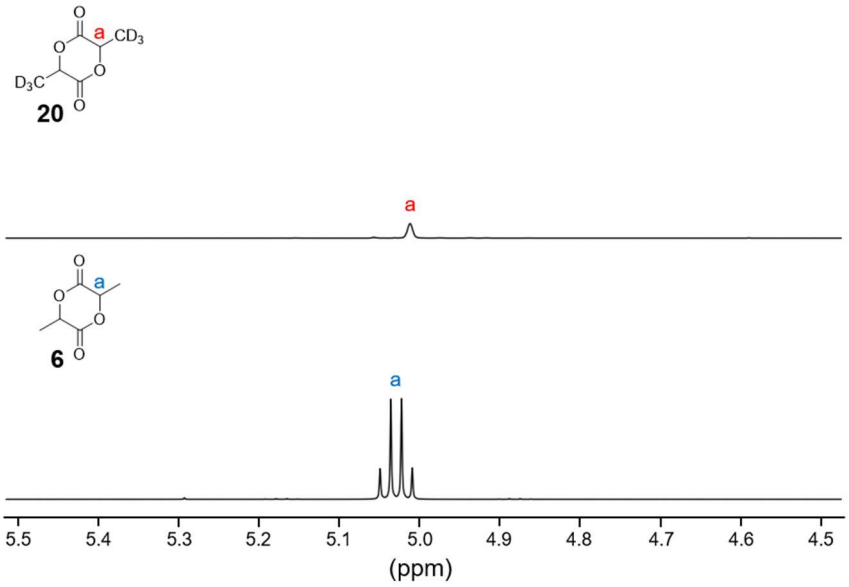

Figure 2.6 Evidence for lactide-d_6 **20** (top) from ^{1}H NMR showing a singlet at ~5 ppm thought to correspond to the methine proton. This is at similar chemical shift to the methine proton of lactide **6** (bottom).

Considering the difficulties encountered in the synthesis and purification of lactide-d_6 **20**, it was decided that this was not a viable route to producing a deuterated PLGA.

2.2.2 H/D exchange

As an alternative approach to introduce a carbon–deuterium bond into a PLGA monomer, an H/D exchange reaction was carried out on both cyclic monomers. Dos Santos *et al*. demonstrated H/D exchange on both lactide **6** and glycolide **7** via a high-temperature solid-state catalytic isotope exchange process with maximum deuteration of 30% and 24% for lactide and glycolide respectively.[107,108] The hope was to replicate this synthesis and introduce a high enough percentage of deuterium so that a polymer suitable for biological Raman imaging could be synthesised, with the

added advantage of not having to perform a ring closing reaction. The exchange reaction is shown in Scheme 2.9.

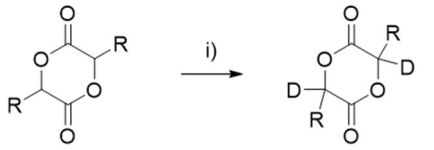

6: R = CH_3
7: R = H

21: R = CH_3
22: R = H

Scheme 2.9 An H/D exchange reaction to produce deuterated cyclic monomers **21/22**. R = CH_3 (lactide **6**) and R = H (glycolide **7**). Reagents and conditions: i) Lindlar catalyst (5 wt%), D_2 gas, 1 h, 90°C for glycolide, 100°C for lactide.

For deuterated lactide **21**, NMR spectroscopy could be used to calculate the extent of labelling by comparing the integral of the methine proton before and after deuteration, when the methyl protons are always set to 3.00 (Table 2.4).

Table 2.4 Percentage deuteration of lactide calculated from ^{1}H NMR.

Condition	CH_3 integral	CH integral	% Deuteration
Before deuteration	3.00	0.94	0.00
1 h deuteration	3.00	0.93	1.06
5 h deuteration	3.00	0.91	3.20

The results in Table 2.4 show that low levels of deuteration had been achieved, however, mass spectrometry by electron ionisation indicated higher levels of labelled product. The relative abundancies of *m/z* 144 (unlabelled), 145 (mono-labelled) and 146 (di-labelled) were 49.3, 31.5 and 6.3 respectively. ^{2}H NMR of the isolated product **21** confirmed that there was deuterium present, but the signal is very weak. The spontaneous Raman spectrum of the product shows a small, broad deuterium stretch at ~2160 cm^{-1} (Figure 2.7).

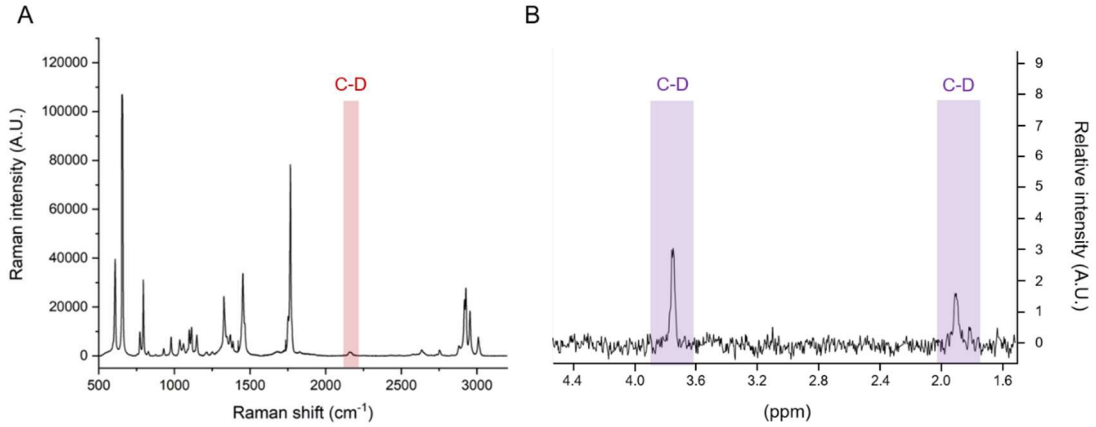

Figure 2.7 Evidence for the deuteration of lactide by spontaneous Raman spectroscopy, λ_{ex} 785 nm (A) and ^{2}H NMR (B).

For glycolide **7**, which only contains methylene protons, the percentage of deuteration could not be estimated by NMR, so mass spectrometry was used solely. The exchange reaction on glycolide seemed to be much less efficient, with the relative abundancies of *m/z* 116 (unlabelled) and 117 (mono-labelled) being 100.0 and 7.7 respectively. Again, there were peaks present in the ^{2}H NMR spectrum, but in the spontaneous Raman spectrum there was not a clear carbon-deuterium stretch (sharp peaks are due to interference from cosmic rays) (Figure 2.8).

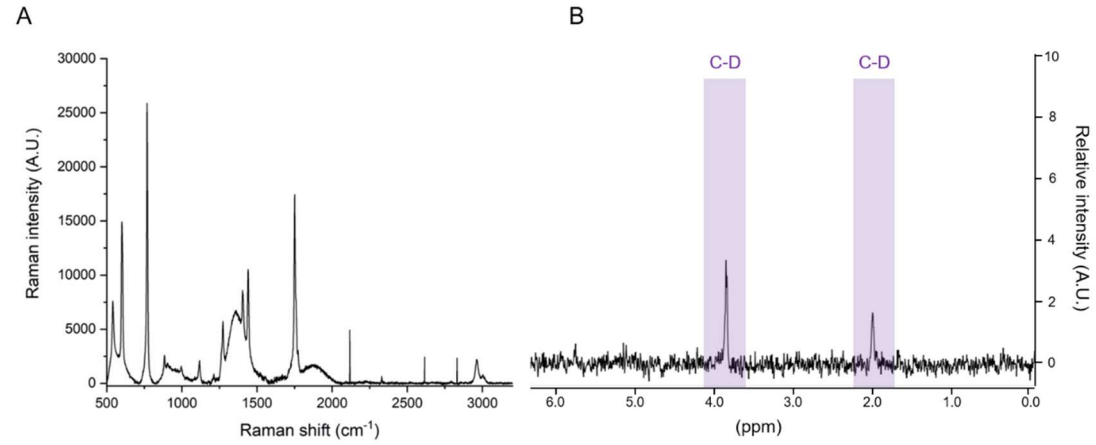

Figure 2.8 Analysis of deuterated glycolide by spontaneous Raman spectroscopy, λ_{ex} 785 nm (A) and ^{2}H NMR (B).

2.3 Routes to Deuterated Polymers

2.3.1 Ring opening polymerisation

2.3.1.1 Synthesis of PLGA

PLGA was synthesised from lactide and glycolide using stannous octanoate as the catalyst and dodecanol as the co-initiator (Scheme 2.10). The reaction was carried out as a melt in the absence of solvent, as this can reduce reaction times and lead to a higher molecular weight polymer.

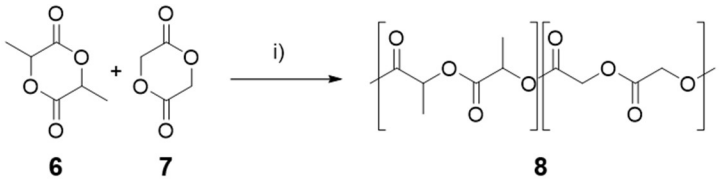

Scheme 2.10 Synthesis of PLGA **8** via a tin catalysed ROP of lactide **6** and glycolide **7**. Reagents and conditions: i) stannous octanoate (1 mol %), dodecanol (1 mol %), 120°C, 0.5 h.

Glycolide **7** had a higher reactivity than lactide **6**, probably due to the steric hindrance of the methyl group on lactide, so the starting ratio of the monomers were adjusted to ~60 lactide: 40 glycolide to give ~50:50 PLGA **8**. NMR spectroscopy is used to find the ratio of PLA to PGA in the final, purified polymer (Figure 2.9) according to Equation 2.1 below.

$$\%\ \mathrm{PLA} = \left(\frac{\frac{\mathrm{CH_3\ integral}}{3}}{\frac{\mathrm{CH_3\ integral}}{3} + \frac{\mathrm{CH_2\ integral}}{2}} \right) \times 100$$

$$\%\ \mathrm{PGA} = \left(\frac{\frac{\mathrm{CH_2\ integral}}{2}}{\frac{\mathrm{CH_3\ integral}}{3} + \frac{\mathrm{CH_2\ integral}}{2}} \right) \times 100$$

Equation 2.1 The percentage of PLA and PGA in the final polymer can be determined by NMR integrals.

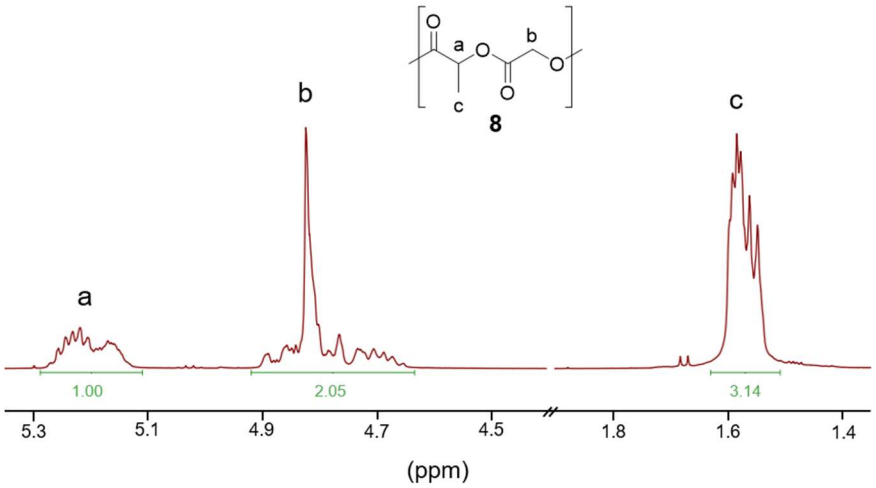

Figure 2.9 ^{1}H NMR spectrum of PLGA **8** synthesised with ROP where the peak integrals can be used to calculate the ratio of PLA and PGA.

PLGA **8** was also characterised by spontaneous Raman spectroscopy, which shows characteristic peaks for CH_2, CH_3 and carbonyl bonds (C=O), but no peaks in the cell silent region (Figure 2.10). This highlights the need for bioorthogonal labels to be able to selectively image the polymer in the cell-silent region.

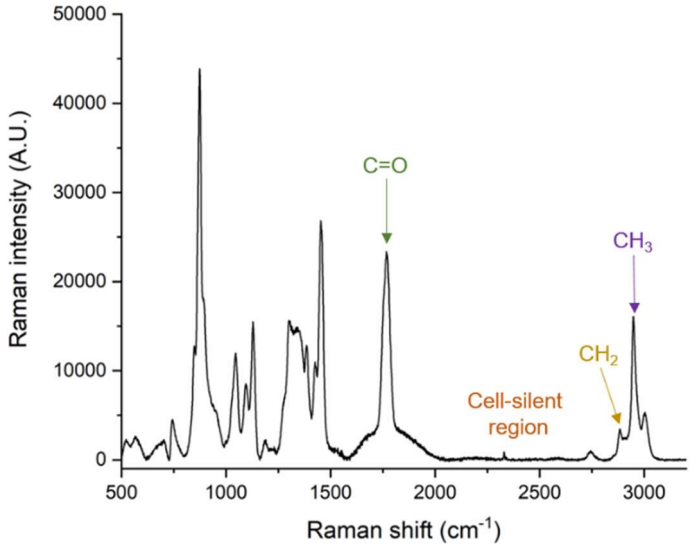

Figure 2.10 Analysis of PLGA **8** with spontaneous Raman spectroscopy, λ_{ex} 785 nm.

2.3.1.2 Synthesis of PLGA-D

ROP was employed to form deuterated PLGA from the labelled cyclic monomers whose synthesis is described in Section 2.2.2. Since the labelled lactide **21** showed

the most significant carbon-deuterium peak by spontaneous Raman (Figure 2.7), the PLGA synthesis was attempted with this lactide **21** and commercial, unlabelled glycolide **7**. The ROP proceeded successfully and polymer was precipitated. Although the polymer did show some weak peaks in the ^{2}H NMR, there were no C-D peaks apparent in the spontaneous Raman, so this polymer was not taken forward to further studies.

2.3.2 Polycondensation polymerisation

As described above, the cyclic deuterated lactide **21** formed via the H/D exchange reaction did not produce a strong enough deuterium signal when polymerised, probably due to the fact that the monomer was only ~3% deuterated. On the other hand, the lactic acid d_3 **18** synthesised via the alkylation route (Section 2.2.1) was 100% deuterated. Considering the difficulties faced producing cyclic lactide from this deuterated monomer, an alternative polycondensation polymerisation route was explored.

Polymers may be formed through condensation reactions where water is produced as a by-product. Several groups have reported syntheses of high molecular weight PLGA from lactic and glycolic acid by first dehydrating to form oligomers and then adding a tin catalyst to drive the formation of higher molecular weight polymers.[109,110]

Deuterated PLGA was successfully synthesised using this approach from a mixture of commercial lactic acid **4** and glycolic acid **5**, and the lactic acid-d_3 **18** synthesised in-house (Scheme 2.11). The reaction was set up in a round bottomed flask fitted with an air condenser packed with molecular sieves, in the hope that they would absorb the water produced. Since the boiling point of lactic acid is 122°C, the temperature was increased gradually from 100–150°C in the first step of the synthesis so as not to evaporate any of the lactic acid.

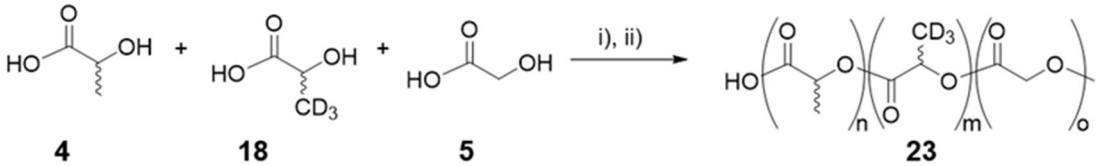

4 **18** **5** **23**

Scheme 2.11 Synthesis of PLGA-D **23** via a polycondensation reaction. Reagents and conditions: i); 150°C, 8 h, ii); $SnCl_2$, *p*-TSA, 180°C, 8 h.

Although the polymerisation was successful, the precipitated polymer **23** was brown in colour, which resulted in issues when it was analysed by spontaneous Raman. The

polymer had a high background signal, and a large, broad peak at ~1800 cm^{-1}, which was hypothesised to be due to the brown colour. Also, very low laser powers had to be used (<1%) or the signal would top out due to the high background.

The synthesis in Scheme 2.11 was repeated, but using commercial lactic acid-d_3, and this time the precipitated polymer was colourless, with M_n = 4553 Da and Đ = 1.84. When analysed by spontaneous Raman, there was still a high background but the polymer peaks, including carbon-deuterium peaks in the cell silent region, were observed (Figure 2.11).

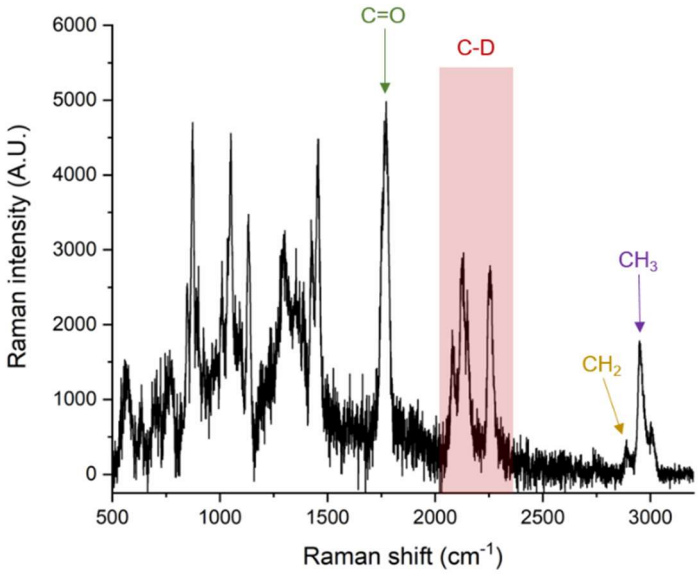

Figure 2.11 Analysis of PLGA-D **23** with spontaneous Raman spectroscopy, λ_{ex} 785 nm.

Although the Raman signal was weak, this polymer was taken forward to further experiments for making nanoparticles and carrying out SRS imaging. It was hypothesised that there were small amounts of impurity present in the in-house lactic acid-d_3 **18**, which caused discolouration upon polymerisation and extended heating. The monomer could have been purified by distillation to remove these impurities, but this would have been difficult and low yielding on a small scale.

2.4 Synthesis of PLGA-alkyne

As mentioned in Chapter 1, alkyne tags are an alternative chemical group which produce peaks in the cell-silent region, and usually have a stronger Raman cross-section than deuterium. An alkyne tagged analogue of PLGA (PLGA-alkyne **25**) was synthesised by Dr Stefan Cairns.[111]

Synthesis of Bioorthogonal Raman Labelled Polymers

To introduce the alkyne functionality to PLGA, the telechelic properties of the polymer were exploited by carrying out a trans-esterification reaction, catalysed by stannous octanoate, with a five-membered 1,3-dioxolan-4-one ring bearing an alkyne functionality **24** (Scheme 2.12).

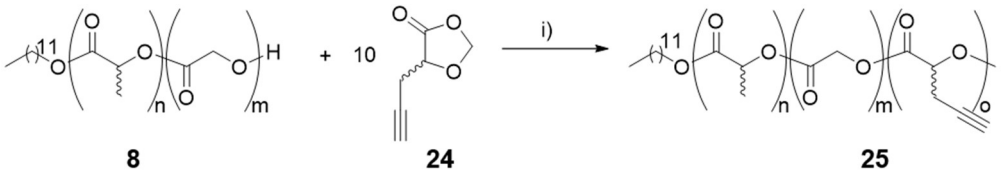

8 **24** **25**

Scheme 2.12 Synthesis of PLGA-alkyne **25**. Reagents and conditions: i) $Sn(oct)_2$, toluene, 110°C, 24 h. Synthesis carried out by Dr Stefan Cairns.[111]

Recent work has shown that 1,3-dioxolan-4-ones (DOX) are a versatile and sustainable family of monomers for ring opening polymerisation, and can often be synthesised from amino acids.[112] There is no parent amino acid containing the alkyne functionality, so propargyl-DOX **24** was synthesised from propargyl bromide **26** and ethyl glyoxalate **27** in a zinc catalysed Barbier reaction, as previously reported (Scheme 2.13).[113,114]

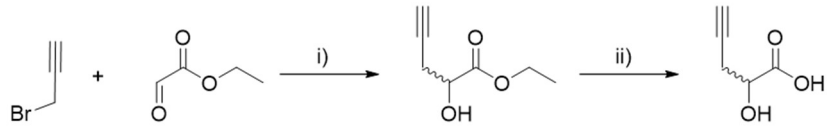

26 **27** **28** **29**

Scheme 2.13 Synthesis of propargyl α-hydroxy acid **29**. Reagents and conditions: i); Zn, Et_2O/THF, 0°C, 16 h, ii); HCl/H_2O, 100°C, 24 h. Synthesis carried out by Dr Stefan Cairns.[111]

To obtain the ring closed propargyl-DOX **24**, the propargyl α-hydroxy acid **29**, paraformaldehyde **30**, and *para*-toluene sulfonic acid were dissolved in benzene and refluxed in a Dean-Stark apparatus to remove water, as previously reported,[112] to give the desired product **24** in 66% yield (Scheme 2.14).

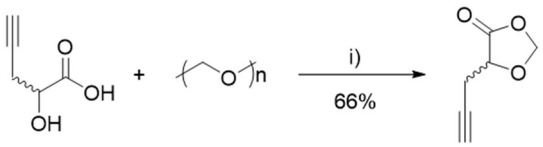

29 **30** **24**

Scheme 2.14 Synthesis of propargyl DOX **24**. Reagents and conditions: i) para-TSA, 110°C, 6 h. Synthesis carried out by Dr Stefan Cairns.[111]

Synthesis of Bioorthogonal Raman Labelled Polymers

Reaction of propargyl DOX **24** with pre-formed PLGA **8** gave rise to statistical distribution of the alkyne units throughout the polymer chain (M_n = 5900 Da, Đ = 1.88), with the incorporation confirmed in the diffusion ordered spectroscopy (DOSY) NMR (Figure 2.12).

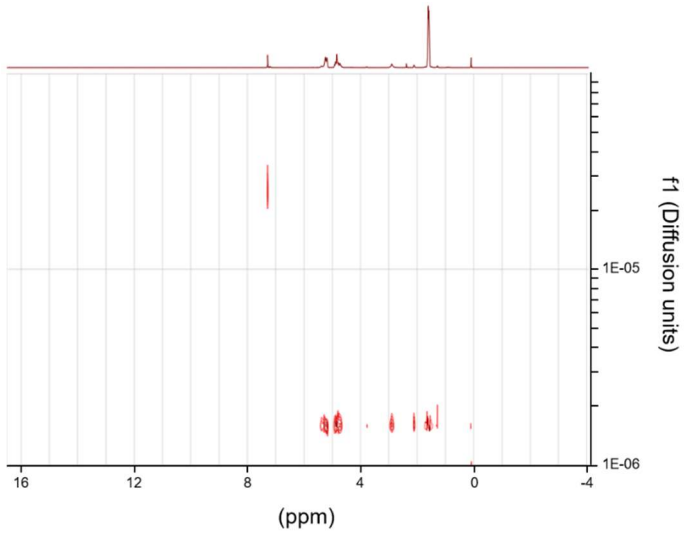

Figure 2.12 Analysis of PLGA-alkyne **25** with DOSY NMR. The polymer ^{1}H peaks all have the same diffusion coefficient, which confirms that the alkyne units have been incorporated into the existing PLGA chain.

The PLGA-alkyne **25** was then characterised by spontaneous Raman spectroscopy, and was found to have a single, sharp alkyne peak at 2128 cm^{-1} (Figure 2.13).

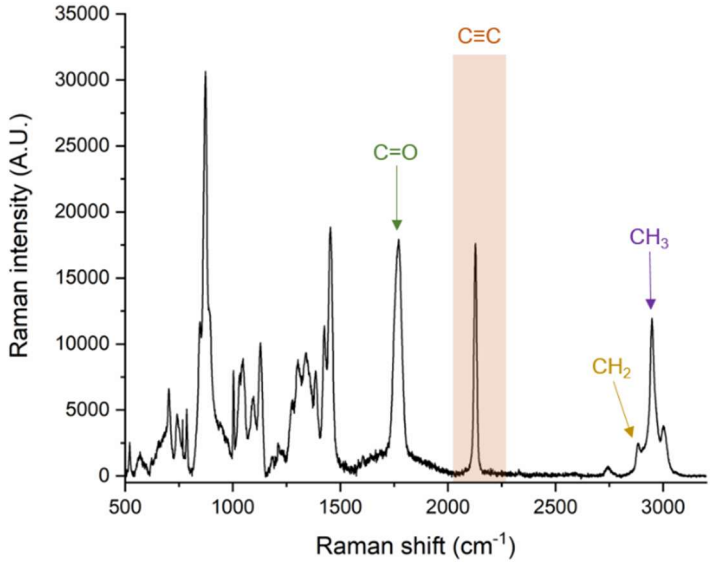

Figure 2.13 Analysis of PLGA-alkyne **25** with spontaneous Raman spectroscopy showing a strong alkyne signal at 2128 cm^{-1}, λ_{ex} 785 nm.

The PLGA-alkyne **25** shows a very strong alkyne signal, with a much higher intensity than the multiple carbon-deuterium peaks in the PLGA-D **23** spectrum (Figure 2.11), making it an attractive candidate for further Raman studies.

2.5 Conclusions

In this chapter, the synthesis of unlabelled PLGA **8**, along with the syntheses of bioorthogonally labelled PLGA-D **23** and PLGA-alkyne **25** are described. Two routes to produce deuterated monomers were investigated, an alkylation route with CD_3I and an H/D exchange with deuterium gas. The H/D exchange approach gave very low levels of exchange, and the PLGA produced from these monomers did not show C-D peaks when analysed by spontaneous Raman. The alkylation route gave lactic acid-d_3 that was fully deuterated, but ring-closing this to the cyclic lactide-d_6 proved difficult. A direct polycondensation polymerisation method, as opposed to ROP, was successfully used to synthesise PLGA-D from both commercial lactic acid-d_3 and that synthesised in-house. However, the PLGA-D obtained from the in-house material was brown in colour and did not give a Raman signal. On the other hand, the commercial lactic acid-d_3 produced a colourless polymer which produced multiple C-D peaks in the cell-silent region of the Raman spectrum. Scheme 2.15 shows a summary of the reactions attempted to produce PLGA-D. In addition, PLGA-alkyne was synthesised by Dr Stefan Cairns which produced a single, strong alkyne peak in the cell-silent region. Both of these polymers were taken onto further studies as candidates to synthesise NPs for SRS imaging.

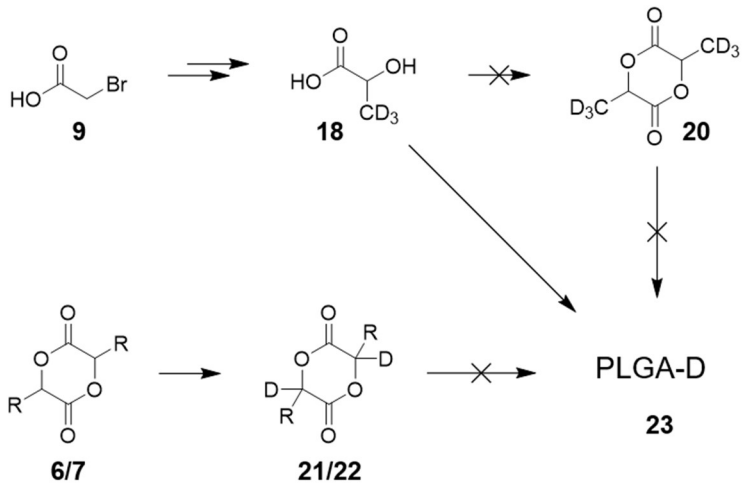

Scheme 2.15 Summary of reactions attempted to produce PLGA-D **23**. Lactic acid-d_3 **18** was produced over five steps from bromoacetic acid **9**, but ring closing to lactide-d_6 **20** was unsuccessful. A H/D exchange reaction was used to produce deuterated lactide and glycolide **21/22**, but the resulting polymer did not have a carbon-deuterium signal by spontaneous Raman. PLGA-D **23** was successfully synthesised by a polycondensation synthesis from commercial lactic acid-d_3.

Chapter 3 Synthesis of Nanoparticles for Drug Delivery

3.1 Introduction to Nanomaterials

Nanomaterials are defined as ‘a material containing particles where one or more dimensions is in the size range 1–100 nm’, with these dimensions known as the nanoscale.[115] There are various classes of nanomaterials including carbon based materials,[116] metals,[117] and organic polymeric nanoparticles (NPs), which will be the focus of this thesis (Figure 3.1).

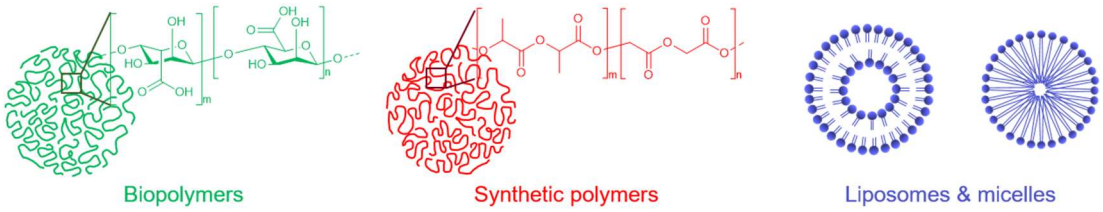

Figure 3.1 Examples of organic materials used to make nanoparticles. Biopolymers (e.g. alginate and chitosan), synthetic polymers (e.g. PLGA/PLA) and lipid-based materials (e.g. liposomes and micelles) are all commonly used to fabricate nanomaterials.

Owing to the nanoscale size of these particles, they exhibit strikingly different physical and chemical properties to their bulk counterparts. Polymer nanoparticles are colloidal systems, have an extremely high surface area to volume ratio, and are governed by quantum mechanics, undergoing Brownian motion in suspension.[118] These properties can be exploited for many scientific applications.

3.1.1 Nanomaterials for drug delivery

The use of nanomaterials in medical research is becoming increasingly popular as efforts to deliver more targeted and personalised treatments are realised.[119–121] In both clinical and research settings, nanomedicines are being exploited for targeted drug delivery giving superior pharmacokinetic properties over a free drug, and diagnostics.[122] In the case of biodegradable polymeric NPs, drug molecules can be incorporated into the polymer matrix and then as the polymer degrades *in vivo*, sustained release of the drug is achieved.[94]

3.1.2 Characterisation of nanomaterials

3.1.2.1 Electron microscopy

The invention of the electron microscope was vital for the discovery and characterisation of nanomaterials. In contrast to conventional light microscopy, electron microscopes focus a high-energy beam of electrons onto a specimen to achieve superior magnification and resolution. Light microscopy is limited by the diffraction of light to a resolution of around 200 nm,[123] whereas electron microscopes are capable of resolving down to 0.1 nm,[124] making them necessary for the visualisation of NPs. Both transmission electron microscopy (TEM) and scanning electron microscopy (SEM) are commonly used to characterise NP size and morphology.

Figure 3.2 shows a comparison of PLGA NPs imaged by brightfield microscopy (A), TEM (B), and SEM (C). An advantage of brightfield microscopy is that the nanoparticles can be imaged in suspension, whilst for TEM and SEM the nanoparticles must be dried as part of the sample preparation. For TEM, a drop of the nanoparticle suspension is dried on a copper grid at room temperature, and for SEM the nanoparticles are dried in an oven before sputter-coating with a layer of gold to allow elucidation of 3D particle morphology. A disadvantage of characterising nanoparticles in a dried state is that they may aggregate upon evaporation of the water, meaning that the image obtained is not representative of the particles in suspension. However, for sizing the nanoparticles, it is necessary to use electron microscopy. Recently, advances in cryogenic electron microscopy have shown that freezing the NPs in suspension allows preservation of the particle distribution.[125]

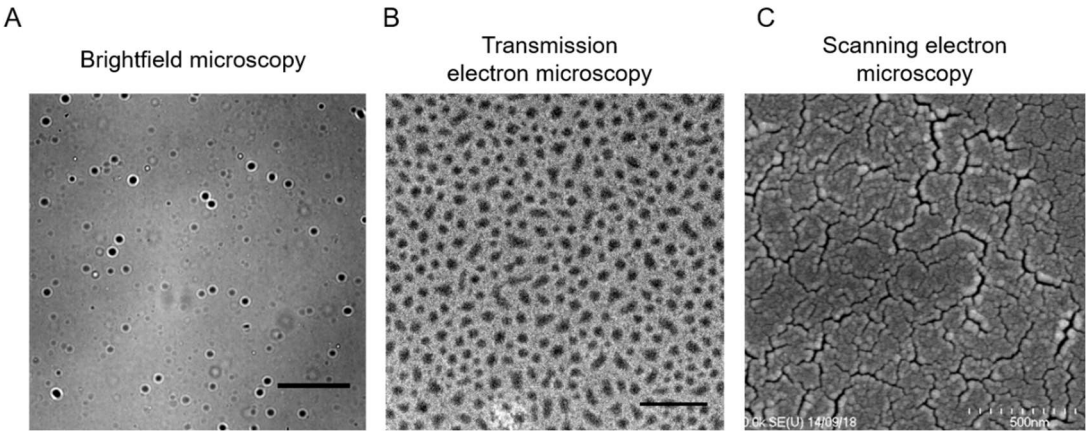

Figure 3.2 Comparison of different microscopy techniques available for nanoparticle characterisation. A) Brightfield microscopy, scale bar = 5 μm; B) TEM, scale bar = 500 nm; C) SEM, scale bar = 500 nm.

3.1.2.2 Light scattering techniques

Nanoparticles move around in suspension in a so called 'random walk' known as Brownian motion. This property can be exploited by light scattering techniques to measure a particle's hydrodynamic diameter, defined as a hard sphere diffusing at the same rate of the particle of interest, using the relationship defined in the Stokes-Einstein equation (Equation 3.1). Two light scattering techniques will be discussed in this chapter, dynamic light scattering (DLS) and nanoparticle tracking analysis (NTA), and both measure the velocity of Brownian motion, known as the diffusion coefficient (D), and equate this to hydrodynamic diameter.[126]

$$d_H = \frac{kT}{3\pi\eta D}$$

Equation 3.1: The Stokes-Einstein equation. Where d_H = hydrodynamic diameter, k = Boltzmann's constant, T = temperature, η = viscosity of the dispersant and D = diffusion coefficient.

A limitation of light scattering is that hydrodynamic diameter is measured, not absolute particle size, and this assumes that the particle is spherical. Equation 3.1 also highlights the importance of knowing the temperature and viscosity of the dispersant when taking measurements.

DLS measures the hydrodynamic diameter from a bulk solution of particles and also provides a number for the dispersity of the NP suspension, the polydispersity index (PdI). PdI is scaled between zero and one, with a higher PdI corresponding to a more

disperse sample. A disadvantage of DLS is that size results can be skewed by the presence of a small number of large particles since light scattering intensity is proportional to particle diameter to the power of six.[127]

In contrast to DLS, NTA tracks individual particles and measures their Brownian motion, and thus provides more detailed information about the size distribution of the sample.[128] Figure 3.3 shows the NTA experimental set-up. NPs are suspended in a solvent and injected into a sample chamber. A monochromatic laser is then shone at the sample, and the light scattered by the particles is detected by a camera operating at 30 frames per second to visualise the particles and measure their Brownian motion.[129,130] A further advantage of NTA is that because individual particles are tracked and counted in a known volume, particle concentration can also be estimated.

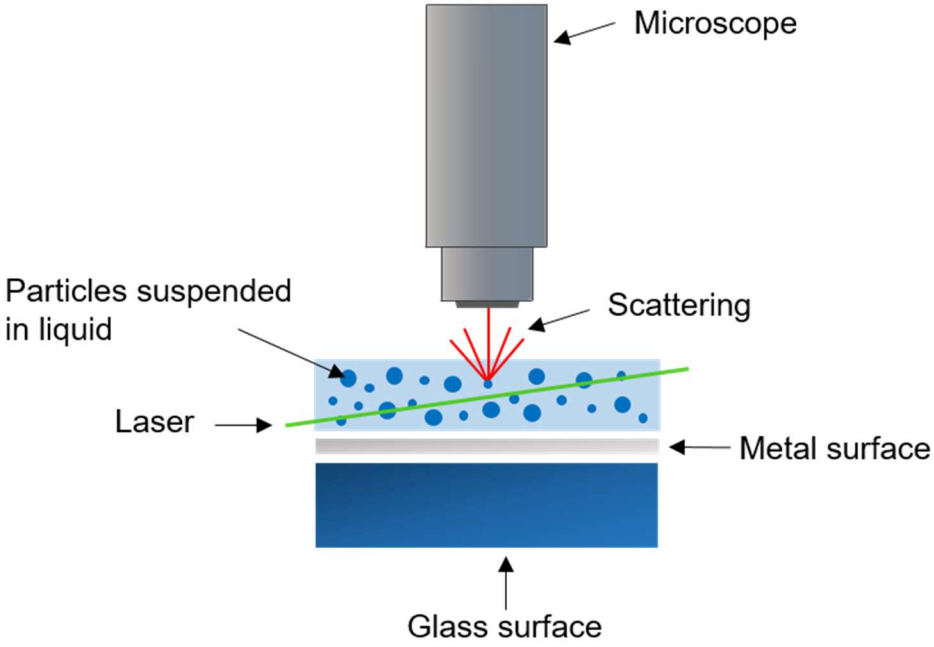

Figure 3.3 Nanoparticle tracking analysis. A sample of NPs suspended in liquid is irradiated with a laser, and the light scattered by the NPs is detected by a camera, allowing the NPs to be tracked.[129]

3.2 Nanoparticle Synthesis

There have been many methods for NP fabrication reported in the literature, and the choice of synthesis will depend on the desired application of the resulting NPs, for example, the physical properties of the drug payload to be encapsulated and

delivered.[131] These methods can generally be divided into emulsion-based techniques where shear force is used to create nanodroplets, and techniques where NPs spontaneously form without the need for an emulsion.

3.2.1 The emulsification-evaporation method

The emulsification-evaporation method is one of the most commonly used techniques for the synthesis of NPs for drug delivery because of its ability to encapsulate a wide range of drug payloads from small molecules to proteins.[132] A visual schematic of the standard emulsification-evaporation method used in this work to produce blank (with no drug payload) NPs is shown in Figure 3.4.

The polymer dissolved in dichloromethane (DCM), an organic solvent that is not water-miscible, was emulsified with an aqueous phase containing an emulsification agent (poly(vinyl alcohol)) and a surfactant (sodium dodecyl sulphate), to form a stable oil-in-water emulsion. This emulsion was then stirred at room temperature overnight to allow complete evaporation of the DCM, resulting in hardened polymer NPs that could be collected by centrifugation.

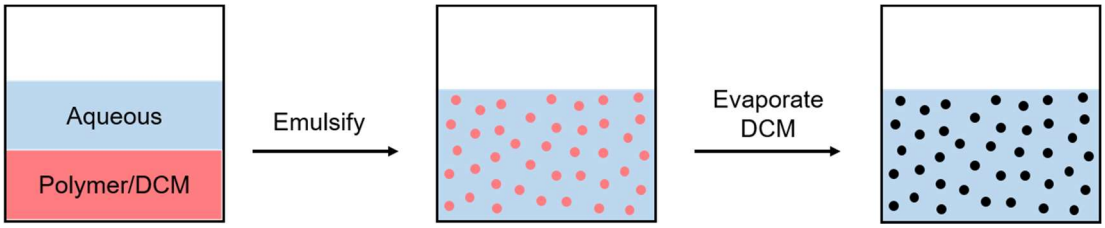

Figure 3.4 The emulsification-evaporation method. The polymer dissolved in an organic solvent is emulsified with an aqueous phase containing an emulsification agent and a surfactant to form a stable emulsion. The organic solvent is then evaporated to form hardened NPs.

The process shown in Figure 3.4 above can be used to encapsulate hydrophobic drugs by simply adding them to the organic phase with the polymer. In order to encapsulate hydrophilic drugs, including protein and peptide therapeutics, the process is modified to a double emulsion method. The protein, dissolved in an aqueous buffer, is first emulsified with the polymeric organic phase. This primary emulsion is then immediately emulsified with the secondary aqueous phase, containing the emulsification agent, to form a water-in-oil-in-water emulsion.

The emulsification-evaporation conditions were optimised for controlled NP formation, and to limit particle aggregation.

3.2.1.1 Emulsion formation

The method of forming the oil-in-water emulsion was found to be critical for controlling the size of the resulting particles. Preliminary experiments used a vortex to form the emulsion, and this resulted in large microparticles being formed. The presence of these larger particles was evident as there was sedimentation in the emulsions; larger particles in suspension do not undergo Brownian motion as their larger mass means that gravity, resulting in sedimentation, is the dominant force. The size of these particles was variable, and determined to be between 0.5 and 5 μm by TEM (Figure 3.5 A).

In contrast, when the emulsion was formed with a probe tip sonicator, where the sonicator is submerged in the liquid, a stable emulsion of NPs was formed. The formation of these NPs was also confirmed by TEM (Figure 3.5 B).

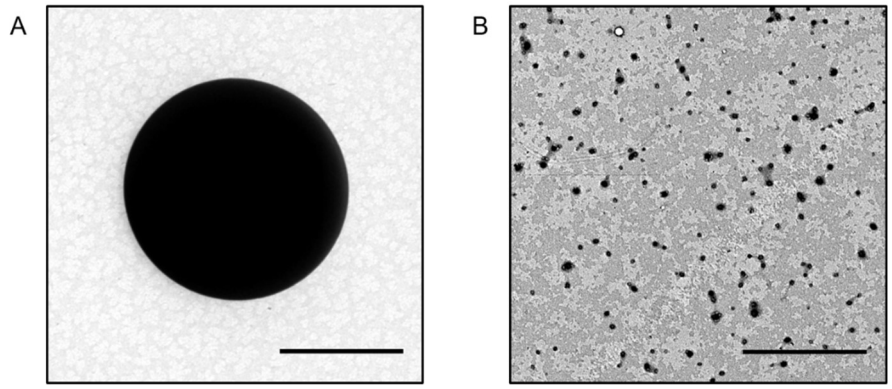

Figure 3.5 TEM analysis of micro and nanoparticles. A) When a vortex was used to create the emulsion, microparticles were formed. B) A probe-tip sonicator formed nanoparticles. Scale bars = 2 μm.

3.2.1.2 Evaporation time

Evaporation time was also found to be an important variable to ensure the complete evaporation of DCM. Issues with aggregation were encountered when the evaporation time was not long enough, as residual DCM can cause the NPs to form aggregates when centrifuged.[133] To find the time needed for complete DCM evaporation, the emulsion was sampled at regular time points, and any residual DCM was extracted into deuterated chloroform before analysing with ^{1}H NMR.

Figure 3.6 shows that the majority of DCM had evaporated after two hours, however, an expanded view of the NMR showed that there was a small amount of DCM

remaining after six hours. The emulsions were therefore stirred overnight to ensure complete DCM evaporation.

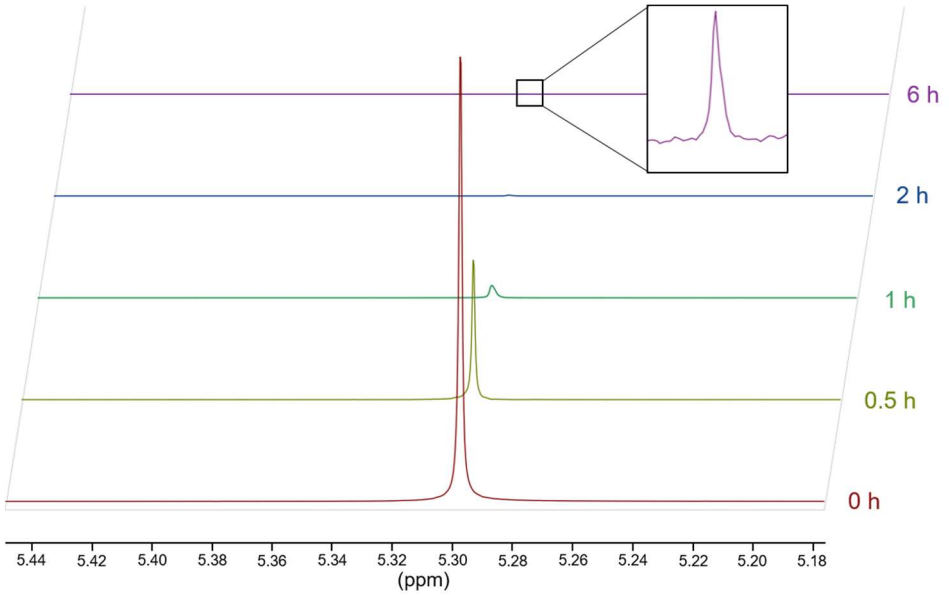

Figure 3.6 Evaporation of DCM. The emulsion was sampled over time and analysed with ^{1}H NMR for the presence of DCM. Inset shows an expanded view of the 6 hour sample.

3.2.1.3 Centrifugation time

Particle aggregation was an ongoing problem, even with the extended evaporation times. NP aggregation is irreversible, as opposed to agglomeration in which loose interactions can be reversed by vortexing (Figure 3.7).[134]

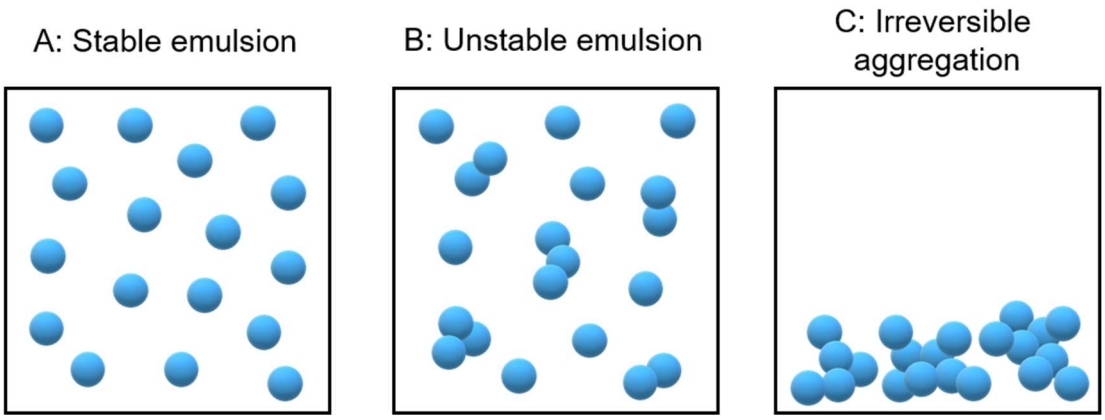

Figure 3.7 Nanoparticle aggregation is irreversible. Particles in suspension (A) can join together into reversible agglomerates (B) or irreversible aggregates (C).

Most literature preparations for PLGA NPs describe washing the particles three times with deionised water, which involves repeated centrifugation cycles and resuspension

in fresh water. When trying to replicate this protocol, it was found that after one centrifugation cycle, the NP pellet could be resuspended with vortexing, however, with a further cycle of centrifugation, the NP pellet would not go back into suspension. This indicates that the NPs had formed irreversible aggregates.

In an attempt to limit this aggregation, different centrifugation speeds were investigated for NP isolation. A NP emulsion was formed using the standard emulsification-evaporation method and, after an overnight evaporation, the NP emulsion was split into nine samples and each was centrifuged for ten minutes at speeds between 2,408 and 16,278 × g. The NP pellets were then resuspended in water, and analysed by DLS for particle size and PdI (Figure 3.8).

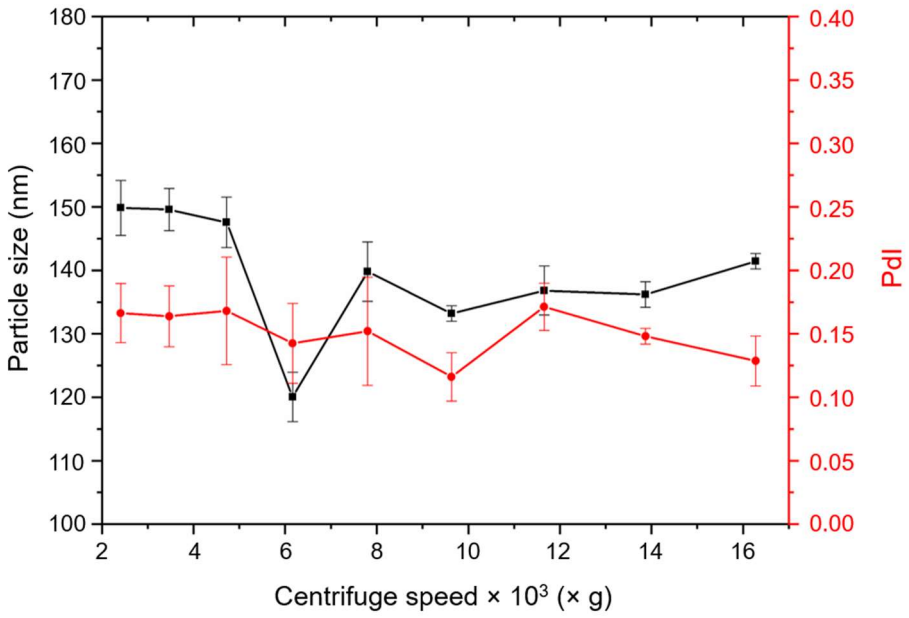

Figure 3.8 Investigation of optimum centrifugation speed. NPs were centrifuged for ten minutes at different speeds and then their particle size and PdI were measured with DLS. Three measurements were taken for each sample, error bars show standard error of the mean.

Figure 3.8 shows that particle size decreases with increasing centrifugation speed until 6,164 × g, where it begins to increase again. The hypothesis for this trend is that the lower speeds do not have enough centrifugal force to pellet smaller particles, leading to an increase in the average size, and that higher centrifugation speeds cause particle aggregation. The PdI is fairly constant across all conditions at ~0.15, which can be classed as a monodisperse sample.[135] 6,164 × g was chosen as the optimum centrifugation speed for the NPs as it gave the smallest particle size. Furthermore, at this speed the particles could be centrifuged twice and still go back

into suspension, however, a further centrifugation cycle still caused aggregation. The NPs were therefore washed only once with deionised water.

3.2.1.4 Lyophilisation

Many protocols lyophilise NPs for long-term storage, as aggregation usually increases over time in an aqueous suspension. To investigate the aqueous stability of the NPs, the particle size was measured by DLS when the NPs were freshly made (day zero) and then two, six and ten days after this (Figure 3.9). This shows that the PLGA-alkyne NPs are stable over ten days, with no significant difference in particle size between day zero and day ten. However, the PLGA-D NPs do show a significant increase in size over time, indicating that they are aggregating and lyophilisation should be explored.

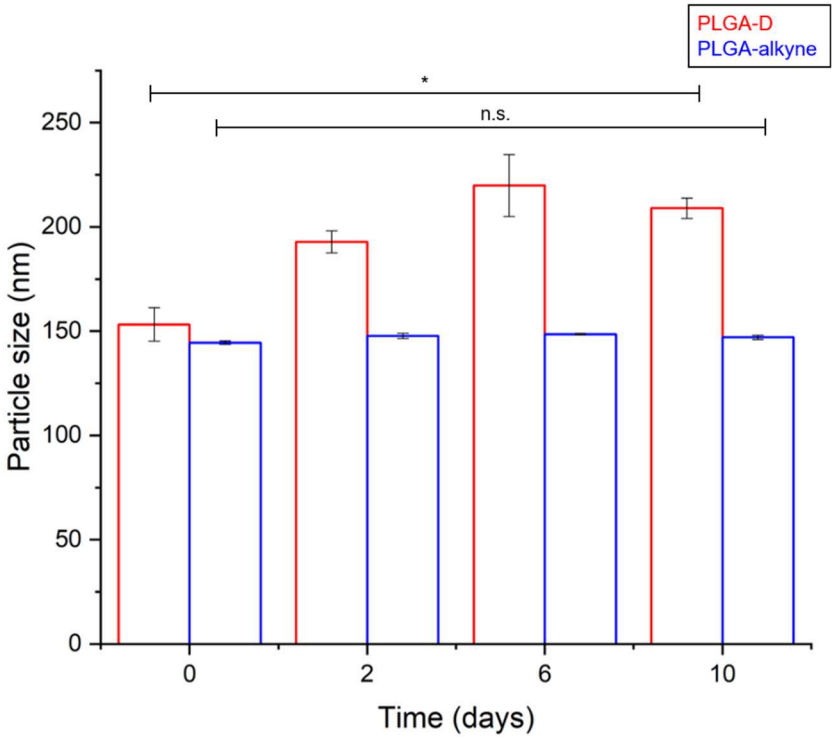

Figure 3.9 Aqueous stability of PLGA-D and PLGA-alkyne NPs over time. Particle size was measured in triplicate by DLS at each time point. Error bars show standard error of the mean, *: p <0.05, n.s.: p >0.05, one-way ANOVA.

Lyophilisation of PLGA NPs produced by the emulsification-evaporation method was achieved by resuspending the NP pellet in water, before freezing in liquid nitrogen and lyophilising overnight to give a white powder. However, this powder proved difficult to get back into suspension even after repeated vortexing, indicating that the particles were aggregated.

NPs can undergo irreversible aggregation caused by freezing stress, so cryoprotectants are often added to the formulation before lyophilisation.[136,137] Sucrose was investigated as a cryoprotectant in an attempt to prevent aggregate formation. A standard NP suspension was split into five samples, and one was left non-lyophilised as a control. The other four samples were lyophilised in 0, 1, 2 and 3% sucrose (w/v) in water. The lyophilised powders were then resuspended in water, and their particle size analysed by DLS, and compared to the non-lyophilised control.

Figure 3.10 shows that the non-lyophilised control had an average particle size of ~150 nm. When the NPs were lyophilised in water only, DLS confirmed that aggregates were forming as the average particle size increased dramatically to ~380 nm, with a large variability between measurements. The addition of 1, 2 or 3% sucrose seems to be successful in protecting the NPs from freeze damage, as the resuspended NPs had a very similar particle size to that of the control.

Although DLS showed that NPs lyophilised with sucrose had a similar average particle size to a non-lyophilised sample, cell death was observed when these NPs were used in biological experiments, so the NPs were prepared freshly every time.

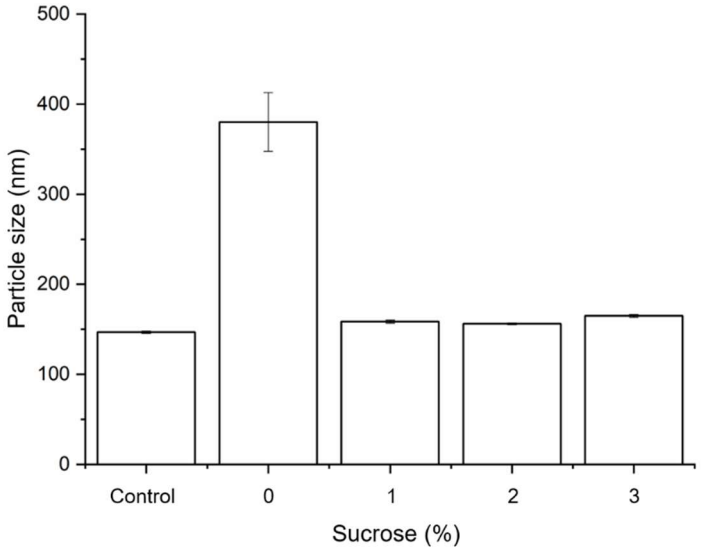

Figure 3.10 Lyophilisation of NPs with sucrose. NP samples were lyophilised with 0, 1, 2 and 3% sucrose and their particle size compared to a non-lyophilised control by DLS. Three measurements were taken for each sample, error bars show standard error of the mean.

3.2.1.5 Optimised protocol

The optimised emulsification-evaporation protocol, using a probe tip sonicator to form the emulsion, evaporating the DCM overnight, and centrifuging at 6,164 × g for ten

minutes, was used to synthesise NPs from PLGA **8**, and also the two bioorthogonally labelled polymers (PLGA-D **23** and PLGA-alkyne **25**). DLS was used to compare the properties of the NPs produced from these three polymers (Figure 3.11). The average particle size and PdI for the three polymers are listed in Table 3.1.

Table 3.1 Particle size and PdI of PLGA, PLGA-D and PLGA-alkyne NPs.

Polymer	Particle size (nm)	PdI
PLGA **8**	147	0.10
PLGA-D **23**	180	0.15
PLGA-alkyne **25**	129	0.17

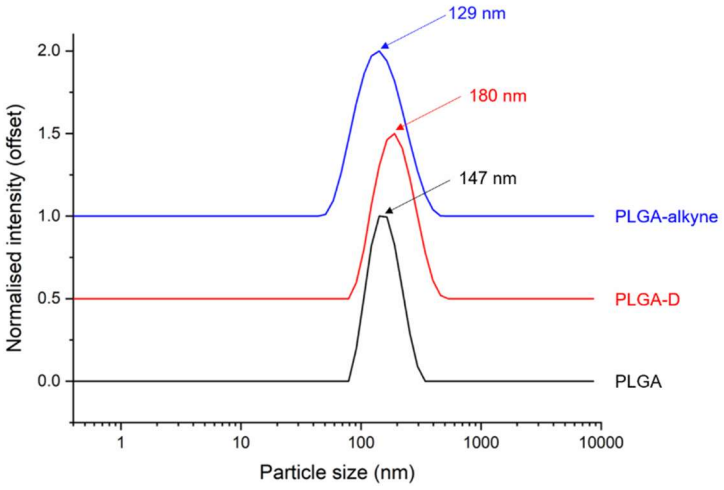

Figure 3.11 DLS characterisation of NPs. The optimised emulsification-evaporation method was used to synthesise PLGA, PLGA-D and PLGA-alkyne NPs and their average particle sizes were 147, 180 and 129 nm respectively. Spectra are normalised between 0 and 1 and offset for clarity.

The data in Table 3.1 and Figure 3.11 show that the emulsification-evaporation method can be used to form NPs of comparable size and dispersity from PLGA **8** and the two bioorthogonally labelled analogues PLGA-D **23** and PLGA-alkyne **25**. The NPs are all less than 200 nm in size, meaning that they have a high chance of entering cells by either endocytosis or phagocytosis.[138,139]

All of the DLS characterisation had been carried out in water, but since these NPs would be added to cells and tissues, their particle size was also investigated in Dulbecco's modified Eagle's medium (DMEM) supplemented with 10% fetal calf serum. Figure 3.12 shows the particle size distribution obtained from the DLS analysis

of PLGA-alkyne NPs, from the same batch, analysed in both water and DMEM. This shows that the size of the NP peak is unchanged at ~190 nm. In the trace for the NPs in media, there are two other smaller peaks which are also present in the media blank, presumably due to proteins and serum.

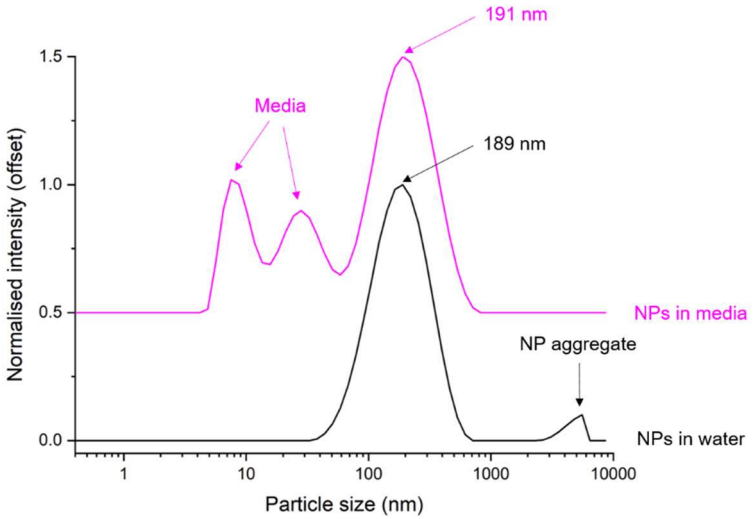

Figure 3.12 Analysis of NP size in water and media. NPs were produced from PLGA-alkyne, split into two and then resuspended in either water or DMEM, and their particle size analysed by DLS. Spectra are normalised between 0 and 1 and offset for clarity.

In Figure 3.12, the NPs suspended in water also shows that there is a larger aggregate of NPs at ~6000 nm. As mentioned in Section 3.1.2.2, large particles are disproportionally represented in DLS, since light scattering is proportional to diameter to the power of six, so this could be due to only a small amount of aggregated particles. DLS can also suffer from contaminants in the samples such as dust, and this can be minimised by pre-filtering samples through 0.45 µm filters.

3.2.2 The nanoprecipitation method

The nanoprecipitation method is an alternative NP synthesis which was also explored for PLGA NPs. The polymer was dissolved in a water miscible solvent (in this case acetonitrile), and upon dropping this solution into an aqueous phase, NPs spontaneously formed in a process known as solvent diffusion.[140] The acetonitrile could then be removed *in vacuo* to yield the hardened NPs. Advantages of this method over the emulsification-evaporation method are that no shear force has to be applied to form the emulsion, which could alter the structure of protein therapeutics being encapsulated, and no surfactants or stabilisers have to be added to the aqueous phase. A disadvantage of the nanoprecipitation method is that it is difficult to

encapsulate hydrophilic drugs in this way, although a two-step nanoprecipitation method for protein loading has been described by Morales-Cruz *et al*.[141]

The NPs produced by the nanoprecipitation method were isolated by centrifugation, resuspended in water and analysed by DLS and TEM (Figure 3.13).

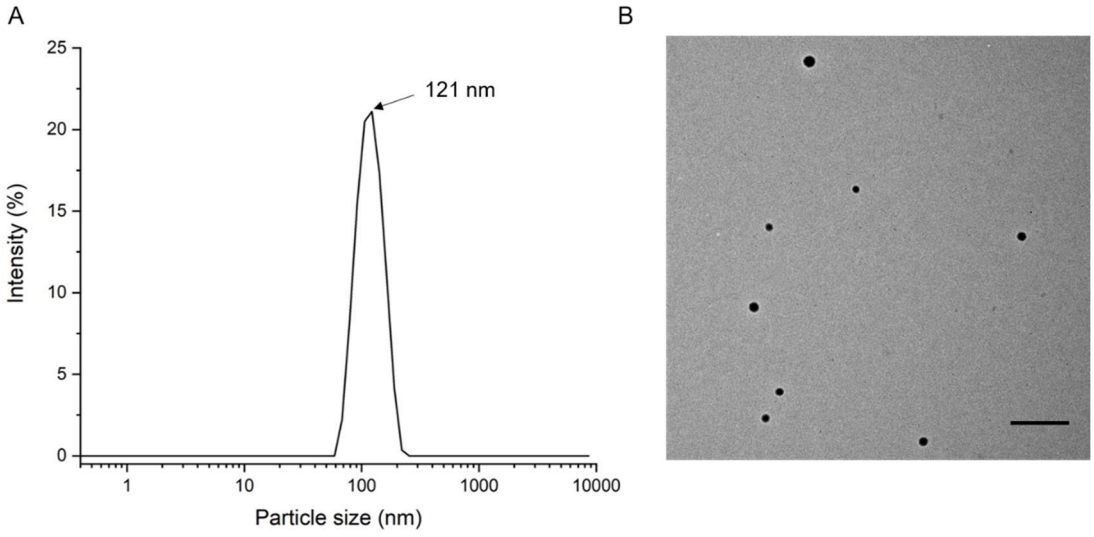

Figure 3.13 Characterisation of NPs produced with the nanoprecipitation method. A) DLS showed that the average NP size was 121 nm and the PdI was 0.07. B) TEM confirmed the size and monodispersity of the NPs. Scale bar 500 nm.

The NPs produced by the nanoprecipitation method had a smaller particle size (~120 nm), and with a PdI of 0.07 could be considered very monodisperse. However, because of the popularity of the emulsification-evaporation method in the literature for encapsulating a wide range of drug payloads, this method was taken forward to produce NPs for further studies.

3.3 Nanoparticle Concentration

Since the NPs produced were going to be used for biological experiments, it was vital to reliably know the concentration of the NPs in order to have reproducible experiments. In the optimised NP preparation protocol, the polymer was weighed out accurately, so a concentration of the polymer solution was known. However, it would be unreliable to assume full conversion of all the polymer to NPs, and the centrifugation and removal of the supernatant during the isolation and washes could also contribute to loss of the NPs.

Often, NPs are lyophilised so that the powder can be weighed out to resuspend the NPs into a suspension of known concentration. The lyophilisation protocol described in Section 3.2.1.4 used sucrose as a cryoprotectant, but this seemed to cause toxicity when these particles were incubated with cells, meaning that this technique could not be used to find NP concentration. Alternative methods of finding NP concentration were investigated which could be used to measure each batch of NPs.

3.3.1 Concentration by absorption

The NP suspension in water had a UV absorbance at 220 nm due to the carbonyl bonds in the polymer backbone. Absorbance is related to concentration in a linear fashion according to the Beer-Lambert Law,[142] so it was attempted to produce a calibration curve of the absorption of known NP concentrations. In triplicate, PLGA NPs were prepared using the optimised emulsification-evaporation method and were then lyophilised, without sucrose, to find the weight of the dry NPs. The NPs were then resuspended in water and each of the three samples was analysed by UV spectroscopy to find the absorbance at 220 nm of the NPs at 600, 300, 150 and 75 μg mL^{-1}. The standard curve produced is shown in Figure 3.14.

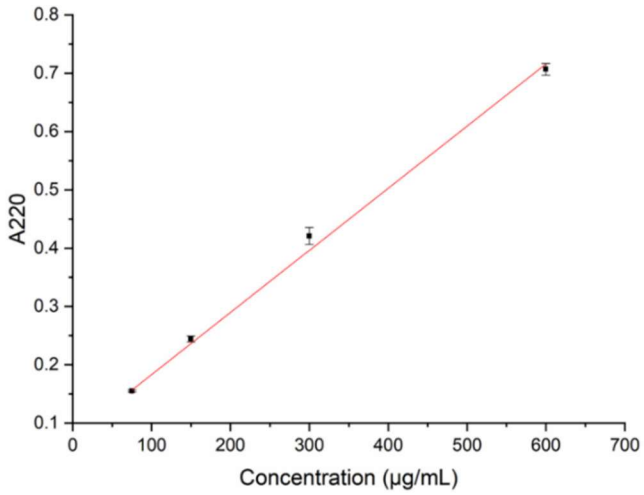

Figure 3.14 Concentration of PLGA NPs by absorption at 220 nm. In triplicate, NPs were prepared and lyophilised before resuspending in water where known concentrations were analysed for absorbance at 220 nm. Three technical replicates were taken for each value and then the nine values were pooled to find the mean. Error bars show standard error of the mean. R^2 = 0.997.

Figure 3.14 shows that there is a linear relationship between A_{220} and concentration for the PLGA NPs which could be used to find the concentration of an unknown sample. However, when the experiment was repeated with PLGA-alkyne NPs, the

relationship was not linear, so could not be used to find the concentration of an unknown sample. This method of finding NP concentration was therefore not pursued further.

3.3.2 Concentration by nanoparticle tracking analysis

As discussed in Section 3.1.2.2, NTA is another way of finding particle concentration as it tracks individual particles in a known volume of solvent. NPs produced from all three polymers (PLGA **8**, PLGA-D **23** and PLGA-alkyne **25**) were analysed by NTA, which gave their particle size distribution and equivalent concentrations in particles mL^{-1} (Figure 3.15). The particle size distribution data is much more detailed than that obtained from DLS (Figure 3.11), because individual particles are being tracked instead of a measurement being taken from the bulk suspension. This makes NTA highly suited to analysing polydisperse samples, or samples with aggregates.

To give more accurate NP concentration data, the samples were diluted until in the optimum range of 1–8 × 10^8 particles mL^{-1} was reached, as recommended by the manufacturer. As the tracks of individual particles are recorded to measure Brownian motion, having too many particles in the field of view makes it harder to resolve different tracks. On the other hand, having too few particles will lead to statistically unreliable results.

The concentrations of NPs synthesised from 10 mg of the PLGA **8**, PLGA-D **23** and PLGA-alkyne **25** polymers are listed in Table 3.2. The yield of NPs obtained from the PLGA-alkyne polymer **25** is significantly higher than that obtained from PLGA **8** and PLGA-D **23**. One reason for this could be the increased hydrophobicity of PLGA-alkyne, meaning that it will have a higher solubility in DCM. During the emulsification-evaporation process, the polymer dissolved in DCM is mixed with an aqueous phase (Figure 3.4). Any polymer not fully soluble in DCM could partition into the aqueous layer, causing a loss of yield of the NPs. Using polymer with too low a molecular weight would cause the same problem.

Table 3.2 Concentration of NPs produced from 10 mg of PLGA, PLGA-D and PLGA-alkyne.

Polymer	Concentration ($\times 10^9$ particles mL^{-1})
PLGA **8**	13.6
PLGA-D **23**	7.4
PLGA-alkyne **25**	42.6

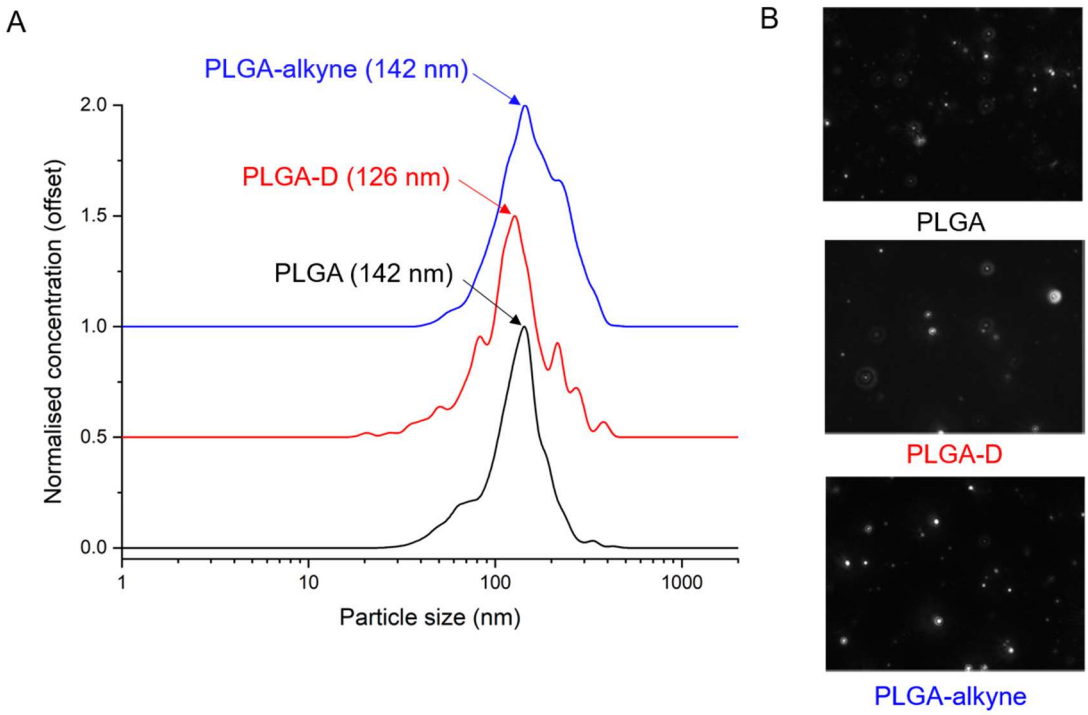

Figure 3.15 Analysis of NPs with NTA. A) Particle size distributions are obtained for PLGA (black), PLGA-D (red) and PLGA-alkyne (blue) NPs. B) Representative images obtained from the NTA camera of the three types of NPs. The NPs are visualised by the way they scatter light allowing their Brownian motion to be tracked, which is proportional to their size.

3.4 Nanoparticle Targeting

NPs are often targeted in a passive way, for example to tumours, where the gaps between tight junctions in blood vessels around the tumour and an increased secretion of permeability factors leads to accumulation of NPs, known as the enhanced permeation and retention effect.[143] NPs can also be modified with targeting ligands on their surface with the aim of increasing drug efficacy, and reducing off-target effects. Examples of active targeting ligands are sugars, peptides and

antibodies (Figure 3.16),[144] and various strategies can be employed to attach them to the surface of the NPs.

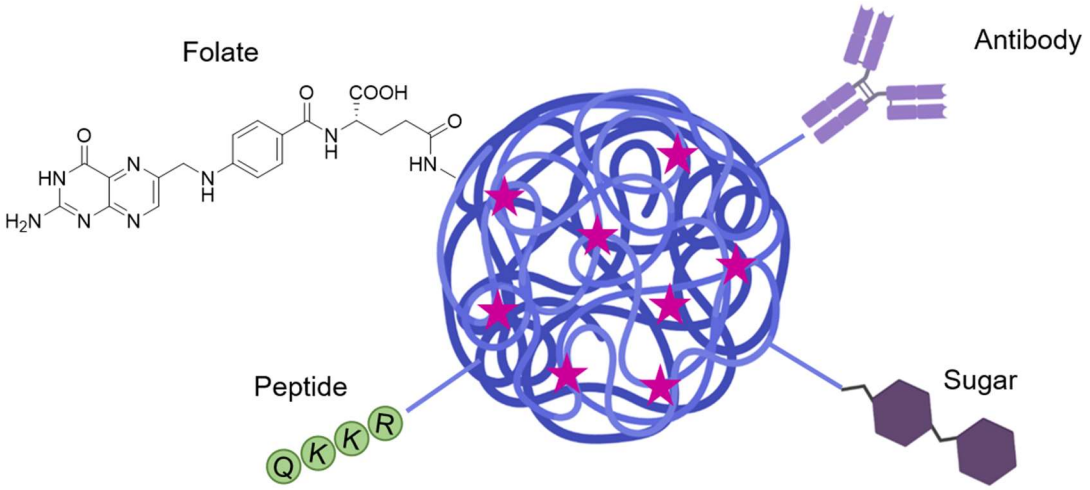

Figure 3.16 Nanoparticle targeting strategies. Drug loaded NPs can be targeted with antibodies, sugars, peptides and folate to direct them to a certain cell-type. Image created with Biorender.com.

Antibodies are an obvious choice of targeting ligand because of their exquisite specificity of binding for their target antigen, whereas sugars are important for targeting cell surface receptors. Peptides and folate can be used to target cancer cells, which over-express certain factors.[145,146] As well as targeting, peptides can also enhance cell permeability of NPs.[147] Even with targeting ligands, NPs can still interact with off-target cells. Recently, Figueroa *et al.* designed virus mimetic NPs where two binding interactions are needed to trigger endocytosis of the NPs, giving superior cellular selectivity.[148]

3.4.1 Avidin-lipid conjugates

Previous work in the Williams group used PLGA NPs with surface antibodies to the neural / glial antigen 2 (NG2) protein to specifically target them to OPCs.[20] Conjugation of the NG2 antibody to the NP surface was achieved by exploiting the avidin-biotin binding capabilities. Avidin is a tetrameric protein that can bind four molecules of the small molecule biotin with extremely high affinity (K_d = 1.3 × 10^{-15} M).[149] Avidin-lipid conjugates were synthesised as described by Park *et al.*,[150] and were then added into the NP preparation. The hypothesis is that the lipid tail will bury

into the hydrophobic NP, leaving the avidin on the surface which can then bind biotinylated NG2 antibody, which is commercially available.

It was attempted to replicate this protocol so that surface avidin could be conjugated to the surface of the Raman labelled NPs. Palmitic acid **31**, a 13-carbon long carboxylic acid, was first activated as its *N*-hydroxysuccinimide (NHS) ester **33** to increase its activity towards the ε-NH_2 of lysine residues on avidin (Figure 3.17 A)

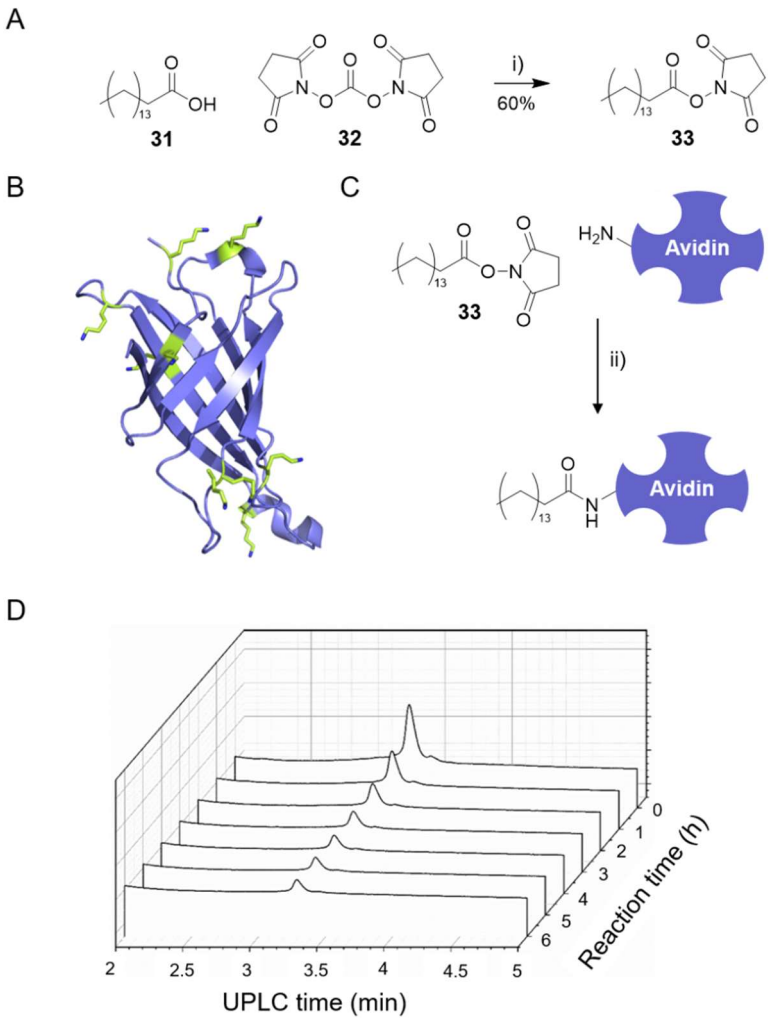

Figure 3.17 Formation of avidin-lipid conjugates. A) Synthesis of NHS-palmitic acid **33**. Reagents and conditions: i) DCM, triethylamine, bis(2,5-dioxopyrrolidin-1-yl) carbonate **32**, rt, 8 h. B) Structure of avidin with lysine residues highlighted in green. PDB 1VYO. C) Lysine conjugation, where the NHS-palmitic acid reacts with a free amine to form an amide bond with the protein. Reagents and conditions: ii) NHS-palmitic acid **33** (10 eq.) 1 M HEPES pH 8, 0.2% sodium deoxycholate, ~24 h. D) Reaction monitoring with UPLC. NHS-palmitic acid was incubated with avidin, and the avidin peak was observed to decrease over time by UPLC. However, no new product peak was seen emerging.

The NHS-palmitic acid **33** was then incubated with avidin in a ten-fold molar excess, in the hope that this activated NHS ester would react with surface accessible lysine residues (Figure 3.17 B) and conjugate the lipid chain through an amide bond (Figure 3.17 C).

The reaction was monitored by ultra-performance liquid chromatography (UPLC) and the avidin peak could be seen reducing over time, but no new product peak was clearly seen (Figure 3.17 D). The reaction was found to be unsuccessful without the addition of the surfactant sodium deoxycholate, which was needed to disrupt unreactive micelles of NHS-palmitic acid thought to form in the aqueous buffer.

The success of this conjugation reaction was debatable, since no product peak was seen appearing over time on the UPLC trace. Analysis of the modified protein by mass spectrometry and gel electrophoresis was also inconclusive. The modified avidin band was similar to native avidin in the gel electrophoresis, and the modified avidin gave very low signal in the mass spectrometry. The NHS-palmitic acid **33** was added in a ten-fold molar excess, so it is possible that multiple labelling events could take place on different protein molecules producing a heterogeneous product that is hard to analyse. However, the solubility of the avidin-lipid conjugates was also thought to be a problem as precipitation was observed in the reaction mixture over time. The addition of lipid chains to the protein would decrease its hydrophilicity, so the solubility in HEPES buffer would be expected to decrease. Addition of low levels of dimethyl sulfoxide (DMSO) to the reaction mixture did not seem to help with the precipitation, and analysis of the protein concentration before and after the reaction (Nanodrop, A_{280}) confirmed that the concentration decreased.

Before adding the avidin-lipid conjugates to the NP synthesis, they were dialysed against 1 M HEPES to remove excess NHS-palmitic acid **33** and the sodium deoxycholate. To incorporate the avidin-lipid conjugates into the NPs, the standard emulsification-evaporation method was followed (Section 3.2.1), but with addition of the avidin-lipid conjugates to the aqueous phase. During the emulsion formation, the avidin-lipid conjugates should position themselves with the hydrophobic lipid tail pointing into the NP centre, leaving the avidin on the NP surface (Figure 3.18).

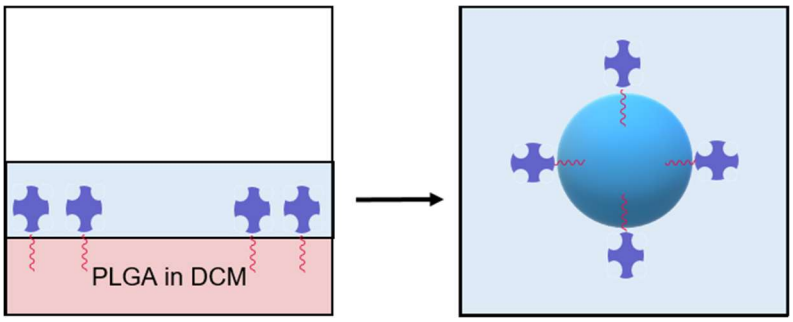

Figure 3.18 Incorporation of avidin lipid conjugates into NPs.

3.4.2 Biotin horseradish peroxidase assay

In order to check if there was surface avidin on the NPs capable of binding biotin, a colorimetric assay was carried out using biotinylated horseradish peroxidase (biotin-HRP). The biotin binding affinity of NPs prepared in the presence of avidin (Figure 3.20 A) or avidin-lipid conjugates (Figure 3.20 B) was compared to standard NPs prepared without any avidin. The NPs were firstly all analysed by NTA to determine their concentration so that the same number of particles (2×10^9 particles mL^{-1}) could be used for each condition.

The NPs were incubated with biotin-HRP for before isolating the NPs by centrifugation, and washing once with PBS to remove residual biotin-HRP. 3,3',5,5'-Tetramethylbenzidine (TMB) **34** was then added to the NPs which is an aromatic compound that produces a blue colour in the presence of peroxidase, and turns yellow upon acidification (Figure 3.19).[151] The NPs were incubated with TMB before the addition of 1 M hydrochloric acid which caused the samples to turn yellow, and their absorbance was measured at 450 nm (A_{450}). A higher A_{450} value corresponds to more bound biotin HRP, which in turn indicates more surface avidin on the NPs.

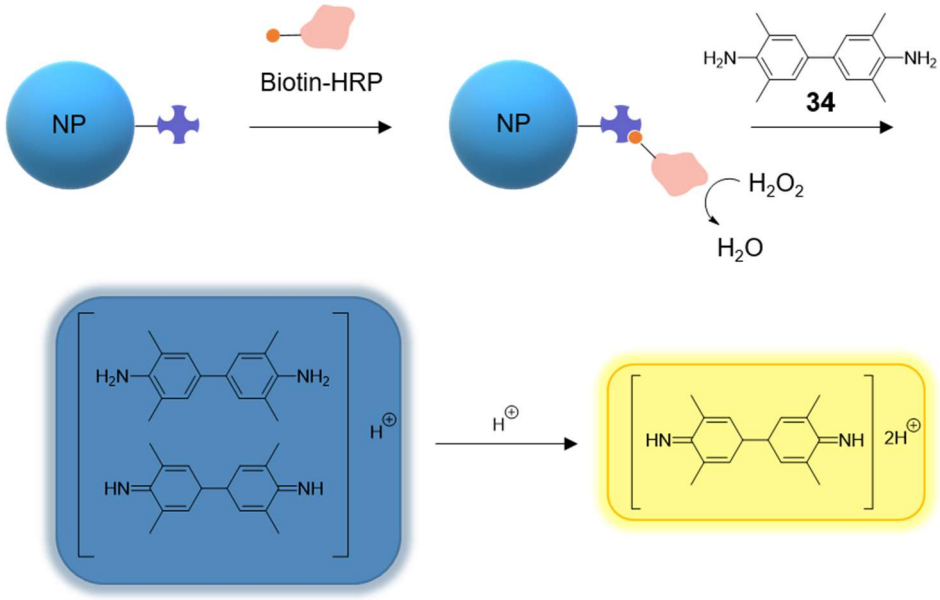

Figure 3.19 The biotin-HRP assay for quantification of surface avidin. NPs were incubated with biotin-HRP which will bind to avidin. After washing the NPs, TMB **34**, which acts as a hydrogen donor, was then added which produces a blue charge transfer complex in the presence of HRP. Acidification with 1 M HCl trapped the complex, resulting in a yellow colour that could be analysed by UV spectroscopy at 450 nm.

There was no significant increase in A_{450} between either the avidin or avidin-lipid NPs and the control NPs, indicating there was no avidin on the NP surfaces. The control NPs (no avidin) had an A_{450} value of ~3 showing that the assay has a high background, probably caused by small amounts of residual biotin-HRP that were not removed by the wash step. The A_{450} values obtained from these experiments are listed in Table 3.3. When a control was carried out of the assay without the addition of biotin-HRP, no blue or yellow colours were observed.

3.4.3 Chemical conjugation of avidin

Instead of relying on avidin-lipid conjugates, two chemical reactions were explored to conjugate avidin to a preformed NP through a covalent bond.

3.4.3.1 Carbamate formation

The PLGA **8** and PLGA-alkyne **25** polymers used to produce the NPs have a free alcohol on their end groups. In an attempt to conjugate avidin to these alcohol groups, the amines on the avidin were first activated with 1,1-carbonyldiimidazole so that they could then react with the NP alcohol groups to form a carbamate bond (Figure 3.20

C). Padiya *et al.* reported an imidazole carbonylation in water on a variety of substrates, and these conditions were replicated with avidin (Scheme 3.1).[152]

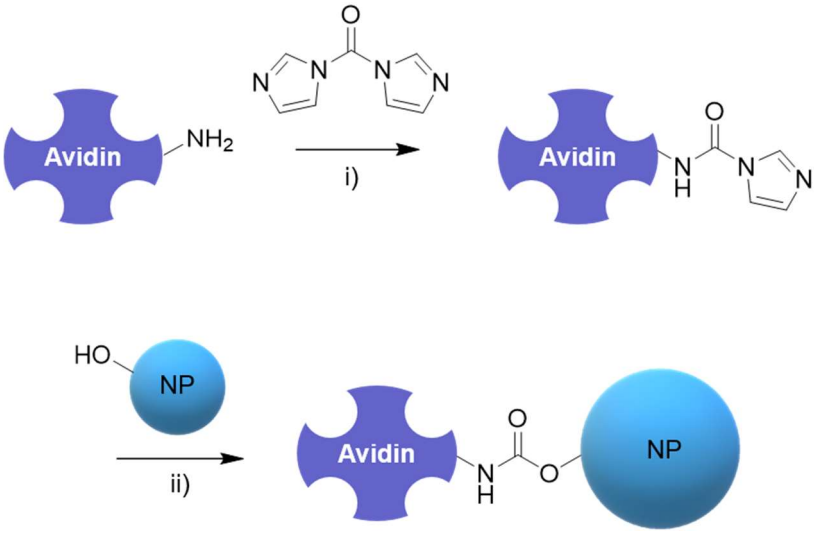

Scheme 3.1 Conjugation of avidin through a carbamate bond. Amide groups on avidin were first activated with 1,1-carbonyldiimidazole before reacting with the OH end groups on NPs to form a carbamate. Reagents and conditions: i) 1,1-carbonyldiimidazole, PBS, 0 °C, 1 h; ii) NPs, 0 °C, 1 h then 0 °C – rt over 1 h.

The biotin-HRP assay was repeated with these NPs, but again, no increase in biotin binding was observed over the control NPs. These results are listed in Table 3.3.

3.4.3.2 Copper catalysed azide alkyne click reaction (CuAAC)

The CuAAC reaction is a widely used bioorthogonal reaction used to conjugate labels to biomolecules in a biological environment.[153] It involves the reaction of an alkyne and an azide to form a triazole bond. One of the bioorthogonal polymers (PLGA-alkyne **25**) contains terminal alkynes that could be available for click reactions. It was attempted to 'click' biotin azide onto preformed PLGA-alkyne NPs so that avidin could then bind to this biotin (Figure 3.20 D). Avidin is tetrameric, so it would still be possible to bind the biotinylated NG2 antibody onto another one of avidin's binding sites.

Copper sulphate, sodium ascorbate and tris(3-hydroxypropyltriazolylmethyl)amine (THPTA), a water soluble ligand,[153] were first stirred in water to reduce the copper, before the addition of biotin-azide and PLGA-alkyne NPs to initiate the click reaction. The resulting NPs were then resuspended in a solution of avidin in PBS, and were stirred overnight at room temperature to allow conjugation of avidin Scheme 3.2.

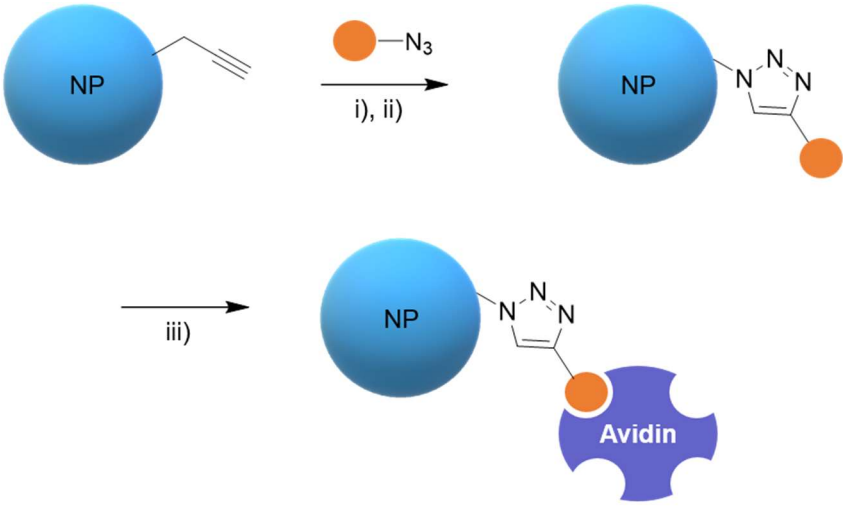

Scheme 3.2 Conjugation of biotin azide to NPs through a CuAAC reaction. Reagents and conditions: i) Copper sulphate, sodium ascorbate, tris(3-hydroxypropyltriazolylmethyl)amine, water, rt, 15 min; ii) biotin-PEG3-azide conjugate, PLGA-alkyne NPs, water, rt, 4 h; iii) isolated NPs, avidin, PBS, rt, 18 h.

A summary of all targeting reactions are shown below in Figure 3.20.

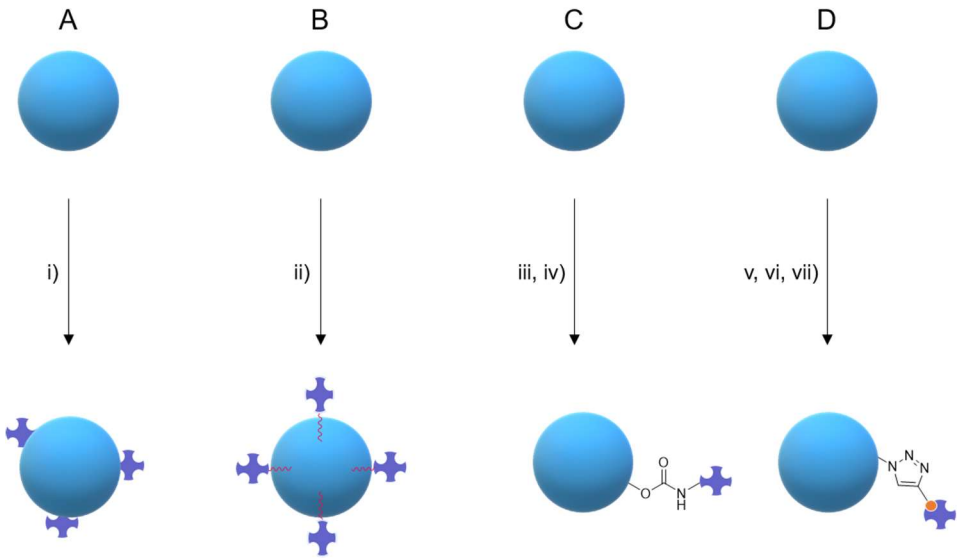

Figure 3.20 Summary of NP targeting strategies. A) Surface deposition of avidin. Reagents and conditions: i) NPs, avidin, rt, 18 h. B) Avidin lipid conjugates. Reagents and conditions: ii) Standard emulsification-evaporation method with avidin lipid conjugates added to the aqueous phase. C) Carbamate conjugation of avidin. Reagents and conditions: iii) 1,1-carbonyldiimidazole, PBS, 0 °C, 1 h; iv) NPs, 0 °C, 1 h then 0 °C – rt over 1 h. D) v) Copper sulphate, sodium ascorbate, tris(3-hydroxypropyltriazolylmethyl)amine, water, rt, 15 min; vi) biotin-PEG3-azide conjugate, PLGA-alkyne NPs, water, rt, 4 h; vii) isolated NPs, avidin, PBS, rt, 18 h.

Again, analysis of these NPs with the biotin-HRP assay showed that there was no increase in biotin binding over control NPs (Table 3.3). The reaction could have been unsuccessful because the hydrophobic alkyne groups would most likely be pointing towards the inside of the NP and therefore inaccessible to react with biotin azide.

Table 3.3 Biotin-HRP assay results from all the targeting strategies attempted. For each sample of the NPs, the assay was carried out in triplicate and the A_{450} shown is the average.

Sample	A_{450}	Standard deviation
Control (PLGA NPs)	2.99	±0.06
Avidin (PLGA NPs)	3.07	±0.02
Avidin-lipid (PLGA NPs)	3.07	±0.02
Control (PLGA-alkyne NPs)	3.11	±0.005
Carbamate (PLGA-alkyne NPs)	3.08	±0.005
Click reaction (PLGA-alkyne NPs)	3.09	±0.005

3.5 Conclusions

In this chapter, the formation of polymeric NPs has been described by both the emulsification-evaporation and nanoprecipitation methods. Optimisation of the emulsification-evaporation method revealed the best emulsification method, evaporation time and centrifugation speed to produce particles of ~150 nm and low dispersity from PLGA **8**, PLGA-D **23** and PLGA-alkyne **25** polymers. Because of the tendency of the PLGA-D NPs to aggregate over time, it was decided to make them fresh before every biological experiment. The NP concentration could be found by analysing with NTA, which is vital for the reproducibility of the biological experiments described in Chapter 4. It was found through analysis by DLS and NTA that the bioorthogonal polymers PLGA-D and PLGA-alkyne produced NPs with comparable properties to the FDA approved PLGA NPs.

Various methods were investigated to conjugate avidin to the surface of the NPs so that a biotinylated targeting antibody could be attached. However, it was found that

avidin-lipid conjugates, and attempts to covalently bind avidin to the NP surface through carbamate and triazole bonds, did not produce significantly higher biotin binding than control, unconjugated NPs.

Chapter 4 Raman Imaging of Bioorthogonal Nanoparticles

4.1 Introduction

Imaging drug delivery systems in a biological environment is of vital importance to elucidate their uptake, mode of action and ultimate fate. In this chapter, the bioorthogonally labelled NPs prepared in Chapter 3 were administered to a number of biological models of the brain, and the behaviour of the NPs was investigated by imaging them with SRS microscopy.

4.1.1 Models of the brain

In order to study the effects of a drug or treatment on the brain, biological models mimicking the brain, and various disease states, have been developed including single cells, organoids, brain tissue slices and whole animal models.

4.1.1.1 Cell culture

Cell culture is one of the simplest ways of modelling the effects of a treatment to brain cells.[154] Immortal cell lines are often used as they are easy to culture, but these are transformed to allow their extended artificial culture over a long period, which means that they frequently develop different behaviour to their *in vivo* counterparts. The misidentification or contamination of cell lines can also lead to problems.[155] In contrast, primary cells are isolated from fresh tissue and thus retain more *in vivo* characteristics and provide a more realistic model, but can only be cultured for a limited time.[156] Cell cultures are usually grown 2D on a flat surface, but can also been grown in 3D cellular aggregates called spheroids, which can give a more realistic picture of, for example, a tumour.[157]

To test the intracellular Raman activity of the NPs, primary rat microglia were utilised as proof of principle cells. Microglia are part of the immune response in the brain, and act as phagocytes to engulf foreign objects.[2] It was thought that microglia would be likely to internalise the NPs and allow imaging.[158] The microglia used were isolated from postnatal rat pups before every experiment.

4.1.1.1 *Ex vivo* slice culture

A disadvantage of cell culture experiments is that the cells are grown in a 2D environment on a dish, which is not representative of their *in vivo* state. The *ex vivo*

culture of brain slices has been used to bridge the gap between cell culture and whole organism studies.[159,160] In this way, individual cells retain a similar tissue microenvironment as they would in a living organism. Slice cultures are a much more economical and high-throughput way of studying the effects of a drug on the brain compared to using live mice, and have been used as a screening platform.[161] Samples of tissue from human brains obtained during surgery have also been sliced and cultured for up to two weeks to provide a model for glioblastoma.[162]

4.1.1.1 *In vivo* studies

Moving on to study the effects of research in live animals is vital for understanding the mode of action of the treatment in a whole organism. Cell and *ex vivo* tissue cultures study cells or organs in isolation from the myriad of other processes that are present in the body. While this is important for the simplification of early research, *in vivo* testing is important pre-clinical research that will have to be investigated before moving the treatment on to humans. For example, studies treating animals with NPs have shown that the NPs are likely to accumulate in the liver.[163] This is an important consideration when deciding on the appropriate dose to balance therapeutic effect at the desired site with potential liver toxicity.

Mouse lines can be bred to model some aspects of the disease symptoms of MS. Shiverer mice contain a mutation causing an absence of myelin basic protein, a major component of myelin sheaths, leading to a lack of compact myelin, and can be a useful tool in MS research.[164] Experimental autoimmune encephalomyelitis (EAE) can be induced as an autoimmune T-cell driven mouse model of inflammation and demyelination in the central nervous system, which can model some of the early changes found in relapsing-remitting MS in humans, and Theiler's murine encephalomyelitis virus also causes demyelination.[165] Experimental demyelination can also be caused by treatment of mice with the toxin cuprizone,[166] which gives global demyelination, or injection such as lysophosphatidyl choline (LPC) toxin into the brain or spinal cord to produce focal areas of demyelination.[167] The choice of these models depends on the biological question to be answered. For example, the EAE model has been used successfully to test therapeutics working against T-cell driven inflammation,[168] which have translated to humans. However, this would be an inappropriate model for testing therapeutics for enhancing remyelination, which might be better tested in a toxin-induced model where there is a well-described time course of demyelination and remyelination.

4.2 Cell Viability Assay

The toxicity of the NPs in microglia was first assessed using the CellTiter-Glo luminescent viability assay (Promega). PLGA is an FDA approved polymer with a long and proven safety record,[169] so it was important to compare the toxicity of the new bioorthogonal polymers (PLGA-D **23** and PLGA-alkyne **25**) to PLGA NPs. NPs were formed using the emulsification-evaporation method and analysed with NTA to find particle size and concentration. The NPs were added to microglia in culture at 1, 2, and 4 × 10^9 particles mL^{-1}. After a 24 hour incubation, the enzyme luciferase was added to the microglia, which reacts with adenosine tri-phosphate (ATP) and causes luminescence.[170] Higher luminescence is attributed to a higher number of metabolically active cells. The luminescence of NP treated cells was compared to untreated, control cells that had been cultured for the same amount of time (Figure 4.1). The mean luminescence of the control cells was set to 100%, and was used to scale the mean luminescence of the NP treatment conditions.

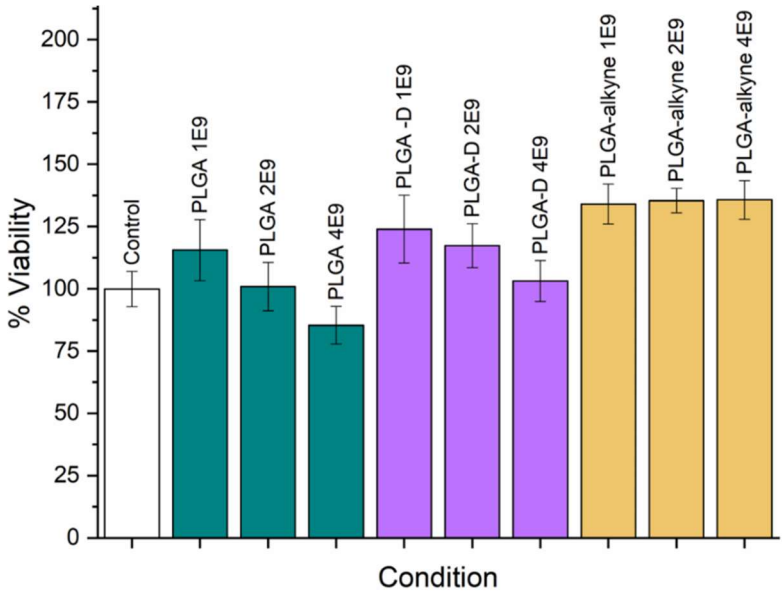

Figure 4.1 Toxicity of the NPs to microglia in culture. PLGA, PLGA-D and PLGA-alkyne NPs were added to microglia at 1, 2, and 4 × 10^9 particles mL^{-1} and after a 24 h incubation, viability was assessed with the CellTiter-Glo luminescence assay. The luminescence of the untreated cells was set to 100%. The values for three biological replicates, with three wells per condition, were pooled and averaged. Error bars show standard error of the mean.

Figure 4.1 shows that all of the NP concentrations tested were non-toxic, retaining 80% or more viability. Interestingly, most of the NP conditions, aside from PLGA NPs at 4

× 10^9 mL^{-1}, had higher cell viability than the control cells. This could mean that the NPs have metabolically activated the cells, leading to more ATP production. A limitation of using the luminescence viability assay as opposed to directly counting single live and dead cells, is that the amount of live cells is only correlated to luminescence. However, the assay clearly shows that all the NPs tested were non-toxic to microglia.

4.3 Cell Pellet Raman Assay

Initial experiments involved incubating PLGA-D and PLGA-alkyne NPs with a monolayer of microglia for 24 hours, then washing, pelleting and lyophilising these cells to give a solid cell pellet (Figure 4.2 A). The wash step served to remove any NPs that were not associated with the microglia.

Figure 4.2 B shows analysis of the microglia treated with NPs by spontaneous Raman spectroscopy. The red, lower spectrum shows the Raman signal obtained from the cell pellet treated with PLGA-D NPs. This shows characteristic cellular peaks of CH_3 at 2939 cm^{-1}, and CH_2 at 2856 cm^{-1} that have been associated with proteins and lipids respectively,[171] and a small, sharp peak at 1004 cm^{-1} in the fingerprint region which is caused by the aromatic group in the amino acid phenylalanine. However, there were no carbon–deuterium peaks present in the cell-silent region between 1800 and 2800 cm^{-1}. This could be because the NPs were not entering the microglia, or because the carbon–deuterium signal was not strong enough to be observed.

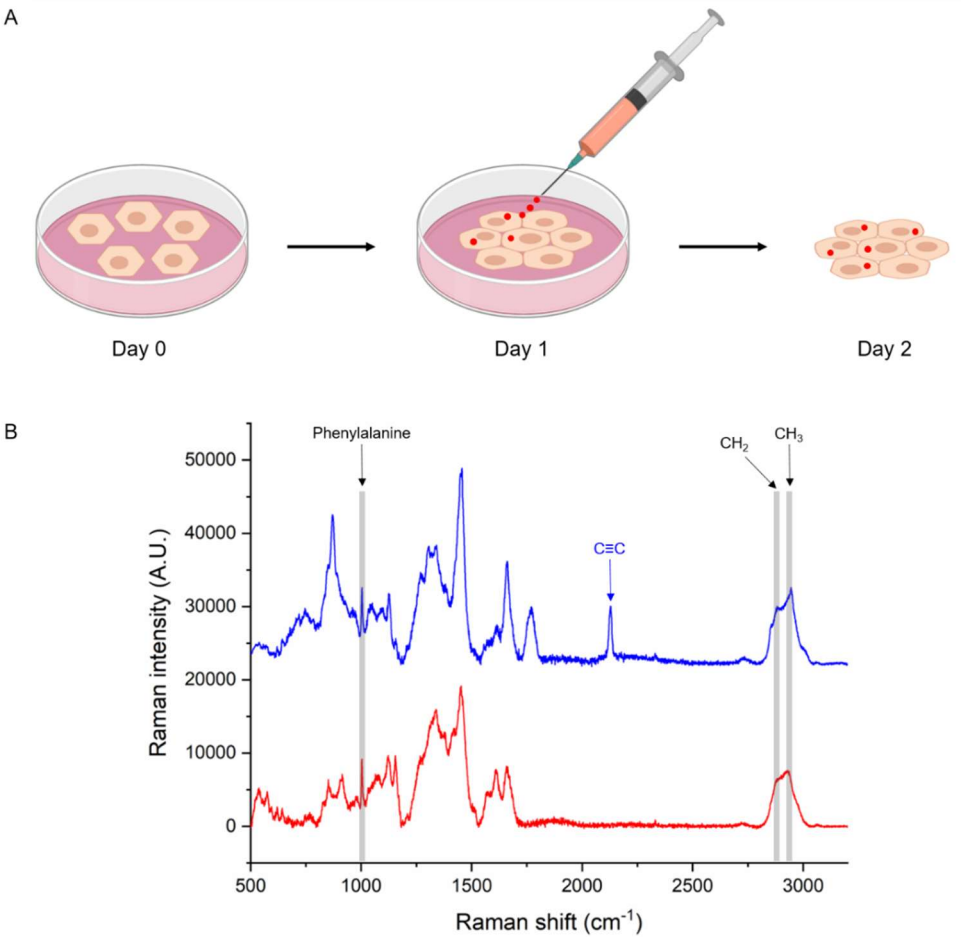

Figure 4.2 Schematic of the cell pellet experiments and characteristic Raman spectra. A) Microglia were plated on day zero and were incubated overnight to allow them to adhere to the dish. The next day, NPs (PLGA-D or PLGA-alkyne) were resuspended in mixed glia media and added to the NPs. After a 24 h incubation, the microglia were washed, trypsinised, and then pelleted by centrifugation. The cell pellet was lyophilised to give a solid. Image created with Biorender.com. B) Spontaneous Raman spectroscopy of microglia plus PLGA-D NPs (red) and PLGA-alkyne NPs (blue), λ_{ex} = 785 nm.

In contrast, the microglia incubated with PLGA-alkyne NPs (blue spectrum) shows the characteristic cellular signatures, and also the bioorthogonal alkyne peak at 2128 cm^{-1}. This indicates that the PLGA-alkyne NPs are entering the cells at a concentration high enough to be detected by spontaneous Raman, and that they are a good candidate for SRS imaging studies.

4.4 Imaging Nanoparticles *in vitro* with SRS Microscopy

4.4.1 Imaging in microglia

Microglia were incubated with PLGA-D and PLGA-alkyne NPs and imaged with SRS microscopy to investigate their intracellular localisation. Again, the microglia were plated on day zero and were left overnight to adhere to the dish before the addition of PLGA-D or PLGA-alkyne NPs at 0.5, 1 and 2 × 10^9 particles mL^{-1}. After a 24 h incubation with the NPs, the microglia were washed to remove free NPs, and then fixed.

The fixed cells were then imaged with a custom-built SRS microscope (Figure 4.3), which consists of a tuneable pump laser and a spatially and temporally overlapped Stokes laser. The energy difference between the pump and Stokes lasers was tuned to match a molecular vibration of interest and thus create an image of this vibration.

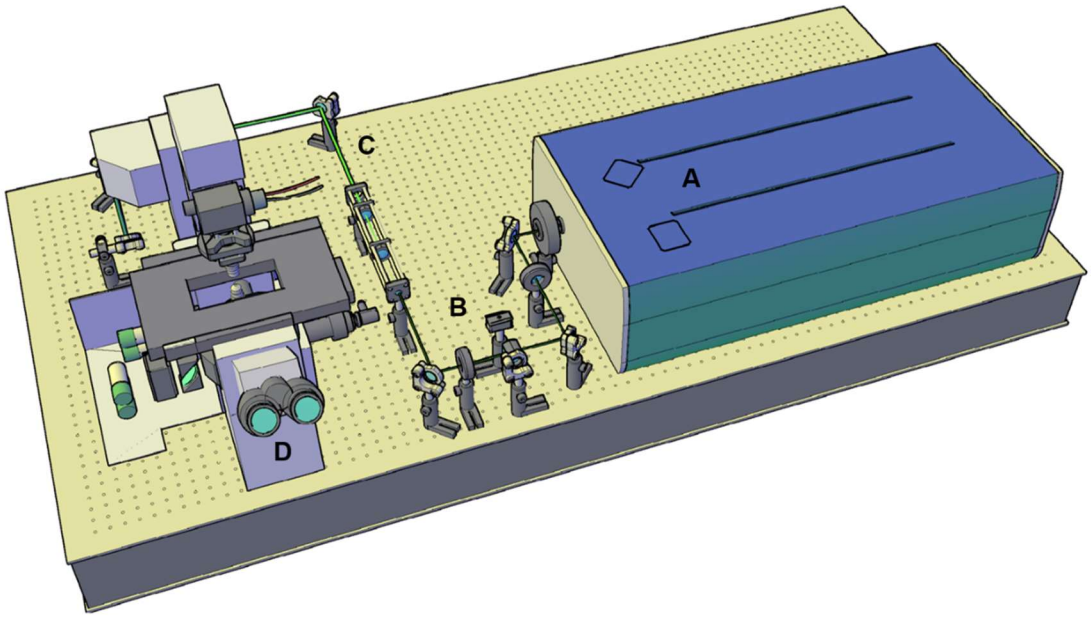

Figure 4.3 A schematic of the custom-built SRS microscope at The University of Edinburgh. An APE picoEMERALD laser system (A) provides two spatially and temporally overlapped beams. These are aligned through a series of focusing mirrors (B) to a beam expander (C) and then an FV1000 confocal scanning microscope (D). Image created by Dr Martin Lee.

When imaging the NP resonance (2253 cm^{-1} for PLGA-D NPs and 2128 cm^{-1} for PLGA-alkyne NPs), an off-resonance image ~30 cm^{-1} away from the top of the on-resonance peak was also acquired. This off-resonance image was always subtracted from the NP on-resonance image using Fiji,[172] to ensure that the on-resonance signal

was derived from the NPs. Figure 4.4 shows an example of this process in images of microglia treated with PLGA-alkyne NPs.

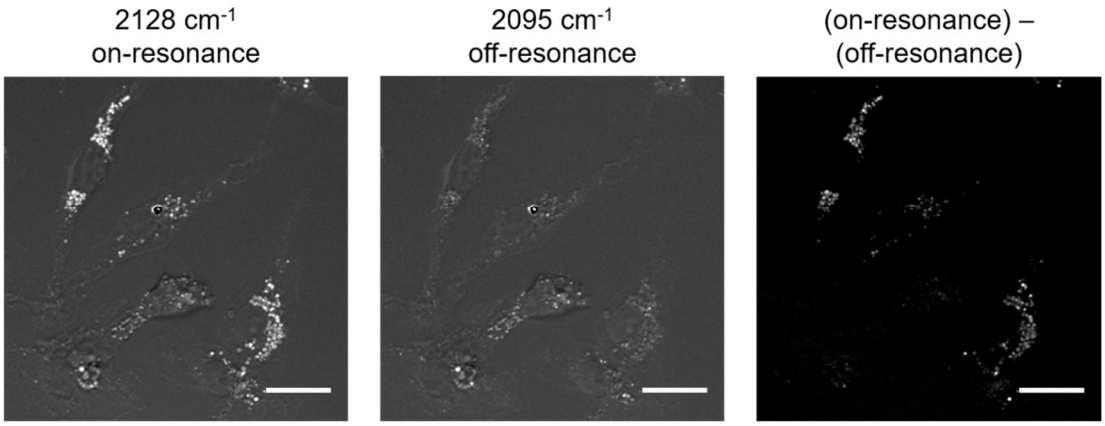

Figure 4.4 Image analysis of SRS images showing microglia treated with PLGA-alkyne NPs. Images were acquired at 2128 cm^{-1} (on-resonance) and 2095 cm^{-1} (off-resonance). Subtraction of the off-resonance signal from the on-resonance gave an image showing signal derived from the NPs only. Brightness and contrast settings are consistent throughout all images. Scale bars = 20 µm.

To prove further that the signal in the images was derived from the bioorthogonal peaks on the NPs, SRS images were taken over a ~100 wavenumber interval, centred on the bioorthogonal peak derived from spontaneous Raman. This creates a hyperspectral image, where a range of spectral data for each pixel is captured. This shows that image intensity depends on a narrow spectral component that is most likely a vibrational response rather than another competing process, which are usually broader. For example, the PLGA-D has a peak at ~2253 cm^{-1} in its spontaneous Raman spectrum, so 21 SRS images were obtained between 2200 and 2311 cm^{-1}. An area of NP intensity in the images was highlighted, and the intensity of this area was plotted over the stated wavenumbers using Fiji.

Figure 4.5 A shows a comparison of the C-D peak obtained from the SRS images (red dots) and the spontaneous Raman spectroscopy (black line). This shows a good agreement between the SRS and spontaneous peaks. This process was repeated for the PLGA-alkyne peak, which also showed good agreement to its corresponding spontaneous Raman peak (Figure 4.5 B).

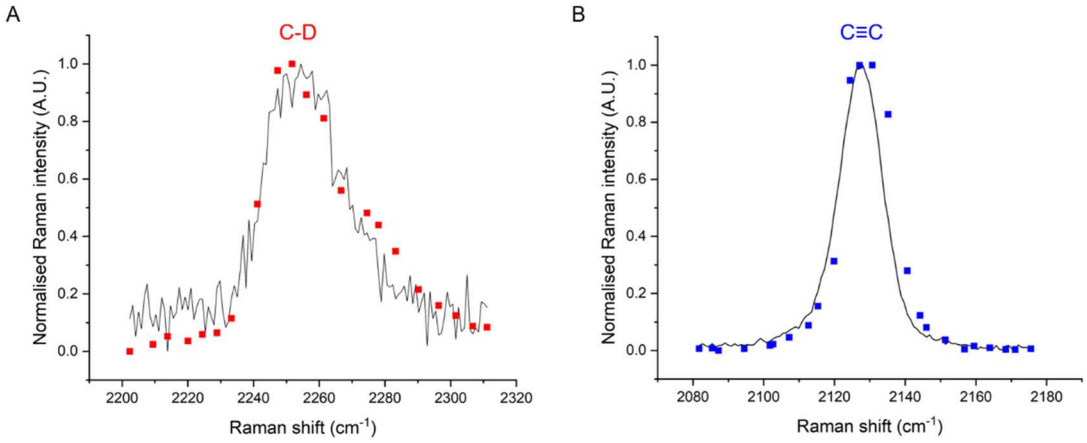

Figure 4.5 Comparison of bioorthogonal peaks obtained from spontaneous Raman and SRS. A) The C-D peak at 2253 cm^{-1} analysed by spontaneous Raman (black line) and SRS (red squares). B) The C≡C peak at 2128 cm^{-1} analysed by spontaneous Raman (black line) and SRS (blue squares).

Figure 4.6 shows the images obtained from microglia incubated with PLGA-D NPs. Tuning the energy difference between the lasers to 2939 cm^{-1} excites CH_3 bonds which are indicative of cellular proteins. Similarly, tuning to 2856 cm^{-1} excites CH_2 bonds which highlights the lipid-rich cell membranes, and are notably absent from the nuclei. Although the cell pellet experiment with PLGA-D NPs was inconclusive as to whether the NPs had entered the microglia or not, Figure 4.6 shows that the NPs had been internalised. Tuning to one of the bioorthogonal carbon-deuterium peaks at 2253 cm^{-1} allows the NPs to be visualised free of competing cellular vibrational components, although background still arises from competing refractive and thermal effects which are observed in the off-resonance images.[173] The NPs were observed at all of the concentrations tested, and in the images in Figure 4.6, the off-resonance background has been subtracted from the carbon-deuterium signal at 2253 cm^{-1}.

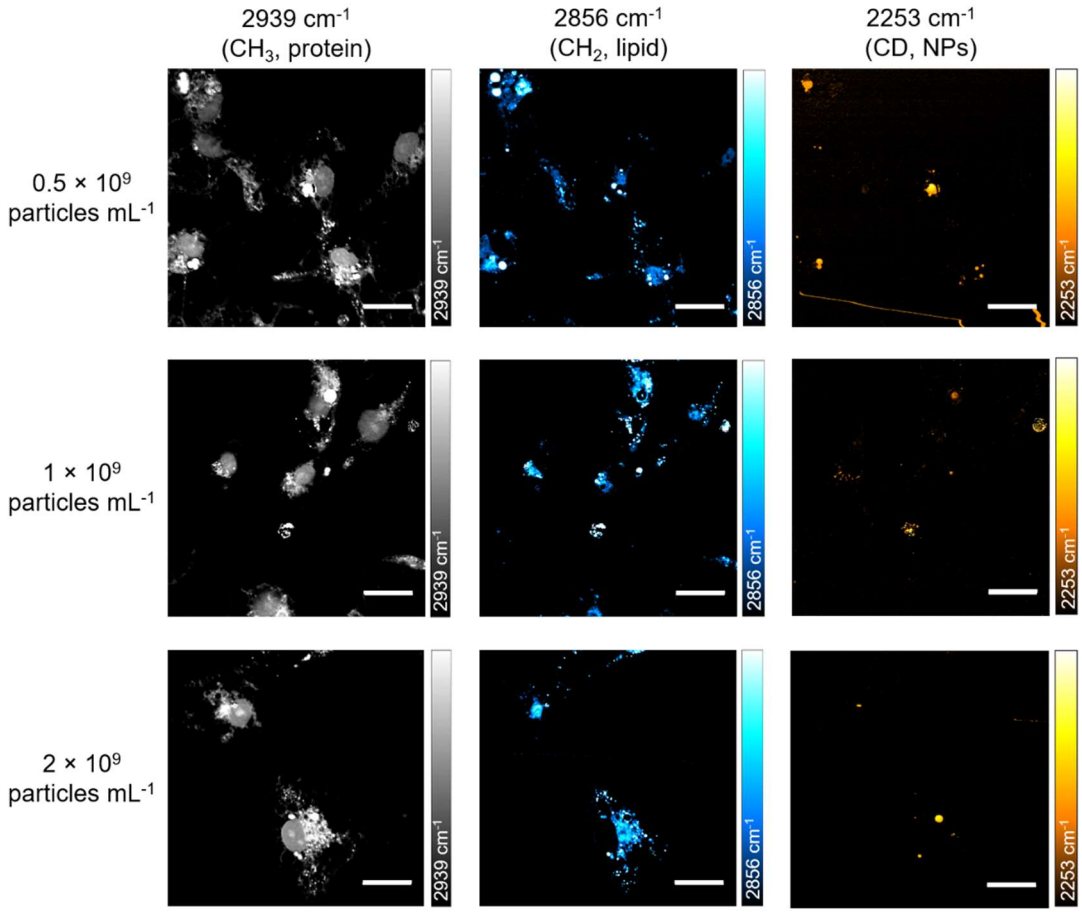

Figure 4.6 PLGA-D NPs visualised in microglia by SRS microscopy. PLGA-D NPs were added to microglia at 0.5, 1 and 2 × 10^9 particles mL^{-1}, and after a 24 h incubation the microglia were washed twice to remove free NPs and then fixed with 4% formaldehyde. The fixed cells were imaged by SRS microscopy. Brightness and contrast settings are inconsistent across these images to enhance contrast. Scale bars = 20 μm.

This experiment was repeated with PLGA-alkyne NPs at 0.5, 1 and 2 × 10^9 particles mL^{-1}. The protein (2939 cm^{-1}), lipid (2856 cm^{-1}) and alkyne (2128cm^{-1}) stretches were excited, with these images shown in Figure 4.7. Again, the NPs were visible at all concentrations and the alkyne images in Figure 4.7 are a product of the alkyne signal at 2128 cm^{-1} minus the off-resonance background. Over many biological replicates imaging both NPs with microglia, it became clear that the PLGA-alkyne NPs gave a stronger Raman signal and were observed more homogeneously throughout the cells, which is consistent with the spontaneous Raman results. Because of this, further experiments were carried out with the PLGA-alkyne NPs only.

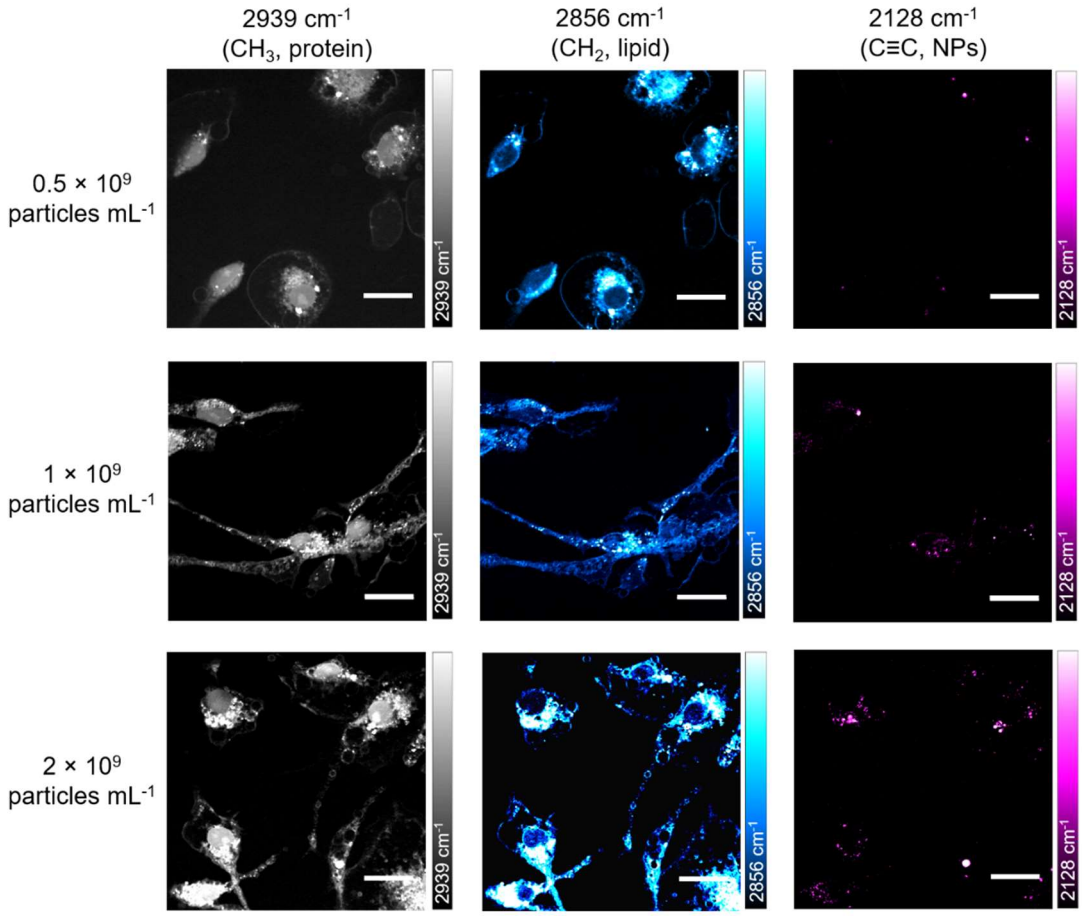

Figure 4.7 PLGA-alkyne NPs visualised in microglia by SRS microscopy. PLGA-alkyne NPs were added to microglia at 0.5, 1 and 2 × 10^9 particles mL^{-1}, and after a 24 h incubation the microglia were washed twice to remove free NPs and then fixed with 4% formaldehyde. The fixed cells were imaged by SRS microscopy. Brightness and contrast settings are inconsistent across these images to enhance contrast. Scale bars = 20 μm.

4.4.2 3D nanoparticle localisation

The automated scanning of the lateral optical directions (X and Y) together with the optical axis (Z direction) allows confocal microscopy to construct 3D images of cells. SRS is also capable creating 3D cell images.[174] Microglia treated with PLGA-alkyne NPs were imaged in this way to investigate the intracellular localisation of the NPs. Figure 4.8 shows these microglia in red, together with the orthogonal XZ and YZ planes, giving a 3D representation of the cell. The PLGA-alkyne NPs are represented in green, and when both the cellular and NP signals are overlaid, they appear yellow. The orthogonal views show that these yellow areas are within the cell body, confirming

that the NPs have been taken up into the microglia rather than just associated with the cell surface.

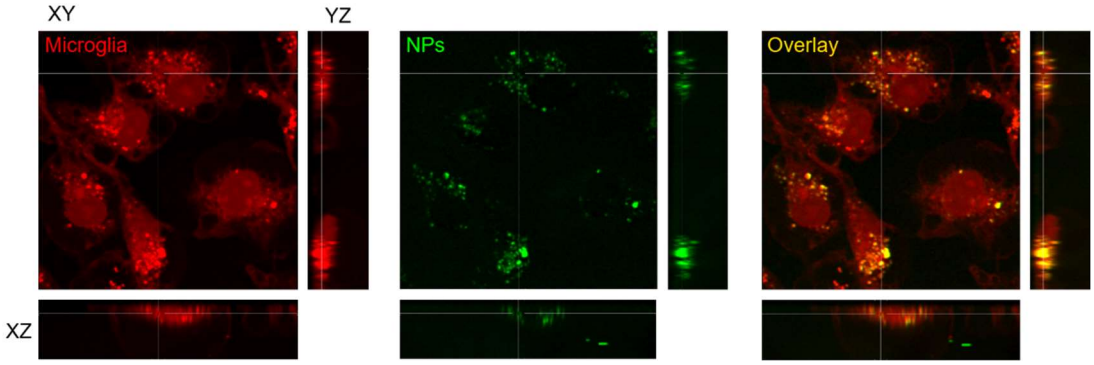

Figure 4.8 Z-stack representation of PLGA-alkyne NPs in microglia. Microglia are shown in red and NPs in green, which overlay to give yellow. The orthogonal views in the XZ and YZ planes show that the NPs are internalised inside the microglia.

4.4.3 Time dependent analysis of microglia

The uptake of PLGA-alkyne NPs to microglia was investigated by fixing and imaging cells at different time points. Different dishes of microglia were fixed before addition of the NPs (t = 0), and then at 12, 24, 36, and 48 hours after addition. Two biological replicates were carried out from populations of primary rat microglia isolated from different litters of rat pups. For each biological replicate, three fields of view were imaged for each time point.

For each image, quantification was carried out using Fiji to find the average alkyne intensity per cell. Firstly, the off-resonance image was subtracted from both the protein and alkyne on-resonance images (Figure 4.4). A threshold was then applied to the protein image to create a mask of the cells (Figure 4.9 A) which was made binary (Figure 4.9 B). A limitation of this threshold is that thin protrusions from the microglia were lost, but NPs were mainly observed in the cell body and not in these protrusions. The alkyne intensity within this cell mask could then be measured. Only areas above 50.26 μm^2 (equivalent circular diameter of 8 μm) were analysed to exclude anything too small to be a cell, and to segment the mask into individual cells (Figure 4.9 C). This provided a list of the mean alkyne intensity per cell for each field of view.

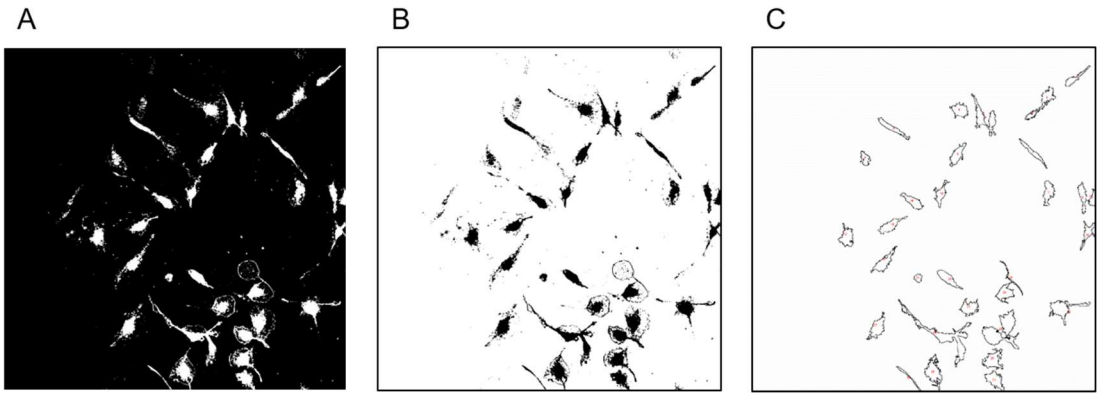

Figure 4.9 Quantitative analysis of alkyne intensity within a cell mask using Fiji. A) A threshold was applied to the cellular protein image to create a mask of the cell. B) This mask was then made binary. C) The alkyne intensity was measured within this mask in areas above 50.26 μm^2.

The intensity of alkyne measured between the two biological replicates showed high variation. For the first replicate, the maximum intensity was ~200 arbitrary units and for the second replicate, this increased to ~3000 arbitrary units. The microglia used in the two replicates were isolated from different litters of rat pups which could lead to differences, and primary cells are also heterogeneous in population.[175] Microglia are also known to have varied states of activation in response to injury or trauma,[176,177] which will affect the amount of phagocytosis they carry out, and in turn, the amount of alkyne intensity observed within the cells. The intensity of SRS data can also change from day to day due to the gain functions and alignment of the microscope. These sources of variability mean that it is possible to draw comparisons between individual time points in a biological replicate, as these come from the same batch of primary cells and were imaged on the same day, but it is difficult to compare between biological replicates which is why the data were not pooled.

Figure 4.10 A and B show representative images of the cells at each time point from biological replicates one and two respectively. Both show that there is no alkyne intensity at time zero before NP addition, and that NPs are visible from 12 hours. The mean alkyne intensity per cell was plotted as a box plot over time for each replicate. In replicate one (Figure 4.10 C), alkyne intensity increases up until 24 hours, and then begins to decrease until 48 hours where the alkyne intensity is not significantly different to before the addition. In replicate two (Figure 4.10 D) the alkyne intensity continues to increase until 48 hours.

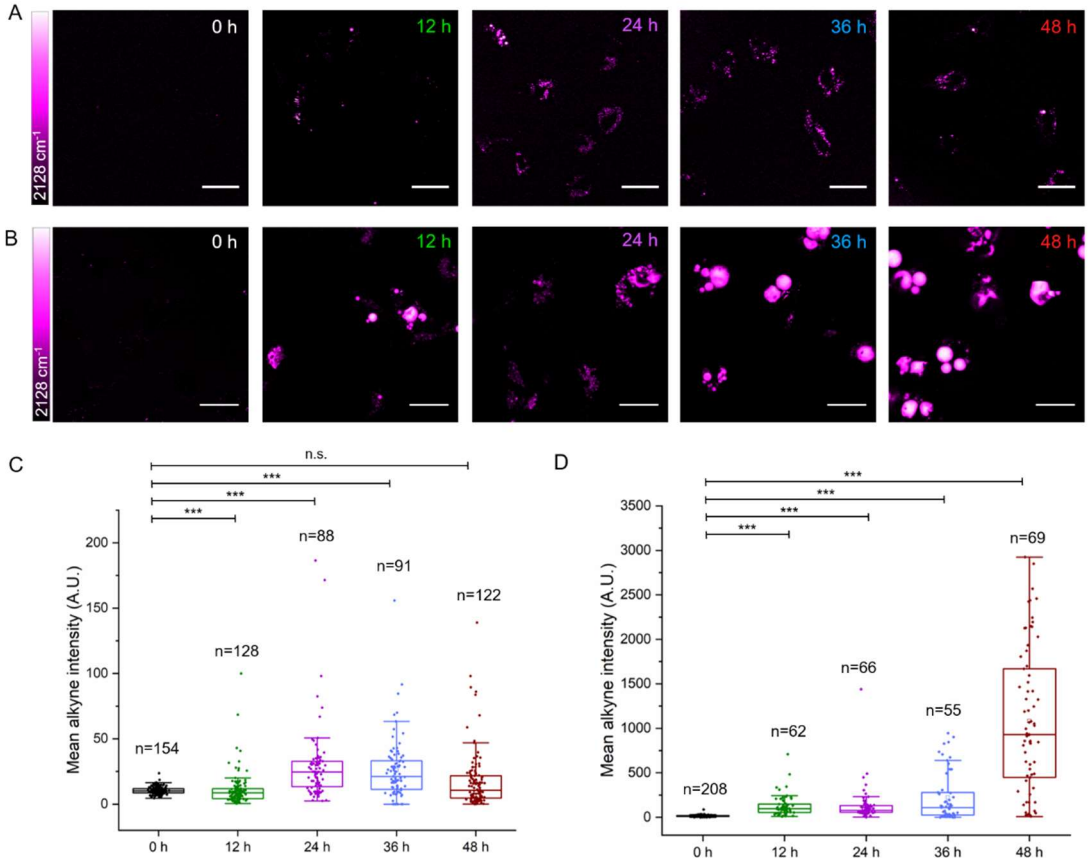

Figure 4.10 Time course analysis of the uptake of PLGA-alkyne NPs into microglia. Microglia were treated with PLGA-alkyne NPs at 2 × 10^9 particles mL^{-1}, and at 0, 12, 24, 36 and 48 hours after the NP addition, the cells were fixed and imaged with SRS. A and B show representative images from replicate one and two respectively. Brightness and contrast settings are consistent throughout all images. Scale bars = 20 μm. C and D show image quantification for replicated one and two respectively. For each time point, the alkyne intensity was quantified for individual cells over three fields of view with n giving the number of cells quantified per condition. ***: $p < 0.001$; n.s.: $p > 0.05$, Mann-Whitney U test.

In replicate two (Figure 4.10 D), the number of cells counted decreases from ~200 at time zero to ~60 at the other time points. This suggests that cells may have been dying, although this concentration of PLGA-alkyne NPs was shown to be non-toxic in Figure 4.1.

4.4.4 Imaging PLGA-alkyne NPs loaded with rhodamine

To investigate if the bioorthogonal PLGA-alkyne NPs were capable of encapsulating and delivering drugs to microglia, the NPs were loaded with rhodamine, which is a red-fluorescent dye (λ_{ex} 528 nm, λ_{em} 553 nm), as a model payload. The rhodamine loaded NPs were prepared using the standard emulsification-evaporation method with

the addition of rhodamine to the organic phase. The alkyne signal from the NPs and the fluorescent signal from rhodamine allowed a multimodal imaging platform to be used to study the localisation of the NPs and their payload in microglia (Figure 4.11).

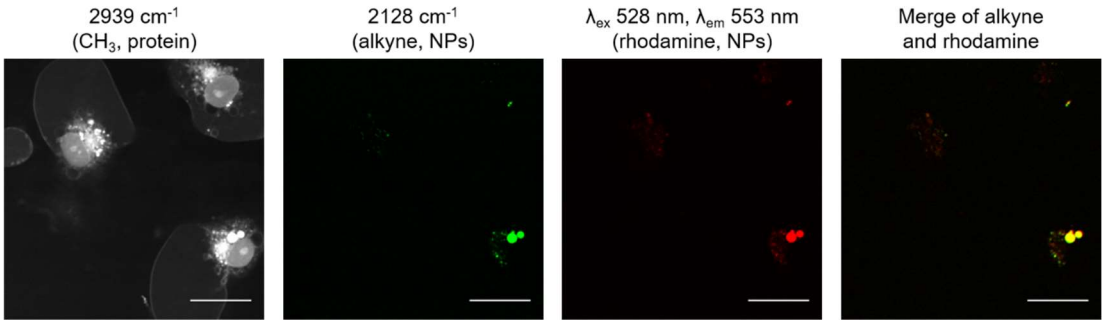

Figure 4.11 Multimodal imaging of PLGA-alkyne NPs loaded with rhodamine. Microglia were incubated with PLGA-alkyne NPs encapsulating the fluorescent dye rhodamine at 2 × 10^9 particles mL^{-1} for 24 hours before washing and fixing the cells. They were then imaged with both SRS and two-photon fluorescence microscopies, which showed that the alkyne signal of the NPs (green, 2128 cm^{-1}) co-localises with the fluorescent signal of rhodamine (red; λ_{ex} 528 nm, λ_{em} 553 nm). Scale bars = 20 µm.

Figure 4.11 shows SRS and two-photon fluorescence (TPF) imaging of microglia incubated with rhodamine loaded PLGA-alkyne NPs. Tuning to 2128 cm^{-1} with SRS shows the location of the NPs (green), and the red fluorescence channel allowed visualisation of rhodamine (red). Overlaying these two images showed that the rhodamine and alkyne signals co-localise well (yellow), which indicates that the rhodamine is encapsulated inside the NP and shows the potential of these NPs to be used for both imaging and drug delivery.

4.5 Imaging Nanoparticles *ex vivo* with SRS Microscopy

The PLGA-alkyne NPs were then imaged in *ex vivo* cortical mouse brain slices. These slices were isolated from postnatal mice pups and were cultured on inserts for six days before the addition of NPs. These six days were allowed to elapse because there can be significant cell death when slices are first cultured due to the cutting process. NPs were added to the slices at 2 × 10^8, 2 × 10^9 and 2 × 10^{10} particles mL^{-1} followed by a 24 hour incubation period (Figure 4.12 A).

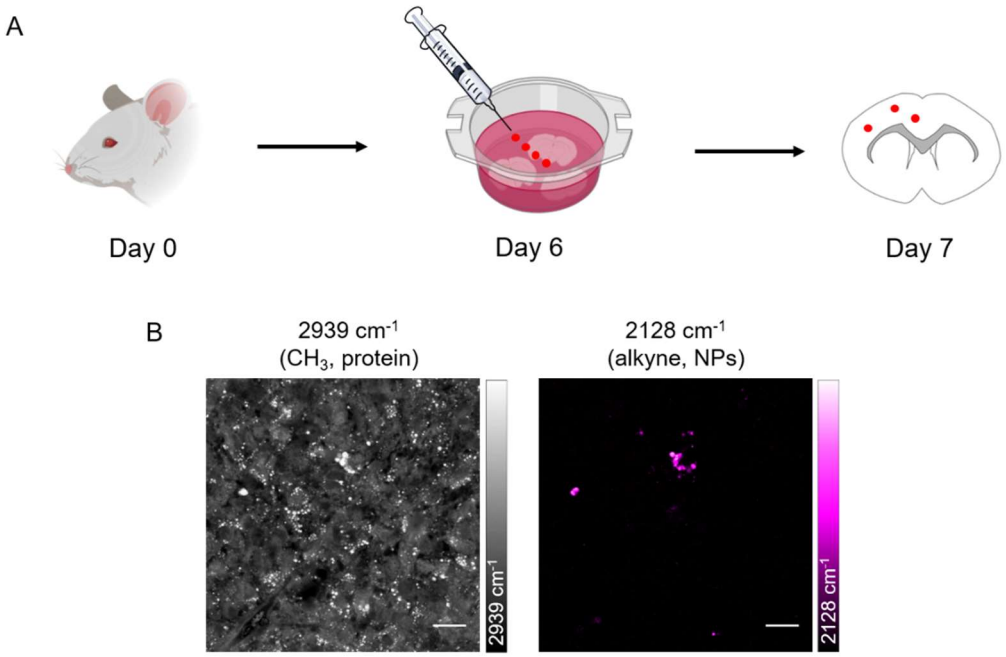

Figure 4.12 Imaging PLGA-alkyne NPs in *ex vivo* mouse brain slices. A) Brains were isolated and sliced from P5 mice pups and were cultured for 6 days before the addition of PLGA-alkyne NPs at 2 × 10^8, 2 × 10^9 and 2 × 10^{10} particles mL^{-1}. After 24 hours of incubation, the slices were washed and fixed. Image created with Biorender.com. B) Representative images of the slices treated with 2 × 10^{10} particles mL^{-1}, showing proteins in grey (2939 cm^{-1}) and PLGA-alkyne NPs in magenta (2128 cm^{-1}). Scale bars = 20 μm.

Figure 4.12 B shows the SRS images obtained from brain slices treated with PLGA-alkyne NPs at 2 × 10^{10} particles mL^{-1}. Tuning to the protein stretch at 2939 cm^{-1} shows the morphology of the tissue, and tuning to the alkyne frequency at 2128 cm^{-1} shows that there are NPs visible on the slice. The image analysis of the brain tissue is much more complex than the microglia cultures due to overlapping protein signals from the different types of cells and extracellular proteins. It was therefore not possible to determine what kind of cell the NPs were inside using these images.

4.5.1 Immunohistochemical analysis

To determine if the NPs in the brain slice had been internalised within cells, and what type of cells these were, immunohistochemical analysis was carried out on the tissue. Immunohistochemistry allows the fluorescent imaging of specific proteins by binding antibodies to them. A primary antibody specific to the protein of interest is first incubated with the tissue, followed by incubation with a secondary fluorescent

antibody, which will bind to the primary antibody. In this way, multiple proteins can be visualised in the same tissue using different fluorescent dyes.

In the brain slices, microglia were stained red using antibodies against IBA1, a microglial specific protein,[178] and oligodendroglia were stained green using antibodies against OLIG2, an oligodendroglial specific nuclear protein. Fluorescence images could also be obtained on the SRS set-up, which allowed multimodal imaging on the same area of the brain slices to be carried out. Figure 4.13 shows representative images of the immunostained brain slices treated with PLGA-alkyne NPs at 2×10^{8}, 2×10^{9} and 2×10^{10} particles mL^{-1} with microglia in red, oligodendroglia in green and NPs in magenta.

The NPs were visible at all concentrations tested, and the immunohistochemical staining showed that the NPs were associated with the microglia. Z-stack analysis of the tissue confirmed that the NPs had been internalised inside the microglia (Figure 4.13 B), and there were no NPs observed within the oligodendroglia. This result was expected, as oligodendroglia are not usually phagocytes, and without additional targeting ligands, the NPs would not be expected to associate with them. However, this gives these NPs the potential for targeted drug delivery to microglia.

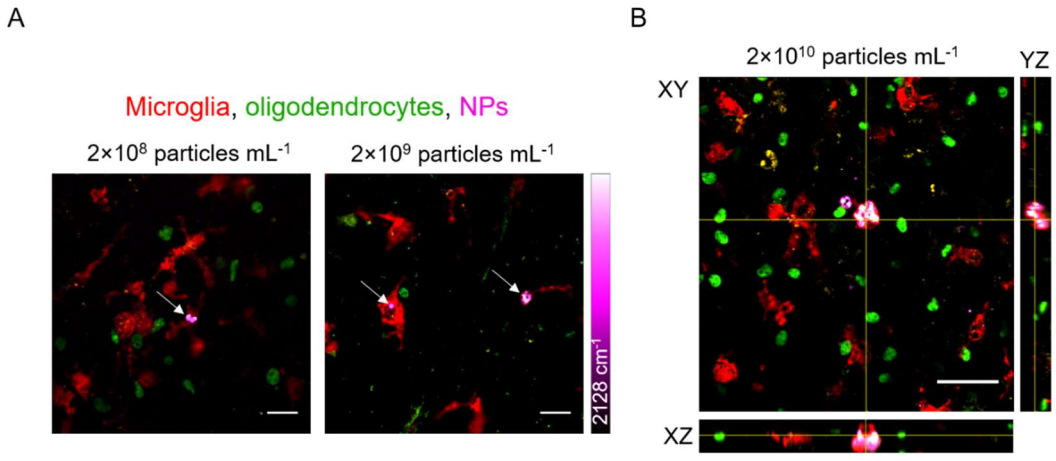

Figure 4.13 Immunohistochemical analysis of *ex vivo* brain slices. A) SRS and TPF images showing microglia in red (IBA1, Alexa Fluor® 568 nm), oligodendroglia in green (OLIG2, Alexa Fluor® 488 nm) and PLGA-alkyne NPs in magenta. White arrows indicate the location of NPs inside the microglia. Scale bars = 20 μm. B) Orthogonal views (XZ and YZ) from Z-stack analysis show that the NPs have been internalised inside a microglia. Scale bar = 50 μm.

4.5.2 Time dependent analysis of brain slices

An experiment was carried out to investigate the behaviour of NPs incubated with *ex vivo* brain slices over time. An advantage of carrying out this time dependent analysis on slices rather than microglia cultures is that the slices could be cultured for several weeks. In the microglia time course experiment (Section 4.4.4), the maximum time point imaged was 48 hours, but in this experiment, PLGA-alkyne NPs were added to the slices which were then fixed and imaged one, three and seven days after NP addition. For this experiment, microglia were again stained red using antibodies against IBA1, and the nucleic acid stain SYTO 9 (λ_{ex} 485 nm, λ_{em} 498 nm) was used to stain all nuclei green, which allowed quantification of the cells.

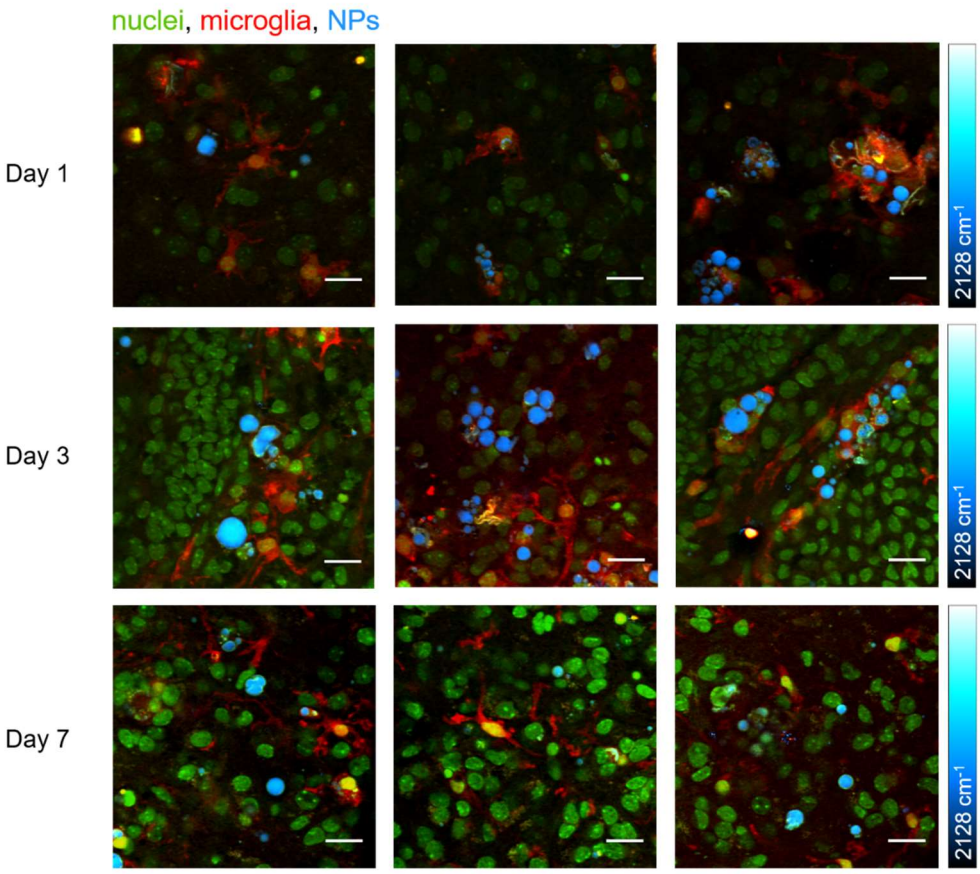

Figure 4.14 Time dependent analysis of PLGA-alkyne NPs in *ex vivo* brain slices. NPs were added at 1 × 10^{11} particles mL^{-1} and then the slices were fixed and imaged with SRS and TPF microscopies one, three and seven days after NP addition. Microglia were stained red using antibodies against IBA1 (Alexa Fluor® 568 nm), nuclei were stained green using SYTO 9 (λ_{ex} 485 nm, λ_{em} 498 nm) and the NPs are shown in cyan hot (SRS at 2128 cm^{-1}). Three representative images are shown for each time point. Brightness and contrast setting for the NP signal (cyan) are consistent throughout. Scale bars = 20 µm.

Figure 4.14 shows three representative images from each time point tested. Again, multimodal imaging was carried out, with TPF showing microglia in red and nuclei in green, and SRS showing the location of the NPs in cyan. This shows that there were NPs visible at every time point, and that they were associated with the microglia.

Two methods of quantification were used to determine the amount of NPs present in the tissue over time. The first method was to count the number of microglia that contained NPs at each time point. The images showed areas where there were large aggregates of microglia and NPs, making it impossible to count individual cells. For the purposes of this quantification, these areas were discounted, and only a sample of the image was counted. Examples of areas counted and discounted are shown in Figure 4.15 A and B respectively. The same overall area was quantified for each field of view. The total number of microglia were counted, with a microglia only counted if it had a visible nucleus, and then the number of microglia containing NPs was counted. This allowed the percentage of microglia containing NPs to be calculated for each time point. This showed that the percentage of microglia containing NPs increased from day one to three, and had decreased again by day seven (Figure 4.15 C).

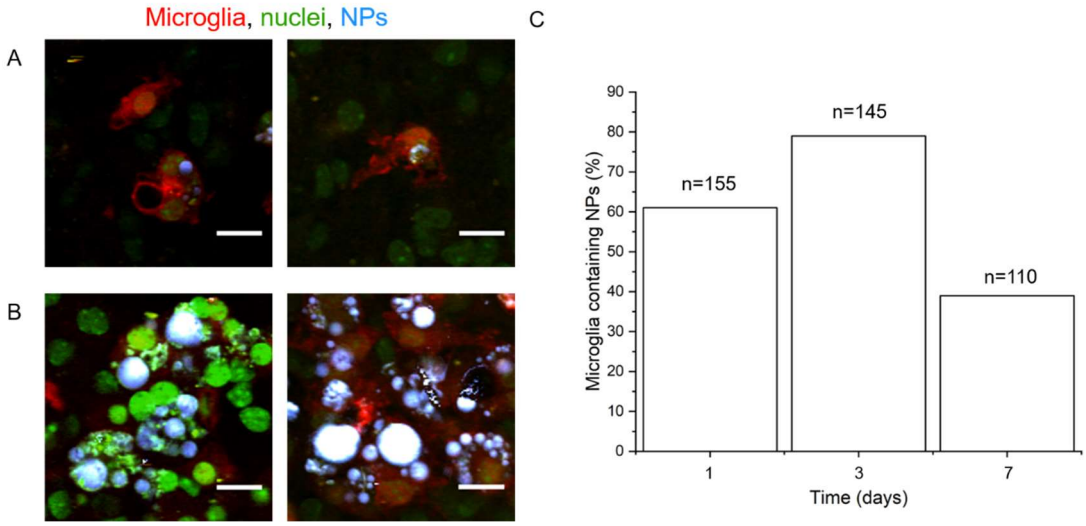

Figure 4.15 Counting the number of microglia containing NPs in *ex vivo* brain slices. A) Examples of areas containing well-separated microglia with clearly visible nuclei that were included in the quantification. Scale bars = 15 µm. B) Examples of areas containing aggregates of cells and NPs that were excluded from the quantification. Scale bars = 15 µm. C) Bar chart showing the percentage of microglia containing NPs over time where n = the total number of cells counted for each time point.

A disadvantage of this method is that only a sample of the slice could be quantified, and the clumps that contained most of the NP intensity had to be discounted. To overcome this, a second method was used to quantify the alkyne intensity within a microglial mask over the whole field of view using Fiji. A microglia threshold mask was created from the red fluorescence channel as described previously (Figure 4.9). There was some interaction between the SRS and fluorescence channels meaning that there was no fluorescence signal where there were NPs (Figure 4.16 A). When the mask was created, the fill holes function was used to fill in these gaps. Nine fields of view from two brain slice replicates were imaged for each time point, and the mean alkyne intensity was calculated for each field of view. This shows that the alkyne intensity significantly increases between one and three days, and then decreases back to day one levels after seven days (Figure 4.16 B).

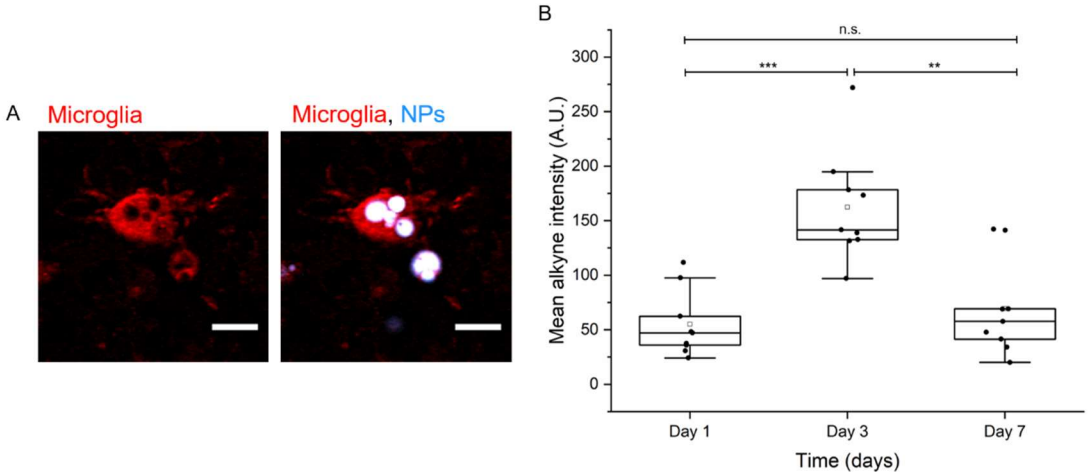

Figure 4.16 Quantifying alkyne intensity over time in *ex vivo* brain slices. A) Images showing microglia in red and PLGA-alkyne NPs in cyan hot. Where there are NPs present, there is an absence of fluorescent signal. Scale bars = 15 μm. B) Box plot showing the mean alkyne intensity per field of view over time. Each dot represents one field of view. ***: $p < 0.001$; **: $p < 0.01$; n.s.: $p > 0.05$, Mann-Whitney U test.

Both methods of quantification show that the intensity of NPs increases between one and three days. This confirms what was observed in the microglia culture time course, where there was an induction period in the uptake of NPs. Microglia were counted as positive for containing NPs if there was any visible alkyne signal, so this does not take into account the size of the NP aggregate.

The intensity of NPs inside the microglia significantly increased between one and three days. This could be because the microglia are internalising more NPs over time,

or because they are being packaged together in a larger structure, which will result in a higher alkyne intensity. NPs internalised by phagocytosis will be encapsulated in phagosomes inside the cell, and over time, these are likely to mature to lysosomes.[179] This could be confirmed by staining for lysosomes, which should correlate well with the areas of NPs. Lysosomal degradation of the NPs could also account for the significant decrease in alkyne intensity observed between three and seven days.

4.6 Imaging Nanoparticles *in vivo* with SRS Microscopy

After successfully imaging the PLGA-alkyne NPs in both primary microglia cultures and *ex vivo* mouse brain slices, the next step was to study the interaction of the NPs with the brain of a live organism. Two methods of delivery to live mice were investigated; direct injection into the brain and intranasal delivery (Figure 4.17).

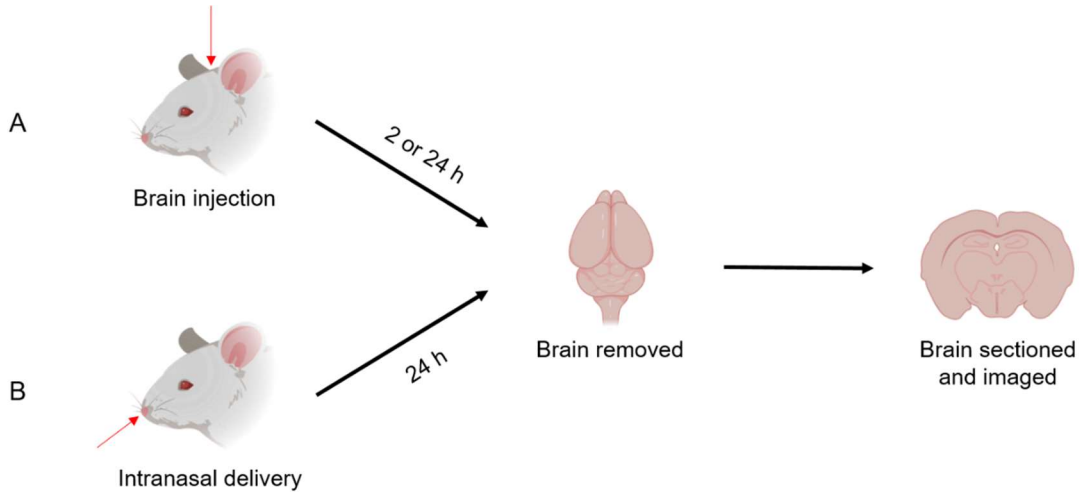

Figure 4.17 Methods of delivering NPs to the brain of live mice. A) 2 µL of PLGA-alkyne NPs at 4 × 10^{11} particles mL^{-1} were directly injected into the mouse brain by stereotactic surgery. At two or 24 hours after NP injection, the mice were perfused with formaldehyde, the brains removed and cut into 100 µm sections. Live animal work was carried out by Amanda Boyd. B) 50 µL of PLGA-alkyne NPs at 1 × 10^{11} particles mL^{-1} were delivered to mice intranasally. 24 hours after delivery, the mice were perfused with formaldehyde, the brains removed and cut into 100 µm sections. Live animal work was carried out by Dr Matthew Swire and Amanda Boyd.

4.6.1 Direct injection to mouse brain

PLGA-alkyne NPs were directly injected into the corpus callosum of a live mouse using stereotactic surgery. Stereotactic surgery is a technique where three-

dimensional coordinates mapped from a dissected mouse brain are used to perform surgery at a specific location.[180] To investigate the behaviour of the NPs in mice over time, groups of mice were sacrificed two and 24 hours after NP injection, the brains were removed, sectioned and imaged with SRS.

The stereotactic surgery method meant that the injection coordinates were known, so the NPs were most likely to be found in this area, however, when tuning to the alkyne stretch at 2128 cm^{-1}, no NPs were visible in the brain sections. Due to animal licence requirements, only 2 µL of NPs could be injected into the brain. It is possible that this concentration is too low to be visualised by SRS, or that the NPs became too dispersed throughout the brain to locate. Backflow of NPs after the injection needle was removed could also mean that the NPs failed to enter the brain, although the needle was held in place for four minutes after the injection to minimise the chance of backflow.

4.6.2 Intranasal delivery

Intranasal administration of drugs is emerging as an attractive method of delivery to the brain, as the BBB can be bypassed in this way via the olfactory and trigeminal pathways.[181,182] This technique has been used previously to deliver therapeutics directly to the brain.[183,184] Gambaryan *et al*. demonstrated how intranasal delivery of PLGA NPs loaded with the Parkinson's disease drug L-DOPA (M_w = 197.2 Da, Appendix 2) gave a sustained therapeutic effect over free L-DOPA delivered intranasally.[185] Additionally, PLGA NPs have been used to deliver the antipsychotic drug olanzapine (M_w = 314.5 Da, Appendix 2),[186] antiepileptic peptide drugs,[187] and another Parkinson's disease drug rotigotine (M_w = 329.5 Da, Appendix 2), intranasally.[188]

Adult mice were administered 50 µL of PLGA-alkyne NPs at 1 × 10^{11} particles mL^{-1} intranasally, and after 24 hours, their brains were removed and imaged. Imaging focused on the sections containing the olfactory bulb, as this is the expected intranasal route, but no NPs were observed by SRS. Again, it is unclear whether this is because the NPs never entered the brain, they were too disperse, or the correct section had not been imaged. An automated high-throughput way of screening the brain sections for alkyne signal could assist in finding any NPs in future studies. It has been reported that intranasal drug delivery can be limited by low mucosal permeability and enzymatic degradation,[189] although encapsulation of drugs into a biodegradable NP should help overcome these issues.

4.7 Conclusions

In this chapter, the new, bioorthogonally labelled PLGA-D and PLGA-alkyne NPs were imaged with SRS microscopy in biological models of the brain. Both NPs were first imaged in primary microglia cultures, with the PLGA-alkyne NPs giving a stronger signal. For this reason, the subsequent studies were only carried out with PLGA-alkyne NPs. Image analysis revealed that the NPs were internalised within microglia, and time course studies showed how the NPs were taken up over time, highlighting differences between batches of microglia.

The PLGA-NPs were then imaged in *ex vivo* brain slices, where immunohistochemistry showed that the NPs were selectively taken up into microglia over oligodendorglia. This gives them potential for targeted drug delivery to microglia. Two delivery methods were then investigated in live mice; direct brain injection and intranasal, however, no NPs were visualised in the brains by SRS. It is not known if the NPs did not enter the brain, or if their low concentration or diffuse distribution did not allow imaging.

Chapter 5 Future Work

In this thesis, SRS microscopy was successfully used to image bioorthogonally Raman labelled polymer NPs in biological models of the brain. Nanoscience is a fast-growing technology in the field of drug delivery, and has great potential for the delivery of therapeutics across the blood brain barrier.[190] The ability to track NPs *in vitro* and *in vivo* is vital for conferring their function, lifetime and safety, and SRS microscopy provides an ideal platform to image NPs free of cellular background.

In Chapter 1, previous strategies to image polymeric and liposomal NPs were discussed which included fluorescence, confocal Raman and coherent Raman microscopies. Small, spectroscopically bioorthogonal labels (C-D, C≡N and C≡C) which produce peaks in the cell silent region have also been shown to increase the contrast of NPs in cellular and tissue models.

Chapter 2 discussed the synthetic route to two spectroscopically biorthogonal analogues of PLGA: PLGA-D and PLGA-alkyne. Deuterated lactic acid was used in a polycondensation reaction to synthesise PLGA-D, whilst PLGA-alkyne was formed via ROP from a cyclic propargyl DOX monomer. The same chemistry used to synthesise propargyl DOX could be applied to the deuterated lactic acid to form a cyclic monomer, and therefore a higher molecular weight polymer. However, this would not increase the Raman signal of the PLGA-D.

Since alkyne peaks are generally small and sharp, multiple alkyne-containing tags can be imaged at once, as has been shown previously.[191] This method could also be applied to PLGA, where multiple alkyne analogues are synthesised giving rise to a palette of NPs suitable for multi-colour Raman imaging. These NPs could be used to label different cell populations and track their fate when mixed, similar to previous studies with fluorescent NPs.[62]

In Chapter 3, the synthesis of NPs with the emulsification-evaporation method was described. Several targeting strategies were then discussed to attempt to conjugate avidin to the surface of the NPs, however, none of these strategies produced avidin binding significantly higher than the control. An additional strategy for targeting PLGA NPs is to react proteins onto a carboxylic acid polymer end group, which is more easily functionalised than the alcohol end group that was present in PLGA-alkyne. Previous work has used this reaction to conjugate human serum albumin to PLGA NPs,[192] and

these conditions could be replicated to bind avidin. The carboxylic acid end group would first be activated to its NHS ester, which could then form an amide bond with a free amine on the avidin (Scheme **5.1**). Alternatively, this chemistry could be utilised to conjugate the NP directly to the targeting antibody.

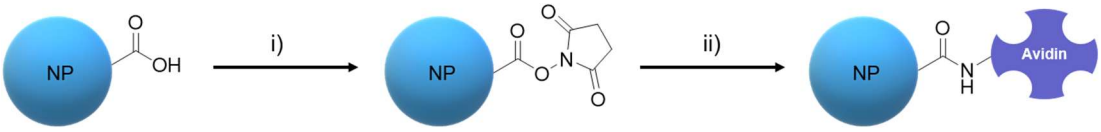

Scheme 5.1 Conjugation of avidin to a NP through an amide bond. EDC and NHS could be used to activate a carboxylic acid polymer end group to its NHS ester (i). Addition of avidin would then cause reaction of this NHS ester with a lysine residue, joining avidin to the NP through an amide bond.

Once NG2 targeted PLGA-alkyne NPs were available, they could be used to deliver drugs to OPCs,[20] and SRS microscopy could be used to image their intracellular localisation. Targeted NPs could also be incubated with a mixed culture of OPCs and microglia followed by immunostaining and multimodal SRS and TPF imaging to investigate if the NG2 targeting would mean they were preferentially internalised in OPCs, or still engulfed by microglia. This experiment could also be repeated in *ex vivo* brain slices, and would provide important information about the ability of these NPs to target OPCs.

It was shown in Chapter 4 that PLGA-alkyne NPs were selectively internalised in microglia over oligodendrocytes in *ex vivo* brain slices, showing that they have a potential for targeted drug delivery to microglia. Future work could focus on loading therapeutics into the PLGA-alkyne NPs, which was shown to be possible by using rhodamine as a model payload, and delivering them to microglia.

Preliminary experiments were carried out in collaboration with Dr Dirk Seiger, who studies the role of microglia in glioblastoma using zebrafish models. In these models, it has been shown that microglia will migrate to a tumour and, instead of performing a protective phagocytic role as expected, will initiate tumour growth.[193] Understanding this mechanism of action, and finding drugs to reverse it, is important research in efforts to treat glioblastoma. PLGA-alkyne NPs could be used to deliver drugs to microglia in these models, and image their location with SRS. Initial experiments confirmed that the NPs were non-toxic to zebrafish, and zebrafish were imaged with SRS microscopy after a 24 hour incubation with PLGA-alkyne NPs in their water (Figure 5.1). Although no alkyne signal was observed, this showed that SRS is

suitable for the imaging of zebrafish, and future studies injecting NPs into the brain could allow both imaging and drug delivery.

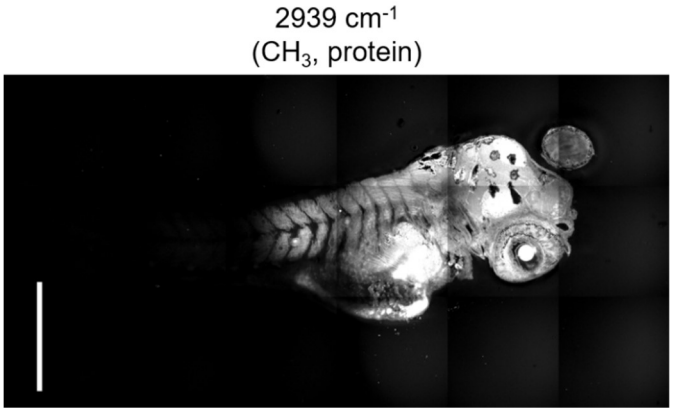

Figure 5.1 Imaging zebrafish with SRS microscopy. Tuning to the protein stretch at 2939 cm^{-1} allows imaging of the zebrafish. Scale bar = 500 μm.

In Chapter 4, *in vivo* studies were described where PLGA-alkyne NPs were either injected into the mouse brain, or delivered intranasally, before sacrificing the mice and imaging sections of the fixed brain. In both of these experiments, the alkyne signal of the NPs could not be found. In future experiments, PLGA-alkyne NPs loaded with a fluorescent dye could be administered as the fluorescent signal would be brighter than the SRS alkyne signal, and it would be quicker to sort through the sections to find the NP location, however, neurons in brains are often autofluorescent which may make it difficult to detect NPs. Furthermore, delivery of a higher concentration of NPs may help be certain of their detection after *in vivo* delivery. Emerging technology has also shown that live mice can be fitted with transparent cranial windows to allow brain imaging in a live animal.[194,195] The combination of this technology with the PLGA-alkyne NPs could be used to track the NPs live in a mouse brain with SRS microscopy.

Although NP drug delivery is popular in pre-clinical studies, translation to humans is still limited by concerns about long-term distribution, safety and degradation.[196] Imaging NPs is therefore an important technique for answering these questions. Other issues such as relatively low drug loading and targeting efficiency also need to be overcome.[197] NPs will naturally accumulate in macrophages,[198] the liver,[199] and tumours,[200] and therefore drug delivery to these targets could be more easily realised along with NP imaging. Medina *et al.* recently developed PLGA NPs quantum dot conjugates to study the *in vivo* fate of the NPs, and if they passed the BBB.[201] They found that under healthy conditions, there was limited passage into the brain, but that

when there was a tumour this disrupted the BBB and allowed the NPs to enter. At a higher concentration, the PLGA-alkyne NPs could be used to visualise if and how these NPs cross the BBB, providing important information about the potential of PLGA NPs to deliver drugs to the brain.

Chapter 6 Materials and Methods

6.1 General Procedures

6.1.1 Chemical synthesis

All non-aqueous reactions were carried out in oven-dried glassware which was assembled hot and then allowed to cool under a dry nitrogen atmosphere. Unless otherwise stated, all starting materials and reagents were used as received from the supplier. Dry solvents were dried via a solvent purification system (SPS) using activated alumina. Saturated aqueous solutions of inorganic salts are represented as (volume, sat. aq.).

^{1}H and ^{13}C NMR spectra were obtained on Brucker instruments at the stated frequency using TMS as a reference and residual solvent as an internal standard. Infrared spectra were recorded neat on a Shimadzu IRAffinity-1 with a diamond optic. Gel permeation chromatography was carried out in THF at a flow rate of 1 mL min^{-1} at 35°C on a Viscotek 270 GPC Max triple detection system (Malvern Instruments) with 2 × mixed bed styrene/DVB columns (300 × 7.5 mm). Data was processed using OmniSEC 5.0 using either the triple detection or conventional calibration method and calibrating with polystyrene standards. Mass spectra were obtained on a MAT 900 XP mass spectrometer (electron ionisation). Melting points were determined on a Gallenkamp Electrothermal Melting Point apparatus and are uncorrected. Reverse phase UPLC was performed on a Waters Acquity system using a binary solvent manager and PDA equipped with a Waters BEH C4, 1.7 µm, 100 × 2.1 mm column using water (0.1% TFA) and acetonitrile as an eluent at a flow rate of 0.2 mL min^{-1}. R_f values were obtained on Merck Silicagel 60 aluminium backed plates. Flash column chromatography was carried out using Geduran ® Si 60 silica (40–60 µm) (Merck Millipore) under positive pressure. Eluent compositions are stated as volume/volume ratios.

6.1.2 Nanoparticle synthesis

Nanoparticle emulsions were formed using a probe tip sonicator (Soniprep 150, MSE). Nanoparticles were pelleted by centrifugation on a VWR Microstar 17 centrifuge. For TEM analysis, NP suspensions in water were dropped onto TEM grids and then allowed to dry at room temperature. TEM images were obtained on a JEOL JEM-1400 Plus TEM. Representative images were collected on a GATAN OneView camera. For

SEM analysis, NP suspensions in water were mounted on aluminium stubs with carbon tabs attached and dried under vacuum, before the specimens were sputter coated with 20 nm gold palladium and viewed using a Hitachi S-4700 scanning electron microscope. Brightfield images were acquired with a Nikon Eclipse TE 2000-U inverted microscope at 20–22°C using a 20 × (CFI Fluor, N.A. 0.5, Nikon) objective and recorded with an EMCCD (iXon Ultra 897, Andor Technology) at -50°C. Dynamic light scattering was carried out on a Zetasizer Nano ZS (Malvern Panalytical) in water at 25°C. Nanoparticle tracking analysis was carried out on a Nanosight LM10 (Malvern Panalytical) in PBS with the temperature measured for each individual run. UV analysis was obtained on a Varian Cary ® UV-vis Spectrophotometer, Agilent. Lyophilisation was achieved by freezing samples in liquid nitrogen and then freeze drying on a Lablyo mini (Frozen in Time Ltd) freeze drier. NPs were resuspended in the appropriate media and warmed to 37°C before addition to microglia and brain slices.

Table 6.1 Preparation of standard solutions for NP reactions.

Solution	Preparation
Aqueous phase for NP synthesis	100 mg Poly(vinyl) alcohol, (Mw 31,000–50,000, 98–99% hydrolysed) 20 mg Sodium dodecyl sulphate 10 mL dH_2O
1 M HEPES, pH 8	119.15 g HEPES 500 mL dH_2O, adjusted to pH 8 with NaOH (3 M, aq.)
Sodium deoxycholate solution	20 mg Sodium deoxycholate solution 10 mL 1 M HEPES

6.1.3 Tissue culture

Cells were counted by taking 9 µL of cell suspension into a haemocytometer and averaging the cell count obtained from four 1 mm^2 grids. All media and reagents were warmed to 37°C before addition to cells/slices. Cell fixation was achieved by covering the cells with a solution of 4% formaldehyde (2 mL) for 10 minutes at room temperature before washing three times with PBS (3 × 2 mL). Unless otherwise stated, PBS refers to 1 × PBS at pH 7.4. The plate reader used for viability assays was a GloMax Microplate Reader (Promega).

Table 6.2: Preparation of standard solutions for tissue culture.

Solution	Preparation
1 × PBS	100 mL 10 × PBS pH 7.4 (Gibco) 900 mL dH_2O
Fixing solution	1 mL 37% Formaldehyde (Sigma Aldrich) 9 mL 1 × PBS
Mixed glia media	1 L Dulbecco's modified Eagle's medium (Gibco) 100 mL Fetal calf serum 1 mL Penicillin-streptomycin
Slice media	25 mL Minimal essential media (Invitrogen) 12.5 mL Heat-inactivated horse serum (Invitrogen) 12.5 mL Earle's balanced salt solution (Invitrogen) 500 µL Glutamax supplement (Invitrogen) 500 µL Penicillin-streptomycin 250 µL Fungizone (Invitrogen) 722 µL 45% Glucose (Sigma Aldrich)
Blocking solution (for immunostaining)	1.5 mL Heat-inactivated horse serum 1 g Bovine serum albumin 2.5 mL Triton (10%, (v/v) aq.) 45 mL 1 × PBS

6.1.4 Spontaneous Raman

Spontaneous Raman spectra were acquired on a confocal Raman spectrometer (inVia Raman microscope, Renishaw). A 297 mW (206 mW after objective) 785 nm diode laser or a 200 mW 532 nm laser excitation source was used to excite the sample through a 20× or 50× objective. The instrument was calibrated using a silicon wafer before each use so that the silicon peak was 520.5 cm^{-1}. All spectra were background subtracted using the background correction algorithm available on the Wire 4.4 software.

Since glass has a high Raman background, all spectra were acquired on CaF_2 slides. The slides were washed in ethanol (70%, aq.) between samples and reused.

6.1.5 Stimulated Raman scattering

Images were acquired using a custom-built multi-modal microscope. A picoEmerald (APE, Berlin, Germany) laser gave a tuneable pump laser (720–990 nm, 7 ps, 80 MHz repetition rate) and a spatially and temporally overlapped Stokes laser (1064 nm, 5–6 ps, 80 MHz repetition rate). Back scattered RFP two-photon fluorescence signals were filtered using the following series of filters: FF552-Di02, FF440/520-Di01 (Semrock) and HQ610/75m (Chroma). For SRS measurements, the Stokes beam was modulated with a 20 MHz EoM. Forward scattered light was collected by a 20×

Olympus XLUMPLFLN Objective, 1.00 NA lens and filtered using ET890/220m filter (Chroma). A telescope focused the light onto an APE silicon photodiode connected to an APE lock-in amplifier which was fed into the analogue unit of the microscope.

The pump laser was tuned to 810.5 nm (2930 cm^{-1}), 816 nm (2850 cm^{-1}), 867.5 nm (2128 cm^{-1}) and 858.3 nm (2252 cm^{-1}) and laser powers after the objective were measured up to 40-70 mW for the pump laser and up to 70 mW for the Stokes laser. All images were recorded at 512 × 512 or 1024 × 1024 pixels with a pixel dwell time between 2 and 20 µs by FV10-ASW software (Olympus).

All cells were grown on FluoroDish Cell Culture Dishes (World Precision Instruments) which have an optical glass bottom for high quality imaging. Since SRS focuses on a specific wavenumber, the background signal from glass is not an issue. New dishes were used for each experiment. A sweep of SRS images was obtained to check if the SRS peak matched the wavenumber of the spontaneous peak as a form of calibration.

6.1.6 Image analysis

All images were processed using Fiji (ImageJ) software[172] by assigning false colour assignments and scale bars. When acquiring SRS images, an off-resonance image was always acquired ~30 cm^{-1} away from the target resonance. When processing the images, this off-resonance was subtracted from the on-resonance using the image calculator functionality on ImageJ.

6.2 Experimental Procedures for Chapter 2

6.2.1 Synthesis of lactic acid-d_3

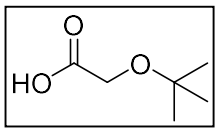

2-(*tert*-Butoxy)acetic acid 11

Potassium *tert*-butoxide **10** (32.0 g, 283 mmol) was dissolved in anhydrous THF (~100 mL). Bromoacetic acid **9** (15.8 g, 113 mmol) was dissolved in THF (10 mL) and added dropwise to the potassium *tert*-butoxide solution with stirring. Upon addition, a pale yellow solid precipitated. The reaction mixture was heated to reflux and stirred for one hour. The THF was removed *in vacuo* and ether (~50 mL) was added to the residue. Hydrochloric acid (~50 mL, 3M, aq.) was added until all of the solid had dissolved, and the aqueous phase was acidic. The aqueous phase was extracted twice with ether (2 × 50 mL) and then the combined organic layers were washed with brine (~50 mL sat. aq.), dried ($MgSO_4$) and the ether

removed *in vacuo* to give the desired product **11** as a yellow oil (13.6 g, 103 mmol, 91%). **R_f** (DCM:MeOH 4:1) = 0.52; **IR** (neat cm^{-1}) 2976, 2937 (C-H), 1732 (C=O); **^{1}H NMR** δ (400 MHz, $CDCl_3$) 4.02 (2H, s, C*H*$_2$), 1.26 (9H, s, (C*H*$_3$)$_3$); **^{13}C NMR** δ (126 MHz, $CDCl_3$) 173.2 (C), 75.8 (C) 60.1 (CH_2) 27.4 (3 × CH_3). The spectroscopic data are in good agreement with the literature.[202]

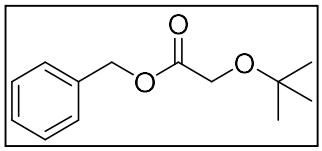

Benzyl 2-(*tert*-butoxy)acetate 13

2-(*tert*-Butoxy)acetic acid **11** (9.00 g, 68.0 mmol), 4-(dimethylamino)pyridine (0.830 g, 6.80 mmol) and phenylmethanol (14.1 mL, 136 mmol) were dissolved in anhydrous DCM (150 mL). 1-Ethyl-3(3-dimethylaminopropyl)carbodiimide (14.3 g, 74.8 mmol) was added portion-wise and the mixture was left stirring at room temperature under argon for ~18 hours until the reaction was confirmed to be complete by TLC. The mixture was washed with hydrochloric acid (~100 mL, 0.5 M, aq.), brine (~100 mL, sat. aq.) and $NaHCO_3$ (~100 mL sat. aq.). The organic layer was dried ($MgSO_4$) and the DCM removed *in vacuo* to give a yellow oil. The oil was further purified by flash column chromatography (Hexane:EtOAc 9:1) to give the desired product **13** as a colourless oil (12.5 g, 56.0 mmol, 82%). **R_f** (Hexane:EtOAc 9:1) = 0.20; **IR** (neat cm^{-1}) 2974 (C-H), 1759 (C=O), 1456 (ArC=C); **^{1}H NMR** δ (600 MHz, $CDCl_3$) 7.37-7.30 (5H, m, Ar*H*), 5.17 (2H, s, C*H*$_2$), 4.06 (2H, s, C*H*$_2$), 1.22 (9H, s, (C*H*$_3$)$_3$); **^{13}C NMR** δ (151 MHz, $CDCl_3$) 171.2 (C), 135.7 (C), 128.6 (2 × ArCH), 128.4 (2 × ArCH), 128.4 (ArCH), 74.6 (C), 66.5 (CH_2), 60.9 (CH_2), 27.3 (3 × CH_3); ***m/z*** (EI), 222.1 ([$M^{+\cdot}$], 1.3%), 166.1 (100), 107.0 (36.6); **HRMS** (EI) [$M^{+\cdot}$] found 222.1257, $C_{13}H_{18}O_3$ requires 222.1251.

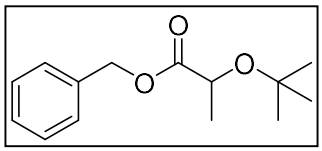

Benzyl 2-(*tert*-butoxy)propanoate 15

Benzyl 2-(*tert*-butoxy)acetate **13** (0.500 g, 2.25 mmol) was dissolved in anhydrous THF (10 mL) under argon and cooled to -78°C before adding LiHMDS (5.63 mL, 5.63 mmol, 1 M in THF) dropwise. The mixture was stirred at -78°C for 1 hour before adding iodomethane (0.280 mL, 4.50 mmol) that had previously been filtered through anhydrous potassium carbonate. The mixture was then allowed to warm to room temperature over 30 minutes. The reaction was confirmed to be complete by TLC, and hydrochloric acid (~25 mL, 0.5 M, aq.) was added until the reaction mixture was acidic. The THF was removed *in*

vacuo and ether (~20 mL) was added to the mixture. The organic layer was separated, and the aqueous layer was extracted with ether (3 × 10 mL). The combined organic layers were washed with brine (~10 mL, sat. aq.) and $NaHCO_3$ (~10 mL, sat. aq.) before drying ($MgSO_4$). The ether was removed *in vacuo* to give a yellow oil which was further purified by flash column chromatography (Hexane:EtOAc 9.5:0.5) to give the desired product **15** as a colourless oil (0.170 g, 0.710 mmol, 32%). **R_f** (Hexane:EtOAc 9.5:0.5) = 0.24; **IR** (neat cm^{-1}) 2976 (C-H), 1753 (C=O), 1456 (ArC=C); **^{1}H NMR** δ (600 MHz, $CDCl_3$) 7.37-7.20 (5H, m, Ar*H*), 5.18 (1H, d, *J* = 12.3 Hz, CH_AH_B), 5.14 (1H, d, *J* = 12.3 Hz, CH_AH_B), 4.16 (1H, q, *J* = 6.9 Hz, C*H*CH_3), 1.35 (3H, d, *J* = 6.9 Hz, CHCH_3), 1.17 (9H, s, (CH_3)$_3$); **^{13}C NMR** δ (151 MHz, $CDCl_3$) 174.9 (C), 135.9 (C), 128.6 (2 × ArCH), 128.4 (2 × ArCH), 128.3 (ArCH), 75.0 (C), 67.6 (CH), 66.4 (CH_2), 27.8 (3 × CH_3), 20.6 (CH_3). The spectroscopic data are in good agreement with the literature.[203]

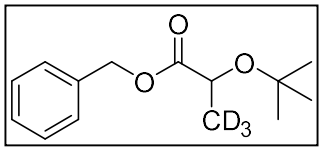

Benzyl 2-(*tert*-butoxy)(3,3,3-$^2H_3$)propanoate 14

Benzyl 2-(*tert*-butoxy)acetate **13** (0.500 g, 2.25 mmol) was dissolved in anhydrous THF (10 mL) under argon and cooled to -78°C before adding LiHMDS (5.63 mL, 5.63 mmol, 1 M in THF) dropwise. The mixture was stirred at -78°C for 1 hour before adding iodomethane-d_3 (0.280 mL, 4.50 mmol) that had previously been filtered through anhydrous potassium carbonate. The mixture was then allowed to warm to room temperature over 30 minutes. The reaction was confirmed to be completed by TLC, and hydrochloric acid (~25 mL, 0.5 M, aq.) was added until the reaction mixture was acidic. The THF was removed *in vacuo* and ether (~20 mL) was added to the mixture. The organic layer was separated, and the aqueous layer was extracted with ether (3 × 10 mL). The combined organic layers were washed with brine (~10 mL, sat. aq.) and $NaHCO_3$ (~10 mL, sat. aq.) before drying ($MgSO_4$). The ether was removed *in vacuo* to give a yellow oil which was further purified by flash column chromatography (Hexane:EtOAc 9.5:0.5) to give the desired product **14** as a colourless oil (0.24 g, 1.01 mmol, 45%). **R_f** (Hexane:EtOAc 9.5:0.5) = 0.24; **IR** (neat cm^{-1}) 2974 (C-H), 1753 (C=O), 1456 (ArC=C); **^{1}H NMR** δ (600 MHz, $CDCl_3$) 7.39-7.28 (5H, m, Ar*H*), 5.18 (1H, d, *J* = 12.3 Hz, CH_AH_B), 5.14 (1H, d, *J* = 12.3 Hz, CH_AH_B), 4.15 (1H, s, C*H*CD_3), 1.18 (9H, s, (CH_3)$_3$); **^{13}C NMR** δ (151 MHz, $CDCl_3$) 174.8 (C), 135.8 (C), 128.5 (2 × ArCH), 128.3 (2 × ArCH), 128.2 (ArCH), 74.9 (C), 67.4 (CH), 66.4 (CH_2), 27.7 (3 × CH_3), 19.7 (CD_3, sept); ***m/z*** (EI),

239.2 ([$M^{+\cdot}$], 1.9%), 166.1 (100), 136.1 (26.9), 107.0 (66.0); **HRMS** (EI) [$M^{+\cdot}$] found 239.1600, $C_{14}H_{17}D_3O_3$ requires 239.1596.

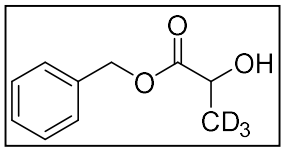

Benzyl 2-hydroxy(3,3,3-$^2H_3$)propanoate 17

Method A: Benzyl 2-(*tert*-butoxy)(3,3,3-$^2H_3$)propanoate **14** (0.760 g, 3.18 mmol) and triisopropylsilane (0.160 mL, 0.800 mmol) were dissolved in anhydrous DCM (8 mL) under argon and TFA (2 mL) was added dropwise. The mixture was stirred at room temperature for ~48 hours until confirmed complete by TLC. The DCM and TFA were removed *in vacuo*, the residue dissolved in DCM (20 mL) and washed with $NaHCO_3$ (~20 mL, sat. aq.) before drying ($MgSO_4$). The DCM was removed *in vacuo* to give a yellow oil which was further purified by flash column chromatography (Hexane:EtOAc 7:3) to give the desired product **17** as a colourless oil (0.390 g, 2.13 mmol, 67%).

Method B: Benzyl 2-(*tert*-butoxy)(3,3,3-$^2H_3$)propanoate **14** (0.500 g, 2.10 mmol) was dissolved in anhydrous DCM (20 mL) and cooled to -78°C before adding titanium tetrachloride (2.10 mL, 2.10 mmol, 1 M in DCM) dropwise over 10 minutes. After the addition was complete, TLC analysis confirmed the reaction to be complete. The mixture was warmed to room temperature before quenching with ammonium chloride (~50 mL, sat. aq.). The aqueous phase was extracted with DCM (3 × 20 mL), the combined organic layers washed with brine (~50 mL, sat. aq.), dried ($MgSO_4$) and the DCM removed *in vacuo* to give a yellow oil. This oil was further purified by flash column chromatography (Hexane:EtOAc 7:3) to give the desired product **17** as a colourless oil (0.360 g, 1.98 mmol, 94%). $\mathbf{R_f}$ (Hexane:EtOAc 7:3) = 0.44; **IR** (neat cm^{-1}) 3463 (OH), 1732 (C=O); **^{1}H NMR** δ (600 MHz, $CDCl_3$) 7.40-7.32 (5H, m, Ar*H*), 5.22 (2H, s, CH_2), 4.31 (1H, d, *J* = 4.4 Hz, C*H*), 2.77 (1H, d, *J* = 4.4 Hz, O*H*); **^{13}C NMR** δ (151 MHz, $CDCl_3$) 175.7 (C), 135.4 (C), 128.8 (2 × ArCH), 128.7 (ArCH), 128.4 (2 × ArCH), 67.4 (CH_2), 66.9 (CH), 19.8 (CD_3, sept); ***m/z*** (EI), 183.1 ([$M^{+\cdot}$], 6.5%), 91.1 (100), 48.0 (56.2); **HRMS** (EI) [$M^{+\cdot}$] found 183.0972, $C_{10}H_9D_3O_3$ requires 183.0969.

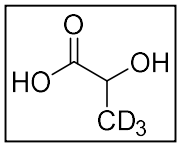

2-Hydroxy(3,3,3-$^2H_3$)propanoic acid 18

Benzyl 2-hydroxy(3,3,3-$^2H_3$)propanoate **17** (2.70 g, 14.7 mmol), Pd/C 10% (0.54 g, 20% by weight) and THF (100 mL) were stirred under

hydrogen at room temperature for 3 hours before the reaction was confirmed complete by TLC. The reaction mixture was filtered through a celite pad before removing the THF under a stream of nitrogen. The residue was dissolved in water (~50 mL) and then washed with ether (~50 mL) before the aqueous phase was lyophilised to give the desired product **18** as a colourless oil (1.24 g, 13.4 mmol, 91%). $\mathbf{R_f}$ (DCM:MeOH 4:1) = 0.71; **^{1}H NMR** δ (500 MHz, D_2O) 4.39 (1H, s, C*H*); **^{2}H NMR** δ (500 MHz, THF) 1.45 (3D, s, CD_3); **^{13}C NMR** δ (126 MHz, D_2O) 178.6 (C), 66.3 (CH), 18.45 (CD_3, sept). The spectroscopic data are in good agreement with the commercial product (Sigma Aldrich).

6.2.2 H/D exchange

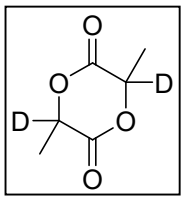

Dimethyl($^2H_2$)-1,4-dioxane-2,5-dione 21

Lactide **6** (0.5 g, 3.5 mmol) was dissolved in THF (5 mL) before adding Lindlar catalyst (2.50 g) and stirring until homogenous. The THF was then removed *in vacuo* to leave a thin film of solid coating the flask. The flask was evacuated and then deuterium gas was introduced via a balloon. After 1 hour, THF (20 mL) was added to the flask and a sample was removed for crude ^{2}H NMR. The catalyst was removed by centrifugation before the THF was removed *in vacuo* to give the desired product **21** as a colourless solid. **^{1}H NMR** δ (500 MHz, $CDCl_3$) 5.03 (1.86 H, q, *J* = 6.7 Hz, C*H*), 1.70 (6H, d, *J* = 6.7 Hz, CH_3); **^{2}H NMR** δ (500 MHz, THF) 1.90 (s), 3.75 (s); **^{13}C NMR** δ (126 MHz, $CDCl_3$) 167.5 (C), 72.5 (CH), 16.0 (CH_3).

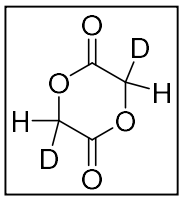

(3,6-$^2H_2$)-1,4-Dioxane-2,5-dione 22

Glycolide **7** (0.500 g, 4.30 mmol) was dissolved in THF (5 mL) before adding Lindlar catalyst (2.50 g) and stirring until homogenous. The THF was then removed *in vacuo* to leave a thin film of solid coating the flask. The flask was evacuated and then deuterium gas was introduced via a balloon. After 1 hour, THF (20 mL) was added to the flask and a sample was removed for crude ^{2}H NMR. The catalyst was removed by centrifugation and then the THF was removed *in vacuo* to give the desired product **22** as a colourless solid. **^{1}H NMR** δ (500 MHz, $CDCl_3$) 4.95 (3.72 H, s, CH_2); **^{2}H NMR** δ (126 MHz, THF) 1.90 (s), 3.75 (s); **^{13}C NMR** δ (500 MHz, $CDCl_3$) 163.5 (C), 65.1 (CH_2).

6.2.3 Ring closing reactions

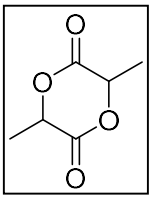

3,6-Dimethyl-1,4-dioxane-2,5-dione 6

Method A: D,L-Lactic acid **4** (1.17 g, 11.0 mmol, 85% aq.) was heated to 230°C for 6 hours to dehydrate and form oligomers, using a Dean-Stark trap to remove the water. Tin(II) 2-ethylhexanoate (0.68 µL, 0.1 wt%) was added to the PLA oligomers in a Kugelrohr glass oven under high vacuum. The temperature was gradually increased to 230°C and the reaction was maintained at this temperature for 2 hours to distil off crude lactide as a colourless liquid. The crude lactide was further purified by flash column chromatography (Hexane:EtOAc 7:3) to give the desired product **6** as a colourless solid (30.0 mg, 0.25 mmol, 2%).

Method B: Ammonium hydroxide (1.53 g, 11.0 mmol, 28% aq.) was added dropwise to D,L-lactic acid **4** (1.17 g, 11.0 mmol, 85% aq.) and the reaction mixture was stirred overnight at room temperature to produce ammonium lactate. Toluene (400 mL) and ytterbium(III) trifluoromethanesulfonate (0.069 g, 0.10 mmol) were added to the ammonium lactate and the mixture was heated to reflux overnight using a Dean-Stark trap to remove the water. TLC analysis showed the presence of lactide in the reaction mixture. The reaction mixture was extracted with ethyl acetate (~100 mL) and water (~100 mL). The organic layer was dried ($MgSO_4$) and the toluene and ethyl acetate removed *in vacuo* to give a colourless oil which was further purified by flash column chromatography (Hexane:EtOAc 7:3) to give the desired product **6** as a colourless solid (0.04 g, 0.29 mmol, 3%).

Method C: D,L-Lactic acid **4** (1.17 g, 11.0 mmol, 85% aq.) and H-beta zeolite (0.500 g), which had previously been calcined at 550°C overnight, were refluxed in toluene (10 mL) for 3 hours using a Dean-Stark trap to remove the water. TLC analysis showed the presence of lactide and PLA oligomers. The reaction mixture was filtered to remove the zeolite, and then acetonitrile (10 mL) and water (10 mL) were added. The mixture was separated and the organic layer washed with water (10 mL). The organic layer was dried ($MgSO_4$) and the toluene and acetonitrile removed *in vacuo* to give the desired product **6** as a colourless solid (0.54 g, 4.8 mmol, 34%). **mp** 99-101°C; **IR** (neat cm^{-1}) 2995 (C-H), 1727 (C=O); $\mathbf{R_f}$ (Hexane:EtOAc 7:3) = 0.43; **^{1}H NMR** δ (500 MHz, $CDCl_3$) 5.05 (2H, q, *J* = 6.7 Hz, C*H*), 1.70 (6H, d, *J* = 6.7 Hz, CH_3); **^{13}C NMR** δ (126 MHz, $CDCl_3$) 167.5 (C), 72.5 (CH), 16.0 (CH_3). The spectroscopic data are in good agreement with the literature.[95]

6.2.4 Polymerisations

6.2.4.1 Ring opening polymerisation

Lactide **6** (0.380 g, 2.60 mmol) and glycolide **7** (0.160 g, 1.40 mmol) were added to a flask under nitrogen which was heated to 120°C. The monomers were allowed to fully melt and then dodecanol (4.50 µL, 20.0 µmol) and stannous octoate (6.50 µL, 20.0 µmol) were added. The melt was stirred at 120°C for 20 minutes during which time the melt solidified and stirring stopped. The flask was then cooled to room temperature, quenched with MeOH (3 drops) and DCM (~1 mL) was added to dissolve the polymer. The polymer was then precipitated into ice-cold MeOH (~50 mL), the MeOH decanted off and the polymer dried *in vacuo* until constant weight to yield the desired product **8** as a white amorphous solid (0.360 g, 67%). **IR** (neat cm^{-1}) 2995, 2947 (C-H), 1747 (C=O); **^{1}H NMR** (500 MHz, $CDCl_3$) δ 5.25-5.15 (1H, m, PLA C*H*), δ 4.90-4.65 (2H, m, PGA CH_2), δ 1.35-1.50 (3H, m, PLA CH_3); **GPC** M_n = 8 733 Da, Đ = 1.27. The spectroscopic data are in good agreement with the literature.[204]

6.2.4.2 Polycondensation polymerisation for PLGA-D

D,L-Lactic acid **4** (0.100 g, 0.940 mmol, 85% in water), L-lactic acid-d_3 **18** (Sigma) (0.100 g, 0.910 mmol, 85% in water) and glycolic acid **5** (0.060 g, 0.790 mmol) were dehydrated at 150°C for 8 hours in a flask fitted with an air condenser containing molecular sieves, to form oligomers. Tin chloride (1.3 mg, 0.5 wt%) and *para*-toluene sulfonic acid (1.3 mg, 0.5 wt%) were then added to the oligomers followed by heating to 180°C for a further 8 h. The crude polymer was dissolved in DCM (2 mL) and precipitated into a 50:50 mixture of ice cold hexane/ether (100 mL) to yield the desired product **23** as a colourless solid which was dried *in vacuo* until constant weight (0.073 g, 28%). **^{1}H NMR** (400 MHz, Chloroform-d) δ 5.30-5.13 (1H, m, C*H*), 4.93-4.56 (2H, m, CH_2), 1.64-1.51 (3H, m, CH_3). **GPC** M_n = 4553 g/mol, Đ = 1.84.

6.3 Experimental Procedures for Chapter 3

6.3.1 General nanoparticle methods

6.3.1.1 Emulsification evaporation method

A solution of PLGA **8,** PLGA-D **23** or PLGA-alkyne **25** (10-20 mg) in DCM (1 mL) was added to the aqueous NP phase (10 mL). The two phases were emulsified using a probe tip sonicator for 2 minutes. The resulting emulsion was stirred at room temperature overnight to allow evaporation of the DCM. The NPs were collected by

centrifugation at 6,164 × g for 10 minutes, the supernatant removed and the NPs washed once with water.

6.3.1.2 Nanoprecipitation method

A solution of PLGA **8** (20 mg) in acetonitrile (1 mL) was added dropwise to water (5 mL) to spontaneously form an emulsion. The acetonitrile was removed *in vacuo* and the nanoparticles were collected by centrifugation at 9,632 × g for 10 minutes before washing once with water.

6.3.1.3 Centrifugation study

PLGA NPs (synthesised from 10 mg polymer) were synthesised using the general emulsification evaporation method, and before centrifugation, the NP emulsion was split between nine Eppendorf vials. Each of these Eppendorf vials were centrifuged for 10 minutes at speeds varying between 2,408 and 16,278 × g. The NPs were then analysed by DLS for size and polydispersity.

6.3.1.4 Lyophilisation study

PLGA NPs were synthesised using the general emulsification evaporation method (20 mg PLGA) and were then resuspended in water and split into 5 Eppendorf vials. One sample was not lyophilised as a control. The other 4 samples were lyophilised with 0, 1, 2 and 3 % (w/v) sucrose. The lyophilised powder was then resuspended in water (1 mL) and the NPs analysed by DLS for size and PdI.

6.3.1.5 Nanoparticle concentration by absorption

In triplicate, NPs (PLGA or PLGA-alkyne) were lyophilised to give a known weight of NPs. The lyophilised powders (~600 mg) were then resuspended in water (1 mL) and known concentrations (600, 300, 150 and 75 μg mL^{-1}), produced by serial dilutions, were analysed by UV spectroscopy at 220 nm to produce a calibration curve.

6.3.2 Nanoparticle targeting

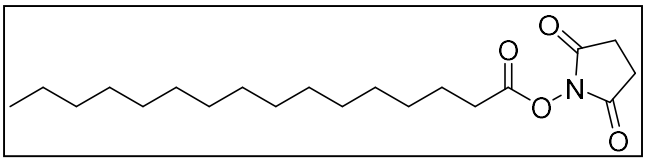

2,5-dioxopyrrolidin-1-yl hexadecanoate 33

Hexadecanoic acid **31** (1.00 g, 3.90 mmol) and triethyl amine (1.10 mL, 7.80 mmol) were dissolved in DCM (20 mL) before adding bis(2,5-dioxopyrrolidin-1-yl) carbonate **32** (1.20 g, 4.68 mmol) portion-wise. The reaction was allowed to stir under argon overnight until confirmed completed by TLC. The reaction mixture was washed with hydrochloric acid (40 mL, 1 M, aq.), and the aqueous layer extracted twice with DCM (2 × 20 mL). The combined

organic layers were dried ($MgSO_4$) and the DCM removed *in vacuo* to yield the desired product **33** as a colourless solid (0.830 g, 2.35 mmol, 60%). $\mathbf{R_f}$ ($CHCl_3$:MeOH 9.5:0.5) = 0.80; **^{1}H NMR** δ (500 MHz, $CDCl_3$) 2.83 (4H, s, 2 × NHS-CH_2), 2.60 (2H, t, *J* = 7.5 Hz, C(O)CH_2), 1.74 (2H, quin, *J* = 7.5 Hz, CH_2), 1.40 (2H, m, CH_2), 1.28 (22H, m, 11 × CH_2), 0.88 (3H, t, *J* = 6.9 Hz, CH_3); **^{13}C NMR** (500 MHz, $CDCl_3$) δ 169.3 (2 × C), 168.8 (C), 32.0 (CH_2), 31.0 (CH_2), 29.84 (2 × CH_2), 29.8 (2 × CH_2), 29.77 (CH_2), 29.7 (CH_2), 29.5 (2 × CH_2), 29.2 (CH_2), 29.0 (CH_2), 25.7 (2 × CH_2), 24.8 (CH_2), 22.8 (CH_2), 14.26 (CH_3). The spectroscopic data are in good agreement with the literature.[205]

6.3.2.1 Avidin-lipid conjugates

Avidin (from egg white) was dissolved in sodium deoxycholate solution (0.5 mL). The concentration found by UV spectroscopy was 1.19 mg mL^{-1} (8.9 nmol). A solution of 2,5-dioxopyrrolidin-1-yl hexadecanoate **33** (5.2 µL, 89 nmol, 6 mg mL^{-1} in DMSO) was added to the avidin solution and left to react at room temperature overnight. The reaction was monitored by the disappearance of the avidin peak by UPLC. Once the reaction was complete, the protein was purified by dialysis against HEPES (1 M aq.) for 24 h.

Table 6.3 UPLC method for the analysis of avidin. Waters BEH C4, 1.7 µm, 100 × 2.1 mm column, 60°C.

Time (mins)	%A (H_2O + 0.1% TFA)	%B (MeCN)
0	80	20
15	60	40
17	60	40
22	80	20

Incorporation into NPs: The general emulsification evaporation method from above was followed but the aqueous phase was modified to be the aqueous NP phase (5 mL) and avidin lipid conjugates in HEPES (5 mL) synthesised from a starting concentration of 1 mg mL^{-1} avidin (5 mL).

6.3.2.2 Carbamate conjugation of avidin to NPs

In duplicate, avidin (5.00 mg, 75.0 nmol) and 1,1-carbonyldiimidazole (1.00 mg, 6.20 µmol) were stirred in PBS (5 mL) at 0°C for 1 hour before the addition of either PLGA or PLGA-alkyne NPs (synthesised from 10.0 mg of polymer) to each of one of the reaction mixtures. The NPs were allowed to stir with the reaction mixture for 1 hour at

0°C before warming to room temperature and stirring for a further hour. The NPs were then isolated by centrifugation at 6,164 × g for 10 minutes.

6.3.2.3 Adsorption of avidin to NPs

PLGA-alkyne NPs (synthesised from 10 mg polymer) were added dropwise into 1 mg mL^{-1} avidin (5 mL) in PBS and allowed to stir at room temperature overnight. The NPs were then isolated by centrifugation at 6,164 × g for 10 minutes.

6.3.2.4 Click reaction of biotin azide to NPs

Copper sulphate (0.02 mg, 0.16 μmol), sodium ascorbate (0.05 mg, 0.24 μmol) and tris(3-hydroxypropyltriazolylmethyl)amine (0.07 mg, 0.16 μmol) were stirred in water (10 mL), that had previously been degassed with nitrogen, at room temperature for 15 minutes. Biotin-PEG3-azide conjugate (1.40 mg, 3.20 μmol) and PLGA-alkyne NPs (synthesised from 10 mg of PLGA alkyne, 1.6 μmol) were added to the reaction mixture, which was stirred at room temperature for 4 hours. The NPs were isolated by centrifugation at 6,164 × g for 10 minutes and were then resuspended in avidin at 1 mg mL^{-1} in PBS (5 mL) and stirred overnight at room temperature.

6.3.2.5 Biotin-HRP assay

In triplicate, 2 × 10^9 particles mL^{-1} of the various NPs in PBS (200 μL) were added to 1 mL Eppendorf vials before adding biotin-HRP (Thermo Fisher Scientific) at 1 mg mL^{-1} (100 μL) and incubating in the dark for 20 minutes. The Eppendorf vials were then centrifuged at 6,164 × g for 10 minutes to remove the biotin-HRP and washed once with PBS. The pellet was resuspended in PBS (200 μL) and TMB substrate solution (Thermo Fisher Scientific) (200 μL) was added to produce a blue colour and precipitate. After incubation in the dark for 20 minutes, hydrochloric acid (100 μL, 1 M aq.) was added to produce a yellow coloured solution that also had some blue precipitate. The Eppendorf vials were centrifuged once more at 6,164 × g for ten minutes to pellet the precipitate, and the supernatant was analysed by UV spectroscopy at 450 nm.

6.4 Experimental Procedures for Chapter 4

6.4.1 Isolation of microglia

Mixed glia cultures were isolated from postnatal day 1-2 rat pups, and after 10 days, microglia were isolated by shaking the culture flasks relying on differential adhesion of oligodendrocyte precursor cells, microglia and astrocytes.[206] To improve adherence

of microglia, all culture dishes were coated in poly-D-lysine before plating the cells by covering dishes in a 1 μg mL^{-1} aqueous solution and incubating at 37°C for one hour. The solution was removed and the cells were washed once with sterile water. Microglia were cultured in mixed glia media and were incubated at 37°C in a humidified atmosphere with 7.5% CO_2 and media changes every 2-3 days.

6.4.2 Viability assay

Microglia were plated at 5 × 10^4 cells per well in a 96 well plate and left overnight to adhere to the well. PLGA, PLGA-D and PLGA-alkyne NPs, resuspended in mixed glia media, were then added at 1, 2 and 4 × 10^9 particles mL^{-1} and incubated for 24 hours. Each condition was carried out in triplicate. Viability was then assessed using the CellTiter-Glo ® assay (Promega). 100 μL of luciferase was added to each well, the plate was shaken for 2 minutes before a ten minute incubation at room temperature. The amount of luminescence was then assessed with a plate reader, with higher luminescence associated with more ATP and therefore more living cells. Three biological replicates of this experiment were carried out.

6.4.3 Cell pellets

Microglia were cultured overnight in a T75 flask before NPs (PLGA-D or PLGA-alkyne) were added followed by a further overnight incubation. The media was removed and the cells washed twice with PBS (2 × 15 mL) to remove any free NPs. Cell detachment was then achieved by the addition of 0.25% trypsin-EDTA solution (5 mL) and incubation at 37°C for 20-30 minutes. The reaction was quenched by the addition of mixed glia media (10 mL), before the cells were pelleted by centrifugation at 1000 min^{-1} for 5 minutes. The media was aspirated and the cells re-suspended in water (1 mL) before lyophilisation to give a solid which was subsequently analysed by spontaneous Raman spectroscopy.

6.4.4 SRS experiments on microglia

Microglia were plated at 3 × 10^5 cells per well in FluoroDish Cell Culture Dishes (World Precision Instruments) and left overnight to adhere to the dish. NPs (alkyne or deuterium) were then added at concentrations between 0.5 and 2 × 10^9 particles mL^{-1}, followed by a 24 hour incubation. The media was then removed and the cells were washed twice with PBS (2 × 2 mL) before fixation and imaging with SRS.

6.4.4.1 Time course experiments

Microglia were plated at 3×10^5 cells per well in FluoroDish Cell Culture Dishes (World Precision Instruments) and left overnight to adhere to the dish. The control (t=0 h) cells were fixed before addition of the NPs. PLGA-alkyne NPs were then added to the remaining dishes at 2×10^9 particles mL^{-1}. At 12, 24, 36 and 48 h, individual dishes were fixed and imaged with SRS. For each time point, three fields of view were imaged and the alkyne intensity per cell was quantified using ImageJ as described below.

6.4.4.2 Image quantification

- For each field of view, the protein, alkyne and off-resonance images were opened in ImageJ and the off-resonance was subtracted from the other two images using the image calculator functionality (process → image calculator).

- A threshold (image → adjust → threshold) was then applied to the protein image to create a mask of just the cells. This mask was then made binary (process → binary → make binary).

- To count the alkyne intensity within the cell mask only, the set measurements window was opened and in the redirect to box the alkyne image was selected (analyze → set measurements → redirect to). The measurements selected were area, mean, max and min grey values.

- To then measure the values, the cell mask was selected and then the analyze particles functionality was used (analyze → analyze particles). The minimum size was set to 50.26 μm^2 to exclude anything that is not a cell, and to also segment into individual cells. The outlines were shown to produce an image with the individual cells and a list of the measurements within these cells was created.

- Three fields of view per time point were analysed and represented as a box plot with each dot representing one cell. The Mann-Whitney U test was used to assess significance.

6.4.4.3 Encapsulation of rhodamine

Rhodamine loaded PLGA-alkyne NPs were prepared using the standard emulsification-evaporation method with the addition of rhodamine (2 mg) to the organic phase. Microglia were plated at 3×10^5 cells per well in FluoroDish Cell Culture Dishes (World Precision Instruments) and left overnight to adhere to the dish. Rhodamine loaded PLGA-alkyne NPs were added at 2×10^9 particles mL^{-1} followed

by a 24 hour incubation. The microglia were then washed, fixed and imaged with SRS and TPF.

6.4.5 *Ex-vivo* cortical slices

Brains were isolated from P5 C57BL6/N mice pups in cold Hibernate-A medium (Thermo Fisher) on ice and cut into 300 µm cortical slices using a vibratome (Leica). The slices were then transferred to Millipore milli cell-CM organotypic inserts (30 mm, hydrophilic PTFE, 0.4 µm, Merck-Millipore) in slice media, and were maintained at 37°C and 7.5% CO_2 with media changes every two days. After 6 days in culture, alkyne NPs were added at 2×10^8, 2×10^9, and 2×10^{10} particles mL^{-1} for 24 hours. The slices were then washed twice with PBS (2 × 2 mL) before fixation. Slices were fixed with 4% formaldehyde (2 mL) for one hour at room temperature before washing three times with PBS (3 × 2 mL).

6.4.5.1 Immunohistochemistry analysis

Fixed slices in a 6 well plate were incubated with blocking solution (1 mL per well) for 2 hours before adding the primary antibodies. Rabbit polyclonal anti-IBA1 (1/500, Abcam, AB178846) and mouse monoclonal anti-OLIG2 (1/500, Merck Millipore, MABN50) were diluted in blocking solution and 500 µL was added to each well. The slices were then shaken at 4°C for 1.5 days before washing three times for 1 hour with blocking solution (3 × 2 mL). The secondary antibodies, goat anti-rabbit 568 (1/1000, Life Technologies, A11011), and donkey anti-mouse 488 (1/1000, Thermo Fisher Scientific, A21202) were diluted in blocking solution and then incubated with the slices (500 µL per well) with gentle agitation overnight, in the dark at 4°C. The slices were then washed once for 10 minutes followed by three 1 hour washes with PBS (4 × 2 mL) and finally imaged using TPF microscopy.

6.4.5.2 Time course on slices

Cortical slices were isolated as above, and three organotypic inserts were prepared with three slices per insert. On day five, alkyne NPs were added at 1×10^{11} particles mL^{-1} to each of the inserts by dropping the NPs suspended in 300 µL of media on top of the slices. At one, three and seven days after the addition of the NPs, the slices from one insert were fixed. The slices were then stained with anti-IBA1 for microglia as above. To stain nuclei in the tissue, Syto 9 Green Fluorescent Nucleic Acid Stain (Invitrogen, S34854) was diluted in PBS (1/1000) and 500 µL incubated with the slices for 2 minutes before washing three times with PBS (3 × 2 mL). The slices were then imaged using TPF and SRS microscopies. GFP two-photon fluorescence signals

were filtered using filters: FF520-Di02, FF495-Di03 and FF01-504/12. YFP two-photon fluorescence signals were filtered using: FF520-Di02, ET570lp (chroma) and FF01-542/27. All other fliters were from Semrock. Nine fields of view from two slices were imaged for each time point.

6.4.5.3 Image quantification

The images from the time course studies were quantified in two ways.

1. The average alkyne intensity within the microglia was measured for each field of view by creating a mask as described in Section 6.4.4.2.
2. The percentage of microglia containing NPs was quantified for each field of view. In most of the images there were large clumps of microglia and NPs, making it hard to count individual cells, so these areas were discounted from the quantification. For each field of view, three squares of 140×140 pixels were analysed and the number of microglia, with a microglia only being counted if it had a clear nuclear signal, and the number of microglia containing NPs were counted.

6.4.5 *In vivo* experiments

Animal work was carried out in accordance with the University of Edinburgh regulations under Home Office rules.

6.4.5.1 Direct injection to mouse brains

PLGA-alkyne NPs were injected into the corpus callosum of 16 week old C57BL/6 male mice. The mice were anaesthetized with isoflurane and a hole was drilled through the skull at stereotactic coordinates 1.2 mm posterior, 0.5 mm lateral, 1.4 mm deep to bregma. 2 µL of PLGA-alkyne NPs at 4×10^{11} particles mL^{-1} in PBS were then injected into this hole over 4 minutes using a 30 gauge needle attached to a Hamilton syringe, driven by a KD Scientific Nano pump, which was left in situ for 4 minutes to reduce backflow. At 2, or 24 hours after NP addition (2 mice per time point), mice were perfused with 4% formaldehyde in PBS, and the brains harvested. The brains were stored in 4% formaldehyde for 24 hours before being transferred to PBS. The brains were cut into 100 µm sections using a vibratome (Leica) prior to imaging with SRS microscopy.

6.4.5.2 Intranasal delivery to mice

Three adult C57BL/6 mice were treated with PLGA-alkyne NPs intranasally. The mice were anaesthetised with isoflurane and then 50 µL of PLGA-alkyne NPs at 1×10^{11}

particles mL^{-1} in PBS was placed on the nostril until absorbed. The mice were held upside down to ensure absorption into the nostrils. 24 hours after NP addition, the mice were perfused with 4% formaldehyde in PBS, and the brains harvested. The brains were stored in 4% formaldehyde for 24 hours before being transferred to PBS. The brains were cut into 100 µm sections using a vibratome (Leica) prior to imaging with SRS microscopy.

References

1 M. Lassonde, S. Candel, J. Hacker, A. Quadrio-Curzio, T. Onishi, V. Ramakrishnan and M. McNutt, *The challenge of neurodegenerative diseases in an aging population*, 2017.

2 F. Vilhardt, Microglia: Phagocyte and glia cell, *Int. J. Biochem. Cell Biol.*, 2005, **37**, 17–21.

3 M. V Sofroniew and H. V Vinters, Astrocytes: biology and pathology., *Acta Neuropathol.*, 2010, **119**, 7–35.

4 B. Ettle, J. C. M. Schlachetzki and J. Winkler, Oligodendroglia and Myelin in Neurodegenerative Diseases: More Than Just Bystanders?, *Mol. Neurobiol.*, 2016, **53**, 3046–3062.

5 T. Patel, J. Zhou, J. M. Piepmeier and W. M. Saltzman, Polymeric nanoparticles for drug delivery to the central nervous system, *Adv. Drug Deliv. Rev.*, 2012, **64**, 701–705.

6 E. J. Münzel and A. Williams, Promoting remyelination in multiple sclerosis-recent advances, *Drugs*, 2013, **73**, 2017–2029.

7 P. Morrell and R. H. Quarles, in *Basic Neurochemistry: Molecular, Cellular and Medical Aspects*, Lippincott-Raven, Philadelphia, 6th Editio., 1999.

8 R. J. M. Franklin and C. ffrench-Constant, Remyelination in the CNS: From biology to therapy, *Nat. Rev. Neurosci.*, 2008, **9**, 839–855.

9 U. Funfschilling, L. M. Supplie, D. Mahad, S. Boretius, S. Aiman, J. Edgar, B. G. Brinkmann, C. M. Kassmann, I. D. Tzvetanova, W. Sereda, C. T. Moraes, J. Frahm, S. Goebbels and K.-A. Nave, Glycolytic oligodendrocytes maintain myelin and long-term axonal integrity, *Nature*, 2012, **485**, 517–521.

10 Y. Lee, B. M. Morrison, Y. Li, S. Lengacher, M. H. Farah, P. N. Hoffman, Y. Liu, A. Tsingalia, L. Jin, P. W. Zhang, L. Pellerin, P. J. Magistretti and J. D. Rothstein, Oligodendroglia metabolically support axons and contribute to neurodegeneration, *Nature*, 2012, **487**, 443–448.

11 H. F. McFarland and R. Martin, Multiple sclerosis: A complicated picture of autoimmunity, *Nat. Immunol.*, 2007, **8**, 913–919.

12 M. M. Goldenberg, Multiple sclerosis review., *Pharm. Ther.*, 2012, **37**, 175–184.

13 A. J. Green, J. M. Gelfand, B. A. Cree, C. Bevan, W. J. Boscardin, F. Mei, J. Inman, S. Arnow, M. Devereux, A. Abounasr, H. Nobuta, A. Zhu, M. Friessen, R. Gerona, H. C. von Büdingen, R. G. Henry, S. L. Hauser and J. R. Chan, Clemastine fumarate as a remyelinating therapy for multiple sclerosis (ReBUILD): a randomised, controlled, double-blind, crossover trial, *Lancet*, 2017, **390**, 2481–2489.

14 P. Brugarolas and B. Popko, Remyelination therapy goes to trial for multiple sclerosis, *Neurol. Neuroimmunol. NeuroInflammation*, 2014, **1**, e26.

15 S. E. R. Halford, G. Cruickshank, L. Dunn, S. Erridge, L. Godfrey, C. Herbert, S. Jefferies, J. S. Lopez, C. McBain, M. Pittman, R. Sleigh, C. Watts, M. F. Webster-Smith and A. J. Chalmers, Results of the OPARATIC trial: A phase I dose escalation study of olaparib in combination with temozolomide (TMZ) in patients with relapsed glioblastoma (GBM)., *J. Clin. Oncol.*, 2017, **35**, 2022.

16 E. E. Konofagou, Y.-S. Tung, J. Choi, T. Deffieux, B. Baseri and F. Vlachos, Ultrasound-induced blood-brain barrier opening., *Curr. Pharm. Biotechnol.*, 2012, **13**, 1332–45.

17 N. Lipsman, Y. Meng, A. J. Bethune, Y. Huang, B. Lam, M. Masellis, N. Herrmann, C. Heyn, I. Aubert, A. Boutet, G. S. Smith, K. Hynynen and S. E. Black, Blood–brain barrier opening in Alzheimer's disease using MR-guided focused ultrasound, *Nat. Commun.*, 2018, **9**, 1–8.

18 G. A. Silva, Nanotechnology approaches to crossing the blood-brain barrier and drug delivery to the CNS, *BMC Neurosci.*, 2008, **9**, 1–4.

19 J. Kreuter, R. N. Alyautdin, D. A. Kharkevich and A. A. Ivanov, Passage of peptides through the blood-brain barrier with colloidal polymer particles (nanoparticles), *Brain Res.*, 1995, **674**, 171–174.

20 S. Rittchen, A. Boyd, A. Burns, J. Park, T. M. Fahmy, S. Metcalfe and A. Williams, Myelin repair in vivo is increased by targeting oligodendrocyte precursor cells with nanoparticles encapsulating leukaemia inhibitory factor (LIF), *Biomaterials*, 2015, **56**, 78–85.

21 Raman C. V. and Kariamanikkam K. S., *Nature*, 1928, 121, 501–502.

22 K. J. I. Ember, M. A. Hoeve, S. L. McAughtrie, M. S. Bergholt, B. J. Dwyer, M. M. Stevens, K. Faulds, S. J. Forbes and C. J. Campbell, Raman spectroscopy and regenerative medicine: a review, *npj Regen. Med.*, 2017, **2**, 12.

23 L. P. Choo-Smith, H. G. M. Edwards, H. P. Endtz, J. M. Kros, F. Heule, H. Barr, J. S. Robinson, H. A. Bruining and G. J. Puppels, Medical applications of Raman spectroscopy: From proof of principle to clinical implementation, *Biopolymers*, 2002, **67**, 1–9.

24 S. Gomes da Costa, A. Richter, U. Schmidt, S. Breuninger and O. Hollricher, Confocal Raman microscopy in life sciences, *Morphologie*, 2018, **103**, 11–16.

25 R. Michael, A. Lenferink, G. F. J. M. Vrensen, E. Gelpi, R. I. Barraquer and C. Otto, Hyperspectral Raman imaging of neuritic plaques and neurofibrillary tangles in brain tissue from Alzheimer's disease patients, *Sci. Rep.*, 2017, **7**, 1–11.

26 K. Kong, C. Kendall, N. Stone and I. Notingher, Raman spectroscopy for medical diagnostics - From in-vitro biofluid assays to in-vivo cancer detection, *Adv. Drug Deliv. Rev.*, 2015, **89**, 121–134.

27 J. Surmacki, J. Musial, R. Kordek and H. Abramczyk, Raman imaging at biological interfaces: Applications in breast cancer diagnosis, *Mol. Cancer*, 2013, **12**, 1–12.

28 K. Kong, C. J. Rowlands, S. Varma, W. Perkins, I. H. Leach, A. A. Koloydenko, H. C. Williams and I. Notingher, Diagnosis of tumors during tissue-conserving surgery with integrated autofluorescence and Raman scattering microscopy, *Proc. Natl. Acad. Sci.*, 2013, **110**, 15189–15194.

29 H. Shinzawa, K. Awa, W. Kanematsu and Y. Ozaki, Multivariate data analysis for Raman spectroscopic imaging, *J. Raman Spectrosc.*, 2009, **40**, 1720–1725.

30 J. M. P. Nascimento and J. M. B. Dias, Vertex Component Analysis: A Fast Algorith to Unmix Hyperspectral Data, *IEEE Trans. Geosci. Remote Sens.*, 2005, **43**, 898–910.

31 D. Cialla-May, X. S. Zheng, K. Weber and J. Popp, Recent progress in surface-enhanced Raman spectroscopy for biological and biomedical applications: From cells to clinics, *Chem. Soc. Rev.*, 2017, **46**, 3945–3961.

32 I. Bruzas, W. Lum, Z. Gorunmez and L. Sagle, Advances in surface-enhanced Raman spectroscopy (SERS) substrates for lipid and protein characterization: Sensing and beyond, *Analyst*, 2018, **143**, 3990–4008.

33 J. Jiang, C. Auchinvole, K. Fisher and C. J. Campbell, Quantitative measurement of redox potential in hypoxic cells using SERS nanosensors, *Nanoscale*, 2014, **6**, 12104–12110.

34 J. H. Granger, N. E. Schlotter, A. C. Crawford and M. D. Porter, Prospects for point-of-care pathogen diagnostics using surface-enhanced Raman scattering (SERS), *Chem. Soc. Rev.*, 2016, **45**, 3865–3882.

35 C. Zhang, D. Zhang and J.-X. Cheng, *Coherent Raman Scattering Microscopy in Biology and Medicine*, 2015, vol. 17.

36 J. X. Cheng and X. S. Xie, Vibrational spectroscopic imaging of living systems: An emerging platform for biology and medicine, *Science* , 2015, **350**, aaa870-1-aaa870-9.

37 C. L. Evans, E. O. Potma, M. Puoris'haag, D. Cote, C. P. Lin and X. S. Xie, Chemical imaging of tissue in vivo with video-rate coherent anti-Stokes Raman scattering microscopy, *Proc. Natl. Acad. Sci.*, 2005, **102**, 16807–16812.

38 C. L. Evans and X. S. Xie, Coherent Anti-Stokes Raman Scattering Microscopy: Chemical Imaging for Biology and Medicine, *Annu. Rev. Anal. Chem.*, 2008, **1**, 883–909.

39 E. J. Woodbury and W. K. Ng, Ruby Laser Operation in the Near IR, *Proc. IRE*, 1962, **50**, 2367.

40 V. V. Yakovlev, G. I. Petrov, H. F. Zhang, G. D. Noojin, M. L. Denton, R. J. Thomas and M. O. Scully, Stimulated Raman scattering: Old physics, new applications, *J. Mod. Opt.*, 2009, **56**, 1970–1973.

41 W. J. Tipping, M. Lee, A. Serrels, V. G. Brunton and A. N. Hulme, Stimulated Raman scattering microscopy: an emerging tool for drug discovery, *Chem. Soc. Rev.*, 2016, **45**, 2075–2089.

42 L. Wei, F. Hu, Y. Shen, Z. Chen, Y. Yu, C. C. Lin, M. C. Wang and W. Min, Live-cell imaging of alkyne-tagged small biomolecules by stimulated Raman scattering, *Nat. Methods*, 2014, **11**, 410–412.

43 W. Min, C. W. Freudiger, S. Lu and X. S. Xie, Coherent Nonlinear Optical Imaging: Beyond Fluorescence Microscopy, *Annu. Rev. Phys. Chem.*, 2011, **62**, 507–530.

44 C. Krafft, I. W. Schie, T. Meyer, M. Schmitt and J. Popp, Developments in spontaneous and coherent Raman scattering microscopic imaging for biomedical applications, *Chem. Soc. Rev.*, 2016, **45**, 1819–1849.

45 R. K. V Lim, Q. Lin and Q. Lin, Bioorthogonal chemistry : recent progress and future directions, *Chem. Commun.*, 2010, **46**, 1589–1600.

46 H. Yamakoshi, K. Dodo, A. Palonpon, J. Ando, K. Fujita, S. Kawata and M. Sodeoka, Alkyne-tag Raman imaging for visualization of mobile small molecules in live cells, *J. Am. Chem. Soc.*, 2012, **134**, 20681–20689.

47 K. Aljakouch, T. Lechtonen, H. K. Yosef, M. K. Hammoud, W. Alsaidi, C. Kötting, C. Mügge, R. Kourist, S. F. El-Mashtoly and K. Gerwert, Raman Microspectroscopic Evidence for the Metabolism of a Tyrosine Kinase Inhibitor, Neratinib, in Cancer Cells, *Angew. Chemie - Int. Ed.*, 2018, **57**, 7250–7254.

48 F. Hu, Z. Chen, L. Zhang, Y. Shen, L. Wei and W. Min, Vibrational Imaging of Glucose Uptake Activity in Live Cells and Tissues by Stimulated Raman Scattering, *Angew. Chemie - Int. Ed.*, 2015, **54**, 9821–9825.

49 T. W. Bocklitz, S. Guo, O. Ryabchykov, N. Vogler and J. Popp, Raman Based Molecular Imaging and Analytics: A Magic Bullet for Biomedical Applications!?, *Anal. Chem.*, 2016, **88**, 133–151.

50 L. E. Kamemoto, A. K. Misra, S. K. Sharma, M. T. Goodman, L. U. K. Hugh, A. C. Dykes and T. Acosta, Near-infrared micro-Raman spectroscopy for in vitro detection of cervical cancer, *Appl. Spectrosc.*, 2010, **64**, 255–261.

51 S. Cui, S. Zhang and S. Yue, Raman Spectroscopy and Imaging for Cancer Diagnosis, *J. Healthc. Eng.*, 2018, **2018**, 1–11.

52 B. Shashni, Y. Horiguchi, K. Kurosu, H. Furusho and Y. Nagasaki, Application of surface enhanced Raman spectroscopy as a diagnostic system for hypersialylated metastatic cancers, *Biomaterials*, 2017, **134**, 143–153.

53 N. K. Das, Y. Dai, P. Liu, C. Hu, L. Tong, X. Chen and Z. J. Smith, Raman plus X: Biomedical applications of multimodal Raman spectroscopy, *Sensors*, 2017,

17, 1–20.

54 E. Cordero, I. Latka, C. Matthäus, I. W. Schie and J. Popp, In-vivo Raman spectroscopy : from basics to applications, *J. Biomed. Opt.*, 2019, **23**, 1–23.

55 K. Lin, W. Zheng, C. M. Lim and Z. Huang, Real-time In vivo Diagnosis of Nasopharyngeal Carcinoma Using Rapid Fiber-Optic Raman Spectroscopy, *Theranostics*, 2017, **7**, 3517–3526.

56 H. Lui, J. Zhao, D. McLean and H. Zeng, Real-time Raman Spectroscopy for In Vivo Skin Cancer Diagnosis, *Cancer Res.*, 2012, **72**, 2491–2500.

57 C. A. Lieber, S. K. Majumder, D. L. Ellis, D. D. Billheimer and A. Mahadevan-Jansen, In Vivo Nonmelanoma Skin Cancer Diagnosis Using Raman Microspectroscopy, *Lasers Surg. Med.*, 2008, **40**, 461–467.

58 S. Vanden-Hehir, W. J. Tipping, M. Lee, V. G. Brunton, A. Williams and A. N. Hulme, Raman Imaging of Nanocarriers for Drug Delivery, *Nanomaterials*, 2019, **9**, 1–19.

59 O. S. Wolfbeis, An overview of nanoparticles commonly used in fluorescent bioimaging, *Chem. Soc. Rev.*, 2015, **44**, 4743–4768.

60 W.-H. Zhang, X.-X. Hu and X.-B. Zhang, Dye-Doped Fluorescent Silica Nanoparticles for Live Cell and In Vivo Bioimaging, *Nanomaterials*, 2016, **6**, 1–17.

61 M. X. Zhao and E. Z. Zeng, Application of functional quantum dot nanoparticles as fluorescence probes in cell labeling and tumor diagnostic imaging, *Nanoscale Res. Lett.*, 2015, **10**, 1–9.

62 B. Andreiuk, A. Reisch, M. Lindecker, G. Follain, N. Peyriéras, J. G. Goetz and A. S. Klymchenko, Fluorescent Polymer Nanoparticles for Cell Barcoding In Vitro and In Vivo, *Small*, 2017, **13**, 1–13.

63 R. Kalluru, F. Fenaroli, D. Westmoreland, L. Ulanova, A. Maleki, N. Roos, M. Paulsen Madsen, G. Koster, W. Egge-Jacobsen, S. Wilson, H. Roberg-Larsen, G. K. Khuller, A. Singh, B. Nystrom and G. Griffiths, Poly(lactide-co-glycolide)-rifampicin nanoparticles efficiently clear Mycobacterium bovis BCG infection in macrophages and remain membrane-bound in phago-lysosomes, *J. Cell Sci.*, 2013, **126**, 3043–3054.

64 P. Gentile, V. Chiono, I. Carmagnola and P. V. Hatton, An overview of poly(lactic-co-glycolic) Acid (PLGA)-based biomaterials for bone tissue engineering, *Int. J. Mol. Sci.*, 2014, **15**, 3640–3659.

65 D. Tuncel and H. V. Demir, Conjugated polymer nanoparticles, *Nanoscale*, 2010, **2**, 484–494.

66 Y. Braeken, S. Cheruku, A. Ethirajan and W. Maes, Conjugated polymer nanoparticles for bioimaging, *Materials (Basel).*, 2017, **10**, 1–23.

67 T. Chen, W. Xu, Z. Huang, H. Peng, Z. Ke, X. Lu, Y. Yan and R. Liu, Poly(phenyleneethynylene) nanoparticles: Preparation, living cell imaging and potential application as drug carriers, *J. Mater. Chem. B*, 2015, **3**, 3564–3572.

68 G. Feng, Y. Fang, J. Liu, J. Geng, D. Ding and B. Liu, Multifunctional Conjugated Polymer Nanoparticles for Image-Guided Photodynamic and Photothermal Therapy, *Small*, 2017, **13**, 1–12.

69 S. Li, T. Chen, Y. Wang, L. Liu, F. Lv, Z. Li, Y. Huang, K. S. Schanze and S. Wang, Conjugated Polymer with Intrinsic Alkyne Units for Synergistically Enhanced Raman Imaging in Living Cells, *Angew. Chemie - Int. Ed.*, 2017, **56**, 13455–13458.

70 E. A. Gratton, Stephanie, P. A. Ropp, P. D. Pohlhaus, J. C. Luft, V. J. Madden, M. E. Napier and J. M. DeSimone, The effect of particle design on cellular internalization pathways, *Proc. Natl. Acad. Sci.*, 2008, **105**, 11613–11618.

71 T. Chernenko, F. Buyukozturk, M. Miljkovic, R. Carrier, M. Diem and M. Amiji, Label-free Raman microspectral analysis for comparison of cellular uptake and distribution between nontargeted and EGFR-targeted biodegradable polymeric nanoparticles, *Drug Deliv. Transl. Res.*, 2013, **3**, 575–586.

72 C. Matthäus, S. Schubert, M. Schmitt, C. Krafft, B. Dietzek, U. S. Schubert and J. Popp, Resonance Raman spectral imaging of intracellular uptake of β-carotene loaded poly(D, L -lactide-co-glycolide) nanoparticles, *ChemPhysChem*, 2013, **14**, 155–161.

73 B. Robert, Resonance Raman spectroscopy, *Photosynth. Res.*, 2009, **101**, 147–155.

74 E. Smith and G. Dent, *Modern Raman Spectroscopy – A Practical Approach*,

John Wiley & Sons Ltd, Chichester, 2005.

75 C. Matthäus, A. Kale, T. Chernenko, V. Torchilin and M. Diem, New ways of imaging uptake and intracellular fate of liposomal drug carrier systems inside individual cells, based on raman microscopy, *Mol. Pharm.*, 2008, **5**, 287–293.

76 A. D. Frankel and C. O. Pabo, Cellular uptake of the tat protein from human immunodeficiency virus, *Cell*, 1988, **55**, 1189–1193.

77 A. A. Van Apeldoorn, H. J. Van Manen, J. M. Bezemer, J. D. De Bruijn, C. A. Van Blitterswijk and C. Otto, Raman imaging of PLGA microsphere degradation inside macrophages, *J. Am. Chem. Soc.*, 2004, **126**, 13226–13227.

78 T. Chernenko, C. Matthäus, L. Milane, L. Quintero, M. Amiji and M. Diem, Label-free raman spectral imaging of intracellular delivery and degradation of polymeric nanoparticle systems, *ACS Nano*, 2009, **3**, 3552–3559.

79 F. Hu, S. D. Brucks, T. H. Lambert, L. M. Campos and W. Min, Stimulated Raman scattering of polymer nanoparticles for multiplexed live-cell imaging, *Chem. Commun.*, 2017, **53**, 6187–6190.

80 N. A. Belsey, N. L. Garrett, L. R. Contreras-Rojas, A. J. Pickup-Gerlaugh, G. J. Price, J. Moger and R. H. Guy, Evaluation of drug delivery to intact and porated skin by coherent Raman scattering and fluorescence microscopies, *J. Control. Release*, 2014, **174**, 37–42.

81 N. L. Garrett, A. Lalatsa, D. Begley, L. Mihoreanu, I. F. Uchegbu, A. G. Schätzlein and J. Moger, Label-free imaging of polymeric nanomedicines using coherent anti-stokes Raman scattering microscopy, *J. Raman Spectrosc.*, 2012, **43**, 681–688.

82 N. L. Garrett, L. Godfrey, A. Lalatsa, D. R. Serrano, I. F. Uchegbu, A. Schatzlein and J. Moger, Detecting polymeric nanoparticles with coherent anti-stokes Raman scattering microscopy in tissues exhibiting fixative-induced autofluorescence, *Proc. SPIE*, 2015, **9329**, 932922.

83 N. L. Garrett, A. Lalatsa, I. Uchegbu, A. Schätzlein and J. Moger, Exploring uptake mechanisms of oral nanomedicines using multimodal nonlinear optical microscopy, *J. Biophotonics*, 2012, **5**, 458–468.

84 W. M. Pardridge, The blood-brain barrier: Bottleneck in brain drug development,

NeuroRx, 2005, **2**, 3–14.

85 T. P. Haider, C. Völker, J. Kramm, K. Landfester and F. R. Wurm, Plastics of the Future? The Impact of Biodegradable Polymers on the Environment and on Society, *Angew. Chemie - Int. Ed.*, 2019, **58**, 50–62.

86 H. K. Makadia and S. J. Siegel, Poly Lactic-co-Glycolic Acid (PLGA) as biodegradable controlled drug delivery carrier, *Polymers (Basel).*, 2011, **3**, 1377–1397.

87 J.-M. Lü, X. Wang, C. Marin-Muller, H. Wang, P. H. Lin, Q. Yao and C. Chen, Current Advances in Research and Clinical Applications of PLGA-based Nanotechnology, *Expert Rev. Mol. Diagn.*, 2009, **9**, 325–341.

88 M. Mir, N. Ahmed and A. ur Rehman, Recent applications of PLGA based nanostructures in drug delivery, *Colloids Surfaces B Biointerfaces*, 2017, **159**, 217–231.

89 A. Komesu, J. A. R. de Oliveira, L. H. da S. Martins, M. R. W. Maciel and R. M. Filho, Lactic acid production to purification: A review, *BioResources*, 2017, **12**, 4364–4383.

90 O. M. Koivistoinen, J. Kuivanen, D. Barth, H. Turkia, J. P. Pitkänen, M. Penttilä and P. Richard, Glycolic acid production in the engineered yeasts Saccharomyces cerevisiae and Kluyveromyces lactis, *Microb. Cell Fact.*, 2013, **12**, 1–16.

91 C. Engineer, J. Parikh and A. Raval, Effect of copolymer ratio on hydrolytic degradation of poly(lactide-co-glycolide) from drug eluting coronary stents, *Chem. Eng. Res. Des.*, 2011, **89**, 328–334.

92 H. Keles, A. Naylor, F. Clegg and C. Sammon, Investigation of factors influencing the hydrolytic degradation of single PLGA microparticles, *Polym. Degrad. Stab.*, 2015, **119**, 228–241.

93 Y. Hu, W. A. Daoud, K. K. L. Cheuk and C. S. K. Lin, Newly developed techniques on polycondensation, ring-opening polymerization and polymer modification: Focus on poly(lactic acid), *Materials (Basel).*, , DOI:10.3390/ma9030133.

94 O. Dechy-Cabaret, B. Martin-Vaca and D. Bourissou, Controlled ring-opening

polymerization of lactide and glycolide, *Chem. Rev.*, 2004, **104**, 6147–6176.

95 D. K. Yoo, D. Kim and D. S. Lee, Synthesis of lactide from oligomeric PLA: Effects of temperature, pressure, and catalyst, *Macromol. Res.*, 2006, **14**, 510–516.

96 M. Dusselier, P. Van Wouwe, A. Dewaele, P. A. Jacobs and B. F. Sels, Shape-selective zeolite catalysis for bioplastics production, *Science* , 2015, **349**, 78–80.

97 S. Heo, H. W. Park, J. H. Lee and Y. K. Chang, Design and Evaluation of Sustainable Lactide Production Process with an One-Step Gas Phase Synthesis Route, *ACS Sustain. Chem. Eng.*, 2019, **7**, 6178–6184.

98 V. Singh and M. Tiwari, Structure-processing-property relationship of poly(glycolic acid) for drug delivery systems 1: Synthesis and catalysis, *Int. J. Polym. Sci.*, 2010, **2010**, 1–23.

99 CFR - Code of Federal Regulations Title 21, https://www.accessdata.fda.gov/scripts/cdrh/cfdocs/cfcfr/cfrsearch.cfm?fr=175.300, (accessed 3 May 2019).

100 S. Gesslbauer, H. Cheek, A. J. P. White and C. Romain, Highly active aluminium catalysts for room temperature ring-opening polymerisation of rac-lactide, *Dalt. Trans.*, 2018, **47**, 10410–10414.

101 S. Bian, S. Abbina, Z. Lu, E. Kolodka and G. Du, Ring-Opening Polymerization of rac-Lactide with Aluminum Chiral Anilido-Oxazolinate Complexes, *Organometallics*, 2014, **33**, 2489–2495.

102 L. Simón and J. M. Goodman, The Mechanism of TBD-Catalyzed Ring-Opening Polymerization of Cyclic Esters, *J. Org. Chem.*, 2007, **72**, 9656–9662.

103 J. L. Hedrick, R. C. Pratt, B. G. G. Lohmeijer, D. A. Long and R. M. Waymouth, Triazabicyclodecene: A Simple Bifunctional Organocatalyst for Acyl Transfer and Ring-Opening Polymerization of Cyclic Esters, *J. Am. Chem. Soc.*, 2006, **128**, 4556–4557.

104 G. W. Nyce, M. Myers, J. L. Hedrick, E. F. Connor and A. Möck, First Example of N-Heterocyclic Carbenes as Catalysts for Living Polymerization: Organocatalytic Ring-Opening Polymerization of Cyclic Esters,

J. Am. Chem. Soc., 2002, **124**, 914–915.

105 S. Quillard, G. Louam, J. P. Buisson, M. Boyer, M. Lapkowski, A. Pron and S. Lefrant, Vibrational spectroscopic studies of the isotope effects in polyaniline, *Synth. Met.*, 1997, **84**, 805–806.

106 B. Neises and W. Steglich, Simple Method for the Esterification of Carboxylic Acids, *Angew. Chemie Int. Ed. English*, 1978, **17**, 522–524.

107 I. Dos Santos, J.-L. Morgat and M. Vert, Hydrogen isotope exchange as a means of labelling lactides, *J. Label. Compd. Radiopharm.*, 1998, **XLI**, 1005–1015.

108 I. Dos Santos, J.-L. Morgat and M. Vert, Glycolide deuteration by hydrogen isotope exchange using the HSCIE method, *J. Label. Compd. Radiopharm.*, 1999, **42**, 1093–1101.

109 S. Il Moon, C. W. Lee, M. Miyamoto and Y. Kimura, Melt polycondensation of L-lactic acid with Sn(II) catalysts activated by various proton acids: A direct manufacturing route to high molecular weight poly(L-lactic acid), *J. Polym. Sci. Part A Polym. Chem.*, 2000, **38**, 1673–1679.

110 Q. Gao, P. Lan, H. Shao and X. Hu, Direct Synthesis with Melt Polycondensation and Microstructure Analysis of Poly(L-lactic acid-co-glycolic acid), *Polym. J.*, 2002, **34**, 786–793.

111 S. A. Cairns, *Ring-Opening Polymerisation of 1,3-Dioxolan-4-ones*, University of Edinburgh Thesis, 2018.

112 S. A. Cairns, A. Schultheiss and M. P. Shaver, A broad scope of aliphatic polyesters prepared by elimination of small molecules from sustainable 1,3-dioxolan-4-ones, *Polym. Chem.*, 2017, **8**, 2990–2996.

113 G. Dyker and D. Hildebrandt, Total synthesis of heliophenanthrone, *J. Org. Chem.*, 2005, **70**, 6093–6096.

114 R. C. Cambie, E. R. H. Jones and G. Lowe, Chemistry of the Higher Fungi. Part XV. The synthesis of two α-Hydroxy-acids from Poria sinuosa Fr., *J. Chem. Soc.*, 1963, **0**, 3456–3476.

115 European Commission (E.C), Environment: Definition of a nanomaterial.

116 C. Cha, S. R. Shin, N. Annabi and M. R. Dokmeci, Carbon-Based Nanomaterials: Multifunctional Materials for Biomedical Engineering, *ACS Nano*, 2013, **7**, 2891–2897.

117 H. K. K, N. Venkatesh, H. Bhowmik and A. Kuila, Metallic Nanoparticle : A Review, *Biomed. J. Sci. Tech. Res.*, 2018, **4**, 1–11.

118 D. Guo, G. Xie and J. Luo, Mechanical properties of nanoparticles : basics and applications, *J. Phys. B Appl. Phys.*, 2014, **47**, 1–25.

119 S. Senapati, A. K. Mahanta, S. Kumar and P. Maiti, Controlled drug delivery vehicles for cancer treatment and their performance, *Signal Transduct. Target. Ther.*, 2018, **3**, 1–19.

120 Y. Ali, A. Alqudah, S. Ahmad, S. Abd Hamid and U. Farooq, Macromolecules as targeted drugs delivery vehicles: an overview, *Des. Monomers Polym.*, 2019, **22**, 91–97.

121 S. K. Sahoo, S. Parveen and J. J. Panda, The present and future of nanotechnology in human health care, *Nanomedicine Nanotechnology, Biol. Med.*, 2007, **3**, 20–31.

122 L. Y. Rizzo, B. Theek, G. Storm, F. Kiessling and T. Lammers, Recent progress in nanomedicine: Therapeutic, diagnostic and theranostic applications, *Curr. Opin. Biotechnol.*, 2013, **24**, 1159–1166.

123 B. Huang, H. Babcock and X. Zhuang, Breaking the Diffraction Barrier: Super-Resolution Imaging of Cells, *Cell*, 2010, **143**, 1047–1058.

124 D. J. Smith, Ultimate resolution in the electron microscope?, *Mater. Today*, 2008, **11**, 30–38.

125 P. L. Stewart, Cryo-electron microscopy and cryo-electron tomography of nanoparticles, *Wiley Interdiscip. Rev. Nanomedicine Nanobiotechnology*, 2017, **9**, 1–16.

126 J. Stetefeld, S. A. McKenna and T. R. Patel, Dynamic light scattering: a practical guide and applications in biomedical sciences, *Biophys. Rev.*, 2016, **8**, 409–427.

127 J. Hou, H. Ci, P. Wang, C. Wang, B. Lv, L. Miao and G. You, Nanoparticle tracking analysis versus dynamic light scattering: Case study on the effect of

Ca^{2+} and alginate on the aggregation of cerium oxide nanoparticles, *J. Hazard. Mater.*, 2018, **360**, 319–328.

128 V. Filipe, A. Hawe and W. Jiskoot, Critical evaluation of nanoparticle tracking analysis (NTA) by NanoSight for the measurement of nanoparticles and protein aggregates, *Pharm. Res.*, 2010, **27**, 796–810.

129 Malvern Instruments, *Nanoscale Material Characterization: a Review of the use of Nanoparticle Tracking Analysis (NTA)*, 2017.

130 Malvern Instruments, *Whitepaper NTA : Principles and Methodology*, 2015.

131 C. I. C. Crucho and M. T. Barros, Polymeric nanoparticles: A study on the preparation variables and characterization methods, *Mater. Sci. Eng. C*, 2017, **80**, 771–784.

132 I. Muhammad, Z. Nadial, F. Hatem and E. Abdelhamid, Double emulsion solvent evaporation techniques used for drug encapsulation, *Int. J. Pharm.*, 2015, **496**, 173–190.

133 R. L. McCall and R. W. Sirianni, PLGA Nanoparticles Formed by Single- or Double-emulsion with Vitamin E-TPGS, *J. Vis. Exp.*, 2013, **e51015**, 1–8.

134 S. V. Sokolov, K. Tschulik, C. Batchelor-McAuley, K. Jurkschat and R. G. Compton, Reversible or Not? Distinguishing Agglomeration and Aggregation at the Nanoscale, *Anal. Chem.*, 2015, **87**, 10033–10039.

135 Malvern Instruments, *Dynamic Light Scattering Common Terms Defined*, 2011.

136 W. Abdelwahed, G. Degobert, S. Stainmesse and H. Fessi, Freeze-drying of nanoparticles: Formulation, process and storage considerations, *Adv. Drug Deliv. Rev.*, 2006, **58**, 1688–1713.

137 L. Niu and J. Panyam, Freeze concentration-induced PLGA and polystyrene nanoparticle aggregation: Imaging and rational design of lyoprotection, *J. Control. Release*, 2017, **248**, 125–132.

138 L. Shang, K. Nienhaus and G. U. Nienhaus, Engineered nanoparticles interacting with cells: Size matters, *J. Nanobiotechnology*, 2014, **12**, 1–11.

139 J. Zhao and M. H. Stenzel, Entry of nanoparticles into cells: The importance of nanoparticle properties, *Polym. Chem.*, 2018, **9**, 259–272.

140 T. Govender, S. Stolnik, M. C. Garnett, L. Illum and S. S. Davis, PLGA nanoparticles prepared by nanoprecipitation: Drug loading and release studies of a water soluble drug, *J. Control. Release*, 1999, **57**, 171–185.

141 M. Morales-Cruz, G. M. Flores-Fernández, M. Morales-Cruz, E. A. Orellano, J. A. Rodriguez-Martinez, M. Ruiz and K. Griebenow, Two-step nanoprecipitation for the production of protein-loaded PLGA nanospheres, *Results Pharma Sci.*, 2012, **2**, 79–85.

142 D. F. Swinehart, The Beer-Lambert Law, *J. Chem. Educ.*, 1962, **39**, 333–335.

143 J. Fang, H. Nakamura and H. Maeda, The EPR effect: Unique features of tumor blood vessels for drug delivery, factors involved, and limitations and augmentation of the effect, *Adv. Drug Deliv. Rev.*, 2011, **63**, 136–151.

144 K. Ganesh, D. Archana and K. Preeti, Review Article on Targeted Polymeric Nanoparticles : An Overview, *Am. J. Adv. Drug Deliv.*, 2015, **3**, 196–215.

145 V. Le Joncour and P. Laakkonen, Seek & Destroy, use of targeting peptides for cancer detection and drug delivery, *Bioorganic Med. Chem.*, 2018, **26**, 2797–2806.

146 R. Bazak, M. Houri, S. El Achy, S. Kamel, H. Officer, T. Refaat, N. Medicine and R. H. Lurie, Cancer active targeting by nanoparticles: a comprehensive review of literature, *J. Cancer Res. Clin. Oncol.*, 2015, **141**, 769–784.

147 H. Derakhshankhah and S. Jafari, Cell penetrating peptides: A concise review with emphasis on biomedical applications, *Biomed. Pharmacother.*, 2018, **108**, 1090–1096.

148 S. Maslanka Figueroa, A. Veser, K. Abstiens, D. Fleischmann, S. Beck and A. Goepferich, Influenza A virus mimetic nanoparticles trigger selective cell uptake, *Proc. Natl. Acad. Sci.*, 2019, **116**, 9831–9836.

149 O. Livnah, E. A. Bayer, M. Wilchek and J. L. Sussman, Three-dimensional structures of avidin and the avidin-biotin complex, *Proc. Natl. Acad. Sci.*, 1993, **90**, 5076–5080.

150 J. Park, T. Mattessich, S. M. Jay, A. Agawu, W. M. Saltzman and T. M. Fahmy, Enhancement of surface ligand display on PLGA nanoparticles with amphiphilic ligand conjugates, *J. Control. Release*, 2011, **156**, 109–115.

151 P. D. Josephy, T. Eling and R. P. Mason, The Horseradish Peroxidase-catalyzed Oxidation of 3,5,3',5'- Tetramethylbenzidine, *J. Biol. Chem.*, 1982, **257**, 3669–4675.

152 K. J. Padiya, S. Gavade, B. Kardile, M. Tiwari, S. Bajare, M. Mane, V. Gaware, S. Varghese, D. Harel and S. Kurhade, Unprecedented 'in water' imidazole carbonylation: Paradigm shift for preparation of urea and carbamate, *Org. Lett.*, 2012, **14**, 2814–2817.

153 S. I. Presolski, V. P. Hong and M. G. Finn, Copper-Catalyzed Azide-Alkyne Click Chemistry for Bioconjugation, *Curr. Protoc. Chem. Biol.*, 2011, **3**, 153–162.

154 H. M. Gibbons and M. Dragunow, Adult human brain cell culture for neuroscience research, *Int. J. Biochem. Cell Biol.*, 2010, **42**, 844–856.

155 J. R. Lorsch, F. S. Collins and J. Lippincott-Schwartz, Fixing problems with cell lines, *Science (80-.).*, 2014, **346**, 1452–1453.

156 C. Pan, C. Kumar, S. Bohl, U. Klingmueller and M. Mann, Comparative Proteomic Phenotyping of Cell Lines and Primary Cells to Assess Preservation of Cell Type-specific Functions, *Mol. Cell. Proteomics*, 2009, **8**, 443–450.

157 E. C. Costa, A. F. Moreira, D. de Melo-Diogo, V. M. Gaspar, M. P. Carvalho and I. J. Correia, 3D tumor spheroids: an overview on the tools and techniques used for their analysis, *Biotechnol. Adv.*, 2016, **34**, 1427–1441.

158 H. H. Gustafson, D. Holt-Casper, D. W. Grainger and H. Ghandehari, Nanoparticle uptake: The phagocyte problem, *Nano Today*, 2015, **10**, 487–510.

159 H. Zhang, A. A. Jarjour, A. Boyd and A. Williams, Central nervous system remyelination in culture — A tool for multiple sclerosis research, *Exp. Neurol.*, 2011, **230**, 138–148.

160 C. Humpel, Neuroscience forefront review organotypic brain slice cultures: A review, *Neuroscience*, 2015, **305**, 86–98.

161 S. Cho, A. Wood and M. Bowlby, Brain Slices as Models for Neurodegenerative Disease and Screening Platforms to Identify Novel Therapeutics, *Curr. Neuropharmacol.*, 2007, **5**, 19–33.

162 V. M. Ravi, K. Joseph, J. Wurm, S. Behringer, N. Garrelfs, P. d' Errico, Y.

Naseri, P. Franco, M. Meyer-Luehmann, R. Sankowski, M. J. Shah, I. Mader, D. Delev, M. Follo, J. Beck, O. Schnell, U. G. Hofmann and D. H. Heiland, Human organotypic brain slice culture: a novel framework for environmental research in neuro-oncology, *Life Sci. Alliance*, 2019, **2**, 1–15.

163 Y. N. Zhang, W. Poon, A. J. Tavares, I. D. McGilvray and W. C. W. Chan, Nanoparticle–liver interactions: Cellular uptake and hepatobiliary elimination, *J. Control. Release*, 2016, **240**, 332–348.

164 C. Readhead and L. Hood, The dysmyelinating mouse mutations shiverer (shi) and myelin deficient (shimld), *Behav. Genet.*, 1990, **20**, 213–234.

165 A. Denic, A. J. Johnson, A. J. Bieber, A. E. Warrington, M. Rodriguez and I. Pirko, The relevance of animal models in multiple sclerosis research, *Pathophysiology*, 2011, **18**, 1–16.

166 H. H. Sachs, K. K. Bercury, D. C. Popescu, S. P. Narayanan and W. B. Macklin, A new model of Cuprizone-Mediated demyelination/remyelination, *ASN Neuro*, 2014, **6**, 1–16.

167 J. R. Plemel, N. J. Michaels, N. Weishaupt, A. V. Caprariello, M. B. Keough, J. A. Rogers, A. Yukseloglu, J. Lim, V. V. Patel, K. S. Rawji, S. K. Jensen, W. Teo, B. Heyne, S. N. Whitehead, P. K. Stys and V. W. Yong, Mechanisms of lysophosphatidylcholine-induced demyelination: A primary lipid disrupting myelinopathy, *Glia*, 2017, **66**, 327–347.

168 Y. Wang, Y. Mei, D. Feng and L. Xu, Triptolide modulates T-cell inflammatory responses and ameliorates experimental autoimmune encephalomyelitis, *J. Neurosci. Res.*, 2008, **86**, 2441–2449.

169 D. Pappalardo, T. Mathisen and A. Finne-Wistrand, Biocompatibility of Resorbable Polymers: A Historical Perspective and Framework for the Future, *Biomacromolecules*, 2019, **20**, 1465–1477.

170 R. Hannah, M. Beck, R. Moravec and T. Riss, CellTiter-Glo Luminescent Cell Viability Assay: A Sensitive and Rapid Method for Dtermining Cell Vaibility, *Cell Notes*, 2001, 11–13.

171 F.-K. Lu, S. Basu, V. Igras, M. P. Hoang, M. Ji, D. Fu, G. R. Holtom, V. A. Neel, C. W. Freudiger, D. E. Fisher and X. S. Xie, Label-free DNA imaging in vivo

with stimulated Raman scattering microscopy, *Proc. Natl. Acad. Sci.*, 2015, **112**, 11624–11629.

172 J. Schindelin, I. Arganda-Carreras, E. Frise, V. Kaynig, M. Longair, T. Pietzsch, S. Preibisch, C. Rueden, S. Saalfeld, B. Schmid, J. Y. Tinevez, D. J. White, V. Hartenstein, K. Eliceiri, P. Tomancak and A. Cardona, Fiji: An open-source platform for biological-image analysis, *Nat. Methods*, 2012, **9**, 676–682.

173 D. Zhang, M. N. Slipchenko, D. E. Leaird, A. M. Weiner and J.-X. Cheng, Spectrally modulated stimulated Raman scattering imaging with an angle-to-wavelength pulse shaper, *Opt. Express*, 2013, **21**, 13864–13874.

174 R. Smith, K. L. Wright and L. Ashton, Raman spectroscopy: An evolving technique for live cell studies, *Analyst*, 2016, **141**, 3590–3600.

175 B. Stansley, J. Post and K. Hensley, A comparative review of cell culture systems for the study of microglial biology in Alzheimer's disease, *J. Neuroinflammation*, 2012, **9**, 1–8.

176 D. J. Loane and K. R. Byrnes, Role of Microglia in Neurotrauma, *Neurotherapeutics*, 2010, **7**, 366–377.

177 T. T. Tamashiro, C. L. Dalgard and K. R. Byrnes, Primary Microglia Isolation from Mixed Glial Cell Cultures of Neonatal Rat Brain Tissue, *J. Vis. Exp.*, 2012, 1–5.

178 K. Ohsawa, Y. Imai, Y. Sasaki and S. Kohsaka, Microglia/macrophage-specific protein Iba1 binds to fimbrin and enhances its actin-bundling activity, *J. Neurochem.*, 2004, **88**, 844–856.

179 R. M. Dayam and R. J. Botelho, in *Phagocytosis and Phagosomes: Methods and Protocols*, ed. R. Botelho, Springer New York, New York, NY, 2017, pp. 113–123.

180 B. M. Geiger, L. E. Frank, A. D. Caldera-Siu and E. N. Pothos, Survivable Stereotaxic Surgery in Rodents, *J. Vis. Exp.*, 2008, **20**, 1–3.

181 L. R. Hanson and W. H. Frey, Intranasal delivery bypasses the blood-brain barrier to target therapeutic agents to the central nervous system and treat neurodegenerative disease, *BMC Neurosci.*, 2008, **9**, 1–4.

182 S. Talegaonkar and P. R. Mishra, Intranasal delivery: An approach to bypass

the blood brain barrier, *Indian J. Pharmacol.*, 2004, **36**, 140–147.

183 T. P. Crowe, M. H. W. Greenlee, A. G. Kanthasamy and W. H. Hsu, Mechanism of intranasal drug delivery directly to the brain, *Life Sci.*, 2018, **195**, 44–52.

184 J. Scafidi, T. R. Hammond, S. Scafidi, J. Ritter, B. Jablonska, M. Roncal, K. Szigeti-Buck, D. Coman, Y. Huang, R. J. McCarter, F. Hyder, T. L. Horvath and V. Gallo, Intranasal epidermal growth factor treatment rescues neonatal brain injury, *Nature*, 2014, **506**, 230–234.

185 P. Y. Gambaryan, I. G. Kondrasheva, E. S. Severin, A. A. Guseva and A. A. Kamensky, Increasing the Efficiency of Parkinson's Disease Treatment Using a poly(lactic-co-glycolic acid) (PLGA) Based L-DOPA Delivery System, *Exp. Neurobiol.*, 2014, **23**, 246–252.

186 U. Seju, A. Kumar and K. K. Sawant, Development and evaluation of olanzapine-loaded PLGA nanoparticles for nose-to-brain delivery: In vitro and in vivo studies, *Acta Biomater.*, 2011, **7**, 4169–4176.

187 S. Kaur, P. Manhas, A. Swami, R. Bhandari, K. K. Sharma, R. Jain, R. Kumar, S. K. Pandey, A. Kuhad, R. K. Sharma and N. Wangoo, Bioengineered PLGA-chitosan nanoparticles for brain targeted intranasal delivery of antiepileptic TRH analogues, *Chem. Eng. J.*, 2018, **346**, 630–639.

188 C. Bi, A. Wang, Y. Chu, S. Liu, H. Mu, W. H. Liu, Z. M. Wu, K. Sun and Y. Li, Intranasal delivery of rotigotine to the brain with lactoferrin-modified PEG-PLGA nanoparticles for Parkinson's disease treatment, *Int. J. Nanomedicine*, 2016, **11**, 6547–6559.

189 M. Agrawal, S. Saraf, S. Saraf, S. G. Antimisiaris, M. B. Chougule, S. A. Shoyele and A. Alexander, Nose-to-brain drug delivery: An update on clinical challenges and progress towards approval of anti-Alzheimer drugs, *J. Control. Release*, 2018, **281**, 139–177.

190 C. Saraiva, C. Praça, R. Ferreira, T. Santos, L. Ferreira and L. Bernardino, Nanoparticle-mediated brain drug delivery: Overcoming blood-brain barrier to treat neurodegenerative diseases, *J. Control. Release*, 2016, **235**, 34–47.

191 W. J. Tipping, M. Lee, A. Serrels, V. G. Brunton and A. N. Hulme, Imaging drug uptake by bioorthogonal stimulated Raman scattering microscopy, *Chem. Sci.*,

2017, **8**, 5606–5615.

192 S. Manoochehri, B. Darvishi, G. Kamalinia, M. Amini, M. Fallah, S. N. Ostad, F. Atyabi and R. Dinarvand, Surface modification of PLGA nanoparticles via human serum albumin conjugation for controlled delivery of docetaxel, *DARU, J. Pharm. Sci.*, 2013, **21**, 1–10.

193 K. Chia, J. Mazzolini, M. Mione and D. Sieger, Tumor initiating cells induce cxcr4- mediated infiltration of pro-tumoral macrophages into the brain, *Elife*, 2018, **7**, 1–28.

194 G. J. Goldey, D. K. Roumis, L. L. Glickfeld, A. M. Kerlin, R. C. Reid, V. Bonin, D. P. Schafer and M. L. Andermann, Removable cranial windows for long-term imaging in awake mice, *Nat. Protoc.*, 2014, **9**, 2515–2538.

195 Y.-J. Zhao, T.-T. Yu, C. Zhang, Z. Li, Q.-M. Luo, T.-H. Xu and D. Zhu, Skull optical clearing window for in vivo imaging of the mouse cortex at synaptic resolution, *Light Sci. Appl.*, 2018, **7**, 1–9.

196 S. Hassan, G. Prakash, A. Bal Ozturk, S. Saghazadeh, M. Farhan Sohail, J. Seo, M. Remzi Dokmeci, Y. S. Zhang and A. Khademhosseini, Evolution and clinical translation of drug delivery nanomaterials, *Nano Today*, 2017, **15**, 91–106.

197 S. Shen, Y. Wu, Y. Liu and D. Wu, High drug-loading nanomedicines: Progress, current status, and prospects, *Int. J. Nanomedicine*, 2017, **12**, 4085–4109.

198 L. Pang, J. Qin, L. Han, W. Zhao, J. Liang, Z. Xie, P. Yang and J. Wang, Exploiting macrophages as targeted carrier to guide nanoparticles into glioma, *Oncotarget*, 2016, **7**, 37081–37091.

199 N. Mishra, N. P. Yadav, V. K. Rai, P. Sinha, K. S. Yadav, S. Jain and S. Arora, Efficient hepatic delivery of drugs: Novel strategies and their significance, *Biomed Res. Int.*, 2013, **2013**, 1–20.

200 Y. H. Bae and K. Park, Targeted drug delivery to tumors: Myths, reality and possibility, *J. Control. Release*, 2011, **153**, 198–205.

201 D. X. Medina, K. T. Householder, R. Ceton, T. Kovalik, J. M. Heffernan, R. V. Shankar, R. P. Bowser, R. J. Wechsler-Reya and R. W. Sirianni, Optical barcoding of PLGA for multispectral analysis of nanoparticle fate in vivo, *J.*

Control. Release, 2017, **253**, 172–182.

202 C. Gluchowski, T. E. Bischoff, M. E. Garst, L. J. Kaplan, S. W. Dietrich, A. S. Aswad, M. A. Gaffney, K. R. Aoki, C. Garcia and L. A. Wheeler, Synthesis of Chiral and Achiral Pyranenamine Derivatives. Potent Agents with Topical Ocular Antiallergic Activity, *J. Med. Chem.*, 1991, **34**, 392–397.

203 F. Ngadjeua, E. Braud, S. Saidjalolov, L. Iannazzo, D. Schnappinger, S. Ehrt, J. E. Hugonnet, D. Mengin-Lecreulx, D. Patin, M. Ethève-Quelquejeu, M. Fonvielle and M. Arthur, Critical Impact of Peptidoglycan Precursor Amidation on the Activity of L,D-Transpeptidases from Enterococcus faecium and Mycobacterium tuberculosis, *Chem. - A Eur. J.*, 2018, **24**, 5743–5747.

204 C. D. C. Erbetta, R. J. Alves, J. M. Resende, R. F. de S. Freitas and R. Geraldo de Sousa, Synthesis and Characterization of Poly(D,L-Lactide-co-Glycolide) Copolymer, *J. Biomater. Nanobiotechnol.*, 2012, **3**, 208–225.

205 G. Shen, H. Fang, Y. Song, A. A. Bielska, Z. Wang and J. S. A. Taylor, Phospholipid conjugate for intracellular delivery of peptide nucleic acids, *Bioconjug. Chem.*, 2009, **20**, 1729–1736.

206 K. D. McCarthy and J. de Vellis, Preparation of Separate Astroglial and Oligodendroglial Cell Cultures from Rat Cerebral Tissue, *J. Cell Biol.*, 1980, **85**, 890–902.

Appendices

Appendix 1 Common Abbreviations

A.U.	Arbitrary units
ATP	Adenosine triphosphate
BBB	Blood brain barrier
CARS	Coherent anti-Stokes Raman scattering
CNS	Central nervous system
CuAAC	Copper-catalysed azide-alkyne click
Đ	Dispersity
DCM	Dichloromethane
DLS	Dynamic light scattering
DMAP	4-dimethylaminopyridine
DMEM	Dulbecco’s modified Eagle’s medium
DMSO	Dimethyl sulfoxide
DOX	1,3-Dioxolan-4-ones
EDC	1-Ethyl-3-(3-dimethylaminopropyl)carbodiimide
EdU	5’-Ethynyl-2’-deoxyuridine
EGFR	Epidermal growth factor receptor
GPC	Gel permeation chromatography
HRP	Horseradish peroxidase
LIF	Leukaemia inhibitory factor
MS	Multiple sclerosis
NG2	Neural / glial antigen 2
NMR	Nuclear magnetic resonance
NPs	Nanoparticles

NTA	Nanoparticle tracking analysis
OPCs	Oligodendrocyte precursor cells
PCA	Principal component analysis
PdI	Polydispersity index
PGA	Poly(glycolic acid)
PLA	Poly(lactic acid)
PLGA	Poly(lactic acid-*co*-glycolic acid)
PPE	Poly(phenylene ethynylene)
ROP	Ring opening polymerisation
SEM	Scanning electron microscopy
SERS	Surface enhanced Raman spectroscopy
SRG	Stimulated Raman gain
SRL	Stimulated Raman loss
SRS	Stimulated Raman scattering
TEM	Transmission electron microscopy
THPTA	Tris(3-hydroxypropyltriazolylmethyl)amine
TLC	Thin layer chromatography
TMB	Tetramethylbenzidine
TPF	Two photon fluorescence
UPLC	Ultra-performance liquid chromatography
VCA	Vertex component analysis

Appendix 2 Chemical Structures of Small Molecule Drugs

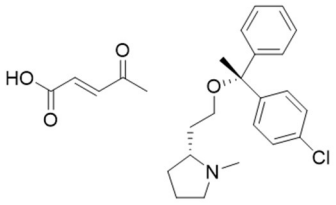

Clemastine fumarate

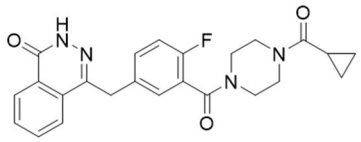

Olaparib

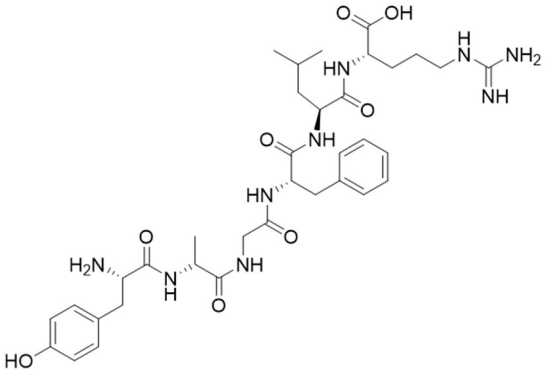

Dalargin

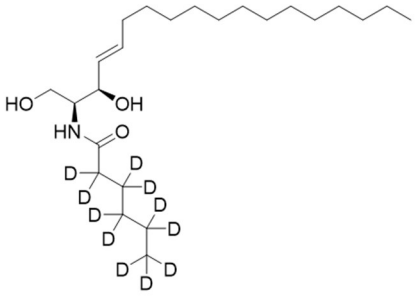

C6-Ceramide-d_{11}

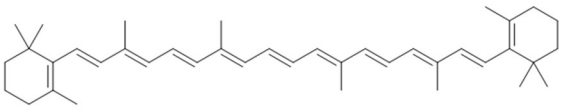

β-Carotene

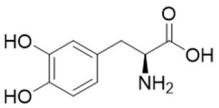

L-DOPA

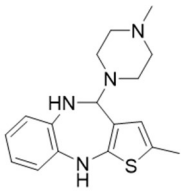

Olanzapine

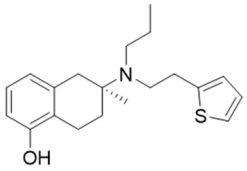

Rotigotine

Appendix 3 Chemical Structures of Polymers

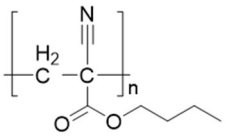

Poly(butylcyanoacrylate)

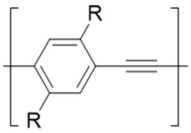

Poly(phenylene ethynylene)

Copyright Clearance Center RightsLink®

Home Account Info Help LIVE CHAT

Title:	Resonance Raman Spectral Imaging of Intracellular Uptake of β-Carotene Loaded Poly(D,L-lactide-co-glycolide) Nanoparticles
Author:	Christian Matthäus, Stephanie Schubert, Michael Schmitt, et al
Publication:	ChemPhysChem
Publisher:	John Wiley and Sons
Date:	Oct 12, 2012

© WILEY-VCH Verlag GmbH & Co. KGaA, Weinheim

Logged in as:
Sally Vanden-Hehir
Account #: 3001395483
LOGOUT

Order Completed

Thank you for your order.

This Agreement between Ms. Sally Vanden-Hehir ("You") and John Wiley and Sons ("John Wiley and Sons") consists of your license details and the terms and conditions provided by John Wiley and Sons and Copyright Clearance Center.

Your confirmation email will contain your order number for future reference.

printable details

License Number	4613111013841
License date	Jun 20, 2019
Licensed Content Publisher	John Wiley and Sons
Licensed Content Publication	ChemPhysChem
Licensed Content Title	Resonance Raman Spectral Imaging of Intracellular Uptake of β-Carotene Loaded Poly(D,L-lactide-co-glycolide) Nanoparticles
Licensed Content Author	Christian Matthäus, Stephanie Schubert, Michael Schmitt, et al
Licensed Content Date	Oct 12, 2012
Licensed Content Volume	14
Licensed Content Issue	1
Licensed Content Pages	7
Type of use	Dissertation/Thesis
Requestor type	University/Academic
Format	Print and electronic
Portion	Figure/table
Number of figures/tables	1
Original Wiley figure/table number(s)	figure 4
Will you be translating?	No
Title of your thesis / dissertation	New tools for visualising nanoparticle drug delivery
Expected completion date	Aug 2019
Expected size (number of pages)	150
Requestor Location	Ms. Sally Vanden-Hehir Office 54 Joseph Black Building David Brewster Road The King' Buildings Edinburgh, EH9 3FJ United Kingdom Attn: Ms. Sally Vanden-Hehir

Publisher Tax ID	EU826007151
Total	0.00 GBP

Would you like to purchase the full text of this article? If so, please continue on to the content ordering system located here: Purchase PDF

If you click on the buttons below or close this window, you will not be able to return to the content ordering system.

ORDER MORE CLOSE WINDOW

Copyright © 2019 Copyright Clearance Center, Inc. All Rights Reserved. Privacy statement. Terms and Conditions.
Comments? We would like to hear from you. E-mail us at customercare@copyright.com

Copyright Clearance Center RightsLink®

Home Account Info Help LIVE CHAT

ACS Publications Most Trusted. Most Cited. Most Read.

Title: Label-Free Raman Spectral Imaging of Intracellular Delivery and Degradation of Polymeric Nanoparticle Systems

Author: Tatyana Chernenko, Christian Matthäus, Lara Milane, et al

Publication: ACS Nano

Publisher: American Chemical Society

Date: Nov 1, 2009

Copyright © 2009, American Chemical Society

Logged in as:
Sally Vanden-Hehir
Account #:
3001395483

LOGOUT

PERMISSION/LICENSE IS GRANTED FOR YOUR ORDER AT NO CHARGE

This type of permission/license, instead of the standard Terms & Conditions, is sent to you because no fee is being charged for your order. Please note the following:

- Permission is granted for your request in both print and electronic formats, and translations.
- If figures and/or tables were requested, they may be adapted or used in part.
- Please print this page for your records and send a copy of it to your publisher/graduate school.
- Appropriate credit for the requested material should be given as follows: "Reprinted (adapted) with permission from (COMPLETE REFERENCE CITATION). Copyright (YEAR) American Chemical Society." Insert appropriate information in place of the capitalized words.
- One-time permission is granted only for the use specified in your request. No additional uses are granted (such as derivative works or other editions). For any other uses, please submit a new request.

If credit is given to another source for the material you requested, permission must be obtained from that source.

BACK CLOSE WINDOW

Copyright © 2019 Copyright Clearance Center, Inc. All Rights Reserved. Privacy statement. Terms and Conditions.
Comments? We would like to hear from you. E-mail us at customercare@copyright.com

Copyright Clearance Center RightsLink®

Home Account Info Help LIVE CHAT

ACS Publications Most Trusted. Most Cited. Most Read.

Title:	Raman Imaging of PLGA Microsphere Degradation Inside Macrophages
Author:	Aart A. van Apeldoorn, Henk-Jan van Manen, Jeroen M. Bezemer, et al
Publication:	Journal of the American Chemical Society
Publisher:	American Chemical Society
Date:	Oct 1, 2004

Copyright © 2004, American Chemical Society

Logged in as:
Sally Vanden-Hehir
Account #:
3001395483

LOGOUT

PERMISSION/LICENSE IS GRANTED FOR YOUR ORDER AT NO CHARGE

This type of permission/license, instead of the standard Terms & Conditions, is sent to you because no fee is being charged for your order. Please note the following:

- Permission is granted for your request in both print and electronic formats, and translations.
- If figures and/or tables were requested, they may be adapted or used in part.
- Please print this page for your records and send a copy of it to your publisher/graduate school.
- Appropriate credit for the requested material should be given as follows: "Reprinted (adapted) with permission from (COMPLETE REFERENCE CITATION). Copyright (YEAR) American Chemical Society." Insert appropriate information in place of the capitalized words.
- One-time permission is granted only for the use specified in your request. No additional uses are granted (such as derivative works or other editions). For any other uses, please submit a new request.

If credit is given to another source for the material you requested, permission must be obtained from that source.

BACK CLOSE WINDOW

Copyright © 2019 Copyright Clearance Center, Inc. All Rights Reserved. Privacy statement. Terms and Conditions.
Comments? We would like to hear from you. E-mail us at customercare@copyright.com

Copyright Clearance Center RightsLink®

Home Account Info Help LIVE CHAT

SPRINGER NATURE

Title:	Live-cell imaging of alkyne-tagged small biomolecules by stimulated Raman scattering
Author:	Lu Wei, Fanghao Hu, Yihui Shen, Zhixing Chen, Yong Yu et al.
Publication:	Nature Methods
Publisher:	Springer Nature
Date:	Mar 2, 2014

Copyright © 2014, Springer Nature

Logged in as:
Sally Vanden-Hehir
Account #:
3001395483
LOGOUT

Order Completed

Thank you for your order.

This Agreement between Ms. Sally Vanden-Hehir ("You") and Springer Nature ("Springer Nature") consists of your license details and the terms and conditions provided by Springer Nature and Copyright Clearance Center.

Your confirmation email will contain your order number for future reference.

printable details

License Number	4611400568070
License date	Jun 17, 2019
Licensed Content Publisher	Springer Nature
Licensed Content Publication	Nature Methods
Licensed Content Title	Live-cell imaging of alkyne-tagged small biomolecules by stimulated Raman scattering
Licensed Content Author	Lu Wei, Fanghao Hu, Yihui Shen, Zhixing Chen, Yong Yu et al.
Licensed Content Date	Mar 2, 2014
Licensed Content Volume	11
Licensed Content Issue	4
Type of Use	Thesis/Dissertation
Requestor type	academic/university or research institute
Format	print and electronic
Portion	figures/tables/illustrations
Number of figures/tables/illustrations	1
High-res required	no
Will you be translating?	no
Circulation/distribution	<501
Author of this Springer Nature content	no
Title	New tools for visualising nanoparticle drug delivery
Institution name	n/a
Expected presentation date	Aug 2019
Portions	Figure 2
Requestor Location	Ms. Sally Vanden-Hehir Office 54 Joseph Black Building David Brewster Road The King' Buildings Edinburgh, EH9 3FJ United Kingdom Attn: Ms. Sally Vanden-Hehir
Total	0.00 GBP

ORDER MORE CLOSE WINDOW

Copyright © 2019 Copyright Clearance Center, Inc. All Rights Reserved. Privacy statement. Terms and Conditions.
Comments? We would like to hear from you. E-mail us at customercare@copyright.com

Copyright Clearance Center RightsLink® Home Account Info Help LIVE CHAT

Title:	Fluorescent Polymer Nanoparticles for Cell Barcoding In Vitro and In Vivo
Author:	Bohdan Andreiuk, Andreas Reisch, Marion Lindecker, et al
Publication:	Small
Publisher:	John Wiley and Sons
Date:	Aug 9, 2017

© WILEY-VCH Verlag GmbH & Co. KGaA, Weinheim

Logged in as:
Sally Vanden-Hehir
Account #:
3001395483
LOGOUT

Order Completed

Thank you for your order.

This Agreement between Ms. Sally Vanden-Hehir ("You") and John Wiley and Sons ("John Wiley and Sons") consists of your license details and the terms and conditions provided by John Wiley and Sons and Copyright Clearance Center.

Your confirmation email will contain your order number for future reference.

printable details

License Number	4612550212027
License date	Jun 19, 2019
Licensed Content Publisher	John Wiley and Sons
Licensed Content Publication	Small
Licensed Content Title	Fluorescent Polymer Nanoparticles for Cell Barcoding In Vitro and In Vivo
Licensed Content Author	Bohdan Andreiuk, Andreas Reisch, Marion Lindecker, et al
Licensed Content Date	Aug 9, 2017
Licensed Content Volume	13
Licensed Content Issue	38
Licensed Content Pages	13
Type of use	Dissertation/Thesis
Requestor type	University/Academic
Format	Print and electronic
Portion	Figure/table
Number of figures/tables	2
Original Wiley figure/table number(s)	Figure 5 Figure 6
Will you be translating?	No
Title of your thesis / dissertation	New tools for visualising nanoparticle drug delivery
Expected completion date	Aug 2019
Expected size (number of pages)	150
Requestor Location	Ms. Sally Vanden-Hehir Office 54 Joseph Black Building David Brewster Road The King' Buildings Edinburgh, EH9 3FJ United Kingdom Attn: Ms. Sally Vanden-Hehir
Publisher Tax ID	EU826007151
Total	0.00 GBP

Would you like to purchase the full text of this article? If so, please continue on to the content ordering system located here: Purchase PDF

If you click on the buttons below or close this window, you will not be able to return to the content ordering system.

ORDER MORE CLOSE WINDOW

Copyright © 2019 Copyright Clearance Center, Inc. All Rights Reserved. Privacy statement. Terms and Conditions.
Comments? We would like to hear from you. E-mail us at customercare@copyright.com

JOHN WILEY AND SONS LICENSE TERMS AND CONDITIONS

Jun 17, 2019

This Agreement between Ms. Sally Vanden-Hehir ("You") and John Wiley and Sons ("John Wiley and Sons") consists of your license details and the terms and conditions provided by John Wiley and Sons and Copyright Clearance Center.

License Number	4611390638326
License date	Jun 17, 2019
Licensed Content Publisher	John Wiley and Sons
Licensed Content Publication	Angewandte Chemie International Edition
Licensed Content Title	Vibrational Imaging of Glucose Uptake Activity in Live Cells and Tissues by Stimulated Raman Scattering
Licensed Content Author	Fanghao Hu, Zhixing Chen, Luyuan Zhang, et al
Licensed Content Date	Jul 16, 2015
Licensed Content Volume	54
Licensed Content Issue	34
Licensed Content Pages	5
Type of use	Dissertation/Thesis
Requestor type	University/Academic
Format	Print and electronic
Portion	Figure/table
Number of figures/tables	1
Original Wiley figure/table number(s)	Figure 5
Will you be translating?	No
Title of your thesis / dissertation	New tools for visualising nanoparticle drug delivery
Expected completion date	Aug 2019
Expected size (number of pages)	150
Requestor Location	Ms. Sally Vanden-Hehir Office 54 Joseph Black Building David Brewster Road The King' Buildings Edinburgh, EH9 3FJ United Kingdom Attn: Ms. Sally Vanden-Hehir
Publisher Tax ID	EU826007151
Total	0.00 GBP
Terms and Conditions	

TERMS AND CONDITIONS

This copyrighted material is owned by or exclusively licensed to John Wiley & Sons, Inc. or one of its group companies (each a"Wiley Company") or handled on behalf of a society with which a Wiley Company has exclusive publishing rights in relation to a particular work (collectively "WILEY"). By clicking "accept" in connection with completing this licensing transaction, you agree that the following terms and conditions apply to this transaction (along with the billing and payment terms and conditions established by the Copyright

Clearance Center Inc., ("CCC's Billing and Payment terms and conditions"), at the time that you opened your RightsLink account (these are available at any time at http://myaccount.copyright.com).

Terms and Conditions

- The materials you have requested permission to reproduce or reuse (the "Wiley Materials") are protected by copyright.

- You are hereby granted a personal, non-exclusive, non-sub licensable (on a stand-alone basis), non-transferable, worldwide, limited license to reproduce the Wiley Materials for the purpose specified in the licensing process. This license, **and any CONTENT (PDF or image file) purchased as part of your order,** is for a one-time use only and limited to any maximum distribution number specified in the license. The first instance of republication or reuse granted by this license must be completed within two years of the date of the grant of this license (although copies prepared before the end date may be distributed thereafter). The Wiley Materials shall not be used in any other manner or for any other purpose, beyond what is granted in the license. Permission is granted subject to an appropriate acknowledgement given to the author, title of the material/book/journal and the publisher. You shall also duplicate the copyright notice that appears in the Wiley publication in your use of the Wiley Material. Permission is also granted on the understanding that nowhere in the text is a previously published source acknowledged for all or part of this Wiley Material. Any third party content is expressly excluded from this permission.

- With respect to the Wiley Materials, all rights are reserved. Except as expressly granted by the terms of the license, no part of the Wiley Materials may be copied, modified, adapted (except for minor reformatting required by the new Publication), translated, reproduced, transferred or distributed, in any form or by any means, and no derivative works may be made based on the Wiley Materials without the prior permission of the respective copyright owner.**For STM Signatory Publishers clearing permission under the terms of the STM Permissions Guidelines only, the terms of the license are extended to include subsequent editions and for editions in other languages, provided such editions are for the work as a whole in situ and does not involve the separate exploitation of the permitted figures or extracts,** You may not alter, remove or suppress in any manner any copyright, trademark or other notices displayed by the Wiley Materials. You may not license, rent, sell, loan, lease, pledge, offer as security, transfer or assign the Wiley Materials on a stand-alone basis, or any of the rights granted to you hereunder to any other person.

- The Wiley Materials and all of the intellectual property rights therein shall at all times remain the exclusive property of John Wiley & Sons Inc, the Wiley Companies, or their respective licensors, and your interest therein is only that of having possession of and the right to reproduce the Wiley Materials pursuant to Section 2 herein during the continuance of this Agreement. You agree that you own no right, title or interest in or to the Wiley Materials or any of the intellectual property rights therein. You shall have no rights hereunder other than the license as provided for above in Section 2. No right, license or interest to any trademark, trade name, service mark or other branding ("Marks") of WILEY or its licensors is granted hereunder, and you agree that you shall not assert any such right, license or interest with respect thereto

- NEITHER WILEY NOR ITS LICENSORS MAKES ANY WARRANTY OR REPRESENTATION OF ANY KIND TO YOU OR ANY THIRD PARTY, EXPRESS, IMPLIED OR STATUTORY, WITH RESPECT TO THE MATERIALS OR THE ACCURACY OF ANY INFORMATION CONTAINED IN THE MATERIALS, INCLUDING, WITHOUT LIMITATION, ANY IMPLIED WARRANTY OF MERCHANTABILITY, ACCURACY, SATISFACTORY QUALITY, FITNESS FOR A PARTICULAR PURPOSE, USABILITY,

INTEGRATION OR NON-INFRINGEMENT AND ALL SUCH WARRANTIES ARE HEREBY EXCLUDED BY WILEY AND ITS LICENSORS AND WAIVED BY YOU.

- WILEY shall have the right to terminate this Agreement immediately upon breach of this Agreement by you.

- You shall indemnify, defend and hold harmless WILEY, its Licensors and their respective directors, officers, agents and employees, from and against any actual or threatened claims, demands, causes of action or proceedings arising from any breach of this Agreement by you.

- IN NO EVENT SHALL WILEY OR ITS LICENSORS BE LIABLE TO YOU OR ANY OTHER PARTY OR ANY OTHER PERSON OR ENTITY FOR ANY SPECIAL, CONSEQUENTIAL, INCIDENTAL, INDIRECT, EXEMPLARY OR PUNITIVE DAMAGES, HOWEVER CAUSED, ARISING OUT OF OR IN CONNECTION WITH THE DOWNLOADING, PROVISIONING, VIEWING OR USE OF THE MATERIALS REGARDLESS OF THE FORM OF ACTION, WHETHER FOR BREACH OF CONTRACT, BREACH OF WARRANTY, TORT, NEGLIGENCE, INFRINGEMENT OR OTHERWISE (INCLUDING, WITHOUT LIMITATION, DAMAGES BASED ON LOSS OF PROFITS, DATA, FILES, USE, BUSINESS OPPORTUNITY OR CLAIMS OF THIRD PARTIES), AND WHETHER OR NOT THE PARTY HAS BEEN ADVISED OF THE POSSIBILITY OF SUCH DAMAGES. THIS LIMITATION SHALL APPLY NOTWITHSTANDING ANY FAILURE OF ESSENTIAL PURPOSE OF ANY LIMITED REMEDY PROVIDED HEREIN.

- Should any provision of this Agreement be held by a court of competent jurisdiction to be illegal, invalid, or unenforceable, that provision shall be deemed amended to achieve as nearly as possible the same economic effect as the original provision, and the legality, validity and enforceability of the remaining provisions of this Agreement shall not be affected or impaired thereby.

- The failure of either party to enforce any term or condition of this Agreement shall not constitute a waiver of either party's right to enforce each and every term and condition of this Agreement. No breach under this agreement shall be deemed waived or excused by either party unless such waiver or consent is in writing signed by the party granting such waiver or consent. The waiver by or consent of a party to a breach of any provision of this Agreement shall not operate or be construed as a waiver of or consent to any other or subsequent breach by such other party.

- This Agreement may not be assigned (including by operation of law or otherwise) by you without WILEY's prior written consent.

- Any fee required for this permission shall be non-refundable after thirty (30) days from receipt by the CCC.

- These terms and conditions together with CCC's Billing and Payment terms and conditions (which are incorporated herein) form the entire agreement between you and WILEY concerning this licensing transaction and (in the absence of fraud) supersedes all prior agreements and representations of the parties, oral or written. This Agreement may not be amended except in writing signed by both parties. This Agreement shall be binding upon and inure to the benefit of the parties' successors, legal representatives, and authorized assigns.

- In the event of any conflict between your obligations established by these terms and conditions and those established by CCC's Billing and Payment terms and conditions,

these terms and conditions shall prevail.

- WILEY expressly reserves all rights not specifically granted in the combination of (i) the license details provided by you and accepted in the course of this licensing transaction, (ii) these terms and conditions and (iii) CCC's Billing and Payment terms and conditions.

- This Agreement will be void if the Type of Use, Format, Circulation, or Requestor Type was misrepresented during the licensing process.

- This Agreement shall be governed by and construed in accordance with the laws of the State of New York, USA, without regards to such state's conflict of law rules. Any legal action, suit or proceeding arising out of or relating to these Terms and Conditions or the breach thereof shall be instituted in a court of competent jurisdiction in New York County in the State of New York in the United States of America and each party hereby consents and submits to the personal jurisdiction of such court, waives any objection to venue in such court and consents to service of process by registered or certified mail, return receipt requested, at the last known address of such party.

WILEY OPEN ACCESS TERMS AND CONDITIONS

Wiley Publishes Open Access Articles in fully Open Access Journals and in Subscription journals offering Online Open. Although most of the fully Open Access journals publish open access articles under the terms of the Creative Commons Attribution (CC BY) License only, the subscription journals and a few of the Open Access Journals offer a choice of Creative Commons Licenses. The license type is clearly identified on the article.

The Creative Commons Attribution License

The Creative Commons Attribution License (CC-BY) allows users to copy, distribute and transmit an article, adapt the article and make commercial use of the article. The CC-BY license permits commercial and non-

Creative Commons Attribution Non-Commercial License

The Creative Commons Attribution Non-Commercial (CC-BY-NC)License permits use, distribution and reproduction in any medium, provided the original work is properly cited and is not used for commercial purposes.(see below)

Creative Commons Attribution-Non-Commercial-NoDerivs License

The Creative Commons Attribution Non-Commercial-NoDerivs License (CC-BY-NC-ND) permits use, distribution and reproduction in any medium, provided the original work is properly cited, is not used for commercial purposes and no modifications or adaptations are made. (see below)

Use by commercial "for-profit" organizations

Use of Wiley Open Access articles for commercial, promotional, or marketing purposes requires further explicit permission from Wiley and will be subject to a fee.

Further details can be found on Wiley Online Library

http://olabout.wiley.com/WileyCDA/Section/id-410895.html

Other Terms and Conditions:

v1.10 Last updated September 2015

Questions? customercare@copyright.com or +1-855-239-3415 (toll free in the US) or +1-978-646-2777.

Copyright Clearance Center RightsLink®

Home Account Info Help LIVE CHAT

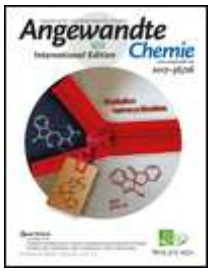

Title:	Raman Microspectroscopic Evidence for the Metabolism of a Tyrosine Kinase Inhibitor, Neratinib, in Cancer Cells
Author:	Karim Aljakouch, Tatjana Lechtonen, Hesham K. Yosef, et al
Publication:	Angewandte Chemie International Edition
Publisher:	John Wiley and Sons
Date:	May 16, 2018

© WILEY-VCH Verlag GmbH & Co. KGaA, Weinheim

Logged in as:
Sally Vanden-Hehir
Account #:
3001395483

LOGOUT

Open Access Article

This article is available under the terms of the Creative Commons Attribution Non-Commercial No Derivatives License CC BY-NC-ND (which may be updated from time to time) and permits **non-commercial** use, distribution, and reproduction in any medium, without alteration, provided the original work is properly cited and it is reproduced verbatim.

For an understanding of what is meant by the terms of the Creative Commons License, please refer to Wiley's Open Access Terms and Conditions.

Permission is not required for **non-commercial** reuse. For **commercial** reuse, please hit the "back" button and select the most appropriate **commercial** requestor type before completing your order.

If you wish to adapt, alter, translate or create any other derivative work from this article, permission must be sought from the Publisher. Please email your requirements to RightsLink@wiley.com.

BACK CLOSE WINDOW

Copyright © 2019 Copyright Clearance Center, Inc. All Rights Reserved. Privacy statement. Terms and Conditions.
Comments? We would like to hear from you. E-mail us at customercare@copyright.com

Copyright Clearance Center RightsLink®

Home Account Info Help LIVE CHAT

Title:	Resonance Raman Spectral Imaging of Intracellular Uptake of β-Carotene Loaded Poly(D,L-lactide-co-glycolide) Nanoparticles
Author:	Christian Matthäus, Stephanie Schubert, Michael Schmitt, et al
Publication:	ChemPhysChem
Publisher:	John Wiley and Sons
Date:	Oct 12, 2012

© WILEY-VCH Verlag GmbH & Co. KGaA, Weinheim

Logged in as:
Sally Vanden-Hehir
Account #: 3001395483
LOGOUT

Order Completed

Thank you for your order.

This Agreement between Ms. Sally Vanden-Hehir ("You") and John Wiley and Sons ("John Wiley and Sons") consists of your license details and the terms and conditions provided by John Wiley and Sons and Copyright Clearance Center.

Your confirmation email will contain your order number for future reference.

printable details

License Number	4613111013841
License date	Jun 20, 2019
Licensed Content Publisher	John Wiley and Sons
Licensed Content Publication	ChemPhysChem
Licensed Content Title	Resonance Raman Spectral Imaging of Intracellular Uptake of β-Carotene Loaded Poly(D,L-lactide-co-glycolide) Nanoparticles
Licensed Content Author	Christian Matthäus, Stephanie Schubert, Michael Schmitt, et al
Licensed Content Date	Oct 12, 2012
Licensed Content Volume	14
Licensed Content Issue	1
Licensed Content Pages	7
Type of use	Dissertation/Thesis
Requestor type	University/Academic
Format	Print and electronic
Portion	Figure/table
Number of figures/tables	1
Original Wiley figure/table number(s)	figure 4
Will you be translating?	No
Title of your thesis / dissertation	New tools for visualising nanoparticle drug delivery
Expected completion date	Aug 2019
Expected size (number of pages)	150
Requestor Location	Ms. Sally Vanden-Hehir Office 54 Joseph Black Building David Brewster Road The King' Buildings Edinburgh, EH9 3FJ United Kingdom Attn: Ms. Sally Vanden-Hehir

Publisher Tax ID	EU826007151
Total	0.00 GBP

Would you like to purchase the full text of this article? If so, please continue on to the content ordering system located here: Purchase PDF

If you click on the buttons below or close this window, you will not be able to return to the content ordering system.

ORDER MORE CLOSE WINDOW

Copyright © 2019 Copyright Clearance Center, Inc. All Rights Reserved. Privacy statement. Terms and Conditions.
Comments? We would like to hear from you. E-mail us at customercare@copyright.com

Copyright Clearance Center RightsLink®

Home Account Info Help LIVE CHAT

ACS Publications Most Trusted. Most Cited. Most Read.

Title: Label-Free Raman Spectral Imaging of Intracellular Delivery and Degradation of Polymeric Nanoparticle Systems

Author: Tatyana Chernenko, Christian Matthäus, Lara Milane, et al

Publication: ACS Nano

Publisher: American Chemical Society

Date: Nov 1, 2009

Copyright © 2009, American Chemical Society

Logged in as:
Sally Vanden-Hehir
Account #:
3001395483

LOGOUT

PERMISSION/LICENSE IS GRANTED FOR YOUR ORDER AT NO CHARGE

This type of permission/license, instead of the standard Terms & Conditions, is sent to you because no fee is being charged for your order. Please note the following:

- Permission is granted for your request in both print and electronic formats, and translations.
- If figures and/or tables were requested, they may be adapted or used in part.
- Please print this page for your records and send a copy of it to your publisher/graduate school.
- Appropriate credit for the requested material should be given as follows: "Reprinted (adapted) with permission from (COMPLETE REFERENCE CITATION). Copyright (YEAR) American Chemical Society." Insert appropriate information in place of the capitalized words.
- One-time permission is granted only for the use specified in your request. No additional uses are granted (such as derivative works or other editions). For any other uses, please submit a new request.

If credit is given to another source for the material you requested, permission must be obtained from that source.

BACK CLOSE WINDOW

Copyright © 2019 Copyright Clearance Center, Inc. All Rights Reserved. Privacy statement. Terms and Conditions.
Comments? We would like to hear from you. E-mail us at customercare@copyright.com

Copyright Clearance Center RightsLink®

Home Account Info Help LIVE CHAT

ACS Publications Most Trusted. Most Cited. Most Read.

Title:	Raman Imaging of PLGA Microsphere Degradation Inside Macrophages
Author:	Aart A. van Apeldoorn, Henk-Jan van Manen, Jeroen M. Bezemer, et al
Publication:	Journal of the American Chemical Society
Publisher:	American Chemical Society
Date:	Oct 1, 2004

Copyright © 2004, American Chemical Society

Logged in as:
Sally Vanden-Hehir
Account #:
3001395483

LOGOUT

PERMISSION/LICENSE IS GRANTED FOR YOUR ORDER AT NO CHARGE

This type of permission/license, instead of the standard Terms & Conditions, is sent to you because no fee is being charged for your order. Please note the following:

- Permission is granted for your request in both print and electronic formats, and translations.
- If figures and/or tables were requested, they may be adapted or used in part.
- Please print this page for your records and send a copy of it to your publisher/graduate school.
- Appropriate credit for the requested material should be given as follows: "Reprinted (adapted) with permission from (COMPLETE REFERENCE CITATION). Copyright (YEAR) American Chemical Society." Insert appropriate information in place of the capitalized words.
- One-time permission is granted only for the use specified in your request. No additional uses are granted (such as derivative works or other editions). For any other uses, please submit a new request.

If credit is given to another source for the material you requested, permission must be obtained from that source.

BACK CLOSE WINDOW

Copyright © 2019 Copyright Clearance Center, Inc. All Rights Reserved. Privacy statement. Terms and Conditions.
Comments? We would like to hear from you. E-mail us at customercare@copyright.com

Copyright Clearance Center RightsLink®

Home Account Info Help LIVE CHAT

SPRINGER NATURE

Title:	Live-cell imaging of alkyne-tagged small biomolecules by stimulated Raman scattering
Author:	Lu Wei, Fanghao Hu, Yihui Shen, Zhixing Chen, Yong Yu et al.
Publication:	Nature Methods
Publisher:	Springer Nature
Date:	Mar 2, 2014

Copyright © 2014, Springer Nature

Logged in as:
Sally Vanden-Hehir
Account #:
3001395483
LOGOUT

Order Completed

Thank you for your order.

This Agreement between Ms. Sally Vanden-Hehir ("You") and Springer Nature ("Springer Nature") consists of your license details and the terms and conditions provided by Springer Nature and Copyright Clearance Center.

Your confirmation email will contain your order number for future reference.

printable details

License Number	4611400568070
License date	Jun 17, 2019
Licensed Content Publisher	Springer Nature
Licensed Content Publication	Nature Methods
Licensed Content Title	Live-cell imaging of alkyne-tagged small biomolecules by stimulated Raman scattering
Licensed Content Author	Lu Wei, Fanghao Hu, Yihui Shen, Zhixing Chen, Yong Yu et al.
Licensed Content Date	Mar 2, 2014
Licensed Content Volume	11
Licensed Content Issue	4
Type of Use	Thesis/Dissertation
Requestor type	academic/university or research institute
Format	print and electronic
Portion	figures/tables/illustrations
Number of figures/tables/illustrations	1
High-res required	no
Will you be translating?	no
Circulation/distribution	<501
Author of this Springer Nature content	no
Title	New tools for visualising nanoparticle drug delivery
Institution name	n/a
Expected presentation date	Aug 2019
Portions	Figure 2
Requestor Location	Ms. Sally Vanden-Hehir Office 54 Joseph Black Building David Brewster Road The King' Buildings Edinburgh, EH9 3FJ United Kingdom Attn: Ms. Sally Vanden-Hehir
Total	0.00 GBP

ORDER MORE CLOSE WINDOW

Copyright © 2019 Copyright Clearance Center, Inc. All Rights Reserved. Privacy statement. Terms and Conditions.
Comments? We would like to hear from you. E-mail us at customercare@copyright.com

Copyright Clearance Center RightsLink® Home Account Info Help LIVE CHAT

Title:	Fluorescent Polymer Nanoparticles for Cell Barcoding In Vitro and In Vivo
Author:	Bohdan Andreiuk, Andreas Reisch, Marion Lindecker, et al
Publication:	Small
Publisher:	John Wiley and Sons
Date:	Aug 9, 2017

© WILEY-VCH Verlag GmbH & Co. KGaA, Weinheim

Logged in as:
Sally Vanden-Hehir
Account #:
3001395483
LOGOUT

Order Completed

Thank you for your order.

This Agreement between Ms. Sally Vanden-Hehir ("You") and John Wiley and Sons ("John Wiley and Sons") consists of your license details and the terms and conditions provided by John Wiley and Sons and Copyright Clearance Center.

Your confirmation email will contain your order number for future reference.

printable details

License Number	4612550212027
License date	Jun 19, 2019
Licensed Content Publisher	John Wiley and Sons
Licensed Content Publication	Small
Licensed Content Title	Fluorescent Polymer Nanoparticles for Cell Barcoding In Vitro and In Vivo
Licensed Content Author	Bohdan Andreiuk, Andreas Reisch, Marion Lindecker, et al
Licensed Content Date	Aug 9, 2017
Licensed Content Volume	13
Licensed Content Issue	38
Licensed Content Pages	13
Type of use	Dissertation/Thesis
Requestor type	University/Academic
Format	Print and electronic
Portion	Figure/table
Number of figures/tables	2
Original Wiley figure/table number(s)	Figure 5 Figure 6
Will you be translating?	No
Title of your thesis / dissertation	New tools for visualising nanoparticle drug delivery
Expected completion date	Aug 2019
Expected size (number of pages)	150
Requestor Location	Ms. Sally Vanden-Hehir Office 54 Joseph Black Building David Brewster Road The King' Buildings Edinburgh, EH9 3FJ United Kingdom Attn: Ms. Sally Vanden-Hehir
Publisher Tax ID	EU826007151
Total	0.00 GBP

Would you like to purchase the full text of this article? If so, please continue on to the content ordering system located here: Purchase PDF

If you click on the buttons below or close this window, you will not be able to return to the content ordering system.

ORDER MORE CLOSE WINDOW

Copyright © 2019 Copyright Clearance Center, Inc. All Rights Reserved. Privacy statement. Terms and Conditions.
Comments? We would like to hear from you. E-mail us at customercare@copyright.com

JOHN WILEY AND SONS LICENSE TERMS AND CONDITIONS

Jun 17, 2019

This Agreement between Ms. Sally Vanden-Hehir ("You") and John Wiley and Sons ("John Wiley and Sons") consists of your license details and the terms and conditions provided by John Wiley and Sons and Copyright Clearance Center.

License Number	4611390638326
License date	Jun 17, 2019
Licensed Content Publisher	John Wiley and Sons
Licensed Content Publication	Angewandte Chemie International Edition
Licensed Content Title	Vibrational Imaging of Glucose Uptake Activity in Live Cells and Tissues by Stimulated Raman Scattering
Licensed Content Author	Fanghao Hu, Zhixing Chen, Luyuan Zhang, et al
Licensed Content Date	Jul 16, 2015
Licensed Content Volume	54
Licensed Content Issue	34
Licensed Content Pages	5
Type of use	Dissertation/Thesis
Requestor type	University/Academic
Format	Print and electronic
Portion	Figure/table
Number of figures/tables	1
Original Wiley figure/table number(s)	Figure 5
Will you be translating?	No
Title of your thesis / dissertation	New tools for visualising nanoparticle drug delivery
Expected completion date	Aug 2019
Expected size (number of pages)	150
Requestor Location	Ms. Sally Vanden-Hehir Office 54 Joseph Black Building David Brewster Road The King' Buildings Edinburgh, EH9 3FJ United Kingdom Attn: Ms. Sally Vanden-Hehir
Publisher Tax ID	EU826007151
Total	0.00 GBP
Terms and Conditions	

TERMS AND CONDITIONS

This copyrighted material is owned by or exclusively licensed to John Wiley & Sons, Inc. or one of its group companies (each a"Wiley Company") or handled on behalf of a society with which a Wiley Company has exclusive publishing rights in relation to a particular work (collectively "WILEY"). By clicking "accept" in connection with completing this licensing transaction, you agree that the following terms and conditions apply to this transaction (along with the billing and payment terms and conditions established by the Copyright

Clearance Center Inc., ("CCC's Billing and Payment terms and conditions"), at the time that you opened your RightsLink account (these are available at any time at http://myaccount.copyright.com).

Terms and Conditions

- The materials you have requested permission to reproduce or reuse (the "Wiley Materials") are protected by copyright.

- You are hereby granted a personal, non-exclusive, non-sub licensable (on a stand-alone basis), non-transferable, worldwide, limited license to reproduce the Wiley Materials for the purpose specified in the licensing process. This license, **and any CONTENT (PDF or image file) purchased as part of your order,** is for a one-time use only and limited to any maximum distribution number specified in the license. The first instance of republication or reuse granted by this license must be completed within two years of the date of the grant of this license (although copies prepared before the end date may be distributed thereafter). The Wiley Materials shall not be used in any other manner or for any other purpose, beyond what is granted in the license. Permission is granted subject to an appropriate acknowledgement given to the author, title of the material/book/journal and the publisher. You shall also duplicate the copyright notice that appears in the Wiley publication in your use of the Wiley Material. Permission is also granted on the understanding that nowhere in the text is a previously published source acknowledged for all or part of this Wiley Material. Any third party content is expressly excluded from this permission.

- With respect to the Wiley Materials, all rights are reserved. Except as expressly granted by the terms of the license, no part of the Wiley Materials may be copied, modified, adapted (except for minor reformatting required by the new Publication), translated, reproduced, transferred or distributed, in any form or by any means, and no derivative works may be made based on the Wiley Materials without the prior permission of the respective copyright owner.**For STM Signatory Publishers clearing permission under the terms of the STM Permissions Guidelines only, the terms of the license are extended to include subsequent editions and for editions in other languages, provided such editions are for the work as a whole in situ and does not involve the separate exploitation of the permitted figures or extracts,** You may not alter, remove or suppress in any manner any copyright, trademark or other notices displayed by the Wiley Materials. You may not license, rent, sell, loan, lease, pledge, offer as security, transfer or assign the Wiley Materials on a stand-alone basis, or any of the rights granted to you hereunder to any other person.

- The Wiley Materials and all of the intellectual property rights therein shall at all times remain the exclusive property of John Wiley & Sons Inc, the Wiley Companies, or their respective licensors, and your interest therein is only that of having possession of and the right to reproduce the Wiley Materials pursuant to Section 2 herein during the continuance of this Agreement. You agree that you own no right, title or interest in or to the Wiley Materials or any of the intellectual property rights therein. You shall have no rights hereunder other than the license as provided for above in Section 2. No right, license or interest to any trademark, trade name, service mark or other branding ("Marks") of WILEY or its licensors is granted hereunder, and you agree that you shall not assert any such right, license or interest with respect thereto

- NEITHER WILEY NOR ITS LICENSORS MAKES ANY WARRANTY OR REPRESENTATION OF ANY KIND TO YOU OR ANY THIRD PARTY, EXPRESS, IMPLIED OR STATUTORY, WITH RESPECT TO THE MATERIALS OR THE ACCURACY OF ANY INFORMATION CONTAINED IN THE MATERIALS, INCLUDING, WITHOUT LIMITATION, ANY IMPLIED WARRANTY OF MERCHANTABILITY, ACCURACY, SATISFACTORY QUALITY, FITNESS FOR A PARTICULAR PURPOSE, USABILITY,

INTEGRATION OR NON-INFRINGEMENT AND ALL SUCH WARRANTIES ARE HEREBY EXCLUDED BY WILEY AND ITS LICENSORS AND WAIVED BY YOU.

- WILEY shall have the right to terminate this Agreement immediately upon breach of this Agreement by you.

- You shall indemnify, defend and hold harmless WILEY, its Licensors and their respective directors, officers, agents and employees, from and against any actual or threatened claims, demands, causes of action or proceedings arising from any breach of this Agreement by you.

- IN NO EVENT SHALL WILEY OR ITS LICENSORS BE LIABLE TO YOU OR ANY OTHER PARTY OR ANY OTHER PERSON OR ENTITY FOR ANY SPECIAL, CONSEQUENTIAL, INCIDENTAL, INDIRECT, EXEMPLARY OR PUNITIVE DAMAGES, HOWEVER CAUSED, ARISING OUT OF OR IN CONNECTION WITH THE DOWNLOADING, PROVISIONING, VIEWING OR USE OF THE MATERIALS REGARDLESS OF THE FORM OF ACTION, WHETHER FOR BREACH OF CONTRACT, BREACH OF WARRANTY, TORT, NEGLIGENCE, INFRINGEMENT OR OTHERWISE (INCLUDING, WITHOUT LIMITATION, DAMAGES BASED ON LOSS OF PROFITS, DATA, FILES, USE, BUSINESS OPPORTUNITY OR CLAIMS OF THIRD PARTIES), AND WHETHER OR NOT THE PARTY HAS BEEN ADVISED OF THE POSSIBILITY OF SUCH DAMAGES. THIS LIMITATION SHALL APPLY NOTWITHSTANDING ANY FAILURE OF ESSENTIAL PURPOSE OF ANY LIMITED REMEDY PROVIDED HEREIN.

- Should any provision of this Agreement be held by a court of competent jurisdiction to be illegal, invalid, or unenforceable, that provision shall be deemed amended to achieve as nearly as possible the same economic effect as the original provision, and the legality, validity and enforceability of the remaining provisions of this Agreement shall not be affected or impaired thereby.

- The failure of either party to enforce any term or condition of this Agreement shall not constitute a waiver of either party's right to enforce each and every term and condition of this Agreement. No breach under this agreement shall be deemed waived or excused by either party unless such waiver or consent is in writing signed by the party granting such waiver or consent. The waiver by or consent of a party to a breach of any provision of this Agreement shall not operate or be construed as a waiver of or consent to any other or subsequent breach by such other party.

- This Agreement may not be assigned (including by operation of law or otherwise) by you without WILEY's prior written consent.

- Any fee required for this permission shall be non-refundable after thirty (30) days from receipt by the CCC.

- These terms and conditions together with CCC's Billing and Payment terms and conditions (which are incorporated herein) form the entire agreement between you and WILEY concerning this licensing transaction and (in the absence of fraud) supersedes all prior agreements and representations of the parties, oral or written. This Agreement may not be amended except in writing signed by both parties. This Agreement shall be binding upon and inure to the benefit of the parties' successors, legal representatives, and authorized assigns.

- In the event of any conflict between your obligations established by these terms and conditions and those established by CCC's Billing and Payment terms and conditions,

these terms and conditions shall prevail.

- WILEY expressly reserves all rights not specifically granted in the combination of (i) the license details provided by you and accepted in the course of this licensing transaction, (ii) these terms and conditions and (iii) CCC's Billing and Payment terms and conditions.

- This Agreement will be void if the Type of Use, Format, Circulation, or Requestor Type was misrepresented during the licensing process.

- This Agreement shall be governed by and construed in accordance with the laws of the State of New York, USA, without regards to such state's conflict of law rules. Any legal action, suit or proceeding arising out of or relating to these Terms and Conditions or the breach thereof shall be instituted in a court of competent jurisdiction in New York County in the State of New York in the United States of America and each party hereby consents and submits to the personal jurisdiction of such court, waives any objection to venue in such court and consents to service of process by registered or certified mail, return receipt requested, at the last known address of such party.

WILEY OPEN ACCESS TERMS AND CONDITIONS

Wiley Publishes Open Access Articles in fully Open Access Journals and in Subscription journals offering Online Open. Although most of the fully Open Access journals publish open access articles under the terms of the Creative Commons Attribution (CC BY) License only, the subscription journals and a few of the Open Access Journals offer a choice of Creative Commons Licenses. The license type is clearly identified on the article.

The Creative Commons Attribution License

The Creative Commons Attribution License (CC-BY) allows users to copy, distribute and transmit an article, adapt the article and make commercial use of the article. The CC-BY license permits commercial and non-

Creative Commons Attribution Non-Commercial License

The Creative Commons Attribution Non-Commercial (CC-BY-NC)License permits use, distribution and reproduction in any medium, provided the original work is properly cited and is not used for commercial purposes.(see below)

Creative Commons Attribution-Non-Commercial-NoDerivs License

The Creative Commons Attribution Non-Commercial-NoDerivs License (CC-BY-NC-ND) permits use, distribution and reproduction in any medium, provided the original work is properly cited, is not used for commercial purposes and no modifications or adaptations are made. (see below)

Use by commercial "for-profit" organizations

Use of Wiley Open Access articles for commercial, promotional, or marketing purposes requires further explicit permission from Wiley and will be subject to a fee.

Further details can be found on Wiley Online Library

http://olabout.wiley.com/WileyCDA/Section/id-410895.html

Other Terms and Conditions:

v1.10 Last updated September 2015

Questions? customercare@copyright.com or +1-855-239-3415 (toll free in the US) or +1-978-646-2777.

Copyright Clearance Center RightsLink®

Home Account Info Help LIVE CHAT

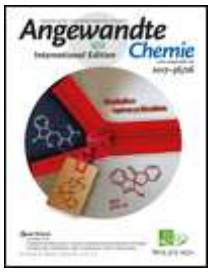

Title:	Raman Microspectroscopic Evidence for the Metabolism of a Tyrosine Kinase Inhibitor, Neratinib, in Cancer Cells
Author:	Karim Aljakouch, Tatjana Lechtonen, Hesham K. Yosef, et al
Publication:	Angewandte Chemie International Edition
Publisher:	John Wiley and Sons
Date:	May 16, 2018

© WILEY-VCH Verlag GmbH & Co. KGaA, Weinheim

Logged in as:
Sally Vanden-Hehir
Account #:
3001395483

LOGOUT

Open Access Article

This article is available under the terms of the Creative Commons Attribution Non-Commercial No Derivatives License CC BY-NC-ND (which may be updated from time to time) and permits **non-commercial** use, distribution, and reproduction in any medium, without alteration, provided the original work is properly cited and it is reproduced verbatim.

For an understanding of what is meant by the terms of the Creative Commons License, please refer to Wiley's Open Access Terms and Conditions.

Permission is not required for **non-commercial** reuse. For **commercial** reuse, please hit the "back" button and select the most appropriate **commercial** requestor type before completing your order.

If you wish to adapt, alter, translate or create any other derivative work from this article, permission must be sought from the Publisher. Please email your requirements to RightsLink@wiley.com.

BACK CLOSE WINDOW

Copyright © 2019 Copyright Clearance Center, Inc. All Rights Reserved. Privacy statement. Terms and Conditions.
Comments? We would like to hear from you. E-mail us at customercare@copyright.com

Note: Copyright.com supplies permissions but not the copyrighted content itself.

1 PAYMENT 2 REVIEW 3 CONFIRMATION

Step 3: Order Confirmation

Thank you for your order! A confirmation for your order will be sent to your account email address. If you have questions about your order, you can call us 24 hrs/day, M-F at +1.855.239.3415 Toll Free, or write to us at info@copyright.com. This is not an invoice.

Confirmation Number: 11825741
Order Date: 06/21/2019

If you paid by credit card, your order will be finalized and your card will be charged within 24 hours. If you choose to be invoiced, you can change or cancel your order until the invoice is generated.

Payment Information

Sally Vanden-Hehir
s1014966@sms.ed.ac.uk
+44 7770420373
Payment Method: n/a

Order Details

Chemical communications

Order detail ID:	71928411
Order License Id:	4613651093308
ISSN:	1364-548X
Publication Type:	e-Journal
Volume:	
Issue:	
Start page:	
Publisher:	ROYAL SOCIETY OF CHEMISTRY
Author/Editor:	Royal Society of Chemistry (Great Britain)

Permission Status: Granted

Permission type: Republish or display content
Type of use: Thesis/Dissertation

Requestor type	Academic institution
Format	Print, Electronic
Portion	chart/graph/table/figure
Number of charts/graphs/tables/figures	1
The requesting person/organization	Sally Vanden-Hehir
Title or numeric reference of the portion(s)	Figure 3
Title of the article or chapter the portion is from	Stimulated Raman scattering of polymer nanoparticles for multiplexed live-cell imaging
Editor of portion(s)	N/A
Author of portion(s)	Fanghao Hu, Spencer D. Brucks, Tristan H. Lambert, Luis M. Campos and Wei Min

Volume of serial or monograph	N/A
Page range of portion	6187-6190
Publication date of portion	2017
Rights for	Main product
Duration of use	Life of current edition
Creation of copies for the disabled	no
With minor editing privileges	no
For distribution to	U.K. and Commonwealth (excluding Canada)
In the following language(s)	Original language of publication
With incidental promotional use	no
Lifetime unit quantity of new product	Up to 499
Title	New tools for visualising nanoparticle drug delivery
Institution name	n/a
Expected presentation date	Aug 2019

Note: This item will be invoiced or charged separately through CCC's **RightsLink** service. More info **$ 0.00**

Total order items: 1

This is not an invoice.

Order Total: 0.00 USD

Confirmation Number: 11825741

Special Rightsholder Terms & Conditions

The following terms & conditions apply to the specific publication under which they are listed

Chemical communications
Permission type: Republish or display content
Type of use: Thesis/Dissertation

TERMS AND CONDITIONS

The following terms are individual to this publisher:

None

Other Terms and Conditions:

STANDARD TERMS AND CONDITIONS

1. Description of Service; Defined Terms. This Republication License enables the User to obtain licenses for republication of one or more copyrighted works as described in detail on the relevant Order Confirmation (the "Work(s)"). Copyright Clearance Center, Inc. ("CCC") grants licenses through the Service on behalf of the rightsholder identified on the Order Confirmation (the "Rightsholder"). "Republication", as used herein, generally means the inclusion of a Work, in whole or in part, in a new work or works, also as described on the Order Confirmation. "User", as used herein, means the person or entity making such republication.

2. The terms set forth in the relevant Order Confirmation, and any terms set by the Rightsholder with respect to a particular Work, govern the terms of use of Works in connection with the Service. By using the Service, the person transacting for a republication license on behalf of the User represents and warrants that he/she/it (a) has been duly authorized by the User to accept, and hereby does accept, all such terms and conditions on behalf of User, and (b) shall inform User of all such terms and conditions. In the event such person is a "freelancer" or other third party independent of User and CCC, such party shall be deemed jointly a "User" for purposes of these terms and conditions. In any event, User shall be deemed to have accepted and agreed to all such terms and conditions if User republishes the Work in any fashion.

3. Scope of License; Limitations and Obligations.

3.1 All Works and all rights therein, including copyright rights, remain the sole and exclusive property of the Rightsholder. The license created by the exchange of an Order Confirmation (and/or any invoice) and payment by User of the full amount set forth on that document includes only those rights expressly set forth in the Order Confirmation and in these terms and conditions, and conveys no other rights in the Work(s) to User. All rights not expressly granted are hereby reserved.

3.2 General Payment Terms: You may pay by credit card or through an account with us payable at the end of the month. If you and we agree that you may establish a standing account with CCC, then the following terms apply: Remit Payment to: Copyright Clearance Center, 29118 Network Place, Chicago, IL 60673-1291. Payments Due: Invoices are payable upon their delivery to you (or upon our notice to you that they are available to you for downloading). After 30 days, outstanding amounts will be subject to a service charge of 1-1/2% per month or, if less, the maximum rate allowed by applicable law. Unless otherwise specifically set forth in the Order Confirmation or in a separate written agreement signed by CCC, invoices are due and payable on "net 30" terms. While User may exercise the rights licensed immediately upon issuance of the Order Confirmation, the license is automatically revoked and is null and void, as if it had never been issued, if complete payment for the license is not received on a timely basis either from User directly or through a payment agent, such as a credit card company.

3.3 Unless otherwise provided in the Order Confirmation, any grant of rights to User (i) is "one-time" (including the editions and product family specified in the license), (ii) is non-exclusive and non-transferable and (iii) is subject to any and all limitations and restrictions (such as, but not limited to, limitations on duration of use or circulation) included in the Order Confirmation or invoice and/or in these terms and conditions. Upon completion of the licensed use, User shall either secure a new permission for further use of the Work(s) or immediately cease any new use of the Work(s) and shall render inaccessible (such as by deleting or by removing or severing links or other locators) any further copies of the Work (except for copies printed on paper in accordance with this license and still in User's stock at the end of such period).

3.4 In the event that the material for which a republication license is sought includes third party materials (such as photographs, illustrations, graphs, inserts and similar materials) which are identified in such material as having been used by permission, User is responsible for identifying, and seeking separate licenses (under this Service or otherwise) for, any of such third party materials; without a separate license, such third party materials may not be used.

3.5 Use of proper copyright notice for a Work is required as a condition of any license granted under the Service. Unless otherwise provided in the Order Confirmation, a proper copyright notice will read substantially as follows: "Republished with permission of [Rightsholder's name], from [Work's title, author, volume, edition number and year of copyright]; permission conveyed through Copyright Clearance Center, Inc. " Such notice must be provided in a reasonably legible font size and must be placed either immediately adjacent to the Work as used (for example, as part of a by-line or footnote but not as a separate electronic link) or in the place where substantially all other credits or notices for the new work containing the republished Work are located. Failure to include the required notice results in loss to the Rightsholder and CCC, and the User shall be liable to pay liquidated damages for each such failure equal to twice the use fee specified in the Order Confirmation, in addition to the use fee itself and any other fees and charges specified.

3.6 User may only make alterations to the Work if and as expressly set forth in the Order Confirmation. No Work may be used in any way that is defamatory, violates the rights of third parties (including such third parties' rights of copyright, privacy, publicity, or other tangible or intangible property), or is otherwise illegal, sexually explicit or obscene. In

addition, User may not conjoin a Work with any other material that may result in damage to the reputation of the Rightsholder. User agrees to inform CCC if it becomes aware of any infringement of any rights in a Work and to cooperate with any reasonable request of CCC or the Rightsholder in connection therewith.

4. Indemnity. User hereby indemnifies and agrees to defend the Rightsholder and CCC, and their respective employees and directors, against all claims, liability, damages, costs and expenses, including legal fees and expenses, arising out of any use of a Work beyond the scope of the rights granted herein, or any use of a Work which has been altered in any unauthorized way by User, including claims of defamation or infringement of rights of copyright, publicity, privacy or other tangible or intangible property.

5. Limitation of Liability. UNDER NO CIRCUMSTANCES WILL CCC OR THE RIGHTSHOLDER BE LIABLE FOR ANY DIRECT, INDIRECT, CONSEQUENTIAL OR INCIDENTAL DAMAGES (INCLUDING WITHOUT LIMITATION DAMAGES FOR LOSS OF BUSINESS PROFITS OR INFORMATION, OR FOR BUSINESS INTERRUPTION) ARISING OUT OF THE USE OR INABILITY TO USE A WORK, EVEN IF ONE OF THEM HAS BEEN ADVISED OF THE POSSIBILITY OF SUCH DAMAGES. In any event, the total liability of the Rightsholder and CCC (including their respective employees and directors) shall not exceed the total amount actually paid by User for this license. User assumes full liability for the actions and omissions of its principals, employees, agents, affiliates, successors and assigns.

6. Limited Warranties. THE WORK(S) AND RIGHT(S) ARE PROVIDED "AS IS". CCC HAS THE RIGHT TO GRANT TO USER THE RIGHTS GRANTED IN THE ORDER CONFIRMATION DOCUMENT. CCC AND THE RIGHTSHOLDER DISCLAIM ALL OTHER WARRANTIES RELATING TO THE WORK(S) AND RIGHT(S), EITHER EXPRESS OR IMPLIED, INCLUDING WITHOUT LIMITATION IMPLIED WARRANTIES OF MERCHANTABILITY OR FITNESS FOR A PARTICULAR PURPOSE. ADDITIONAL RIGHTS MAY BE REQUIRED TO USE ILLUSTRATIONS, GRAPHS, PHOTOGRAPHS, ABSTRACTS, INSERTS OR OTHER PORTIONS OF THE WORK (AS OPPOSED TO THE ENTIRE WORK) IN A MANNER CONTEMPLATED BY USER; USER UNDERSTANDS AND AGREES THAT NEITHER CCC NOR THE RIGHTSHOLDER MAY HAVE SUCH ADDITIONAL RIGHTS TO GRANT.

7. Effect of Breach. Any failure by User to pay any amount when due, or any use by User of a Work beyond the scope of the license set forth in the Order Confirmation and/or these terms and conditions, shall be a material breach of the license created by the Order Confirmation and these terms and conditions. Any breach not cured within 30 days of written notice thereof shall result in immediate termination of such license without further notice. Any unauthorized (but licensable) use of a Work that is terminated immediately upon notice thereof may be liquidated by payment of the Rightsholder's ordinary license price therefor; any unauthorized (and unlicensable) use that is not terminated immediately for any reason (including, for example, because materials containing the Work cannot reasonably be recalled) will be subject to all remedies available at law or in equity, but in no event to a payment of less than three times the Rightsholder's ordinary license price for the most closely analogous licensable use plus Rightsholder's and/or CCC's costs and expenses incurred in collecting such payment.

8. **Miscellaneous.**

8.1 User acknowledges that CCC may, from time to time, make changes or additions to the Service or to these terms and conditions, and CCC reserves the right to send notice to the User by electronic mail or otherwise for the purposes of notifying User of such changes or additions; provided that any such changes or additions shall not apply to permissions already secured and paid for.

8.2 Use of User-related information collected through the Service is governed by CCC's privacy policy, available online here: http://www.copyright.com/content/cc3/en/tools/footer/privacypolicy.html.

8.3 The licensing transaction described in the Order Confirmation is personal to User. Therefore, User may not assign or transfer to any other person (whether a natural person or an organization of any kind) the license created by the Order Confirmation and these terms and conditions or any rights granted hereunder; provided, however, that User may assign such license in its entirety on written notice to CCC in the event of a transfer of all or substantially all of User's rights in the new material which includes the Work(s) licensed under this Service.

8.4 No amendment or waiver of any terms is binding unless set forth in writing and signed by the parties. The Rightsholder and CCC hereby object to any terms contained in any writing prepared by the User or its principals, employees, agents or affiliates and purporting to govern or otherwise relate to the licensing transaction described in the Order Confirmation, which terms are in any way inconsistent with any terms set forth in the Order Confirmation and/or in these terms and conditions or CCC's standard operating procedures, whether such writing is prepared prior to, simultaneously with or subsequent to the Order Confirmation, and whether such writing appears on a copy of the Order Confirmation or in a separate instrument.

8.5 The licensing transaction described in the Order Confirmation document shall be governed by and construed under the law of the State of New York, USA, without regard to the principles thereof of conflicts of law. Any case, controversy, suit, action, or proceeding arising out of, in connection with, or related to such licensing transaction shall be brought, at CCC's sole discretion, in any federal or state court located in the County of New York, State of New York, USA, or in any federal or state court whose geographical jurisdiction covers the location of the Rightsholder set forth in the Order Confirmation. The parties expressly submit to the personal jurisdiction and venue of each such federal or state court.If you have any comments or questions about the Service or Copyright Clearance Center, please contact us at 978-750-8400 or send an e-mail to info@copyright.com.

v 1.1

Close

Confirmation Number: 11825741

Citation Information

Order Detail ID: 71928411

Chemical communications by Royal Society of Chemistry (Great Britain) Reproduced with permission of ROYAL SOCIETY OF CHEMISTRY in the format Thesis/Dissertation via Copyright Clearance Center.

Close

Copyright Clearance Center RightsLink®

Home Account Info Help LIVE CHAT

SPRINGER NATURE

Title:	Label-free Raman microspectral analysis for comparison of cellular uptake and distribution between nontargeted and EGFR-targeted biodegradable polymeric nanoparticles
Author:	Tatyana Chernenko, Fulden Buyukozturk, Milos Miljkovic et al
Publication:	Drug Delivery and Translational Research
Publisher:	Springer Nature
Date:	Jan 1, 2013

Copyright © 2013, Controlled Release Society

Logged in as:
Sally Vanden-Hehir
Account #:
3001395483
LOGOUT

Order Completed

Thank you for your order.

This Agreement between Ms. Sally Vanden-Hehir ("You") and Springer Nature ("Springer Nature") consists of your license details and the terms and conditions provided by Springer Nature and Copyright Clearance Center.

Your confirmation email will contain your order number for future reference.

printable details

License Number	4613090729492
License date	Jun 20, 2019
Licensed Content Publisher	Springer Nature
Licensed Content Publication	Drug Delivery and Translational Research
Licensed Content Title	Label-free Raman microspectral analysis for comparison of cellular uptake and distribution between nontargeted and EGFR-targeted biodegradable polymeric nanoparticles
Licensed Content Author	Tatyana Chernenko, Fulden Buyukozturk, Milos Miljkovic et al
Licensed Content Date	Jan 1, 2013
Licensed Content Volume	3
Licensed Content Issue	6
Type of Use	Thesis/Dissertation
Requestor type	academic/university or research institute
Format	print and electronic
Portion	figures/tables/illustrations
Number of figures/tables/illustrations	1
Will you be translating?	no
Circulation/distribution	<501
Author of this Springer Nature content	no
Title	New tools for visualising nanoparticle drug delivery
Institution name	n/a
Expected presentation date	Aug 2019
Portions	Figure 4
Requestor Location	Ms. Sally Vanden-Hehir Office 54 Joseph Black Building David Brewster Road The King' Buildings Edinburgh, EH9 3FJ

United Kingdom
Attn: Ms. Sally Vanden-Hehir

Total	0.00 GBP

ORDER MORE CLOSE WINDOW

Copyright © 2019 Copyright Clearance Center, Inc. All Rights Reserved. Privacy statement. Terms and Conditions.
Comments? We would like to hear from you. E-mail us at customercare@copyright.com

Note: Copyright.com supplies permissions but not the copyrighted content itself.

1 PAYMENT 2 REVIEW 3 CONFIRMATION

Step 3: Order Confirmation

Thank you for your order! A confirmation for your order will be sent to your account email address. If you have questions about your order, you can call us 24 hrs/day, M-F at +1.855.239.3415 Toll Free, or write to us at info@copyright.com. This is not an invoice.

Confirmation Number: 11825741
Order Date: 06/21/2019

If you paid by credit card, your order will be finalized and your card will be charged within 24 hours. If you choose to be invoiced, you can change or cancel your order until the invoice is generated.

Payment Information

Sally Vanden-Hehir
s1014966@sms.ed.ac.uk
+44 7770420373
Payment Method: n/a

Order Details

Chemical communications

Order detail ID:	71928411
Order License Id:	4613651093308
ISSN:	1364-548X
Publication Type:	e-Journal
Volume:	
Issue:	
Start page:	
Publisher:	ROYAL SOCIETY OF CHEMISTRY
Author/Editor:	Royal Society of Chemistry (Great Britain)

Permission Status: Granted

Permission type: Republish or display content
Type of use: Thesis/Dissertation

Requestor type	Academic institution
Format	Print, Electronic
Portion	chart/graph/table/figure
Number of charts/graphs/tables/figures	1
The requesting person/organization	Sally Vanden-Hehir
Title or numeric reference of the portion(s)	Figure 3
Title of the article or chapter the portion is from	Stimulated Raman scattering of polymer nanoparticles for multiplexed live-cell imaging
Editor of portion(s)	N/A
Author of portion(s)	Fanghao Hu, Spencer D. Brucks, Tristan H. Lambert, Luis M. Campos and Wei Min

Volume of serial or monograph	N/A
Page range of portion	6187-6190
Publication date of portion	2017
Rights for	Main product
Duration of use	Life of current edition
Creation of copies for the disabled	no
With minor editing privileges	no
For distribution to	U.K. and Commonwealth (excluding Canada)
In the following language(s)	Original language of publication
With incidental promotional use	no
Lifetime unit quantity of new product	Up to 499
Title	New tools for visualising nanoparticle drug delivery
Institution name	n/a
Expected presentation date	Aug 2019

Note: This item will be invoiced or charged separately through CCC's **RightsLink** service. More info **$ 0.00**

Total order items: 1

This is not an invoice.

Order Total: 0.00 USD

Confirmation Number: 11825741

Special Rightsholder Terms & Conditions

The following terms & conditions apply to the specific publication under which they are listed

Chemical communications
Permission type: Republish or display content
Type of use: Thesis/Dissertation

TERMS AND CONDITIONS

The following terms are individual to this publisher:

None

Other Terms and Conditions:

STANDARD TERMS AND CONDITIONS

1. Description of Service; Defined Terms. This Republication License enables the User to obtain licenses for republication of one or more copyrighted works as described in detail on the relevant Order Confirmation (the "Work(s)"). Copyright Clearance Center, Inc. ("CCC") grants licenses through the Service on behalf of the rightsholder identified on the Order Confirmation (the "Rightsholder"). "Republication", as used herein, generally means the inclusion of a Work, in whole or in part, in a new work or works, also as described on the Order Confirmation. "User", as used herein, means the person or entity making such republication.

2. The terms set forth in the relevant Order Confirmation, and any terms set by the Rightsholder with respect to a particular Work, govern the terms of use of Works in connection with the Service. By using the Service, the person transacting for a republication license on behalf of the User represents and warrants that he/she/it (a) has been duly authorized by the User to accept, and hereby does accept, all such terms and conditions on behalf of User, and (b) shall inform User of all such terms and conditions. In the event such person is a "freelancer" or other third party independent of User and CCC, such party shall be deemed jointly a "User" for purposes of these terms and conditions. In any event, User shall be deemed to have accepted and agreed to all such terms and conditions if User republishes the Work in any fashion.

3. Scope of License; Limitations and Obligations.

3.1 All Works and all rights therein, including copyright rights, remain the sole and exclusive property of the Rightsholder. The license created by the exchange of an Order Confirmation (and/or any invoice) and payment by User of the full amount set forth on that document includes only those rights expressly set forth in the Order Confirmation and in these terms and conditions, and conveys no other rights in the Work(s) to User. All rights not expressly granted are hereby reserved.

3.2 General Payment Terms: You may pay by credit card or through an account with us payable at the end of the month. If you and we agree that you may establish a standing account with CCC, then the following terms apply: Remit Payment to: Copyright Clearance Center, 29118 Network Place, Chicago, IL 60673-1291. Payments Due: Invoices are payable upon their delivery to you (or upon our notice to you that they are available to you for downloading). After 30 days, outstanding amounts will be subject to a service charge of 1-1/2% per month or, if less, the maximum rate allowed by applicable law. Unless otherwise specifically set forth in the Order Confirmation or in a separate written agreement signed by CCC, invoices are due and payable on "net 30" terms. While User may exercise the rights licensed immediately upon issuance of the Order Confirmation, the license is automatically revoked and is null and void, as if it had never been issued, if complete payment for the license is not received on a timely basis either from User directly or through a payment agent, such as a credit card company.

3.3 Unless otherwise provided in the Order Confirmation, any grant of rights to User (i) is "one-time" (including the editions and product family specified in the license), (ii) is non-exclusive and non-transferable and (iii) is subject to any and all limitations and restrictions (such as, but not limited to, limitations on duration of use or circulation) included in the Order Confirmation or invoice and/or in these terms and conditions. Upon completion of the licensed use, User shall either secure a new permission for further use of the Work(s) or immediately cease any new use of the Work(s) and shall render inaccessible (such as by deleting or by removing or severing links or other locators) any further copies of the Work (except for copies printed on paper in accordance with this license and still in User's stock at the end of such period).

3.4 In the event that the material for which a republication license is sought includes third party materials (such as photographs, illustrations, graphs, inserts and similar materials) which are identified in such material as having been used by permission, User is responsible for identifying, and seeking separate licenses (under this Service or otherwise) for, any of such third party materials; without a separate license, such third party materials may not be used.

3.5 Use of proper copyright notice for a Work is required as a condition of any license granted under the Service. Unless otherwise provided in the Order Confirmation, a proper copyright notice will read substantially as follows: "Republished with permission of [Rightsholder's name], from [Work's title, author, volume, edition number and year of copyright]; permission conveyed through Copyright Clearance Center, Inc. " Such notice must be provided in a reasonably legible font size and must be placed either immediately adjacent to the Work as used (for example, as part of a by-line or footnote but not as a separate electronic link) or in the place where substantially all other credits or notices for the new work containing the republished Work are located. Failure to include the required notice results in loss to the Rightsholder and CCC, and the User shall be liable to pay liquidated damages for each such failure equal to twice the use fee specified in the Order Confirmation, in addition to the use fee itself and any other fees and charges specified.

3.6 User may only make alterations to the Work if and as expressly set forth in the Order Confirmation. No Work may be used in any way that is defamatory, violates the rights of third parties (including such third parties' rights of copyright, privacy, publicity, or other tangible or intangible property), or is otherwise illegal, sexually explicit or obscene. In

addition, User may not conjoin a Work with any other material that may result in damage to the reputation of the Rightsholder. User agrees to inform CCC if it becomes aware of any infringement of any rights in a Work and to cooperate with any reasonable request of CCC or the Rightsholder in connection therewith.

4. Indemnity. User hereby indemnifies and agrees to defend the Rightsholder and CCC, and their respective employees and directors, against all claims, liability, damages, costs and expenses, including legal fees and expenses, arising out of any use of a Work beyond the scope of the rights granted herein, or any use of a Work which has been altered in any unauthorized way by User, including claims of defamation or infringement of rights of copyright, publicity, privacy or other tangible or intangible property.

5. Limitation of Liability. UNDER NO CIRCUMSTANCES WILL CCC OR THE RIGHTSHOLDER BE LIABLE FOR ANY DIRECT, INDIRECT, CONSEQUENTIAL OR INCIDENTAL DAMAGES (INCLUDING WITHOUT LIMITATION DAMAGES FOR LOSS OF BUSINESS PROFITS OR INFORMATION, OR FOR BUSINESS INTERRUPTION) ARISING OUT OF THE USE OR INABILITY TO USE A WORK, EVEN IF ONE OF THEM HAS BEEN ADVISED OF THE POSSIBILITY OF SUCH DAMAGES. In any event, the total liability of the Rightsholder and CCC (including their respective employees and directors) shall not exceed the total amount actually paid by User for this license. User assumes full liability for the actions and omissions of its principals, employees, agents, affiliates, successors and assigns.

6. Limited Warranties. THE WORK(S) AND RIGHT(S) ARE PROVIDED "AS IS". CCC HAS THE RIGHT TO GRANT TO USER THE RIGHTS GRANTED IN THE ORDER CONFIRMATION DOCUMENT. CCC AND THE RIGHTSHOLDER DISCLAIM ALL OTHER WARRANTIES RELATING TO THE WORK(S) AND RIGHT(S), EITHER EXPRESS OR IMPLIED, INCLUDING WITHOUT LIMITATION IMPLIED WARRANTIES OF MERCHANTABILITY OR FITNESS FOR A PARTICULAR PURPOSE. ADDITIONAL RIGHTS MAY BE REQUIRED TO USE ILLUSTRATIONS, GRAPHS, PHOTOGRAPHS, ABSTRACTS, INSERTS OR OTHER PORTIONS OF THE WORK (AS OPPOSED TO THE ENTIRE WORK) IN A MANNER CONTEMPLATED BY USER; USER UNDERSTANDS AND AGREES THAT NEITHER CCC NOR THE RIGHTSHOLDER MAY HAVE SUCH ADDITIONAL RIGHTS TO GRANT.

7. Effect of Breach. Any failure by User to pay any amount when due, or any use by User of a Work beyond the scope of the license set forth in the Order Confirmation and/or these terms and conditions, shall be a material breach of the license created by the Order Confirmation and these terms and conditions. Any breach not cured within 30 days of written notice thereof shall result in immediate termination of such license without further notice. Any unauthorized (but licensable) use of a Work that is terminated immediately upon notice thereof may be liquidated by payment of the Rightsholder's ordinary license price therefor; any unauthorized (and unlicensable) use that is not terminated immediately for any reason (including, for example, because materials containing the Work cannot reasonably be recalled) will be subject to all remedies available at law or in equity, but in no event to a payment of less than three times the Rightsholder's ordinary license price for the most closely analogous licensable use plus Rightsholder's and/or CCC's costs and expenses incurred in collecting such payment.

8. **Miscellaneous.**

8.1 User acknowledges that CCC may, from time to time, make changes or additions to the Service or to these terms and conditions, and CCC reserves the right to send notice to the User by electronic mail or otherwise for the purposes of notifying User of such changes or additions; provided that any such changes or additions shall not apply to permissions already secured and paid for.

8.2 Use of User-related information collected through the Service is governed by CCC's privacy policy, available online here: http://www.copyright.com/content/cc3/en/tools/footer/privacypolicy.html.

8.3 The licensing transaction described in the Order Confirmation is personal to User. Therefore, User may not assign or transfer to any other person (whether a natural person or an organization of any kind) the license created by the Order Confirmation and these terms and conditions or any rights granted hereunder; provided, however, that User may assign such license in its entirety on written notice to CCC in the event of a transfer of all or substantially all of User's rights in the new material which includes the Work(s) licensed under this Service.

8.4 No amendment or waiver of any terms is binding unless set forth in writing and signed by the parties. The Rightsholder and CCC hereby object to any terms contained in any writing prepared by the User or its principals, employees, agents or affiliates and purporting to govern or otherwise relate to the licensing transaction described in the Order Confirmation, which terms are in any way inconsistent with any terms set forth in the Order Confirmation and/or in these terms and conditions or CCC's standard operating procedures, whether such writing is prepared prior to, simultaneously with or subsequent to the Order Confirmation, and whether such writing appears on a copy of the Order Confirmation or in a separate instrument.

8.5 The licensing transaction described in the Order Confirmation document shall be governed by and construed under the law of the State of New York, USA, without regard to the principles thereof of conflicts of law. Any case, controversy, suit, action, or proceeding arising out of, in connection with, or related to such licensing transaction shall be brought, at CCC's sole discretion, in any federal or state court located in the County of New York, State of New York, USA, or in any federal or state court whose geographical jurisdiction covers the location of the Rightsholder set forth in the Order Confirmation. The parties expressly submit to the personal jurisdiction and venue of each such federal or state court.If you have any comments or questions about the Service or Copyright Clearance Center, please contact us at 978-750-8400 or send an e-mail to info@copyright.com.

v 1.1

Close

Confirmation Number: 11825741

Citation Information

Order Detail ID: 71928411

Chemical communications by Royal Society of Chemistry (Great Britain) Reproduced with permission of ROYAL SOCIETY OF CHEMISTRY in the format Thesis/Dissertation via Copyright Clearance Center.

Close

Copyright Clearance Center RightsLink®

Home Account Info Help LIVE CHAT

SPRINGER NATURE

Title:	Label-free Raman microspectral analysis for comparison of cellular uptake and distribution between nontargeted and EGFR-targeted biodegradable polymeric nanoparticles
Author:	Tatyana Chernenko, Fulden Buyukozturk, Milos Miljkovic et al
Publication:	Drug Delivery and Translational Research
Publisher:	Springer Nature
Date:	Jan 1, 2013

Copyright © 2013, Controlled Release Society

Logged in as:
Sally Vanden-Hehir
Account #:
3001395483
LOGOUT

Order Completed

Thank you for your order.

This Agreement between Ms. Sally Vanden-Hehir ("You") and Springer Nature ("Springer Nature") consists of your license details and the terms and conditions provided by Springer Nature and Copyright Clearance Center.

Your confirmation email will contain your order number for future reference.

printable details

License Number	4613090729492
License date	Jun 20, 2019
Licensed Content Publisher	Springer Nature
Licensed Content Publication	Drug Delivery and Translational Research
Licensed Content Title	Label-free Raman microspectral analysis for comparison of cellular uptake and distribution between nontargeted and EGFR-targeted biodegradable polymeric nanoparticles
Licensed Content Author	Tatyana Chernenko, Fulden Buyukozturk, Milos Miljkovic et al
Licensed Content Date	Jan 1, 2013
Licensed Content Volume	3
Licensed Content Issue	6
Type of Use	Thesis/Dissertation
Requestor type	academic/university or research institute
Format	print and electronic
Portion	figures/tables/illustrations
Number of figures/tables/illustrations	1
Will you be translating?	no
Circulation/distribution	<501
Author of this Springer Nature content	no
Title	New tools for visualising nanoparticle drug delivery
Institution name	n/a
Expected presentation date	Aug 2019
Portions	Figure 4
Requestor Location	Ms. Sally Vanden-Hehir Office 54 Joseph Black Building David Brewster Road The King' Buildings Edinburgh, EH9 3FJ

United Kingdom
Attn: Ms. Sally Vanden-Hehir

Total	0.00 GBP

ORDER MORE CLOSE WINDOW

Copyright © 2019 Copyright Clearance Center, Inc. All Rights Reserved. Privacy statement. Terms and Conditions.
Comments? We would like to hear from you. E-mail us at customercare@copyright.com